Coordinated Control of Distributed Energy Resources in Islanded Microgrids

A Thesis by Publication submitted in
Partial Fulfilment of the Requirement for the
Degree of

Doctor of Philosophy

Mohammad Sadegh Golsorkhi Esfahani

Center of Excellence in Power Engineering,
School of Electrical and Information Engineering,

The University of Sydney,
Sydney, Australia

This is to certify that to the best of my knowledge, the content of this thesis is my own work. This thesis has not been submitted for any degree or other purposes.

Date: October 2016

Acknowledgement

My sincere appreciation goes to my supervisor Associate Prof. Dylan D.C. Lu and my associate supervisor Prof. David John Hill for their continuous support of my PhD study and research. Their supervision and encouragement helped me to shape my ideas and organize my research.

I would like to thank Prof. Josep M. Guerrero for providing the opportunity of experimental implementation of my control ideas. I would like to also thank the members of the microgrid research group of Aalborg University, especially Associate Prof. Juan C. Vasquez, Dr. Mehdi Savaghebi and Dr. Qobad Shafiei for their cooperation.

In addition, I would like to express my gratitude The University of Sydney for financial support and providing me with a great research area.

I would like to express my sincere gratitude to my wife for her patience, encouragement and kind support. Last but not the least, I would like to thank my parents for their encouragement and support.

Abstract

As the penetration of the distributed energy resources (DERs) in the power grid increases, new challenges are revealed, including: stability issues, frequency fluctuations, voltage control, protection system coordination, etc. A systematic approach for dealing with those issues is to view the DERs and associated loads as a subsystem or a microgrid (MG). MGs can operate either in the grid connected or islanded modes. As opposed to the grid connected mode, the voltage and frequency regulation and load/generation balancing during islanded mode is solely dependent on the local generation units. Therefore, stable and reliable operation of islanded MGs requires a real time coordinated control scheme. Conventionally, such coordination is achieved by means of the active power-frequency and reactive power-voltage droop control schemes. The conventional droop method, which is based on P-f droop concept in power systems, lacks compatibility with the resistive nature of networks as well as the low inertia of electronically interfaced DER units in MGs. As a result, it features a slow dynamic response but also a low power quality due to frequency and voltage fluctuations.

This PhD research proposes a novel droop concept based on the global positioning system (GPS) and voltage-current (V-I) droop characteristics for coordination of inverter-based DER units in islanded MGs. The concept of V-I droop control is introduced in Chapter 2. In this control approach, each DER is equipped with a GPS receiver, which produces a pulse at frequency of 1Hz (1PPS). Since all GPS receivers are locked to atomic clocks of the GPS satellites, the 1PPS signal can be utilized to synchronize the time reference of the DER units. Using the common time reference and fixing the frequency at the nominal value, all of the units can share a common synchronous rotating reference frame (SRRF). Furthermore, proportional load sharing is achieved by drooping the d and q axis components of the reference voltage with respect to the d and q axis components of current, respectively. The proposed scheme not only circumvents the issue of frequency fluctuations but also is in accordance with the fast dynamics of inverter-based DER units and resistive nature of the networks in islanded MGs.

The V-I droop scheme, in its basic form, relies on availability of GPS signals at each of the DER units. With the intention of improving the MG robustness with respect to GPS signal failure, a new control strategy based on V-I droop concept is presented Chapter 3. In this method, an adaptive reactive power-frequency droop scheme is used as a backup for the V-I droop controller to ensure synchronization in case of a GPS signal failure.

Droop control schemes in general, and the proposed V-I droop strategy in particular are characterized by non-ideal sharing of current among the DER units due to the variations of voltage along the MGs. In order to improve the sharing accuracy of the V-I droop scheme

while regulating the average voltage at the nominal value, a new distributed secondary control method based on consensus protocol is proposed in Chapter 4. In this method, the d-axis droop characteristics is altered so as to regulate the average microgrid voltage to the rated value but also guarantee proper sharing of active power among the DERs. Additionally, the q-axis component of voltage is adjusted to perform proper sharing of current.

Generally, DERs might be supplied from different energy sources, including renewables and storage systems. The intermittency of renewable energy resources on one hand and the limited capacity of the energy storage systems on the other hand, necessitate modification of droop characteristics based on an energy management plan. In Chapter 5, a novel distributed secondary control strategy is introduced for power management of integrated photovoltaic-battery DER units in islanded MGs. The distributed secondary controllers are coordinated based on a leader-follower framework, where the leader restores the MG voltage to the rated value and the followers pursue energy management.

Unbalanced and nonlinear loads, which are quite common in MGs, adversely affect the power quality and sharing accuracy. In order to mitigate those issues, two new solutions are proposed in this thesis. In the first approach (Chapter 6), a new supplementary droop control scheme is added to the V-I droop controller to reduce the voltage unbalance while preventing current and power overload under unbalanced loading conditions. In the second approach (Chapter 7), a hierarchical control scheme, consisting of primary (modified V-I droop) and distributed secondary control levels is introduced to mitigate harmonic distortions and prevent overcurrent stresses under nonlinear and unbalanced loading conditions.

Finally, the conclusions and possible future work are addressed in Chapter 8.

Keywords

Distributed control, distributed energy resources, dispersed storage and generation, droop, global positioning system, inverters, micro-grid, model predictive control, power sharing, power quality, robustness, secondary control, unbalance.

List of Publications

The University of Sydney allows the inclusion of the published material in the body of the thesis for the degree of Doctor of Philosophy. The core of each of the chapters of this thesis has been presented in the following conference and journal papers. I declare that I designed the study, analyzed the data and wrote the draft of each of these publications. The co-authors had a supervisory role.

- **Chapter 2:**

1. M. S. Golsorkhi and D. D. C. Lu, "A Control Method for Inverter-Based Islanded Microgrids Based on V-I Droop Characteristics," ***IEEE Trans. Power Del.***, vol. 30, pp. 1196-1204, Jun. 2015.
2. M. S. Golsorkhi and D. D. C. Lu, "A decentralized power flow control method for islanded microgrids using V-I droop," *in Proc. Iranian Conference on Electrical Engineering (ICEE)*, 2014, pp. 604-609.

- **Chapter 3:**

3. M. Golsorkhi, D.D.C. Lu, and J. Guerrero, "A GPS-Based Decentralized Control Method for Islanded Microgrids," ***IEEE Trans. Power Electron.***, Apr. 2016 (Early access).

- **Chapter 4:**

4. M. Golsorkhi, Q. Shafiee, D.D.C. Lu, and J. Guerrero, "Distributed Voltage Control and Load Sharing for Inverter-Interfaced Microdrid with Resistive Lines," *in Proc. IEEE Energy Conversion Congress and Exposition (ECCE)*, 2016.

- **Chapter 5:**

5. M.S. Golsorkhi, Q. Shafiee, D.D.C. Lu and Josep M. Guerrero, "A Distributed Control Framework for Integrated Photovoltaic-Battery Based Islanded Microgrids," ***IEEE Trans. Smart Grids***, Jul. 2016 (Early access).

- **Chapter 6:**

6. M. S. Golsorkhi and D. D. C. Lu, "A Decentralized Control Method for Islanded Microgrids Under Unbalanced Conditions," ***IEEE Trans. Power Del.***, vol. 31, pp. 1112-1121, Jun. 2016.
7. M. S. Golsorkhi and D. D. C. Lu, "A decentralized negative sequence compensation method for islanded mirogrids," *in Proc. International Symposium on Power Electronics for Distributed Generation Systems (PEDG),* 2015, pp. 1-7.

- **Chapter 7:**

8. M. S. Golsorkhi, D. D. C. Lu, M. Savaghebi, J. C. Vasquez, and J. M. Guerrero, "A GPS-based control method for load sharing and power quality improvement in microgrids," in *Proc. International Power Electronics and Motion Control Conference (IPEMC-ECCE Asia), 2016*, pp. 3734-3740.
9. M.S. Golsorkhi, M. Savaghebi, D.D.C. Lu, J. M. Guerrero, and J. C. Vasquez, "A GPS- Based Control Framework for Accurate Current Sharing and Power Quality Improvement in Microgrids," *Submitted to* ***IEEE Trans. Power Electron***. Sept. 2016 (Early access).

Scholarships and Awards

- International research postgraduate scholarship (IPRS): Feb. 2013-July 2016.
- Australian Postgraduate Award (APA): Feb. 2013-July 2016.
- ABB prize for the best research poster at Student Research Conversazione, University of Sydney, 2014
- Postgraduate Research Support Scheme(PRSS), University of Sydney, 2014 & 2015.

Exchange Studentship

The experimental studies presented in this thesis were conducted in the Intelligent Microgrid Laboratory of Aalborg University, Denmark, where the author spent one year as a guest PhD student.

Contents

Table of figures

List of tables

Chapter 1
Introduction

1-1 Definition of the research problem

Recently, the interest toward the use of distributed energy resources (DERs) has evolved as a response to significant issues, such as scarcity of fossil fuel in future, deregulation of electric utility industries and public awareness on environmental impact of traditional electric power generation. As the penetration of DERs in the power grid increases, new challenges are revealed, including: stability issues, frequency fluctuations, voltage control, protection system coordination, etc. One way to deal with the aforementioned issues is to take a system approach which views DERs and associated loads as a subsystem or a microgrid (MG) [1]. MGs may be disconnected from the rest of the power system, under emergency conditions or as planned, and operated as an island, providing uninterruptable power supply for the local loads. In this sense, the energy problems can be largely solved locally hence improving the system performance and reliability [2].

MGs might consist of several DERs, including renewable energy sources, micro-turbines and storage systems. Each DER has specific limitations in terms of controllability, capacity and response time. Moreover, the loads are more distributed compared to the conventional power systems. Therefore, in order to achieve stable operation as well as good voltage and frequency regulation, a cooperative control of the DERs is of prominent importance.

1-1-1 Control hierarchy in MGs

The MG control has been an active research topic in the past few years. Generally, the control schemes can be categorized into three control levels:

1- Primary control, which is responsible for regulation of the voltage and frequency, sharing the load active and reactive power among the DERs and preventing the flow of circulating currents between the DERs.

2- Secondary control, which aims to improve the power quality, adjust the power generation of DERs according to technical requirements and enable smooth connection/disconnection of the MG from the main network.

3- Tertiary control, which adjusts the power generation of DERs to achieve a cost effective operation.

The control response time increases with the control level, i.e., the primary control is fastest and the tertiary control level is the slowest control level. This thesis is focused on primary and secondary control levels.

1-1-1-1 Primary control level

The most obvious solution for the primary control is utilizing a centralized control. The centralized controller should collect feedback signals including voltages and currents from the DERs and send control commands (e.g., reference voltages, currents) to the DERs. However, the implementation of a centralized controller at the primary level requires a high bandwidth communication link, which increases the system cost. In addition, this scheme is not reliable since even a short time interruption of communication signals or failure of the central controller results in instability.

In order to prevent these problems, decentralized control strategies are adopted in practice. In this case each DER is controlled by a droop-based local controller. Droop control methods utilize some electrical parameters such as frequency (f) and voltage (E) as a signal for coordination of the local controllers.

The conventional droop method, which is inspired from P-f droop method in conventional power systems, coordinates the active (P) and reactive power (Q) generations based on P-f and Q-E droop characteristics. The conventional droop is developed based on the assumptions of small magnitude of the voltage angle, highly inductive network impedance, large inertia of generation sources, and smooth variations of the load. Due to the resistive nature of the network impedance, utilization of power electronics interfaces at the output stage of the DERs, and the small size of the system, those assumptions are invalid in case of low voltage MGs. As a result, the conventional droop method exhibits a poor dynamic response, which in turn causes transient overcurrent stresses on DERs.

1-1-1-2 Secondary control level

In general, the droop control schemes are characterized by some important limitations. Firstly, the load changes give rise to voltage and/or frequency deviations. Secondly, the large value of the network impedance in weak low voltage MGs degrades the load sharing accuracy of the droop-based methods. Thirdly, the advanced energy management policies, such as management of the state of charge of batteries are difficult to implement at the primary level.

To cope with the aforementioned issues, a secondary control level is added to the control structure. In its basic form, the secondary control level is comprised of a central controller, which broadcasts some correction signals to the primary controllers via a low bandwidth communication network [3]. However, the centralized approach exposes a single point of failure, i.e., any failure in the central controller affects the entire system. Moreover, the implementation of centralized control structure requires an extensive and costly communication network [4]. In response to those problems, the distributed secondary control architecture has been proposed in the literature. The distributed control frameworks are comprised of local control agents, which are interconnected through a sparse communication network [5].

Distributed control methods have recently gained attraction in various area of MG control, e.g., for the elimination of voltage and frequency deviations caused by the primary droop controllers [6-10], load power sharing, economic profitability [11], voltage control [12], [13], and state of charge balancing [14-16] as main ones. However, the existing secondary control schemes are mainly based on the assumption of inductive network impedance. Moreover, the potential of distributed control strategies for the coordination of hybrid photovoltaic-battery DER units has not been exploited.

1-1-2 Power quality

Low voltage distribution networks in general and MGs in particular, single-phase loads are more common than three-phase. As a consequence, the load currents are largely unbalanced. Unbalanced load current gives rise to negative sequence voltage [17], which degrades the power quality. The negative sequence voltage and current can be controlled by adjusting the negative sequence output impedance of DERs [18-22], or injecting a negative sequence compensating voltage [23], or a combination of both methods [22]. However, an increase of compensation effort or a decrease of negative sequence impedance alters the flow of negative sequence current in MGs, which in turn degrades the negative sequence current sharing accuracy. On top of that, the conventional current limiting mechanisms cannot function properly under unbalanced conditions. Therefore, some DERs might experience overcurrent stresses.

Another power quality issue in MGs is the harmonic distortion caused by nonlinear loads. In order to enable accurate sharing of nonlinear and unbalanced loads among the DER units, various control methods have been developed [24-27], among which virtual impedance-based schemes are the most widely accepted [25]. The virtual impedance methods achieve proper sharing of negative sequence and harmonic currents by emulating the virtual impedance at the output stage of each unit. However, in weak islanded MG, where the line impedance is considerable, accurate load current sharing requires large virtual impedances which may produce a large voltage distortion [28]. Therefore, there is a trade-off between current sharing accuracy and power quality.

To compensate for the voltage drop on the lines, a virtual capacitance [29] or an adaptive negative virtual resistance [30] can be employed. However, those schemes require the knowledge of line impedances and network topology. An alternative approach is to compensate the voltage distortions by means of a secondary controller [31]. However, the method of [31] has some important limitations. Firstly, to minimize the communication bandwidth, a set of Park and inverse Park transformations are included in the secondary and primary control levels. On the other hand, the reference angles used for those transformations are the local voltage angles, which have a different value for each of the DER units. Therefore, a transformation error arises which interferes with the current sharing scheme and degrades voltage quality. Secondly, this method is not only complex to implement but also suffers from slow dynamic response.

1-2 Objectives of the thesis

The main objectives of the thesis are as follows.

1- Proposing a new droop control strategy with the following key features:
- Fixed frequency operation
- Fast dynamic response
- Compatible with the resistive nature of the network impedance
- Simple control structure

2- Development of distributed secondary control frameworks based on the proposed droop strategy to
- enhance the accuracy of power and current sharing among the DER units, and
- enable the management of renewable energy resources as well as energy storage units in smart MGs.

3- Improvement of current sharing accuracy and power quality of the MG under unbalanced and/or nonlinear loading conditions.

1-3 Specific contributions of the thesis

The thesis can be divided into three main parts, each of which is in accordance with one of the aforementioned objectives.

1-3-1 Part 1

The first stage of the conventional droop method is the active and reactive power calculation block. The use of low pass filters or averaging blocks in power calculation introduces an inherent delay in the droop control characteristics, which slows down the dynamic response.

Over the recent years, several droop-based strategies are proposed in the literature to enhance the dynamics of the conventional droop method [24-26, 32-37]. Despite diversity of the techniques, all of the existing droop based strategies use some form of power-based droop characteristics (P-f /Q-E, P-δ/Q-E or P-V/Q-f droop) as the core of the control scheme and attempt to improve the dynamic response by means of additional control functions. An alternative solution, which is prosed in the second chapter of the thesis, is replacement of power-based droop with a voltage-current (V-I) droop characteristic.

In the proposed method, the DER units are synchronized by using a global positioning system (GPS) as time reference. The load current is shared between the DERs by drooping the d-q voltages of the DERs according to the corresponding currents. The key contributions of the V-I droop scheme are:

- By using GPS timing technology, all of the DER units are synchronized to a common synchronous rotating reference frame. In this sense, the frequency is fixed at the nominal value, hence removing the frequency fluctuations caused by P-f (or Q-f) droop methods.
- Simplifies the nonlinear control problem of P/Q sharing to linear problem of current sharing. This strategy is also consistent with the resistive nature of the network impedance in low voltage MGs.
- Fast dynamic response gained from direct control of current instead of power.
- Since the inverter voltage variations are small, the active and reactive power are also proportionally shared among the units.
- In order to increase damping as well as power sharing accuracy at high loading conditions, when the DERs are vulnerable to overload, a piecewise linear droop function is adopted.

GPS timing technology has been exploited in several MG control strategies for synchronization of DER units [33, 37-39]. Nevertheless, the GPS-based MG control methods have been studied using computer simulations. Therefore, the practical issues concerning GPS synchronization have been largely neglected. The most important issue is the interruption of the GPS signal, which might result in circulating currents between the DERs or instability depending on the duration of interruption. Another issue is the interfacing of the GPS receivers with the local controllers.

In this thesis (Section 2-6), the GPS timing method is implemented in the intelligent MG lab of Aalborg University. In order to enhance the robustness of the V-I droop scheme with respect to GPS interruptions, a new droop control strategy is proposed in Chapter 3. In this method, the reference angle of each DER unit is obtained from a combination of GPS timing and an adaptive Q-f droop controller. In case that the GPS signal of a DER fails, the backup Q-f droop is activated to maintain synchronization with other DERs. The synchronization scheme does not require any information about the availability of GPS signal at other DER units. In addition, stable operation is guaranteed regardless of the number of DERs with GPS failure.

1-3-2 Part 2

In order to improve the power and current sharing accuracy and voltage profile in low-voltage resistive MGs, a distributed secondary control method is proposed in Chapter 4. In this method, the d-axis voltage is adjusted so as to regulate the average MG voltage to the rated value while ensuring proper active power sharing. Moreover, the q-axis voltage is altered such that the load current and accordingly the reactive power are proportionally shared between the DERs.

The increased penetration of rooftop photovoltaic (PV) panels in low voltage distribution networks might cause several technical problems due to the mismatch between generation and demand throughout the day. Therefore, distribution system operators tend to encourage the installation of energy storage units (ESU) as well as controllable loads, which enable active participation of consumers in load/generation balance [40]. This new infrastructure avails providing the local consumers with a high quality and reliable power source in the context of smart MG.

In Chapter 5, a distributed secondary controller is proposed for PV+ESU based MGs in the islanded operation mode. In this method, the leader regulates the voltage in the whole MG, while the followers are responsible to manage the power sharing among the ESUs in the MG. Furthermore, the state of charge management is directly incorporated into the distributed control algorithm. In contrast with the existing methods in [41, 42], where coordination of a single hybrid PV-ESU unit with the other DERs is studied, the proposed approach enables coordinated control of MGs consisting of multiple hybrid PV-ESU units. Additionally, a distributed load shedding and PV curtailment strategy is adapted to assure the State of Charge (SoC) of each ESUs is maintained within safe operating region.

1-3-3 Part 3

As mentioned in Section 1-1-2, unbalanced load currents not only give rise to unbalanced voltages but also adversely affect the performance of the conventional current limiting mechanisms. The later might result in over current stress on the distributed energy resources (DERs) or current harmonics. In order to improve the power quality and protect DERs from overload, a decentralized droop control scheme is presented in Chapter 6. The proposed controller is comprised of three parts, including: 1) V-I droop controller as the current sharing mechanism, 2) A gain scheduled negative sequence droop controller, which adaptively adjusts the negative sequence impedance of the DER, so as to enhance the sharing accuracy of the negative sequence current among the DERs, and 3) A model predictive controller, which is responsible for minimizing the voltage unbalance, improving the current limiting and preventing active power overload.

With the intention of enhancing the current sharing accuracy and power quality in presence of nonlinear and/or unbalanced loads, a hierarchical control strategy is presented in Chapter 7. This control framework is composed of:

1- Adaptive V-I droop control scheme, which adjusts the droop coefficient according to the peak of the output current. This approach highlights the significance of limiting the peak output current of each DG unit within its current ratings.
2- Distributed power sharing controller, which uses a consensus protocol to ensure proportional sharing of average power.
3- Voltage conditioning scheme, which uses a simple integral controller to compensate the voltage deviations and distortions at the Sensitive Load Bus (SLB).

Chapter 2

V-I droop control method

2-1 Introduction

The decentralized control methods utilize P-f and Q-E droop characteristics to control active and reactive power flow in MGs, respectively. The P-f / Q-E droop scheme is based on highly inductive networks, in which active and reactive power flow equations can be decoupled. Moreover, it is characterized by slow dynamics [41] and frequency and voltage drifts with the load change [43]. The aforementioned characteristics are in accordance with the high X/R ratio of the network impedance and large inertia of turbine-governor systems in conventional power systems. Moreover, since the variations of aggregated loads in high voltage systems are smooth, the resulting frequency drifts can be compensated by a low bandwidth secondary controller. In MGs, however, lines impedances are mostly resistive, DERs have a small inertia and frequent step load changes might occur.

Unlike the conventional power systems, the X/R ratio in MGs is not large. Therefore, the active and reactive power flows are highly coupled and at the same time dependent on f (hence δ) and E. That results in poor performance of the conventional droop method, which is based on decoupled P-f and Q-E control. To overcome this issue, different controllers are proposed [25, 26, 32, 33]. In [32] virtual PQ method has been used to simulate an inductive system, where the P-f and Q-E droops are decoupled. In [26] a virtual reactance is introduced at the inverter output to increase the X/R ratio. In [25] a virtual resistance is introduced at the inverter output to make the system prominently resistive, in which P and Q can be controlled by drooping E and f, respectively.

The P-f/Q-E droop scheme suffers from power quality issues including frequency and voltage deviations. Frequency deviations can be eliminated by utilizing P-δ droop instead of the P-f droop [33]. In that method, global positioning system (GPS) is utilized as a time reference, to synchronize DER units. This allows even power sharing by directly controlling DERs power angle (δ). In [34] an adaptive voltage droop method has been introduced to improve voltage regulation at the point of common coupling (PCC) and alleviate the coupling between P and Q droop controllers.

The power droop control methods are intrinsically low bandwidth controllers with slow dynamics. Moreover, increasing droop coefficients results in a degraded dynamic response and ultimately instability [24]. The stability of the P- δ droop method can be improved by adding a supplementary controller, which controls the voltage amplitude based on the variations of P [35]. Ref [44] has replaced the linear supplementary controller by a nonlinear controller to maintain system stability even in case of large signal disturbances. In [24] an adaptive derivative term has been added to the P and Q droop controllers to decrease current overshoot and improve stability.

In [36] an adaptive feed-forward control scheme is proposed to eliminate the dependency of MG performance and stability on droop coefficient and load dynamics. The scheme reshapes the conventional droop characteristics by injecting two supplementary control signals in the voltage control loop. However, the performance of the method is dependent on an identification mechanism, which is used to calculate feed-forward gain. Ref [45] has improved the method by using a gain scheduled scheme.

The existing communication-less MG control methods utilize P-f(δ) and Q-E or P-E and Q-f(δ) droop characteristics. This chapter proposes an alternative approach, in which the problem of power sharing is simplified to current sharing. In this method, the DER units are synchronized by means of GPS timing technology. Assuming a fixed frequency, the reference angle of each of the units is locked to common synchronous rotating reference frame (SRRF). In this context, the active and reactive power generation of the DERs are coordinated through v_d-i_d and v_q-i_q droop characteristics. This approach simplifies the nonlinear control problem of P/Q sharing to linear problem of current sharing. In addition, with the inherent delay of P/Q measurement eliminated, the controller reacts quickly subsequent to load changes. Since the inverter voltage variations are small, the objectives of P and Q sharing are satisfied. By applying the method to a MG, it is shown that the system dynamic response depends on droop function. A piecewise linear droop function is adopted to increase damping as well as power sharing accuracy at high loading conditions, when the DERs are vulnerable to overload.

The majority of the content of this chapter has been published in [46] and [47]. The rest of the chapter is organized, as follows. A detailed literature review on the existing droop control schemes is presented in Section 2-2. In Section 2-3, GPS timing technology is introduced as an effective approach for synchronization of the DER units. The proposed V-I droop strategy is detailed in Section 2-4. The proposed approach is validated by computer simulations (Section 2-5) and experimental results (Section 2-6). Summary and conclusions are discussed in Section 2-7.

2-2 Literature review

In this section, the application of the droop control technique for the MG control is detailed. The shortcomings of the conventional droop are discussed and the proposed solutions are provided.

2-2-1 Droop control fundamentals

The basic idea of the droop strategy comes from the power flow equations of a synchronous generator connected to an infinite bus [48]:

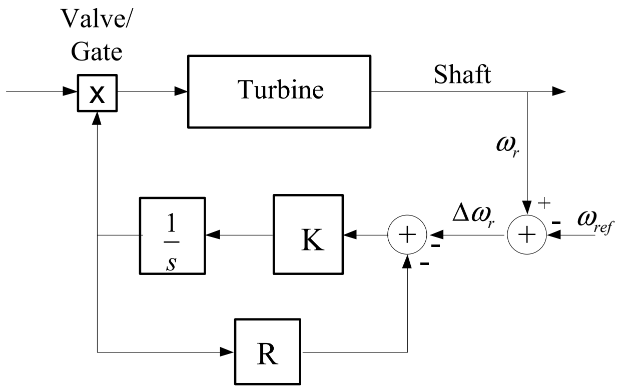

Fig. 2-1 Conventional P-f droop scheme

$$P = \frac{VE}{Z}\sin\delta\sin\theta + \frac{V}{Z}(E\cos\delta - V)\cos\theta \tag{2-1}$$

$$Q = \frac{V}{Z}(E\cos\delta - V)\sin\theta - \frac{VE}{Z}\sin\delta\cos\theta \tag{2-2}$$

where, V, E and δ are the infinite bus voltage, generator emf and generator power angle and Z and θ are the absolute value and angle of the equivalent impedance. In case a pure inductive impedance (θ=90°), the second terms in the above equations are eliminated. For small variations of E and δ the equations can be linearized, as follows:

$$\Delta P = \frac{VE_0}{X}\Delta\delta \tag{2-3}$$

$$\Delta Q = \frac{V}{X}\Delta E \tag{2-4}$$

where E_0 is the rated voltage.

Therefore, the P can be controlled by changing δ (or f) and Q can be controlled by changing E. This has been utilized in power systems to derive droop characteristics. Fig. (2-

1) depicts the conventional P-f droop scheme [49]. The Droop is actually an inner feedback loop (R), which introduces a drop in the speed control loop of the turbine. The speed drop is directly proportional to the valve position, which is proportionally related to the mechanical power. As a result, the plant output frequency drops with the increase of the output power. This characteristic is known as the P-f droop. Since the frequency is constant all over the grid, this characteristic can be utilized for power sharing between different power plants without any communication requirements.

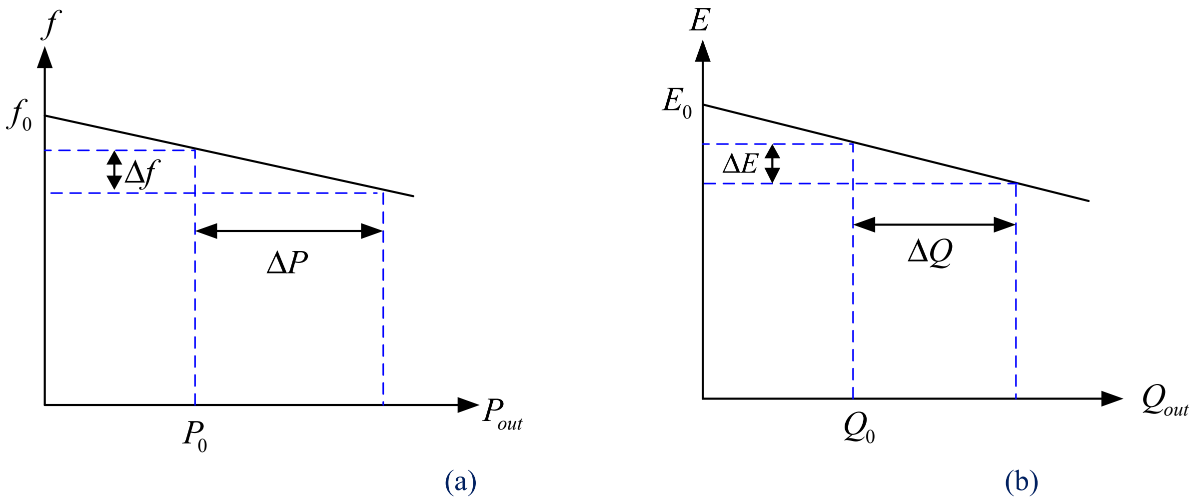

Fig. 2-2 Conventional droop scheme: a) P-f characteristic, b) Q-E characteristic

The idea of P-f droop has been utilized in MGs for active power sharing between the inverter-based DERs. In order to do so, the inertia of the synchronous machines is simulated by using a low pass filter and the frequency of the inverter is varied in accordance to the output power of the inverter. Similarly, the Q-E droop has been introduced for reactive power control. Therefore, we have:

$$f = f_0 - m P \tag{2-5}$$

$$E = E_0 - n Q \tag{2-6}$$

in which f_0, m and n are the rated frequency, P-f droop coefficient and Q-E droop coefficient, respectively.

2-2-2 Implementation of the conventional droop scheme

The block diagram of Fig. 2-3 depicts a voltage-controlled DER connected to the PCC through a line impedance. The DER is controlled by a cascaded control mechanism, including droop, voltage and current controllers. While the inner voltage and current controllers are responsible for regulating the capacitor voltage, the droop controller coordinates the DER with the rest of MG. The inverter is followed by a combination of LC filter and transformer, which eliminates the switching harmonics and provides isolation.

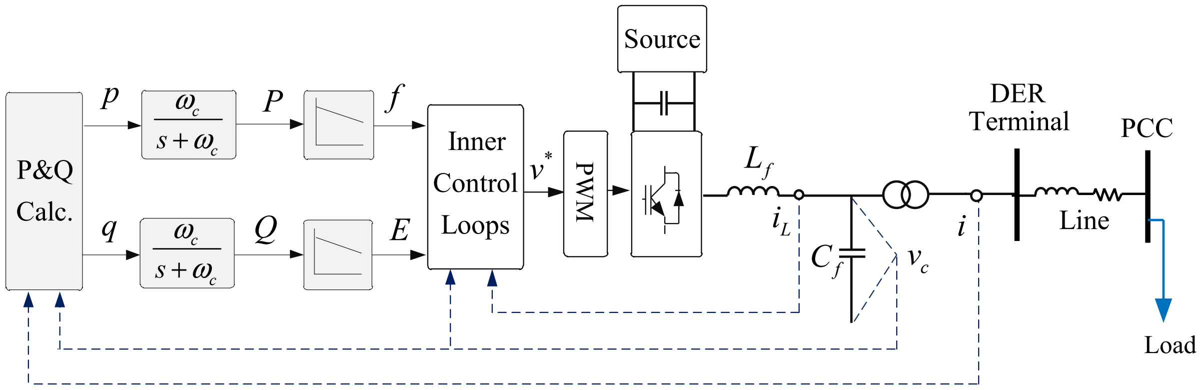

Fig. 2-3 Schematic diagram of the DER

The instantaneous active and reactive power are calculated from the feedback signals, as follows:

$$p = v_{cd}i_d + v_{cq}i_q \tag{2-7}$$

$$q = v_{cd}i_q - v_{cq}i_d \tag{2-8}$$

in which v_c and i are the capacitor voltage and the output current, respectively. Moreover, the subscripts d and q refer to the d and q components of the parameters. The average powers are then obtained by using low pass filters, as follows:

$$P = \frac{\omega_c}{s+\omega_c} p \tag{2-9}$$

$$Q = \frac{\omega_c}{s+\omega_c} q \tag{2-10}$$

in which ω_c is the cut off frequency of the low pass filter. The amplitude and frequency of the inverter voltage are obtained based on P-f and Q-E droop characteristics (equations (2-5) and (2-6)).

The schematic diagram of the inner control loops is depicted in Fig. 2-4. In order to track the sinusoidal reference voltage with zero steady-state error, Park transform technique is used. Park transform converts the feedback signals from the stationary *abc* frame to the synchronous rotating reference frame (SRRF). Assuming sinusoidal and balanced *abc* components, the direct (d) and quadrature (q) components of the converted signal will be dc. Therefore, conventional control techniques (e.g., proportional plus integrator (PI) or lead-lag) can be used to track the reference with zero steady-state error.

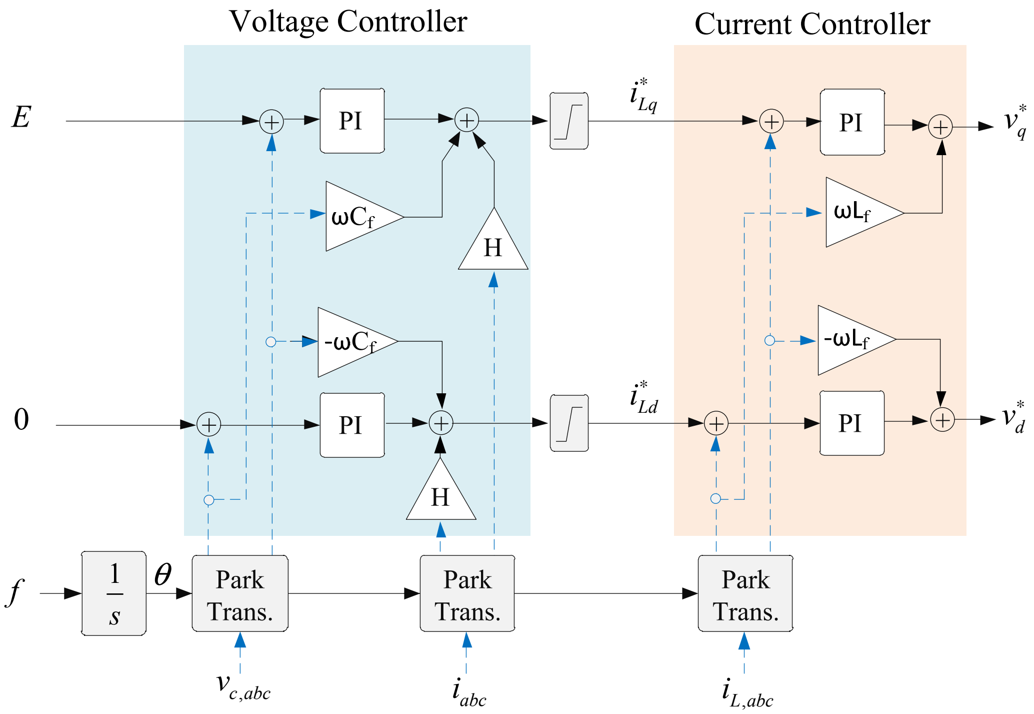

Fig. 2-4 Cascaded voltage-current controller

The angular speed of the SRRF is equal to the fundamental frequency of the MG, which is determined by the P-f droop mechanism. In other words, the angle of the SRRF is the integral of frequency:

$$\theta = 2\pi \int_0^t f(\tau)\, d\tau \tag{2-11}$$

For convenience, the q axis of the SRRF is aligned with the reference voltage. So the d and q axis components of the reference are set to 0 and E, respectively.

The cascaded controller is comprised of a nested control loop including the inner current controller and outer voltage controller. In order to decouple the dynamics of the loops, the inner loop is designed to have a faster dynamics compared to the outer loop.

The voltage controller, which is comprised of a feedback control loop, a capacitor current compensator and a feedforward controller, obtains the reference current, as follows:

$$i_{Lq}^* = \left\{ k_{i-v} \int \left(v_{cq}^* - v_{cq} \right) + k_{p-v} \left(v_{cq}^* - v_{cq} \right) \right\} + \left\{ \omega_0 C_f v_{cd} \right\} + \left\{ H i_q \right\} \tag{2-12}$$

$$i_{Ld}^* = \left\{ k_{i-v} \int \left(v_{cd}^* - v_{cd} \right) + k_{p-v} \left(v_{cd}^* - v_{cd} \right) \right\} + \left\{ -\omega_0 C_f v_{cq} \right\} + \left\{ H i_d \right\} \tag{2-13}$$

in which i_L^*, H, C_f, ω_0, k_{i-v} and k_{p-v} are the filter inductor current, feedforward gain, filter capacitor, fundamental frequency, and PI voltage controller coefficients, respectively.

The first, second and third terms term in the right hand side (RHS) of (2-12) and (2-13) are the feedback signal, the capacitor current estimation and the feedforward signal, respectively. The feedback loop makes use of a proportional plus integral controller to track the reference with zero steady-state error. In order to improve the dynamic response following the disturbances, the estimated value of the fundamental component of the capacitor current and the measured output current are added to the feedback signal.

Two saturation blocks are included to limit the d and q components of the reference current. The current limiting helps prevent the transient over currents during disturbances such as short circuits.

The current controller calculates the PWM reference voltage as a combination of the feedback current controller signal and the inductor voltage drop signal, as follows:

$$v_q^* = \left\{k_{i-i}\int\left(i_{Lq}^* - i_{Lq}\right) + k_{p-i}\left(i_{Lq}^* - i_{Lq}\right)\right\} + \left\{\omega_0 L_f i_{Ld}\right\} \tag{2-14}$$

$$v_d^* = \left\{k_{i-i}\int\left(i_{Ld}^* - i_{Ld}\right) + k_{p-i}\left(i_{Ld}^* - i_{Ld}\right)\right\} + \left\{-\omega_0 L_f i_{Lq}\right\} \tag{2-15}$$

in which L_f, v^*, k_{i-i} and k_{p-i} are the filter inductor, the PWM reference voltage and the PI current controller coefficients, respectively.

2-2-3 Limitations of conventional droop method

An intrinsic feature of the conventional droop method is the dependency of the frequency and voltage on the loading conditions [50]. This results in unwanted frequency deviations which degrade the power quality.

The conventional droop method is that it is derived based on simplifying assumption of inductive network impedance. However, in MGs, the network impedance is mostly resistive [51], which results in poor performance and stability issues.

According to equations (2-1) and (2-2), power plant control is a highly nonlinear problem. Particularly in the MGs the distributed and resistive nature of the network might result in large variations of δ and V. Therefore, droop control, which is based on a linearised model of power flow, might result in poor performance and even instability especially for large load variations. Moreover, since the overload capacity of the inverter based DERs is limited (1.2-1.5 cycles for less than 10ms), the MG collapse scenario is likely to happen due to the poor performance of the power control mechanism.

The small signal stability of the MGs has been studied in [24, 35, 41, 44, 52, 53]. It has been shown that the critical eigenvalues of the MG, which correspond to the power control, might move toward the jω axis as a result of load increase or droop gain increase, or increase of the number of DERs. On the other hand, a low value of droop gain results in poor load sharing.

2-2-4 Modified droop strategies

2-2-4-1 P-δ droop method

One way to avoid the frequency deviation is utilizing P-δ droop instead of P-f droop characteristics [33]. In this method, the reference time of DER units are coordinated by pulses received from the global positioning system (GPS). This way, the voltage angle of each unit can be measured with respect to a common time reference. In order to achieve proportional power sharing among the DERs, the voltage angle of each unit is controlled according to the following active power-angle droop characteristic:

$$\delta = \delta_{rated} - m\left(P_{rated} - P\right) \tag{2-16}$$

in which δ, δ_{rated} and P_{rated} refer to the voltage angle, rated angle and rated power, respectively.

The replacement of the conventional P-f droop scheme with P- δ droop strategy eliminates the issue of dependency of the frequency on the loading conditions. Therefore, the frequency can be fixed at the rated value. However, P-δ droop causes large variations in the voltage angle, which might cause system instability.

In order to enhance the stability of the P-δ droop method, a gain-scheduled angle droop controller is proposed in [37]. In this method, a derivative term is added to the droop control scheme, as following:

$$\delta = \delta_{rated} - m\left(P_{rated} - P\right) + m_d \frac{dP}{dt} \tag{2-17}$$

where the factor m_d is the derivate coefficient. The droop gain, m, is scheduled based on the output power of the unit. However, the introduction of the derivative term in (2-17) makes this method vulnerable to noise.

Inspired by the power system stabilizer (PSS) technique, ref [35] has added a supplementary feedback loop to the P-δ droop scheme to increase the system damping and improve the stability. The supplementary control introduces a change in the voltage amplitude (ΔV) proportional to the active power variations (ΔP). Ref [44] has replaced the linear supplementary controller by a nonlinear controller to ensure system stability even in the case of large signal disturbances. The derivation of the supplementary droop schemes is based on the conventional power control, where the active power must be controlled via the turbine and the reactive power via the excitation system. In case of the inverter-based DERs, the control design can be conducted with much more flexibility by treating the DER as a multi input- multi output (MIMO) system, with voltage angle and amplitude as the inputs and active and reactive power as the outputs. This point of view eliminates the need for decoupling active and reactive power control and naturally encompasses the supplementary control.

2-2-4-2 Droop control with line drop compensation

An adaptive voltage droop strategy has been presented in [34]. In order to take into account the voltage drop from the DER to the load, two terms are added to the voltage droop, as follows:

$$V = V^* - n(P,Q)Q + \left(\frac{RP}{V^*} + \frac{XQ}{V^*} \right) \tag{2-18}$$

In order to cancel the effect of active power on the load voltage, the droop gain is adapted with load variations, as follows:

$$n(P,Q) = n_Q + m_Q Q^2 + m_p P^2 \tag{2-19}$$

in which n_Q , m_Q , m_p are the droop coefficients. The adaptive voltage droop improves voltage profile in the network, especially under heavy loading conditions. However, this method requires the prior knowledge of the network parameters. Moreover, it does not consider the issue of small signal stability.

2-2-4-3 Decoupled P/Q droop method

The active and reactive power flow equations can be decoupled by utilizing a rotational transformation, as follows [32]:

$$\begin{bmatrix} P' \\ Q' \end{bmatrix} = \begin{bmatrix} \sin\theta & -\cos\theta \\ \cos\theta & \sin\theta \end{bmatrix} \begin{bmatrix} P \\ Q \end{bmatrix} \tag{2-20}$$

Consequently P and Q can be controlled by δ and E droop as in the case inductive systems, respectively. However, this transformation requires the knowledge of the effective line impedance. In addition, this technique does not consider the negative impact of nonlinear loads and does not ensure frequency and voltage regulation.

2-2-4-4 Virtual resistance strategy

An alternative solution for improving the system damping and decoupling active and reactive power control is the virtual resistance control method [25]. In this method, a virtual resistance is emulated in the output stage of the inverter by introducing a resistive voltage drop in the voltage control loop. Since the line impedances are quite resistive, the system impedance will be approximately resistive. Therefore, the power flow equations can be decoupled. In this case, P and Q will be controlled by E and δ droop, respectively. However, this method is not applicable to directly coupled DERs. Moreover, the resistive voltage drop results in the undesirable reduction of the DC bus voltage utilization ratio.

2-2-4-5 Adaptive droop control approaches

MG performance and stability considering energy source dynamics has been studied in [53]. In this paper, an islanded MG with four inverter-based distributed generations (DGs), including micro-turbines and fuel cells and an energy storage DER has been studied. Subsequent to a step load change, the output power of all DER inverters changes according to their droop characteristics. However, since the source power cannot follow the electrical power output instantaneously, the DC bus voltage of the inverters drops and the system becomes unstable. A variable droop scheme has been proposed to mitigate this problem. In this method, the droop gain of the storage based DER is increased to a high value right after the load change and then gradually decreased to its initial value. Consequently, the load change is initially carried out by the storage system and then is gradually shared between the other DGs. This paper does not consider the action of micro-turbine governor, which allows for speed variation to regulate the DC bus voltage. Moreover, the distributed nature of the network and the optimum size and position of the storage systems has not been discussed in this paper.

The conventional droop control design is limited to selecting the droop gains. This restricts the design to 1 degree of freedom (1 DOF) and necessitates a tradeoff between the dynamic performance and power sharing. This restriction can be removed by using a modified droop function, as follows [24]:

$$f = f^* - mP - \hat{m}_d \frac{dP}{dt} \tag{2-21}$$

$$V = V^* - nQ - \hat{n}_d \frac{dQ}{dt} \tag{2-22}$$

The adaptive dynamic gains $\hat{m}_d$ and $\hat{n}_d$ allow for adjusting the dynamic performance without affecting the power sharing. Furthermore, they can be adjusted with load changes to increase the system damping. Consequently, the critical eigenvalues can be kept away from the jω axis in spite of the system operating point variations. Yet other factors affecting system stability such as the coupling between active and reactive power and the resistive nature of the network has not been studied in this paper.

2-3 GPS technology – a new synchronization approach

In this section, the motivation of utilizing GPS timing technology for synchronization of DER units is explained. Furthermore, the theoretical background of GPS timing technology and its application for angle synchronization are detailed.

2-3-1 Motivation

Consider the islanded AC MG of Fig. 2-5. The MG is supplied by N voltage-source DER units, which are connected to the point of common coupling (PCC) through line impedances. Each DER is comprised of a DC energy source, a power electronic inverter and a passive filter. The inverter voltage is controlled by means of a cascaded voltage-current control loop, which regulates the filter capacitor voltage, v_{ck}, to its reference value [54]. The output current of DER unit k (k = 1,2,…,N) is calculated as

$$i_k = \frac{v_{ck} - v_{PCC}}{z_{ck} + z_{linek}} \tag{2-23}$$

in which v_{PCC}, z_{ck} and z_{linek} are the PCC voltage, output inductor impedance and line impedance of unit k, respectively.

Equation (2-23) implies that the current of each unit is dependent on the corresponding capacitor voltage. Stable operation of the MG requires the reference voltages of the units to be in synchronism with each other. Conventionally, such synchronization is achieved by using droop control method. The low pass filter used for calculation of the active power introduces a virtual inertia in the system and the P-f droop characteristic acts like a negative feedback, which stabilizes the system [52]. At the same time, it enables proportional sharing of the load between the DERs. However, the dependency of the frequency on load makes this method inferior in terms of power quality [50].

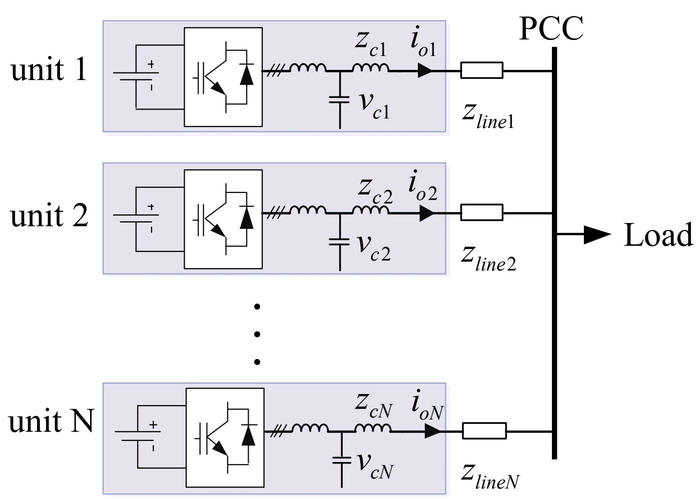

Fig. 2-5 Schematic diagram of an islanded ac MG

The frequency deviations can be compensated by Secondary control schemes. In this approach, which is inspired by secondary control method in power systems, a central controller sends a frequency compensation signal to the DERs. The signal is used by the local controllers to shift the local P-f droop characteristics[6]. So, the steady-state frequency is restored to the nominal value [3]. However, the implementation of the secondary control level requires communication links among the DERs. In addition, the method does not prevent transient frequency fluctuations subsequent to load changes. In case of power systems, such transients are negligible due to the smoothness of load changes. However, in islanded MGs the relatively larger magnitude of instantaneous load changes results in considerable frequency fluctuations.

An alternative approach is fixing the frequency of the reference voltages at the rated value and coordinating the reference angles so as to achieve proper load sharing. This strategy necessitates the use of a common time reference by each of the DER units. Given the distributed nature of the MGs and the required timing accuracy, GPS timing technology has been proposed as the practical solution [33, 46]. In this approach, each DER is equipped with a GPS receiver, which produces a pulse at frequency of 1Hz (1PPS). Since all GPS receivers are locked to atomic clocks of the GPS satellites, the 1PPS signal can be utilized to synchronize the DERs.

2-3-2 Theoretical background

Although GPS is mainly known as a navigation system, it is also an accurate timing system. GPS time synchronization has been widely used in several applications including communications [55], sensor networks [56] and power systems [57].

GPS is comprised of three functional areas, including satellites, GPS receivers and ground sections. Originally, the GPS constellation was composed of 24 satellites, 8 of which were observable at any point on earth. Currently, the number of satellites is increased to 32. Each satellites is equipped with four atomic clocks, which are synchronized with the Coordinated Universal Time (UTC).

Each of the GPS satellites continuously broadcasts a series of information, which are modulated on carrier signals. The carrier signal is effectively a clock signal, which has a fixed frequency. The information includes clock correction factors, satellite’s current position and data regarding the accuracy of the satellite signals. In contrast to conventional radio broadcasts systems which use different frequency bands, all GPS satellites transmit at the same frequency bands. In order to discriminate the signals from different satellites, code division multiple access technique is utilized.

GPS block diagram of a GPS receiver is shown in Fig. 2-6. The GPS waves are received by the antenna and amplified using the preamplifier circuit. The carrier loop tracks the carrier frequency and computes the shift between the receiver clock and the satellite clock. The code loop decodes the signal to extract the information. The processor then uses the time shift and the position of the satellite to obtain the receiver position, as follows [58]:

$$\sqrt{(x_i-u_x)^2+(y_i-u_y)^2+(z_i-u_z)^2}=c(\Delta t_i-t_b) \tag{2-24}$$

where, (x_i , y_i , z_i) are the coordinates of satellite i , (u_x , u_y , u_z) are the coordinates of the receiver, Δt_i is the time shift of the signal received from satellite i, t_b is the bias of the receiver clock with respect to the Universal Coordinated Time (UTC), and c is the speed of light. The unknown variables in (2-24) are the coordinates of the receiver as well as the bias of the receiver clock. Expressing (2-24) for four different satellites, a system of four non-linear equations with four unknown variables is obtained. The equations are then solved by using an iterative method to obtain the receiver location as well as the receiver clock bias. The time bias can be used to accurately compute the UTC time.

For the application of time synchronization in MGs, the receiver position is fixed after installation. Therefore, the receiver position can be calculated once and stored in the memory. Afterwards, only the clock bias of the receiver needs to be computed. So, only one satellite is sufficient for the application. Given the fact that at least eight satellites are observable at any point, the GPS time synchronization systems favors from a redundancy of seven, which makes the system highly reliable.

It should be pointed out the clock bias is a dynamic variable, which changes over time due to the frequency drift of the local oscillator [59]. So, it is important to continuously update the clock bias.

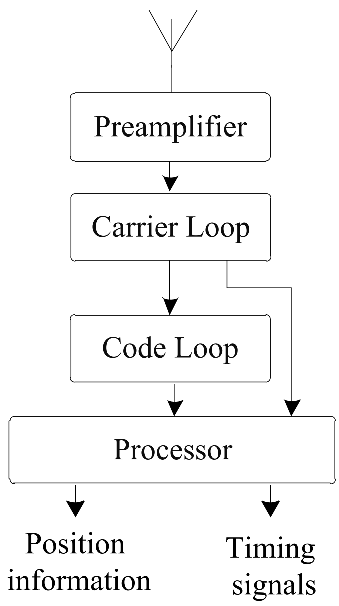

Fig. 2-6 GPS receiver

2-3-3 Angle synchronization

GPS time synchronization has been widely used in several applications including communications [55], sensor networks [56] and power systems [57]. Commonly, accurate time synchronization is achieved based on a timing pulse with a period of 1s. The rise time of the 1 pulse per second signal (1PPS) is synchronized with the UTC time with accuracy of a fraction of microsecond.

The 1PPS GPS signal is connected to one of the inputs of the digital controller. The rising edge of the pulse is captured by the timer module and assigned as t_{cap}. The time offset between the 1PPS signal and the local clock is computed as

$$t_{offset} = \text{mod}\{t_{cap}, 1\} \tag{2-25}$$

in which "mod" refers to modulus. In other words, the offset time is the fractional part of the captured time. It is worth mentioning that the decimal part of t_{cap} bears no information due to periodic nature of the 1PPS signal.

The SRRF phase angle is computed as following:

$$\theta = \text{mod}\left\{\omega_0\left(t - t_{offset}\right), 2\pi\right\} \tag{2-26}$$

in which, $\omega_0 = 2\pi f_0$ is the fundamental angular frequency. Assuming a constant and integer fundamental frequency, the angle of the SRRF at the rising edge of the 1PPS signal ($t = t_{cap}$) is zero. On the other hand, the 1PPS signal is synchronized to the global UTC time. Therefore, the SRRFs of the DERs are synchronized.

The accuracy of synchronization is dependent on the GPS receiver, the timer quantization, and the frequency drift of the local controller oscillator. The maximum phase angle error at time t can be expressed as following:

$$\theta_{err} = \omega_0\left\{e_{GPS} + e_{timer} + \int_{tGPS}^{t} F_d\left(\tau\right) d\tau\right\} \tag{2-27}$$

where, e_{GPS}, e_{timer}, F_d and t_{GPS} are the GPS receiver error, timer quantization error, frequency drift of the oscillator and the instant of time at which the last GPS pulse is captured, respectively.

The GPS and timer quantization errors are typically less than 1 microsecond. The oscillator frequency drift ranges from a few parts per billion for oven controlled crystal oscillators (OCXO) to 100 parts per million (ppm) for typical crystal oscillators. Therefore, the angle error is less than 1° with typical oscillators.

2-4 V-I droop method

2-4-1 Basic concept

The existing communication-less MG control methods are based on the conventional power system droop. In order to exploit the fast dynamics and high flexibility of inverters, while taking advantage of the recent developments in GPS communications, a new droop method is proposed in this chapter.

In the proposed method, the reference frame of each local controller is aligned to a global synchronous rotating reference frame (SRRF) by using GPS timing technology. This alignment enables the local controllers to obtain the *d* and *q* components of local voltages and currents with respect to the global SRRF. Assuming balanced conditions, the Park transform of the voltage is represented by a two dimensional vector, as follows

$$v_{cdq} = \begin{bmatrix} v_{cd} \\ v_{cq} \end{bmatrix} \tag{2-28}$$

It is worth mentioning that in the conventional control methods, the local SRRF is aligned with the output voltage. So, based on the choice of the reference time, either v_{cd} or v_{cq} is zero. In other words, v_{cdq} has one degree of freedom and only conveys the information about the voltage amplitude. In the proposed scheme, however, v_{cdq} has two degree of freedom and entails information about the amplitude as well as phase angle of the output voltage. Therefore, it is possible to control the amplitude and angle of the voltage through adjusting v_{cd} and v_{cq}. In the proposed method the *d* and *q* components of the voltage are adjusted as a function of the output current:

$$\begin{bmatrix} v_{cd}^* \\ v_{cq}^* \end{bmatrix} = \begin{bmatrix} E_0 \\ 0 \end{bmatrix} - \begin{bmatrix} f\left(i_d, i_q\right) \\ g\left(i_d, i_q\right) \end{bmatrix} \tag{2-29}$$

in which v_d^*, v_q^* and i_d, i_q are the d and q axis components of the reference voltage and output current, E_0 is the no load voltage, and f and g are the d and q axis droop functions. By properly selecting the the droop functions, it is possible to realize a decentralized coordinated control, which ensures proportional sharing of load current between the DERs. Assuming $v_{cd} \approx 1pu$ and $v_{cq} \approx 0$, i_q and i_d approximately represent the active and reactive power, respectively. Therefore, even power sharing is guaranteed.

2-4-2 Comparison of current-based and power-based droop concepts

As opposed to the majority of research work in the literature, which focus on proportional sharing of active and reactive load power among the DERs, the proposed method is centred on proper sharing of active (i_d) and reactive (i_q) components of load current among the DER units.

Fig. 2-7 illustrates a comparison between the conventional power sharing and proposed current sharing approaches. The proposed approach eliminates the inherent delay of P and Q measurement by simplifying the power flow control to current flow control. While the power sharing schemes are developed based on linearization of power flow equations (equations (2-1) and (2-2)) with the assumption of inductive network impedance and small power angles, the proposed scheme is based on basic laws of KVL and KCL, which are linear in nature. Furthermore, unlike the conventional droop method, the proposed strategy enables fixed frequency operation.

The current flow control is not only in accordance with the nature of inverters, which cannot tolerate large current overshoots, but also satisfies even power sharing as the voltage variation throughout a MG is usually small.

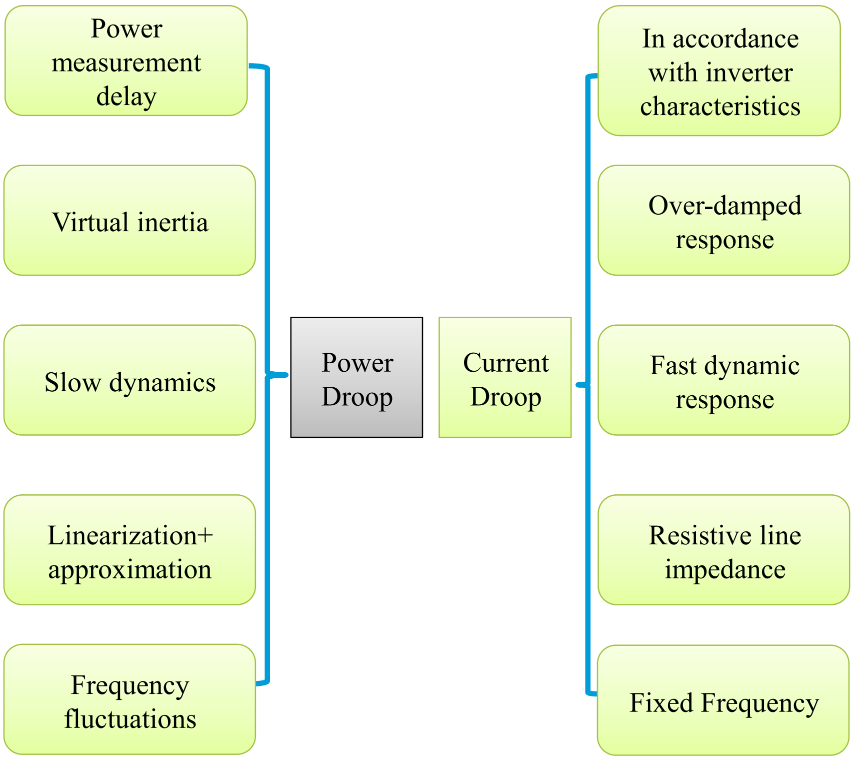

Fig. 2-7 Comparison of power and current based droop schemes

2-4-3 Current sharing in islanded MGs

Fig. 2-8 illustrates a simple MG consisting of two DERs and one load. The DERs are assumed to be dispatchable, i.e., capable of producing active power on demand. Each DER is modelled as a voltage source followed by an LC filter and a transformer, which is modelled by an inductor. The voltage source represents the inverter, with U equal to the average inverter voltage. The DERs are connected to the PCC via low voltage cables.

The capacitor voltage is regulated by a cascaded voltage-current controller. The bandwidth of the current controller is typically selected as ½ of the resonant frequency of the LCL filter ($f_{res} = \sqrt{\left(L_f + L_c\right)/\left(2\pi L_f L_c C_f\right)}$). On the other hand, f_{res} must be smaller than ½ of the switching frequency. For a typical switching frequency of 10kHz, the current control loop should have a bandwidth of a few kHz. The time constant of the outer voltage control loop should be selected larger than the inner current control loop but smaller than the fundamental period (1/50Hz=20ms). Therefore, the time constant of the cascaded controller is in the order of a few milliseconds. To simplify the analysis, dynamics of the cascaded controller are neglected in this section. Hence, the system dynamics can be represented in the synchronous rotating reference frame by the following state space equations:

$$L_1 p i_{1d} = v_{c1d} - V_{PCCd} - \left(-\omega L_1 i_{1q} + R_1 i_{1d}\right) \tag{2-30}$$

$$L_1 p i_{1q} = v_{c1q} - V_{PCCq} - \left(\omega L_1 i_{1d} + R_1 i_{1q}\right) \tag{2-31}$$

$$L_2 p i_{2d} = v_{c2d} - V_{PCCd} - \left(-\omega L_2 i_{2q} + R_2 i_{2d}\right) \tag{2-32}$$

$$L_2 p i_{2q} = v_{c2q} - V_{PCCq} - \left(\omega L_2 i_{2d} + R_2 i_{2q}\right) \tag{2-33}$$

and the constraints:

$$i_{1q} + i_{2d} = i_d^{Load} \tag{2-34}$$

$$i_{1q} + i_{2q} = i_q^{Load} \tag{2-35}$$

in which, L_k and R_k represent the total inductance and total resistance between DER unit k ($k = 1, 2$) and the PCC, respectively. Moreover, V_{PCCd}, i_1, i_2, i^{Load} correspond to the PCC voltage, current of unit 1 and 2 and the load in the *q-d* reference frame, respectively. The prefix "*p*" denotes derivative.

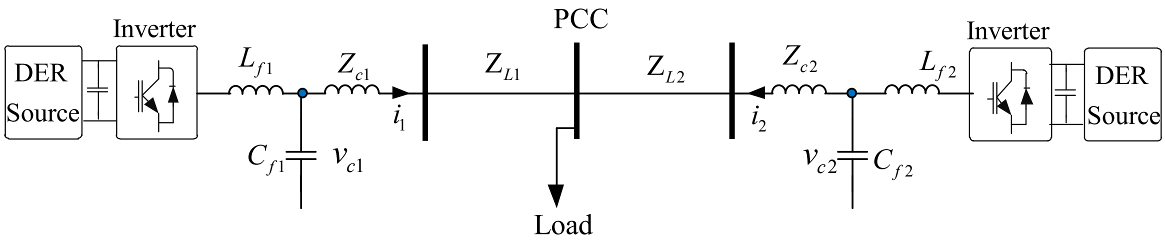

Fig. 2-8 MG model

The load voltage can be eliminated from (2-30)-(2-33) by subtraction, as follows:

$$p\left(L_1 \begin{bmatrix} i_{1d} \\ i_{1q} \end{bmatrix} - L_2 \begin{bmatrix} i_{2d} \\ i_{2q} \end{bmatrix} \right) = \begin{bmatrix} v_{c1d} \\ v_{c1q} \end{bmatrix} - \begin{bmatrix} v_{c2d} \\ v_{c2q} \end{bmatrix} - [Z_1] \begin{bmatrix} i_{1d} \\ i_{1q} \end{bmatrix} + [Z_2] \begin{bmatrix} i_{2d} \\ i_{2q} \end{bmatrix} \tag{2-36}$$

in which,

$$[Z_k] = \begin{bmatrix} R_{ck} + R_{Lk} & -X_{ck} - X_{Lk} \\ X_{ck} + X_{Lk} & R_{ck} + R_{Lk} \end{bmatrix} \tag{2-37}$$

where X_{ck}, R_{ck}, X_{Lk} and R_{Lk} are the reactance and resistance of output transformer and line of unit *k*, respectively.

Equation (2-36) shows that i_q and i_d are related to the difference between the inverters voltages through linear differential equations. Therefore, it is possible to control the sharing of current between the DERs by adjusting the inverters voltages.

2-4-4 Development of the control law

By substituting (2-29) into (2-36) it can be shown that in steady-state conditions, the ratio of the DER currents (i_{1d}/i_{2d} and i_{1q}/i_{2q}) is dependent on the functions *f* and *g* as well as the system parameters. In order to eliminate the adverse effect of transformer impedance on the power sharing and voltage regulation, compensating terms are added to the control law, as follows:

$$\begin{bmatrix} v^*_{ck,d} \\ v^*_{ck,q} \end{bmatrix} = \begin{bmatrix} E_0 \\ 0 \end{bmatrix} + \begin{bmatrix} R_{Tk} & -X_{Tk} \\ X_{Tk} & R_{Tk} \end{bmatrix} \begin{bmatrix} i_{kd} \\ i_{kq} \end{bmatrix} - \begin{bmatrix} f_k\left(i_{kd}, i_{kq}\right) \\ g_k\left(i_{kd}, i_{kq}\right) \end{bmatrix} \tag{2-38}$$

Therefore, steady-state power sharing is only dependent on the droop functions and the line impedance. Since the line impedances in the distribution system are relatively small, even current sharing can be realized by choosing appropriate droop functions. The droop functions can be chosen as a linear combination of i_q and i_d, as follows:

$$\begin{bmatrix} f_k \\ g_k \end{bmatrix} = \begin{bmatrix} m_k & -l_k \\ k_k & n_k \end{bmatrix} \begin{bmatrix} i_{kd} \\ i_{kq} \end{bmatrix} \tag{2-39}$$

in which, the droop coefficients (m, n, l and k) are selected inversely proportional to the DERs ratings. Substituting (2-39) into (2-38) and using (2-36), the system dynamics can be written, as follows:

$$L_1 p\begin{bmatrix} i_{1d} \\ i_{1q} \end{bmatrix} - L_2 p\begin{bmatrix} i_{2d} \\ i_{2q} \end{bmatrix} = \begin{bmatrix} -R_{L1} - m_1 & X_{L1} + l_1 \\ -X_{L1} - k_1 & -R_{L1} - n_1 \end{bmatrix}\begin{bmatrix} i_{1d} \\ i_{1q} \end{bmatrix} - \begin{bmatrix} -R_{L2} - m_2 & X_{L2} + l_2 \\ -X_{L2} - k_2 & -R_{L2} - n_2 \end{bmatrix}\begin{bmatrix} i_{2d} \\ i_{2q} \end{bmatrix} \qquad (2\text{-}40)$$

In case of equal per unit transformer and line impedances, steady-state current sharing error is zero and (2-40) can be simplified to the following equation:

$$L_1 p\begin{bmatrix} e_d \\ e_q \end{bmatrix} = \begin{bmatrix} -R_{L1} - m_1 & X_{L1} + l_1 \\ -X_{L1} - k_1 & -R_{L1} - n_1 \end{bmatrix}\begin{bmatrix} e_d \\ e_q \end{bmatrix} \qquad (2\text{-}41)$$

where, e represents the current sharing error. Since line impedances are small compared to the droop coefficients, the system dynamic response is mostly dependent on the coefficients.

Two extreme cases for the selection of the coefficients are considered here. In the first case, the diagonal coefficients (m and n) are set to zero to have i_q-v_d /i_d-v_q droop characteristics. It is noteworthy to mention the similarity of these characteristics with the conventional droop (P-δ/Q-E). That choice leads to an under-damped response, with damping ratio decreasing with the increase of the coefficients. In the second case, the off-diagonal elements are set to zero. With this choice, the q and d components of the current are approximately decoupled thanks to the small X/R ratio of the lines. Moreover, the increase of coefficients m and n improves both damping and steady state current sharing. However, the droop action causes PCC voltage drop. Therefore, the coefficients should be chosen such that the PCC voltage is in the permissible range.

From (2-40) it can be inferred that steady-state current sharing error is dependent on the mismatch of the line voltage drops and increases with the load rise. On the other hand, the system is more vulnerable under heavy loading conditions, as the DER output currents are strictly limited by the current rating of the inverters' switches. In order to decrease the current sharing error and improve the damping under heavy loading conditions, a piece-wise linear droop function is adopted. Therefore, the droop control law is defined as follows:

$$\begin{bmatrix} v^*_{ck,d} \\ v^*_{ck,q} \end{bmatrix} = \begin{bmatrix} E_0 \\ 0 \end{bmatrix} + \begin{bmatrix} R_{Tk} & -X_{Tk} \\ X_{Tk} & R_{Tk} \end{bmatrix}\begin{bmatrix} i_{kd} \\ i_{kq} \end{bmatrix} - \begin{bmatrix} m_k f\left(i_{kd}\right) \\ n_k f\left(i_{kq}\right) \end{bmatrix} \qquad (2\text{-}42)$$

Fig. 2-9 illustrates a comparison between steady-state error of linear and piece-wise linear droop functions. As for representation, the DER ratings are assumed to be equal and the line 2 impedance is assumed to be zero. Having i_{1d} known, f(i_{2d}) is calculated, as follows:

$$f(i_{2d}) = f(i_{1d}) + \begin{bmatrix} R_{L1} & -X_{L1} \end{bmatrix} i_{1dq} \qquad (2\text{-}43)$$

It is observed that while the maximum of both droop functions are equal, the current sharing error is much smaller for the piece-wise linear droop. Moreover, the higher droop slope at high loading conditions corresponds to an improved dynamic response.

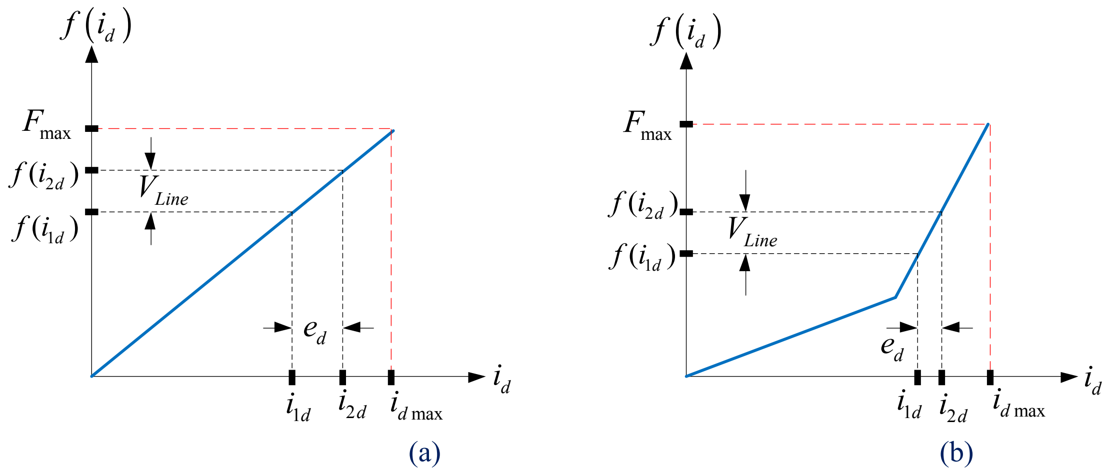

Fig. 2-9 Droop function: (a) linear, (b) piece-wise linear

The power sharing accuracy at high loading conditions can be improved by using any piece-wise linear function with increasing slope. However, to achieve the optimum performance, the function is designed by solving an optimization problem. Expressing the current sharing error of unit *k* as

$$e_k = \frac{i_k}{I_{rated,k}} - \frac{\sum_j i_j}{\sum_j I_{j,rated}}, \tag{2-44}$$

in which $I_{rated,k}$ is the rated current of DER unit *k*, the cost function can be defined as a weighted sum of average current sharing error under low, medium and high loading conditions:

$$\min \quad Cf = C_1\overline{e}_{low} + C_2\overline{e}_{medium} + C_3\overline{e}_{high}, \tag{2-45}$$

where, $\overline{e}_{low}$, $\overline{e}_{medium}$ and $\overline{e}_{high}$ are average current sharing error at low ($0<i<0.5$pu), medium ($0.5\text{pu}<i<0.7$pu) and high ($i>0.7$pu) loading conditions, respectively. In order to emphasize the vulnerability of the system at high loading conditions, the weights C_1, C_2 and C_3 are set to 1, 2 and 8, respectively. The objective is to find the slope of the function at different loading conditions, to minimize the cost function (*Cf*).

The optimization problem is solved numerically. The resulting slopes are 0.3, 1 and 2.16 for low, medium and high loading conditions, respectively. The function f is then extended for negative currents and represented as a look-up table, as shown in table 2-1.

Table 2-1 piece-wise linear function f

***i* (pu)**	***f* (*i*)**
-1	-1
-0.7	-0.35
-0.5	-0.15
0.5	0.15
0.7	0.35
1	1

2-4-5 Block diagram of the controller

The block diagram of the proposed controller is illustrated in Fig. 2-10. The GPS synchronization block calculates the SRRF angle, θ, according to (2-26). The d and q components of the output current are calculated using a park transformation (abc/dq) block. The inverter reference voltage is then obtained according to the droop control law (equation (2-42)).

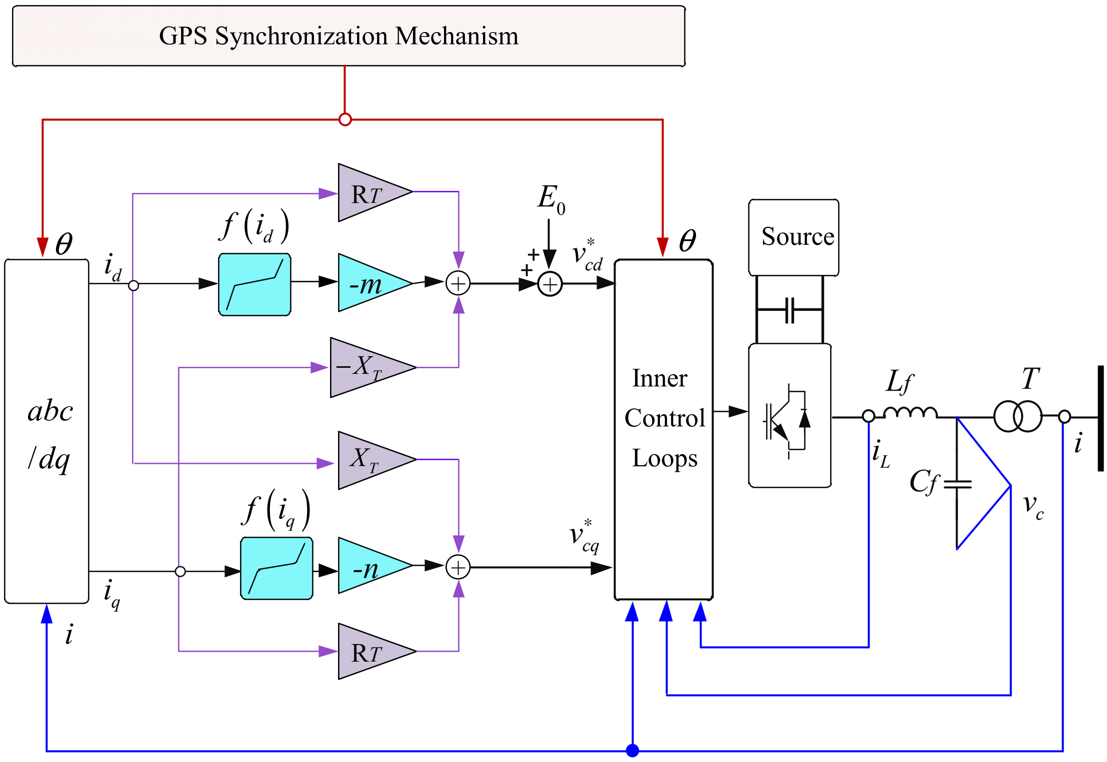

Fig. 2-10 Block diagram of the proposed control scheme

The reference voltage is then fed to inner control loops, which are detailed in Fig. 2-11. The inner loops are a cascaded combination of voltage and current controllers, which are also implemented in SRRF. The voltage controller uses a combination of feedback and feedforward control to obtain the reference current. A current limiter along with an anti-windup feedback is used in the voltage controller to protect the inverter from over-current during transient or fault conditions. The DER operating mode is selected by the automatic switches S1 and S2. When the MG is connected to the grid, the current reference is set to a constant value (upper state). If a disturbance occurs in the upstream network, the MG is islanded and the controller is switched to the droop control mode. The current controller output is fed to the PWM module to control the switching duty cycle.

From the implementation standpoint, the proposed controller is quite similar to the conventional P-f/Q-E droop methods, except utilizing the output transformer impedance in the droop control law. The effect of the impedance variations on the controller performance is discussed in Section 2-5.

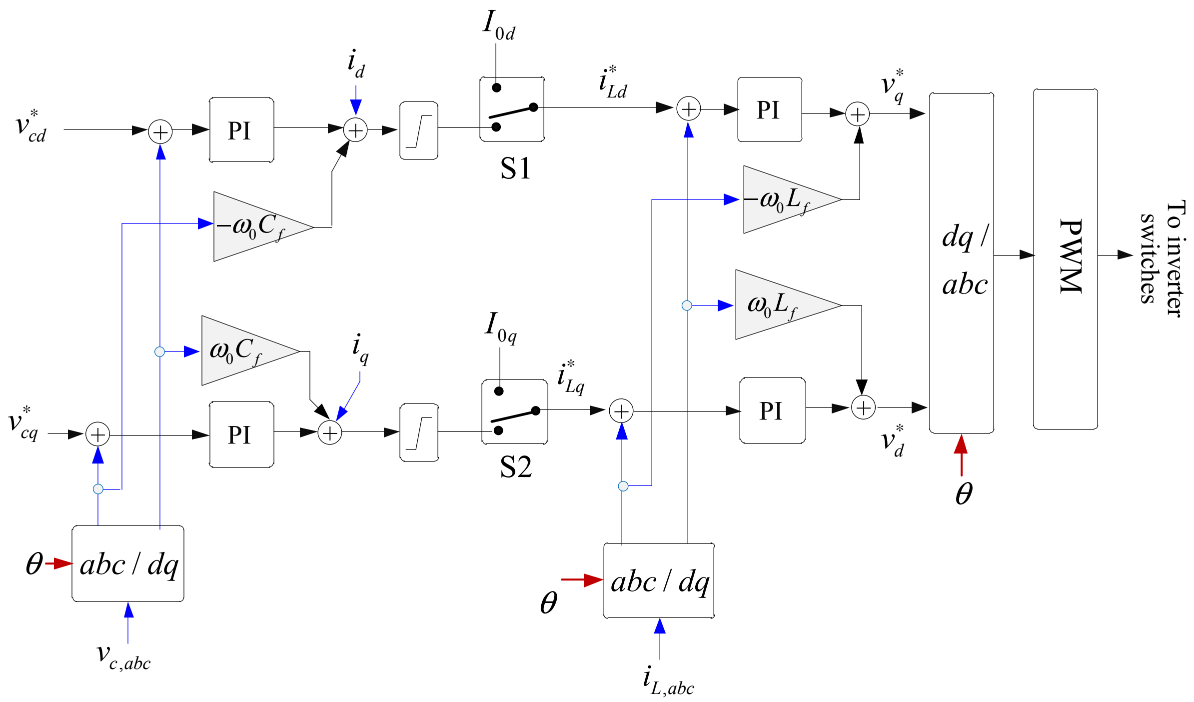

Fig. 2-11 Block diagram of the inner control loops

2-4-6 Small-signal analysis of the proposed method

The derivation of the proposed controller is based on the simplified model, which neglects the dynamics of the cascaded voltage regulator. In this section, small-signal behavior of the proposed control considering the dynamics of the cascaded voltage regulator as well as the LC filter are investigated.

The proposed controller is applied to the MG of Fig. 2-8 and the system is modelled in the synchronous rotating reference frame. The model is formulated in the state-space form with 20 independent states, including filter capacitors voltages, filter inductors currents, voltage and current regulator integrators, DER output currents and load voltage. The system is linearised around the operating point which is calculated by time-domain simulation. The dynamic response and stability is then investigated by eigenvalue analysis using MATLAB Control Design Toolbox.

The system parameters are listed in table 2-2. Each DER has a power rating of 30kW. Lines 1 and 2 are standard low voltage XLPE-16 overhead cables with lengths of 35m and 105m, respectively. The system load is set to 50kW at 0.7 PF lagging to replicate heavy loading conditions. According to EN50160, the 10 minute rms voltage of low voltage networks should remain in the range of 90% to 110% of the nominal value [60]. With the power electronic controllers, the voltage can be maintained in a narrow range. In this thesis, the permissible voltage deviations at the DERs terminals is ±4%. In order to maintain the voltage within the permissible range, the q axis droop coefficient (m) is set to 0.08 and E0 is set to 1.04pu. The system eigenvalues are then calculated for different values of d axis droop coefficient (n).

Table 2-2 System parameters

Discription	Parameter	Value	Unit
System parameters	f_{rated}	50	Hz
	V_{Lrated}	400	V
DER 1 and 2 rating	P	30	kW
	S	45	kVA
DERs filter impedance	Z_f	0.05+j0.16	pu
DER1 and 2 Transformers' impedances	Z_{T1}	0.03 + j0.09	pu
	Z_{T2}	0.02 + j0.06	pu
Line 1 length		35	m
Line 2 length		105	m
Current controller parameters	k_{pi}	10	-
	k_{ii}	15000	-
Voltage controller parameters	k_{pv}	0.025	-
	k_{iv}	200	-
Feedforward gain	H	0.7	-

Fig. 2-12 depicts the loci of the dominant eigenvalues with n increasing from 0.01 to 0.15. As n is increased from 0.01 to 0.06, the dominant eigenvalue (number 1) quickly shifts away from the imaginary axis, but the high frequency eigenvalues slowly move towards the imaginary axis. At n=0.06, the eigenvalue number 2, which moves slowly with increase of n, becomes dominant. This implies a trade-off between power sharing accuracy and dynamic response. However, as n is varied in the range (0.06, 0.15) the high frequency eigenvalues remain far away from the dominant eigenvalue, the real part of which is smaller than -2π*50 *rad/s*. Therefore, the droop controller has a time constant of less than 1 cycle, i.e., it reacts to load changes in the first cycle after the disturbance. The fast coordinated reaction of local controllers ensures that the load change is picked up by all DERs, hence preventing current overshoot. It is worthwhile to mention that the loci of the system eigenvalues with variation of *m* are similar to Fig. 2-12 and are not shown here for conciseness.

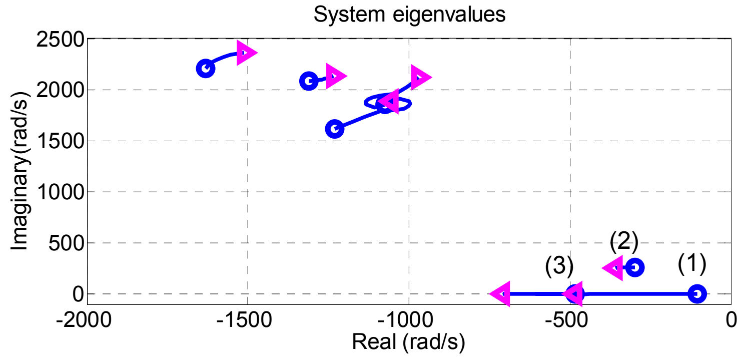

Fig. 2-12 Eigenvalue loci of the proposed method

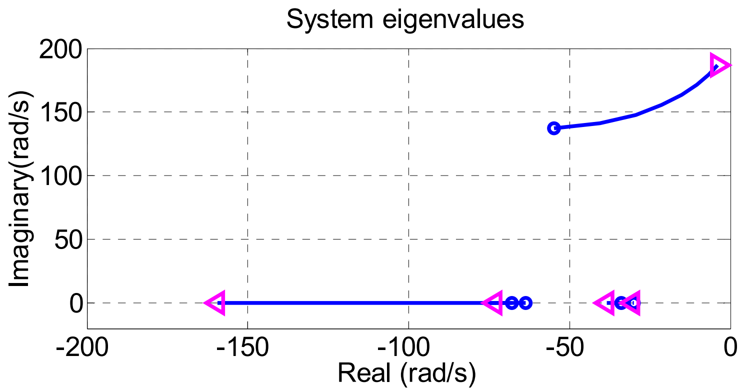

Fig. 2-13 Eigenvalue loci of conventional P-δ droop method

As for comparison, the loci of the dominant eigenvalues with conventional P-δ/Q-E droop are shown in Fig. 2-13. The Q-E droop coefficient is set to 0.08 and the P-δ droop coefficient is varied from 0.05 to 0.5. It can be observed that as the droop coefficient is increased, the dominant eigenvalues shift towards the imaginary axis until the system becomes unstable. This behavior is consistent with the mathematical analysis of Section 2-4-4. Similar results have been reported for P-f/Q-E droop control method [24].

2-5 Simulation results

In order to verify the efficacy of the proposed control method, it is applied to the CIGRE benchmark MG proposed in [61]. The benchmark schematic diagram is depicted in Fig. 2-14. It simulates common low voltage distribution feeders with variety of load types. Five DER units are integrated into the feeder to provide an uninterruptable energy supply. The overhead lines and loads parameters are shown on the diagram. The load power factor is set to 0.7 to replicate worst case conditions in a residential area. The DERs 1 and 2 have the same parameters as listed in Table 2-3. The rest of the parameters are shown in table 2-3. Droop coefficients m and n are set to 0.08 and 0.15, respectively. While m is limited by the permissible voltage deviations (±4%), n is selected based on a trade-off between dynamic response and Q sharing accuracy.

Table 2-3 Benchmark Parameters

Discription	Parameter	Value	Unit
DER 3-5 ratings	S	22.5	kVA
	P	15	kW
DERs Transformers' impedances	Z_{T3}	0.025 + j0.075	pu
	Z_{T4}	0.02 + j0.06	pu
	Z_{T5}	0.03 + j0.09	pu
Proposed method droop coefficients	m	0.08	-
	n	0.15	-
Conventional droop coefficients	k_p	0.1	-
	k_q	0.04	-

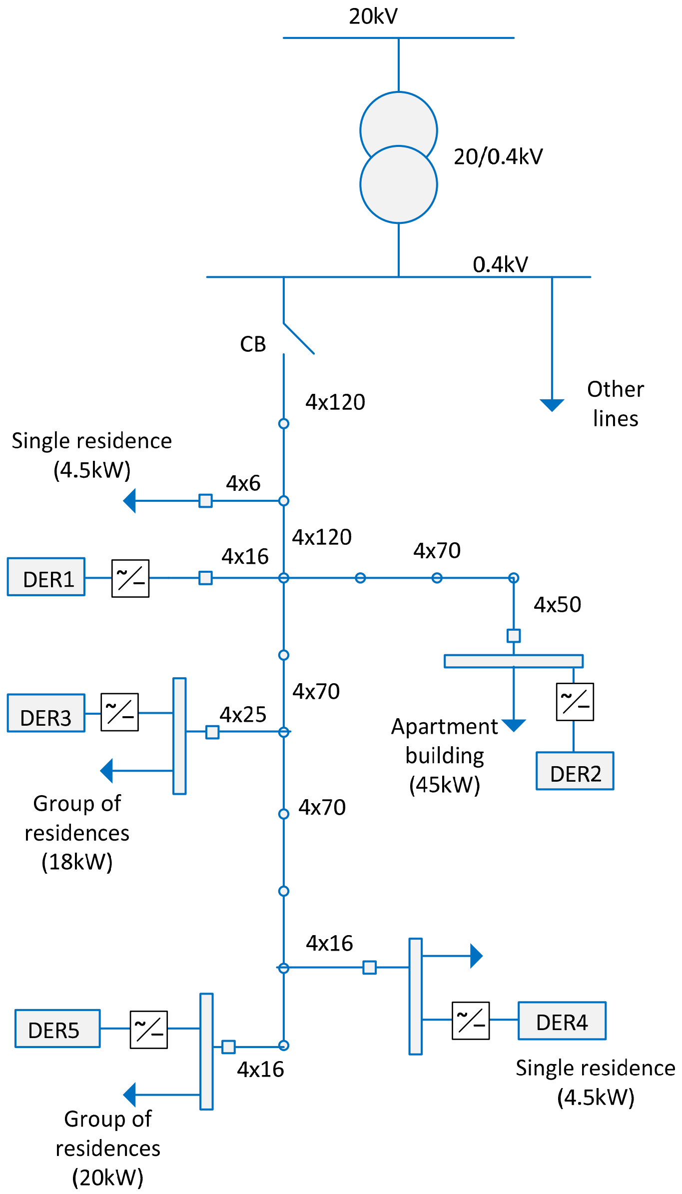

Fig. 2-14 Benchmark MG

The benchmark MG is modelled in MATLAB/Simulink and time-domain simulations are conducted to study the system dynamic response to step load change and fault triggered islanding scenarios.

The first scenario is a step load change at the apartment building. The apartment load is raised from 13.5kW to 45 kW at 0.2s and then reduced back to 13.5kW at 0.7s. The active and reactive powers, output currents and voltages of the DERs with the conventional P-δ droop method are illustrated in Fig. 2-15-(a) to (d), respectively. It is worthwhile to mention that the system response with the P-f droop is quite similar to the P-δ droop and is not shown here for conciseness. It is observed that the system response undergoes several oscillations until settling to the steady-state conditions. Moreover, the reactive power sharing is quite poor due to the small Q-E droop coefficient and unequal pu impedance of DERs transformers. The current sharing is hence poor and the output current of DER_2, which is located close to the apartment building, rises up to 1.03 in the first cycle after the disturbance. This overshoot might stress the inverter switches and threat the system security. The voltages are almost equal due to the low line impedances. The voltage drops from 0.94pu to 0.92pu after the load increase. The poor voltage regulation is caused by a combination of the Q-E droop control action and the voltage drop on the DER transformers.

The system response with the proposed method is depicted in Fig. 2-16. With a time constant of less than 1 cycle, all local controllers react to the load increase in the first cycle after the disturbance. Therefore, the DERs currents rise smoothly and without overshoot. The maximum current of DER_2 is 0.88pu, which is 0.15pu lower than the conventional method case. The active and reactive powers also rise smoothly. Steady-state errors of active and reactive power sharing are initially within $\pm 6\%$ and $\pm 3\%$, respectively. The errors reduce to half after the load increase, ensuring the DERs will not be overloaded during heavy loading conditions. With the load increase the voltage decreases from 1.02pu to 0.98pu, which is in the permissible range ($0.95-1.05$). It is worth mentioning that in Figs. 2-15(d) and 2-16 (d), the waveforms of the voltages are overlapped and hence only the voltage of DER4 is observable.

In the second scenario, the MG initially operates in the grid connected mode, until a fault occurs at the upstream network. The main circuit breaker then opens and the MG is switched to the islanding mode. The simulation results are illustrated in Fig. 2-17. During the fault conditions, the voltage is nearly zero so are the active and reactive powers. At t=0.05 the MG is islanded and the local controllers are switched to the droop control mode. Subsequently, the voltage is raised by the coordinated action of the local controllers. It is observed that the controller responds equally well to islanding, which is a large signal disturbance.

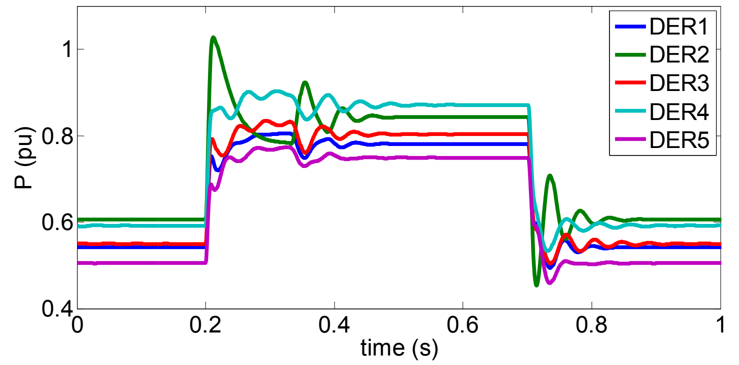

(a)

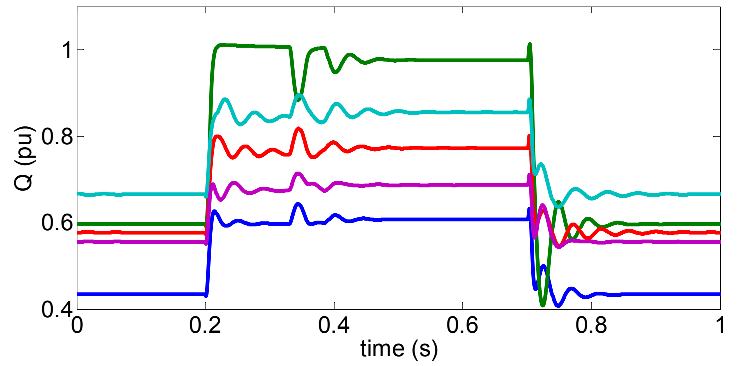

(b)

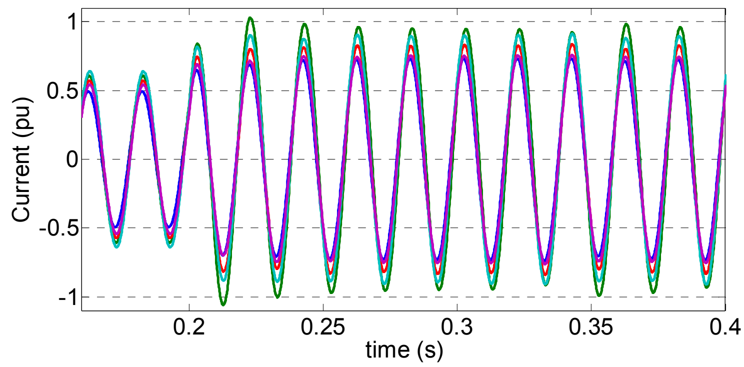

(c)

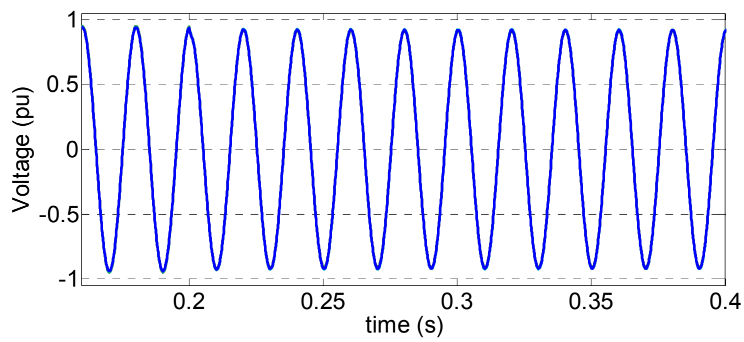

(d)

Fig. 2-15 System response due to a step load change in the apartment building with the conventional droop control method: a) active power, b) reactive power c) current and d) voltage of DER units

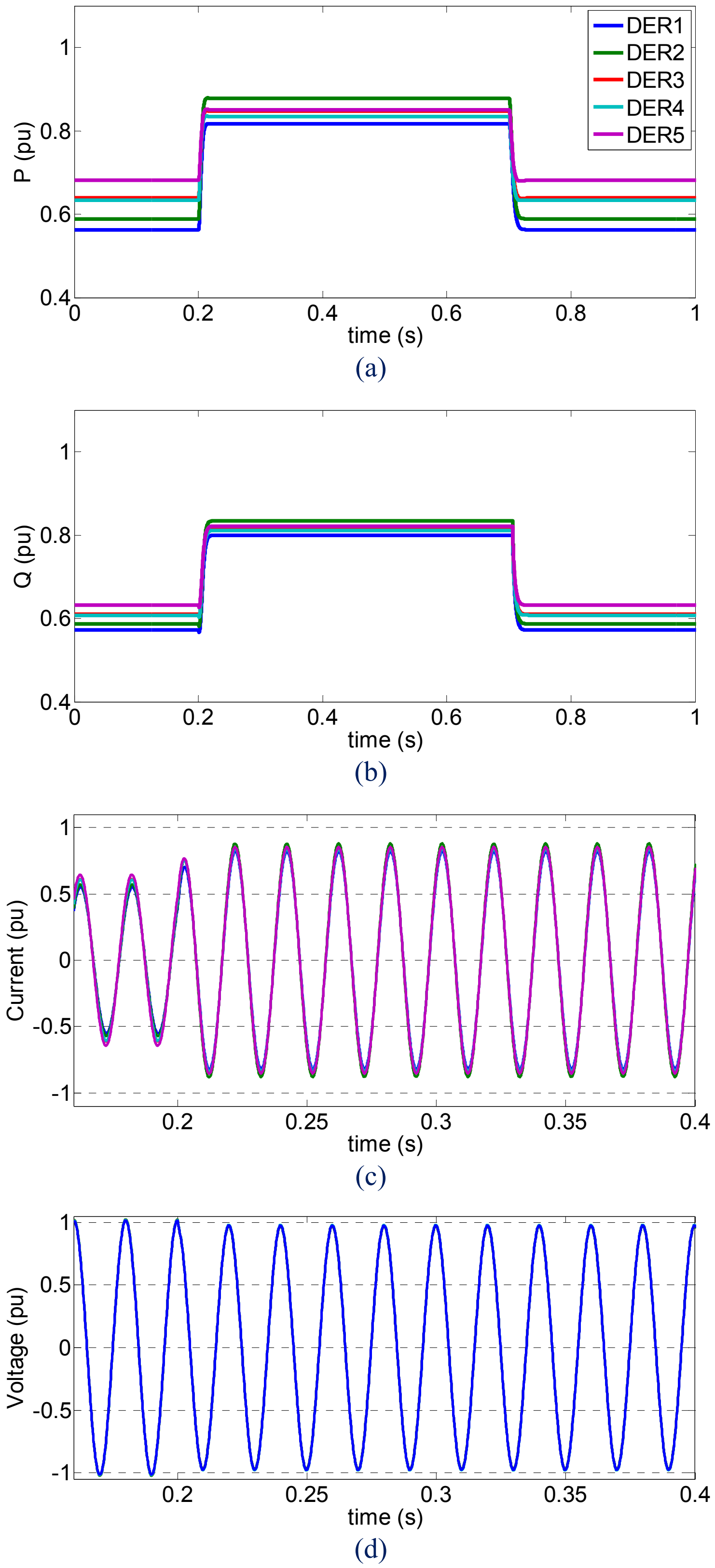

Fig. 2-16 System response due to a step load change in the apartment building with the proposed control method: a) active power, b) reactive power c) current and d) voltage of different DER units

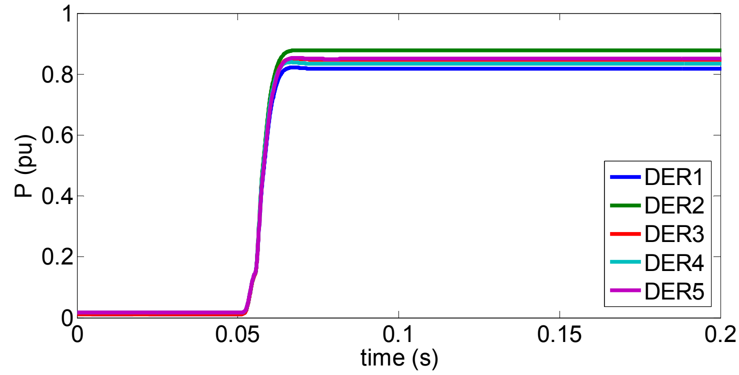

(a)

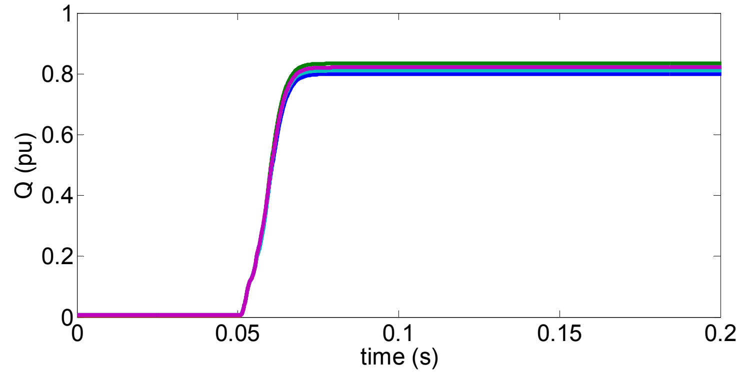

(b)

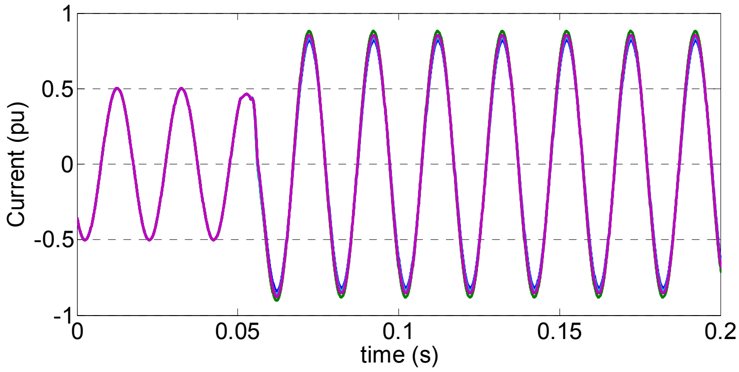

(c)

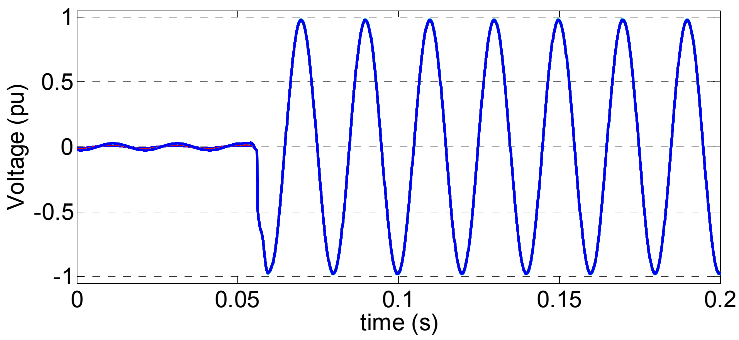

(d)

Fig. 2-17 System response due to a fault triggered islanding with the proposed control method: a) active power, b) reactive power c) current and d) voltage of different DER units

As described in Section 2-2-4, the transformer impedance is utilized in the droop control law to compensate the transformer voltage drop. The impedance might change slightly as a result of temperature variations or aging. In order to evaluate the sensitivity of the proposed method to the transformer parameters variations, the impedance of DER_1 transformer is changed in the range of 90% to 110% of its original value. Scenario 1 is repeated for several different values of the impedance and power sharing error for each DER is calculated as follows:

$$P_{error,x} = \frac{P_x}{P_{rated,x}} - \frac{\sum_{i=1}^{5} P_i}{\sum_{i=1}^{5} P_{i,rated}} \tag{2-46}$$

The reactive power and current sharing errors are calculated similarly. The maximum power and current sharing errors for the proposed method (denoted as P) along with the conventional method (denoted as C) are listed in table 2-4. It is observed that although the variations of the transformer parameters results in an increase of errors, they are still smaller than those of the conventional droop method.

Table 2-4 Power and current sharing error with altered transformer parameters

Description	**Initial load**		**Increased Load**	
	P	**C**	**P**	**C**
Maximum P sharing error	7.9%	9.2%	5.4%	19.8%
Maximum Q sharing error	3.2%	13.5%	2.3%	21.5%
Maximum current sharing error	4.9%	10.1%	3.9%	20.1%

Simulation results show the effectiveness of the proposed method in improving the system dynamic response hence alleviating the current overshoots and stress on the inverter switches. The steady state error of active power sharing can be justified by the fact that perfect even sharing of P is usually neither economic nor necessary. Nonzero error might only result in some DERs reaching the maximum P limit, after which their active power is kept constant.

2-6 Experimental Validation of V-I droop scheme

2-6-1 Laboratory scale MG

The proposed control method has been implemented on a three-phase laboratory scale MG, as shown in Fig. 2-18. The test MG is composed of three inverter-based DERs, three loads and a resistive line model. A variable DC voltage source is used to supply the inverters. Electronically controlled circuit breakers are used to connect/disconnect the inverters and loads from the MG. The DER 1 is included in setup 1 and DERs 2 and 3 are included in setup 2. Each setup is equipped with a dSPACE 1006 controller platform and a GPS timing system.

It is worth mentioning that the experimental implementation could be substantially simplified by using only one dSPACE platform to control all of the three inverters. However, that implementation strategy is in contrary with the distributed nature of MGs, which imposes the use of separate local controllers for individual DERs. More importantly, verifying the efficacy of GPS timing requires at least two separate controller units.

The dSPACE controllers are connected to PCs using Ethernet interface. The "dSPACE Control Desk" program is used to manage the dSPACE controllers and plots/save the signals. The experimental results are captured using the "dSPACE control desk" and plotted in MATLAB.

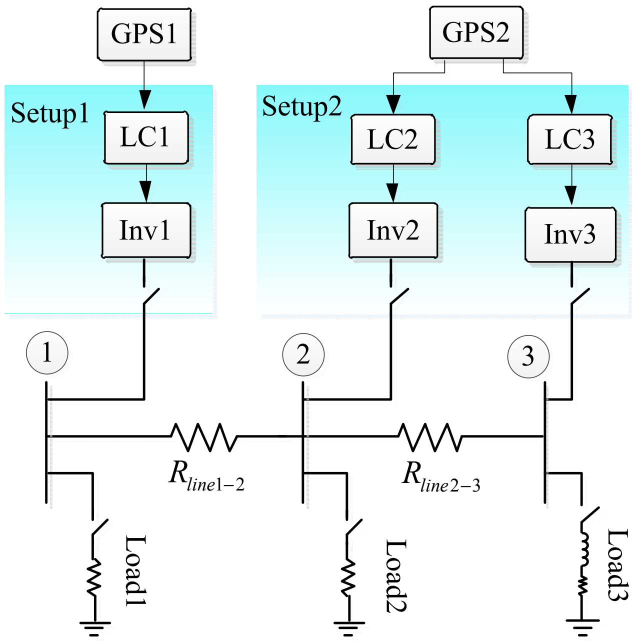

Fig. 2-18 schematic diagram of the experimental setup

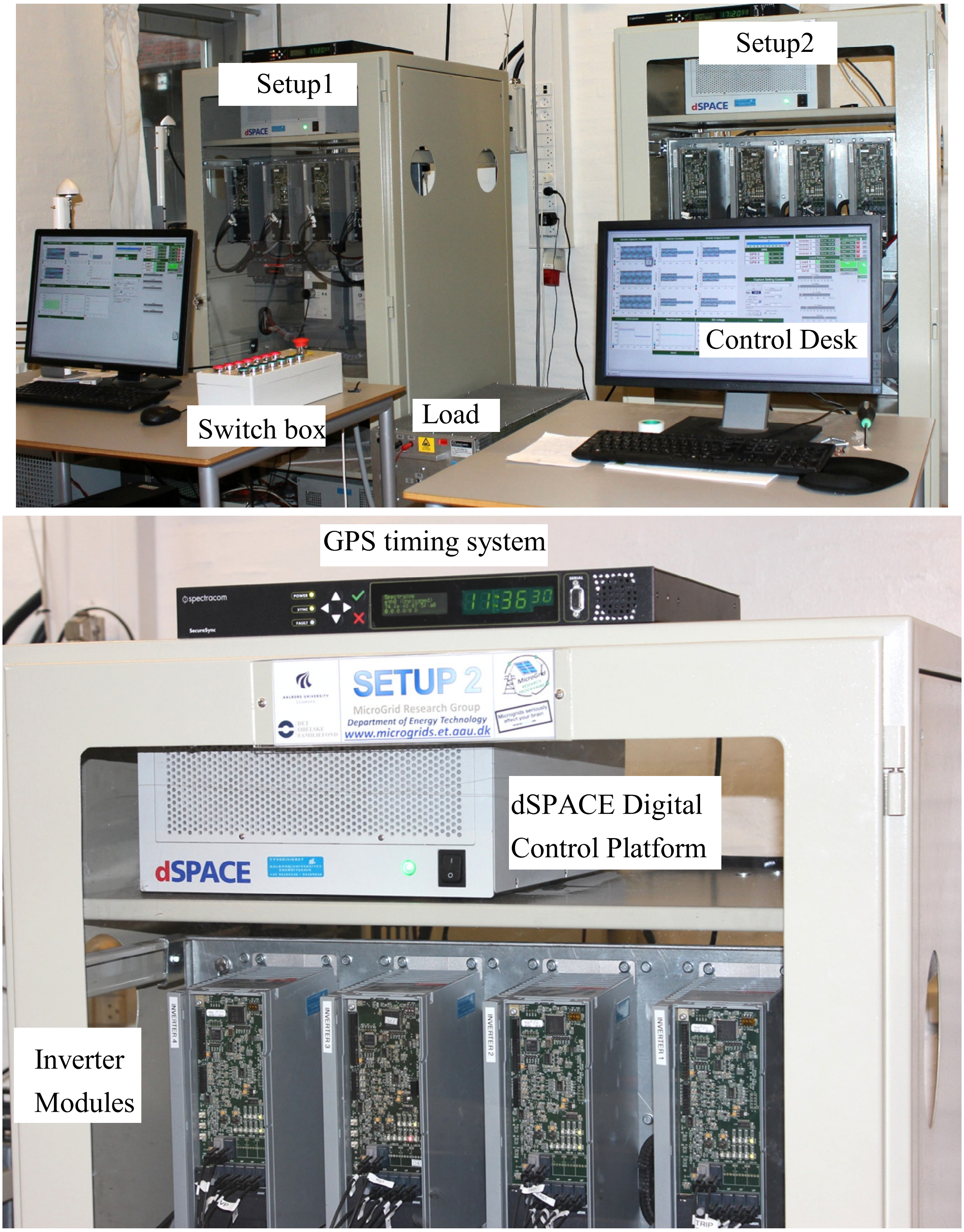

Fig. 2-19 Photos of the experimental setup

The specifications of the experimental hardware as well as control parameters are listed in Table 2-5. The MG is operated at frequency of 50Hz and phase voltage of 220Vrms. The inverters have a rating of 2kVA and are switched at PWM frequency of 10kHz. The load impedances are selected so that the full load power is close to the MG capacity. The LV feeder is modelled by resistive line impedances.

Table 2-5 Parameters of the test MG

Description	**Parameter**	**Value**	**Unit**
Fundamental Frequency	f_0	50	Hz
Rated phase Voltage	V_{rated}	220	Vrms
Inverter Specifications	S_{rated}	2	kVAR
	f_{PWM}	10	kHz
LCL Filter	L_f	8.6	mH
	C_f	4.5	µF
	L_c	1.8	mH
Load impedances	R_1	115	Ω
	R_2	153	Ω
	Z_3	43+j22	Ω
Line Impedances	$R_{line1\text{-}2}$	0.66	Ω
	$R_{line2\text{-}3}$	0.22	Ω
V-I droop coefficients	m	6.5	Ω
	n	25	Ω
Voltage controller parameters	k_{p1}	0.008	S
	kr_1	36	S/s
Current controller parameters	k_{p2}	45	Ω
	k_{r2}	1000	Ω/s

2-6-2 SecureSync timing system

Commonly, accurate time synchronization is achieved based on a timing pulse with a period of 1s. The rise time of the 1 pulse per second signal (1PPS) is synchronized with the UTC time with accuracy of a fraction of microsecond.

GPS receivers are perhaps one of the most widespread communication devices, which are available both as a separate device and as an embedded system in smartphones. However, standard GPS receivers are generally designed for positing and cannot be used for time synchronization. Fortunately, there are quite a few brands which manufacture commercial GPS timing systems, among which Spectracom ® is the top one.

Spectracom, which is a multi-national company, with headquarters in New York, USA, offers a variety of GPS-based timing systems, including SecureSync ® Time and Frequency Reference System, Epsilon GPS Clock, NetClock Public Safety Master Clock and Enterprise Class SecureSync. For the purpose of this project, the latter one was found the most suitable because of the affordable price and availability of a precision 1PPS output. So, we bought the device for laboratory setup.

Fig. 2-20 SecureSync GPS timing system

The picture of SecureSync timing system is shown in Fig. 2-20. The device is equipped with a keypad, three LEDs, an LCD display and a clock display in the front side. The keypad can be used to conduct some basic settings and the LEDs show the status of the device. Normally, the Power and Sync LEDs should light green and the fault LED should be off.

The device features several ports including an Ethernet port, a standard RS232 serial communication port, antenna plug, 1PPS and 10MHz output ports. The most comfortable way for interfacing with the device is Ethernet. The device can be connected to a PC either directly or through a local host/router. After the connection is established, the IP of the device will be displayed on the front LCD. The user interface of the device can be accessed on a PC by entering the IP address in a web browser program.

After turning on, the device searches for the observable satellite signals. As mentioned in Section 2-3-2, four satellite signals are necessary to obtain the position. Once the position is obtained, it is saved in the memory of the device. Afterwards, only one satellite is enough to maintain time synchronization. The signal strengths of the observable satellites as well the historical data of the number of observable satellites can be accessed through interface->GNSS tab.

2-6-3 Interfacing SecureSync timing system with dSPACE controllers

The 1PPS signals from the GPS receivers are depicted in Fig. 2-21. It is observed that the 1PPS signals are synchronized with an accuracy of less than 1μs. The 1PPS signal is captured by dSPACE I/O interface card (DS4002) and used by local controllers to calculate the offset time between the individual local controller clock and the global UTC time (t_{offset}).

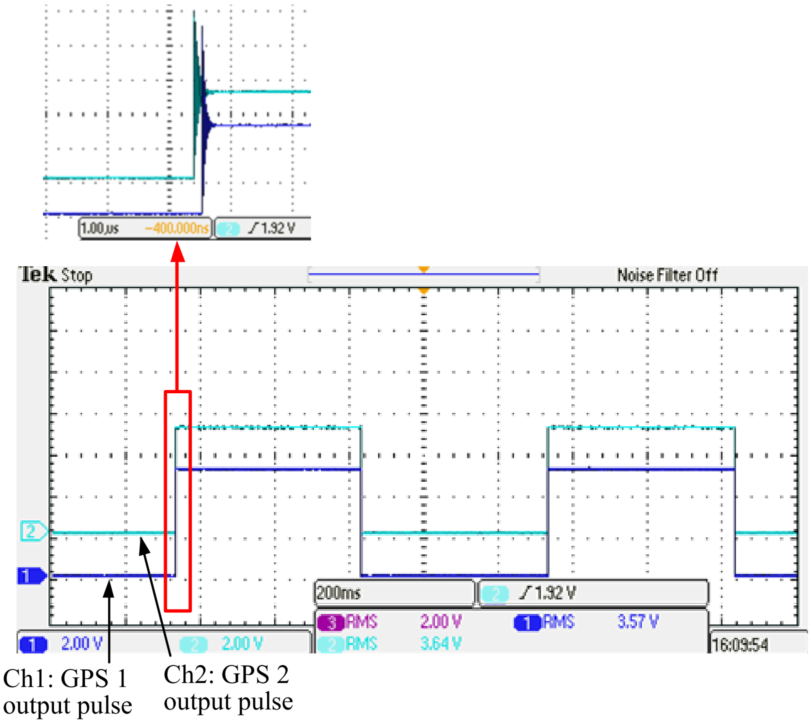

Fig. 2-21 1PPS signals from measured from GPS receivers outputs

2-6-4 Experimental Results

In order to study the performance of the proposed method, three tests are conducted:

- Step load change with the P-V/Q-f droop method
- Step load change with the proposed method
- Connection of a DER to the MG

With the aim of presenting a comparative study, the P-V/Q-f droop method [25], which is conventionally used for MGs with resistive lines, is implemented. The conventional droop parameters are listed in Table 2-6. The P-V and Q-f droop coefficients are designed based on the permissible voltage deviations and pole placement method, respectively. The step load response with the conventional droop method is depicted in Fig. 2-22. Initially, loads 1 and 2 are connected. At t=0.05s, a large reactive load is connected to bus 3. Following the load rise, the active and reactive powers experience overshoot and ringing. The poor dynamic response is mainly originated from the power measurement delay. Moreover, the active power sharing is less accurate at higher loading conditions due to the larger voltage drops on the lines. As a result, the DER3, which is closer to the load, experiences a current overshoot as illustrated in Fig. 2-22 (c).

Table 2-6 Parameters of the Conventional droop

Parameter	Value	Unit
P-V droop coefficient	0.014	1/A
Q-f droop coefficient	0.012	Hz/kVAR

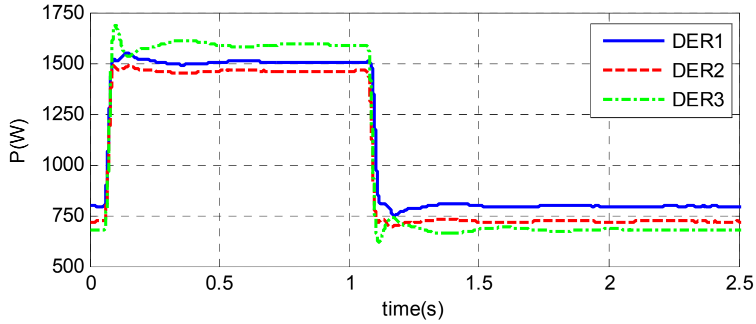

(a)

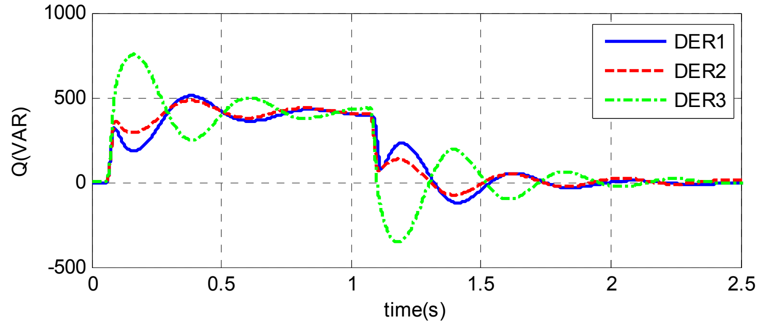

(b)

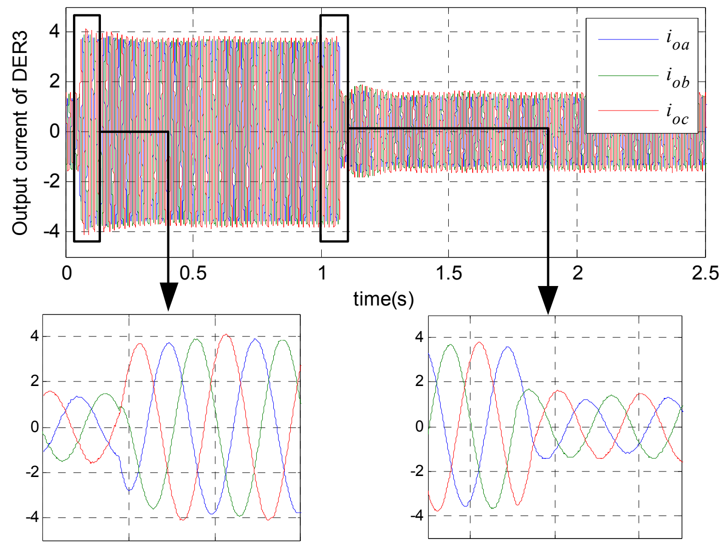

(c)

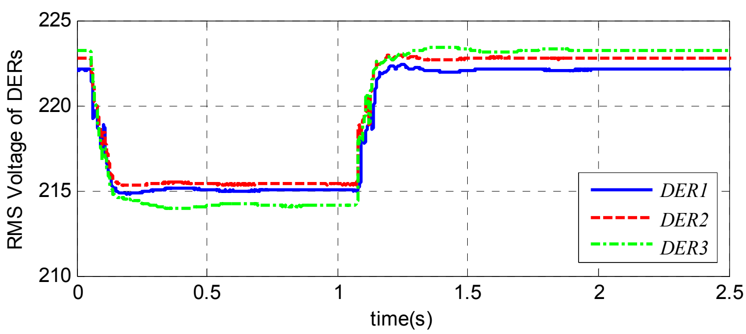

(d)

Fig. 2-22 Experimental Results for test 1 (conventional droop method): a) active powers, b) reactive powers, c) current of DER3 and d) RMS voltages

The step load response with the proposed method is depicted in Fig. 2-23. Comparison of Fig. 2-22 and 2-23 reveals a significant improvement of the dynamic response. Specifically, the transient response of active and reactive power is smooth and the settling time is less than a cycle. As a result, the current of DER 3 rises smoothly. During low loading conditions (at t=0), the active power sharing is not ideal. However, the accuracy of active power sharing is improved at high loading conditions thanks to the piece-wise linear V-I droop characteristics. This helps prevent DERs from overload. Furthermore, the rms voltage is within the permissible range (0.95pu to 1.05 pu), as depicted in Fig. 2-23 (d).

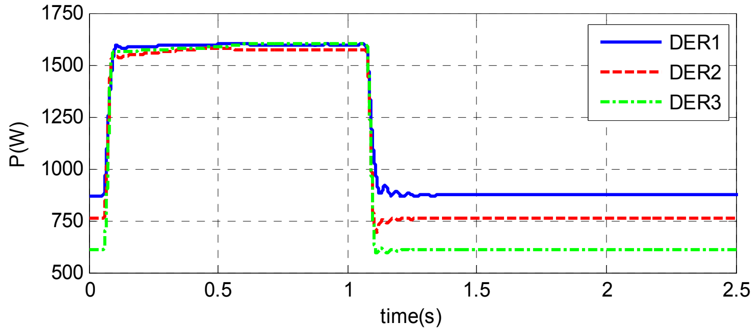

(a)

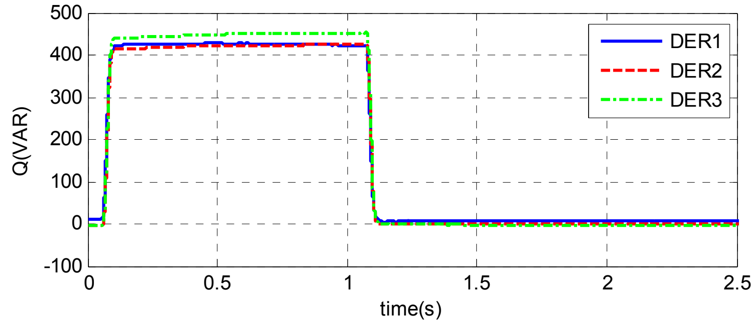

(b)

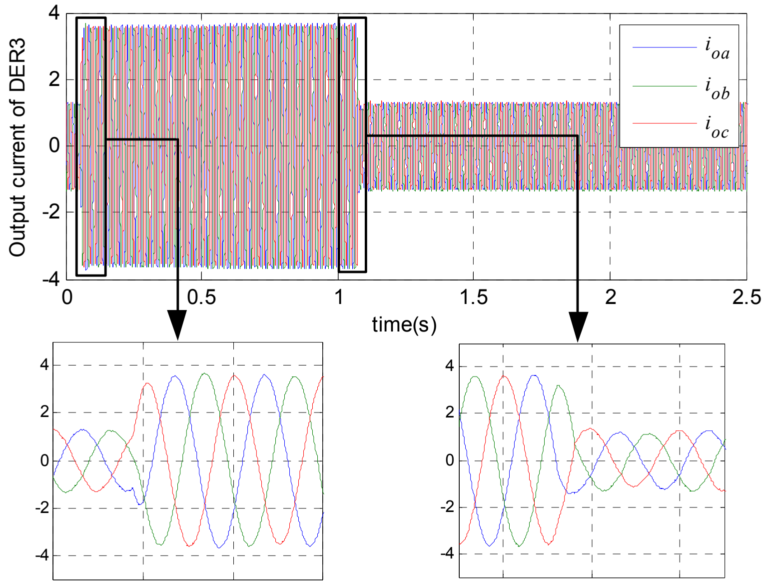

(c)

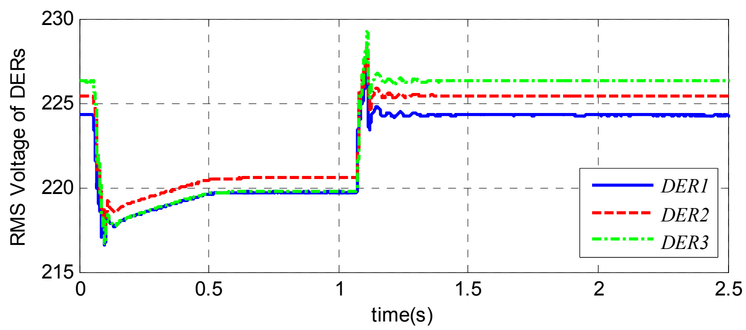

(d)

Fig. 2-23 Experimental Results for test 2 (proposed method): a) active powers, b) reactive powers, c) current of DER3 and d) RMS voltages

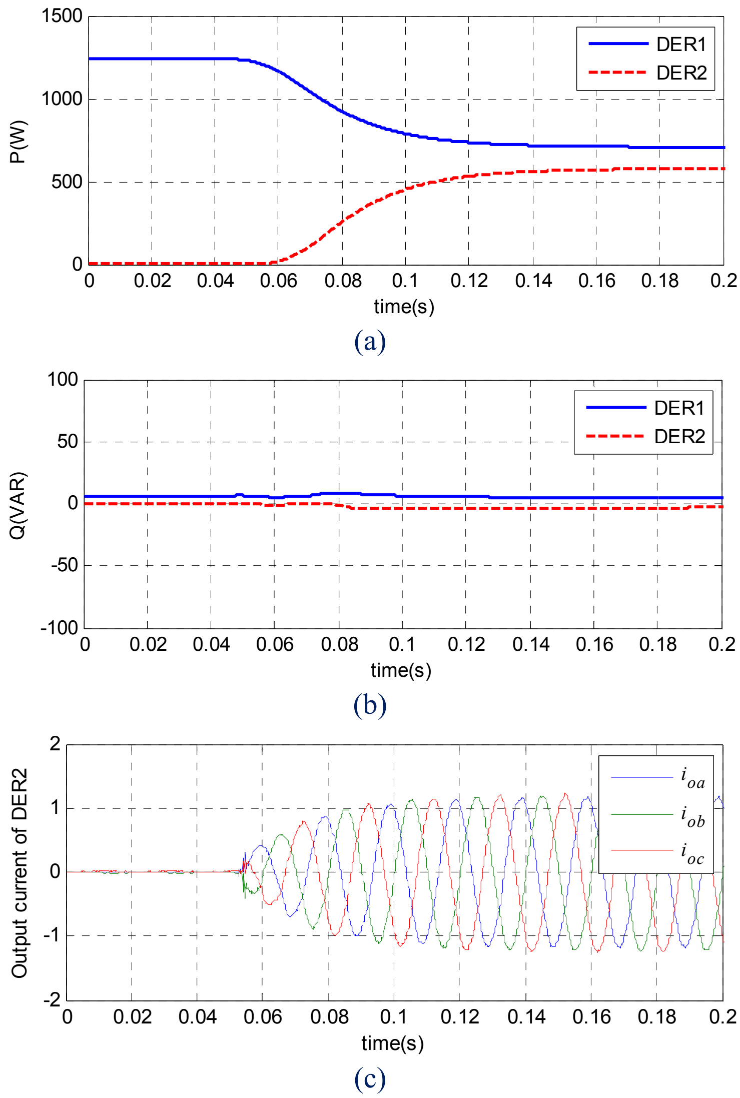

Fig. 2-24 Experimental Results for test 3: a) active powers, b) reactive powers and c) current of DER2

The experimental results for DER connection test are shown in Fig. 2-24. Initially, DER1 and load 1 are connected to the MG. At t=0.05s, DER 2 is connected. It is observed that the load power is shared between the DERs following the connection. The transient of active power and current is smooth and the reactive power remains constant. Therefore, the proposed method enables smooth connection of DERs to the MG without requirement for additional synchronization mechanisms (such as PLL).

2-7 Summary and conclusions

The MGs provide a context for facilitating the integration of renewable energy resources in low voltage networks while delivering a high quality and reliable energy to consumers. However, low inertia, strict current limits and small size of inverter-based DERs on one hand and large step load changes on the other hand make the MGs vulnerable to power quality and stability issues.

This chapter has demonstrated that dynamic and stability of MGs can be improved significantly by designing a droop control scheme in accordance with the characteristics of inverter-based DERs, i.e., low inertia and strict current limits. In this chapter, a new coordinated control method based on V-I droop characteristic is proposed to fulfil the aforementioned aims. In order to improve power sharing accuracy at high loading conditions, when the DERs are vulnerable to overload, a piece-wise linear droop characteristic is adopted.

The proposed control method is analogous to the voltage droop method in DC MGs [62], where the converters output voltages are drooped in accordance to the output current. However, the method is discriminated from the virtual output resistance [25] and virtual inductance [26] methods in AC MGs, which utilize P-E/Q-f droop characteristics for power sharing.

The performance of the droop controller considering the voltage regulator and the filter dynamics is investigated by eigenvalue analysis. The analysis verifies the fast dynamic response and small-signal stability of the method. The method is then applied to the CIGRE benchmark MG and both step load change and islanding scenarios are studied. The simulation results demonstrate a smooth dynamic response, which settles within two cycles after the disturbance. Moreover, the voltage is maintained within 96% to 104% of nominal value. The narrow range of voltage variations on one hand and the fixed frequency operation on the other hand, imply high quality of energy delivered to the consumers.

Chapter 3

Enhancement of the robustness of V-I droop scheme with respect to GPS interruptions

3-1 Introduction

An intrinsic feature of the conventional droop method is the dependency of the frequency on the loading conditions [50]. This results in unwanted frequency deviations which degrade the power quality. The frequency deviations can be compensated by two different approaches:

1-Secondary control schemes: In this approach, which is inspired by secondary control method in power systems, a central controller sends a frequency compensation signal to the DERs. The signal is used by the local controllers to shift the local P-f droop characteristics[6]. So, the steady-state frequency is restored to the nominal value [3]. However, the implementation of the secondary control level requires communication links among the DERs. In addition, the method does not prevent transient frequency fluctuations subsequent to load changes. In case of power systems, such transients are negligible due to the smoothness of load changes. However, in islanded MGs the relatively larger magnitude of instantaneous load changes results in considerable frequency fluctuations.

2- Control methods based on GPS synchronization: An alternative approach is using GPS timing technology [55] to realize constant frequency operation. In this approach, each DER is equipped with a GPS receiver, which produces a pulse at frequency of 1Hz (1PPS). Since all GPS receivers are locked to atomic clocks of the GPS satellites, the 1PPS signal can be utilized to synchronize the DERs.

Recently, several MG control methods based on GPS have been proposed. In [33], a power-angle (P-δ) droop characteristic is introduced to coordinate the power generation of the DERs according to the voltage angles. However, this method suffers from slow dynamic response due to the intrinsic delay of power measurement. In [38], a power management system (PMS) is proposed to calculate the amplitude and angle of the reference voltages of individual DERs according to the power flow requirements. The reference values are then communicated to the local controllers, which regulate the inverter voltages. However, this method requires communication links among DERs. In [39], a decentralized plug and play (P'n'P) control method is proposed to ensure stable operation of meshed MGs subsequent to connection/disconnection of new DERs. However, the requirements of line parameters and load current feedback make the method difficult to implement. In [46], the GPS timing is used to synchronize the rotating reference frames (SRRFs) of the local controllers. The DERs are then coordinated by drooping the d and q axis components of the reference voltage with respect to the d and q axis components of current, respectively.

So far, the GPS-based MG control methods have been studied using computer simulations [33], [38], [39], [46]. Therefore, the practical issues concerning GPS synchronization have been largely neglected. The most important issue is the interruption of the GPS signal, which might result in circulating currents between the DERs or instability depending on the duration of interruption. Another issue is the interfacing of the GPS receivers with the local controllers.

In this chapter, a novel decentralized control method has been proposed to enable practical implementation of GPS timing technology in MG control applications. In this method, the DERs are synchronized by using a combination of GPS timing and an adaptive Q-f droop characteristics. Under normal operating conditions, the DERs are synchronized based on the GPS signals and the frequency is fixed at the nominal value. In case that the GPS signal of a DER fails, the backup Q-f droop is activated to maintain synchronization with other DERs. The synchronization scheme does not require any information about the availability of GPS signal at other DER units. In addition, stable operation is guaranteed regardless of the number of DERs with GPS failure. The scheme is used along with V-I droop control method, to enable coordinated operation without any communication link among DERs.

The salient features of the proposed control strategy in comparison with the previous schemes are summarized in Table 3-1. In this table "Y" and "N" denote yes and no, respectively. Similar to P-δ [33] and V-I [46] droop schemes, the proposed method is independent from network topology/impedances and does not require a communication link between the units. Unlike the other methods, the proposed strategy is robust with respect to GPS failure. In terms of frequency regulation, fixed frequency operation is achieved as long as GPS receivers are functional. However, in case that several units experience GPS failure, the frequency is changed to guarantee safe operation.

Table 3-1 Comparison of the proposed method with the previous schemes

Feature \ Control method	PMS [38]	P'n'P [39]	P-δ [33]	V-I [46]	Proposed
Works without any communication link among DERs	N	Y	Y	Y	Y
Is independent from network topology/impedances	N	N	Y	Y	Y
Has a fast dynamic response	Y	Y	N	Y	Y
Experimental results provided	N	N	N	N	Y
Robust with respect to GPS failure	N	N	N	N	Y
Frequency of operation	Fixed	Fixed	Fixed	Fixed	Fixed/ Var.

The contents of this chapter has been published in [63]. The rest of the chapter is organized as follows: The proposed method is detailed in Section 3-2. The small signal stability of the method is studied in Section 3-3. Experimental results are presented in Section 3-4 to verify the efficacy of the method. Section 3-5 concludes the chapter.

3-2 Proposed Control Method

The schematic diagram of the proposed control method is shown in Fig. 3-1. The controller is composed of a synchronization block, which controls the reference angle of the SRRF (θ) so that the DER is synchronized with the rest of MG followed by a V-I droop controller and cascaded voltage/current controller, which regulates the inverter reference voltage. In order to achieve voltage tracking with zero steady-state error, proportional plus resonant (P+R) control method is used for both voltage and current control loops. The controller output is converted to PWM signals, which control the inverter. The inverter is followed by an LCL filter, which eliminates the switching harmonics.

The V-I droop control law is defined as

$$\begin{bmatrix} v_{cd}^* \\ v_{cq}^* \end{bmatrix} = \begin{bmatrix} E_0 \\ 0 \end{bmatrix} + \begin{bmatrix} R_c & -\omega_0 L_c \\ \omega_0 L_c & R_c \end{bmatrix} \begin{bmatrix} i_d \\ i_q \end{bmatrix} - \begin{bmatrix} r_d f(i_d) \\ r_q i_q \end{bmatrix} \tag{3-1}$$

in which v_c, i, R_c, L_c, r_d, r_q are the filter capacitor reference voltage, output current, inductor resistance and inductance, the d and q axis droop coefficients, respectively. The normalized piece-wise linear function, f, is introduced to improve the current sharing accuracy at high loading conditions, when the DERs are susceptible to over-current. In order to achieve even current sharing, the droop coefficients are selected according to the DER ratings as

$$\frac{r_{d1}}{KVA_1} = \frac{r_{d2}}{KVA_2} = \cdots = \frac{r_{dN}}{KVA_N} \tag{3-2}$$

$$\frac{r_{q1}}{KVA_1} = \frac{r_{q2}}{KVA_2} = \cdots = \frac{r_{qN}}{KVA_N} \tag{3-3}$$

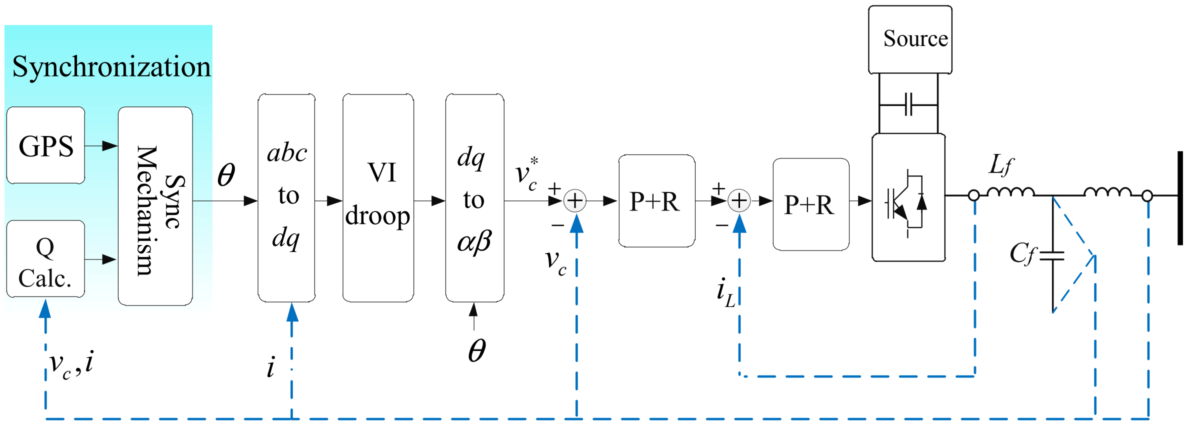

Fig. 3-1 Proposed control method

The schematic diagram of the sync mechanism is shown in Fig. 3-2. It is composed of the GPS timing, adaptive Q-f droop and angle calculation blocks. The GPS timing block calculates the offset time between the local oscillator and the 1PPS signal from the GPS according to the following equation (please refer to Section 2-3-3 for more details):

$$t_{offset} = \mathrm{mod}\{t_{cap}, 1\} \tag{3-4}$$

The offset angle (θ_{offset}) is then obtained by multiplying the offset time with the fundamental frequency.

The function of the adaptive Q-f droop changes depending on the GPS signal status. When the GPS signal is present, the switch S1 is in state I. So the droop frequency, $\delta\omega$, is calculated, according to a piecewise linear characteristic as following:

$$\delta\omega = \begin{cases} k_Q\left(Q - Q_l\right) & \text{if } Q > Q_l \\ k_Q\left(Q + Q_l\right) & \text{if } Q < -Q_l \\ 0 & \text{otherwise} \end{cases} \tag{3-5}$$

where k_Q is the droop coefficient and Q_l is the reactive power limit, which is selected as a fraction of maximum permissible reactive power (e.g., Q_l=0.9Q_{max}). Equation (3-5) implies that while the magnitude of the reactive power is less than the limit, the droop frequency is zero and the DER operates at fixed frequency. However, if the reactive power goes beyond the range, the droop frequency is increased linearly.

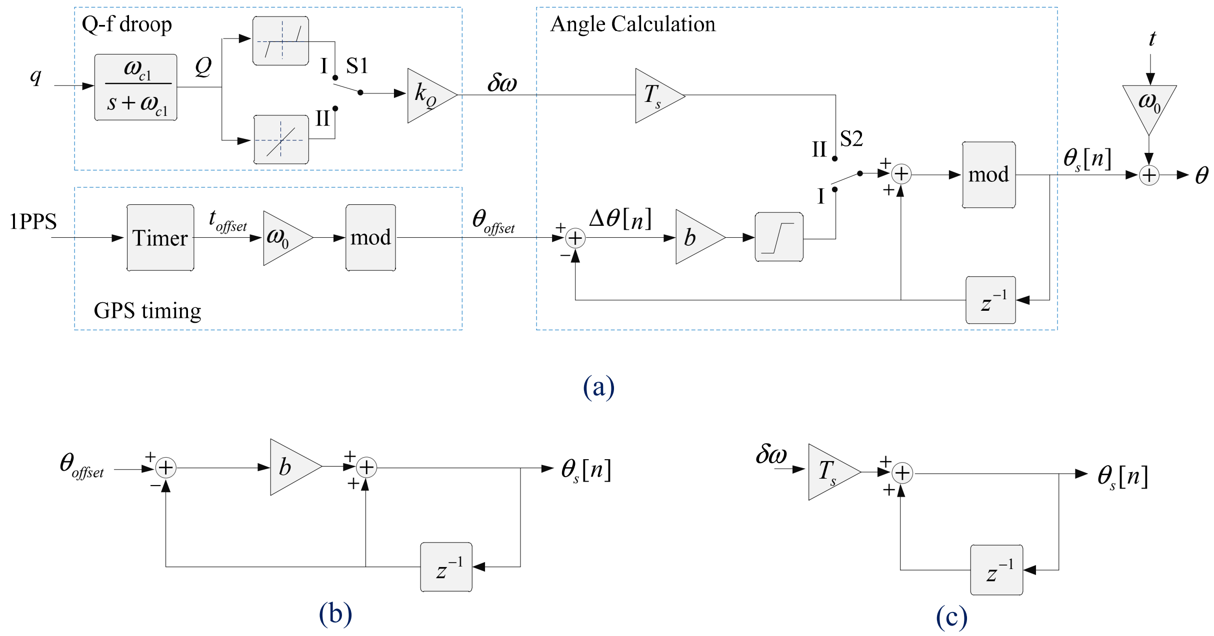

Fig. 3-2 Sync mechanism (a) block diagram, (b) simplified angle calculation block for state 1, (c) simplified angle calculation block for state 2

In case of GPS interruption, the switch S1 is changed to state II. So the droop frequency is calculated, according to a linear characteristic as following:

$$\delta\omega = \left(\frac{Q_{\max} - Q_l}{Q_{\max}} k_Q \right) Q \tag{3-6}$$

in which the droop coefficient is adjusted to have equal maximum droop frequency in both states.

The operation of the adaptive Q-f droop is demosntarted in Fig. 3-3. As for illustration, a 2 DER MG is assumed, in which DER1 (left hand side) is synchronized with the GPS receiver whereas DER2 (right hand side) is experiencing a GPS signal interruption. When the load reactive power is lower than Q_{l1} (operating point x), the frequency is fixed at f_0 and the total load reactive power is supplied by DER1. However, when the load reactive power is increased above Q_{l1}, (operating point o) the frequency rises to f_1 and the load is shared between the DERs.

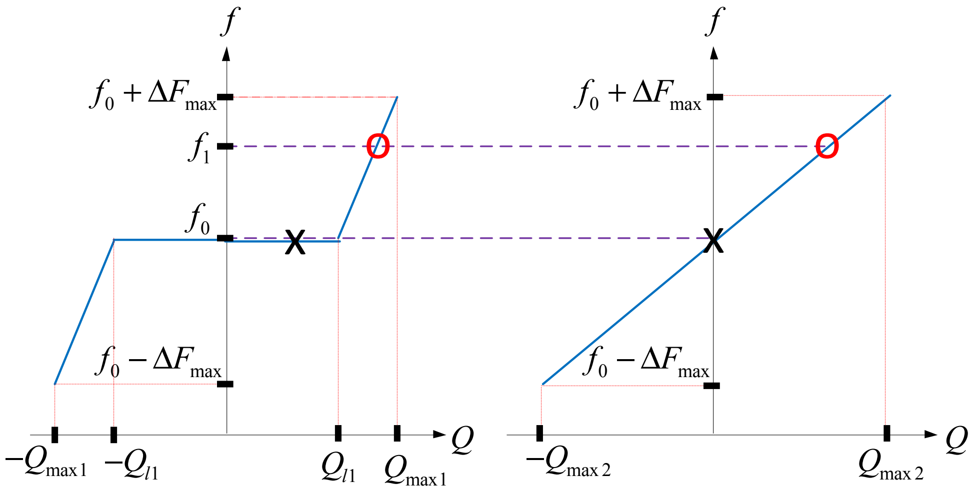

Fig. 3-3 Adaptive Q-f droop operation

Therefore, each DER might operate in one of the following modes:

1- GPS is present and $|Q| < Q_l$: frequency fixed at f_0

2- GPS is present and $|Q| > Q_l$: frequency dependent on Q

3- GPS is interrupted and $Q = 0$: frequency fixed at f_0

4- GPS is interrupted and $Q \neq 0$: frequency dependent on Q

The DERs might switch between the operating modes as a result of GPS interruption/reconnection or load changes. In order to ensure a smooth transfer between different operating modes, an angle calculation scheme is deployed.

The function of angle calculation block is controlled by switch S2. If the DER operates at mode 1, S2 is at state I. Otherwise, S2 is at state II.

In state I, the angle error ($\Delta\theta$) is obtained as the difference between the previous value of the sync angle (θ_s) and the offset angle. The angle error is then multiplied by gain b and saturated and the result is used to update the sync angle. Neglecting the saturation and mod blocks, the angle calculation block is simplified to the diagram shown in Fig. 3-2 (b). The sync angle can be expressed as

$$\theta_s[n] = z^{-1}\theta_s[n] + b\left(\theta_{offset}[n] - z^{-1}\theta_s[n]\right) \tag{3-7}$$

in which b is a constant parameter. Rearranging the terms, the block transfer function is expressed as

$$\frac{\theta_s(z)}{\theta_{offset}(z)} = \frac{b}{1-(1-b)z^{-1}} \tag{3-8}$$

Equation (3-8) represents a low pass filter with a cut-off frequency of

$$\omega_{c1} = -\frac{1}{T_s}\ln\left(1-b\right) \tag{3-9}$$

where T_s is the sampling period. The cut-off frequency of the low pass filter is selected considering the trade-off between smooth mode transition and time synchronization accuracy.

In case the GPS is interrupted or Q goes above Q_l, S2 is switched to state II. Neglecting the “mod” block, the angle calculation block is simplified to the diagram shown in Fig. 3-2 (c). So, the sync angle is updated, as follows:

$$\theta_s[n] = \frac{T_s}{1-z^{-1}}\delta\omega[n] \tag{3-10}$$

Equation (3-10) represents a discrete-time integrator. Therefore, the sync angle is equal to the filtered offset angle or the integral of droop frequency depending on the operating mode. The SRRF angle is calculated as the sum of the sync angle and $\omega_0 t$.

3-3 Small signal analysis of the proposed method

In order to study the small signal stability of the proposed method, a mathematical model of the DER is derived in this section. The inverter reference voltage is represented in the global SRRF as

$$\begin{bmatrix} v_{cd}^* \\ v_{cq}^* \end{bmatrix} = \begin{bmatrix} \cos\delta & \sin\delta \\ -\sin\delta & \cos\delta \end{bmatrix}\begin{bmatrix} v_{cloc,d}^* \\ v_{cloc,q}^* \end{bmatrix} \tag{3-11}$$

where $v_{cloc,d}^*$ is the reference voltage in the local reference frame, which is obtained according to (3-1) and $\delta = \theta - \omega_0 t$ is the angle of difference between the local and global SRRFs.

Assuming the angle δ is small, (3-11) can be approximated as

$$v_{cd}^* = v_{cloc,d}^* + \delta v_{cloc,q}^* \tag{3-12}$$

$$v_{cq}^* = -\delta v_{cloc,d}^* + v_{cloc,q}^* \tag{3-13}$$

In steady-state conditions, the d and q axis voltages and the angle δ settle at the equilibrium point:

$$v_{cloc,d}^* = V_{cd0} \tag{3-14}$$

$$v_{cloc,q}^* = V_{cq0} \tag{3-15}$$

$$\delta = \delta_0 \tag{3-16}$$

$$v_{cd}^{*} = V_{d0} \tag{3-17}$$

$$v_{cq}^{*} = V_{q0} \tag{3-18}$$

To linearize the system, we assume that a small perturbation (from a load change or any other disturbance) occurs in the system. In such a case, (3-12) and (3-13) can be written as

$$V_{d0} + \Delta v_{cd}^{*} = \left(V_{cd0} + \Delta v_{cloc,d}^{*}\right) + \left(\delta_0 + \Delta\delta\right)\left(V_{cq0} + \Delta v_{cloc,q}^{*}\right) \tag{3-19}$$

$$V_{q0} + \Delta v_{cq}^{*} = -\left(\delta_0 + \Delta\delta\right)\left(V_{cd0} + \Delta v_{cloc,d}^{*}\right) + \left(V_{cq0} + \Delta v_{cloc,q}^{*}\right) \tag{3-20}$$

Therefore,

$$\Delta v_{cd}^{*} = \Delta\delta V_{cq0} + \Delta v_{cloc,d}^{*} + \delta_0 \Delta v_{cloc,q}^{*} \tag{3-21}$$

$$\Delta v_{cq}^{*} = -\Delta\delta V_{cd0} - \delta_0 \Delta v_{cloc,\mathrm{d}}^{*} + \Delta v_{cloc,\mathrm{q}}^{*} \tag{3-22}$$

Using (3-1), the perturbation of local voltage reference can be expressed as

$$\begin{bmatrix} \Delta v_{cloc,d}^{*} \\ \Delta v_{cloc,q}^{*} \end{bmatrix} = \begin{bmatrix} R_c & -X_c \\ X_c & R_c \end{bmatrix} \begin{bmatrix} \Delta i_d \\ \Delta i_q \end{bmatrix} - \begin{bmatrix} r_d f'\left(I_{d0}\right)\Delta i_d \\ r_q \Delta i_q \end{bmatrix} \tag{3-23}$$

in which $X_c = \omega_0 L_c$ is the reactance of the output inductor and I_{d0} is the equilibrium value of i_d. Substituting (3-23) into (3-21) and (3-22), we have:

$$\Delta v_{cd}^{*} = \Delta\delta V_{cq0} + \left\{\left(R_c - r_d f'\left(I_{d0}\right)\right)\Delta i_d - X_c \Delta i_q\right\} + \left\{X_c \Delta i_d + \left(R_c - r_q\right)\Delta i_q\right\}\delta_0 \tag{3-24}$$

$$\Delta v_{cd}^{*} = -\Delta\delta V_{cd0} - \left\{\left(R_c - r_d f'\left(I_{d0}\right)\right)\Delta i_d - X_c \Delta i_q\right\}\delta_0 + \left\{X_c \Delta i_d + \left(R_c - r_q\right)\Delta i_q\right\} \tag{3-25}$$

Defining

$$r_d' = r_d f'\left(I_{d0}\right) - R_c \tag{3-26}$$

$$r_q' = r_q - R_c \tag{3-27}$$

and rearranging the terms, (3-24) and (3-25) are simplified to

$$\Delta v_{cd}^{*} = V_{cq0}\Delta\delta + \left(X_c \delta_0 - r_d'\right)\Delta i_d + \left(-X_c - \delta_0 r_q'\right)\Delta i_q \tag{3-28}$$

$$\Delta v_{cq}^{*} = -V_{cd0}\Delta\delta + \left(X_c + \delta_0 r_d'\right)\Delta i_d + \left(X_c \delta_0 - r_q'\right)\Delta i_q \tag{3-29}$$

The angle δ is related to the average time offset (T) and reactive power (Q) as following

$$s\delta = c_1 sT + c_2 Q \tag{3-30}$$

in which c_1 and c_2 are constant coefficients, which depend on the controller operating mode. Moreover, s is the derivative operator.

The average time offset and reactive power are obtained from the instantaneous values as following:

$$sT = -\omega_{c1} T + \omega_{c1} t_{offset} \tag{3-31}$$

$$sQ = -\omega_{c2} Q + \omega_{c2} q \tag{3-32}$$

$$q = v_{cd} i_q - v_{cq} i_d \tag{3-33}$$

in which q is the instantaneous reactive power and ω_{c2} is the cut-off frequency of the low-pass filter.

Substituting (3-33) into (3-32) and linearizing around the equilibrium point, the average reactive power is expressed as

$$s\Delta Q = -\omega_{c2} \Delta Q + \omega_{c2} \left(V_{cd0} \Delta i_q + I_{q0} \Delta v_{cd} - V_{cq0} \Delta i_d - I_{d0} \Delta v_{cq} \right) \tag{3-34}$$

where I_{q0} is the equilibrium value of the i_q.

The reference voltage is fed to the cascaded P+R voltage-current controllers in αβ frame. The P+R controllers can be modelled as PI controller in the SRRF frame as following [64]:

$$i^*_{Ldq} = \frac{k_{r-v}}{2s} \left(v^*_{cdq} - v_{cdq} \right) + k_{p-v} \left(v^*_{cdq} - v_{cdq} \right) \tag{3-35}$$

$$v^*_{Pdq} = \frac{k_{r-i}}{2s} \left(i^*_{Ldq} - i_{Ldq} \right) + k_{p-i} \left(i^*_{Ldq} - i_{Ldq} \right) \tag{3-36}$$

in which k_{p-v}, k_{r-v}, k_{p-i}, k_{r-v} are the proportional and resonant coefficients of the voltage and current controllers, i^*_L and i_L are the reference and measured value of the filter inductor current, v_c is the filter capacitor voltage and v^*_p is the PWM reference voltage, respectively. Moreover, the subscript *dq* refers to the 2 element vector of *d* and *q* components.

The LCL filter dynamics are represented as

$$sL_f i_{Ldq} = -\left[Z_L \right] i_{Ldq} + v_{Pdq} - v_{cdq} \tag{3-37}$$

$$sC_f v_{cdq} = -[Y_c] v_{cdq} + i_{Ldq} - i_{dq} \tag{3-38}$$

$$sL_c i_{dq} = -[Z_c] i_{dq} + v_{cdq} - v_{tdq} \tag{3-39}$$

in which,

$$[Z_L] = \begin{bmatrix} R_L & -X_L \\ X_L & R_L \end{bmatrix},\ [Z_c] = \begin{bmatrix} R_c & -X_c \\ X_c & R_c \end{bmatrix},\ [Y_c] = \begin{bmatrix} 0 & -j\omega C_f \\ j\omega C_f & 0 \end{bmatrix},$$

R_L is the resistance of the filter inductor, X_L is the reactance of the filter inductor, and C_f is filter capacitance.

Combining (3-28)-(3-31) and (3-34)-(3-39), the DER dynamics are expressed in state-space form as following:

$$sx = Ax + B \begin{bmatrix} v_{td} \\ v_{tq} \\ t_{offset} \end{bmatrix} \tag{3-40}$$

where,

$$x = \left[\Delta\delta, \Delta Q, \Delta T, \Delta C_v, \Delta C_s, i_{Ldq}, \Delta v_{cdq}, \Delta i_{dq} \right] \tag{3-41}$$

in which C_v and C_s are the states of the voltage and current controllers, respectively. Specifically,

$$C_v = \frac{1}{s}\left(v_{cdq}^* - v_{cdq} \right) \tag{3-42}$$

$$C_s = \frac{1}{s}\left(i_{Ldq}^* - i_{Ldq} \right) \tag{3-43}$$

The system stability is studied by analysing the eigenvalues of the matrix A. The parameters used in this study are detailed in the Section 3-4. The loci of the dominant eigenvalues with $c_1 = \omega_0$, $c_2 = 0$ (mode 1) and r_q varying from 2.5 to 40Ω are shown in Fig. 3-4. With the increase of r_d , the low frequency eigenvalues (4,5) move away from the imaginary axis. This result implies faster current sharing dynamics. On the other hand, the resonant eigenvalues (labeled as number 6 to number 9) move towards the imaginary axis. Consequently, the LCL filter resonance becomes less damped. Therefore, there is a trade-off between the accuracy of current sharing during transients and the damping of LCL filter resonance.

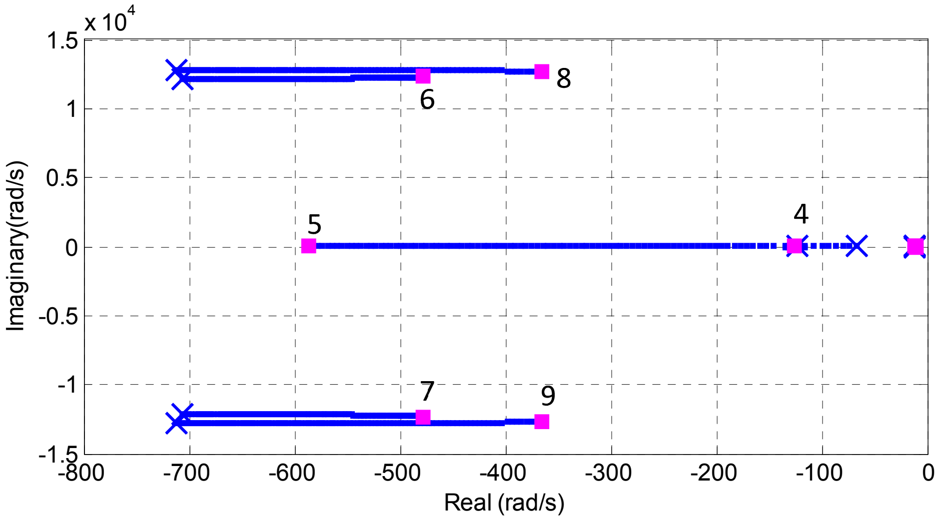

Fig. 3-4 Trajectory of the dominant eigenvalues for r_q varying from 2.5Ω (cross sign) to 40 Ω (square sign)

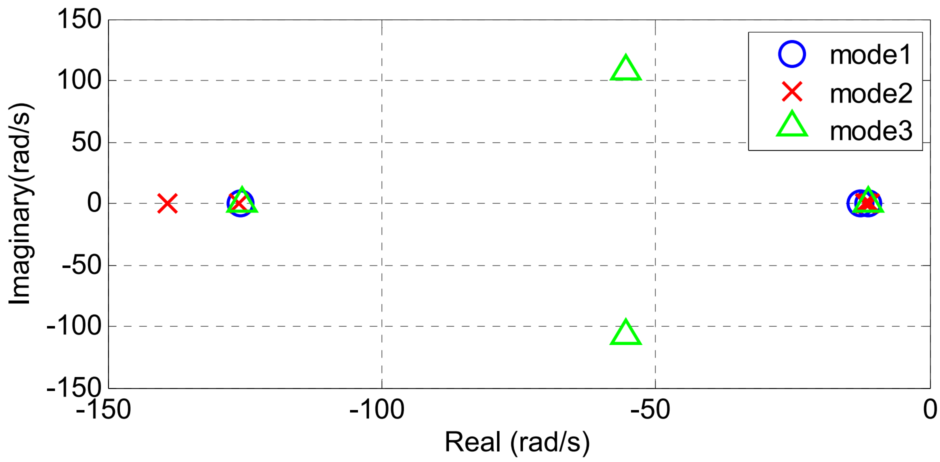

Fig. 3-5 The dominant eigenvalues for modes 1 (blue) , 2 (red) and 4 (green)

The dominant eigenvalues for different operating modes are depicted in Fig. 3-5. It is observed that small signal stability is ensured in all operating modes.

3-4 Experimental Results

The proposed control method has been implemented in the intelligent micogrid lab of Aalborg university. The structure and the parameters of the experimental hardware are detailed in Section 2-6-1. The parameters of the proposed control method are listed in Table 3-2. The droop coefficients r_d and k_Q are selected based on the permissible voltage and frequency deviations, respectively. The q axis droop coefficient is then designed based on the small signal analysis of Section 3-3.

Table 3-2 Parameters of the test MG

Description	Parameter	Value	Unit
V-I droop coefficients	r_d	6.5	Ω
	r_q	25	Ω
Q-f droop parameters	k_Q	0.3	Hz/kVAR
	ω_{c2}	50 π	rad/s
	Q_{max}	1	kVAR
	Q_l	0.9	kVAR
Voltage controller parameters	k_{p1}	0.008	S
	kr_1	36	S/s
Current controller parameters	k_{p2}	45	Ω
	k_{r2}	1000	Ω/s
Sync mechanism LPF	ω_{c1}	4π	rad/s
	b	0.00125	-

The dynamic response of the proposed method with the presence of GPS signals is the same as V-I droop scheme, which has been already presented in Section 2-6-4. Therefore, only the experimental results corresponding with GPS failure and reconnection scenarios are presented in this section, as illustrated in Fig. 3-6. Initially, all of the DERs and loads are connected to the MG and all GPS receivers are active. At t=5s, the GPS signal of DER1 is manually interrupted. So, DER1 uses the linear Q-f droop characteristics to maintain synchronization with DERs 2 and 3. Since DERs 2 and 3 keep the system synchronized to the UTC time, the frequency is fixed at 50Hz. So, Q1 drops to zero and Q_{load} is shared between DERs 2 and 3 according to the v_q-i_q droop characteristics.

At t=25s, the GPS signal of DER2 is interrupted. Following, DER3 attempts to keep the frequency fixed. However, since the Q_{load} is higher than the Q_l, the DER3 is switched to mode 2, changing the frequency according to the piece-wise linear *Q-f* characteristics. Consequently, Q1 rises and Q3 is retained below the maximum value. At t=45s, the GPS of DER 3 is interrupted. As a result, DER3 is also changed to linear droop characteristics. So, Q_{load} is equally shared between the DERs.

At t=65s and 75s, load 3 is disconnected and connected, respectively. It is observed that the step load response is smooth despite the GPS interruptions. At t=90s, the GPS signal of DER 2 is reconnected, changing the DER2 to mode2. At t=110s, the GPS signal of DER1 is reconnected. At this stage, Q2 drops below Q_l and the DERs 1 and 2 synchronize the MG with the UTC time. As a result, the frequency is changed back to 50Hz and Q3 drops to zero. At t=140s, the GPS of DER3 is also connected, switching the DER to mode 1. Subsequently, the reactive power is equally shared between the DERs.

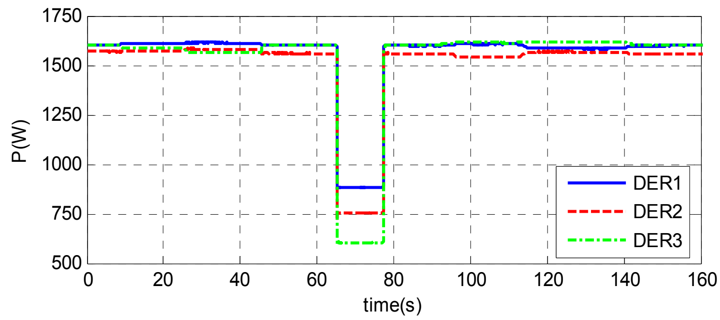

(a)

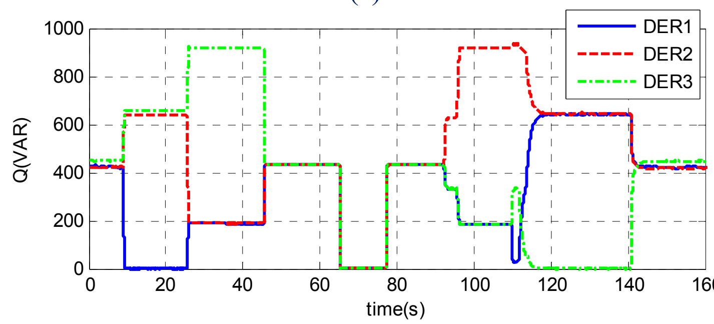

(b)

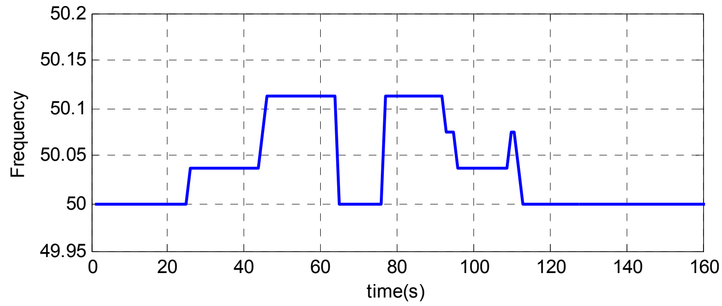

(c)

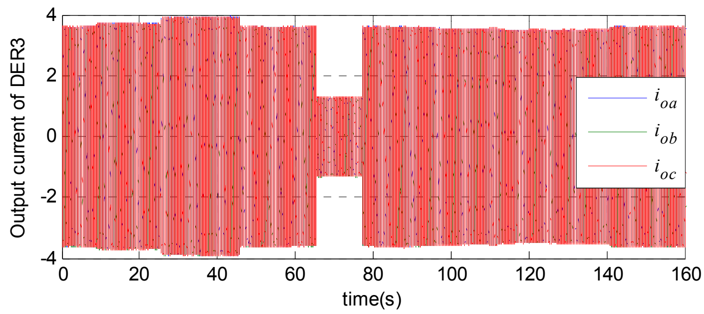

(d)

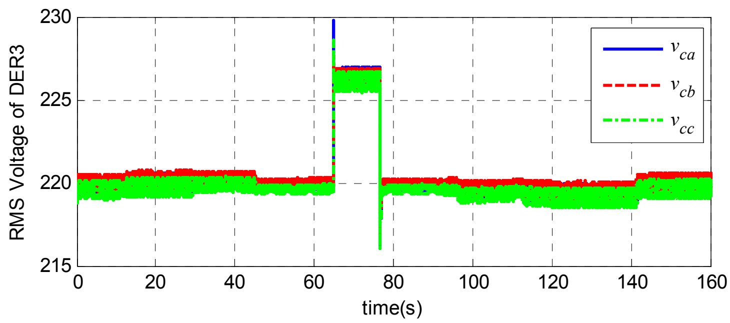

(e)

Fig. 3-6 Experimental Results for test 4: (a) active powers, (b) reactive powers, (c) frequency, (d) current of DER3 and (e) voltage of DER3

Experimental results show that in case of GPS disconnection/reconnection, the DERs change their operating modes so as to maintain synchronization with the MG but also enable fast step load response regardless of the GPS availability. In terms of power quality, fixed frequency operation is achieved as long as sufficient number of DERs receiving the GPS signals. In addition, the voltage profile of the MG is within the permissible range of 0.95 to 1.05pu.

3-5 Conclusions

In this chapter, a novel decentralized control method is proposed for inverter-based islanded MGs. In this method, the SRRFs of the DERs are synchronized to a common reference frame by means of a sync mechanism, which uses a combination of GPS timing and an adaptive Q-f droop controller to align the reference angle of the DERs. In order to coordinate the active and reactive power generation of DERs and follow the load changes with a fast dynamic response, the DER voltage is adjusted according to the V-I droop characteristics.

The proposed control method has been tested using a laboratory-scale MG. The experimental results demonstrate that the proposed method favors from the following features:

- Fixed frequency operation as long as a sufficient number of GPS receivers are functional
- Robustness with respect to GPS signal interruptions
- Overdamped step load response, which eliminates current overshoots
- Improved active power and current sharing at high loading conditions
- Simple connection of the DERs to the MG
- Voltage profile within the permissible range

Chapter 4

A secondary control strategy for microgrids with resistive lines

4-1 Introduction

Despite simple implementation, decentralized MG control methods suffer from voltage and frequency deviations and poor load sharing [4]. To overcome limitation of the decentralized methods and improving their performance, communication-based control approaches are introduced. While centralized methods favor high flexibility and performance, they are considered less practical due to the requirement of an extensive and costly communication network and the fact that the single point-of-failure of the centralized controller affects the whole system [65]. Distributed control architectures have recently gained popularity since they can discharge duties of a central controller with less communication and computation costs, while being resilient to faults or unknown system parameters [6]. Distributed control schemes are composed of local control agents interconnected through a sparse communication network [5]. Each control agent includes primary and secondary control levels. At the primary level, droop control method is used to enable load sharing with a fast dynamic response. Using the information from other agents, the secondary controller eliminates the voltage and frequency deviations caused by load changes and improves power sharing [66].

The existing distributed control schemes are mostly developed based on the assumption of inductive network impedance [6, 67]. For inductive networks the active power and reactive power are decoupled and related with the frequency and voltage, respectively. Therefore, active power-frequency (P-f) and reactive power-voltage (Q-V) droop characteristics are adopted for the primary control level. Moreover, the secondary control methods are introduced to regulate the system frequency and voltage as well as to improve reactive power sharing among the DERs, tackling the limitation of droop control. However, the network impedance is mainly resistive in practice, especially in case of low voltage MGs. In such cases, the existing control methods for inductive systems cannot provide satisfactory performance. In [68], a distributed control method based on $P-\dot{V}$ and Q-f droop characteristics have been proposed for resistive MGs. However, that method suffers from poor dynamic response.

In this chapter, a new distributed secondary control framework is introduced which guarantees voltage regulation and load power sharing in low-voltage resistive MGs. In the primary level of the proposed framework, V-I droop characteristics are used to share the active and reactive components of the load current among the DERs. The use of a resistive droop function not only improves the system damping but also makes the method appropriate for resistive networks. A distributed control scheme is proposed to improve the load sharing and voltage regulation of the V-I droop method. In this method, the d-axis voltage is adjusted so as to regulate the average MG voltage to the rated value while ensuring proper active power sharing. Moreover, the q-axis voltage is altered such that the load current and accordingly the reactive power are proportionally shared between the DERs.

The rest of the chapter is organized as follows. The proposed control method is detailed in Section 4-2. Experimental results are presented in Section 4-3 to verify the efficacy of the proposed method. The chapter is concluded in Section 4-4.

4-2 Proposed Control Method

The sharing accuracy of the droop-based schemes in general and the V-I droop method in particular, is dependent on the line impedances and the distribution of the load in the MG. Particularly, the DER units which have a smaller electrical distance with the load tend to have a larger power output compared to the farther units. On top of that, the voltage deviations caused by the droop characteristics degrades the voltage regulation across the MG. In order to improve the sharing accuracy and voltage regulation, a distributed secondary control method is proposed.

4-2-1 Control structure

The schematic diagram of the proposed control structure for a MG comprising of *n* DER units is illustrated in Fig. 4-1. Each DER includes an energy source, an inverter and an LCL filter, which eliminates the switching harmonics from the output current. The DERs are connected to the point of common coupling (PCC) through line impedances.

Each DER is controlled by a local controller consisting of primary and secondary control layers. The primary control layer is composed of V-I droop controller and the inner control loops, which coordinate the DER units in a decentralized way. The distributed secondary control layer adjusts the offset of the droop characteristics so as to alleviate the effect of line voltage drops on the sharing accuracy and restore the voltage profile within a range of the nominal voltage. The secondary controller of each unit communicates with the neighbor units through a low bandwidth cyber network.

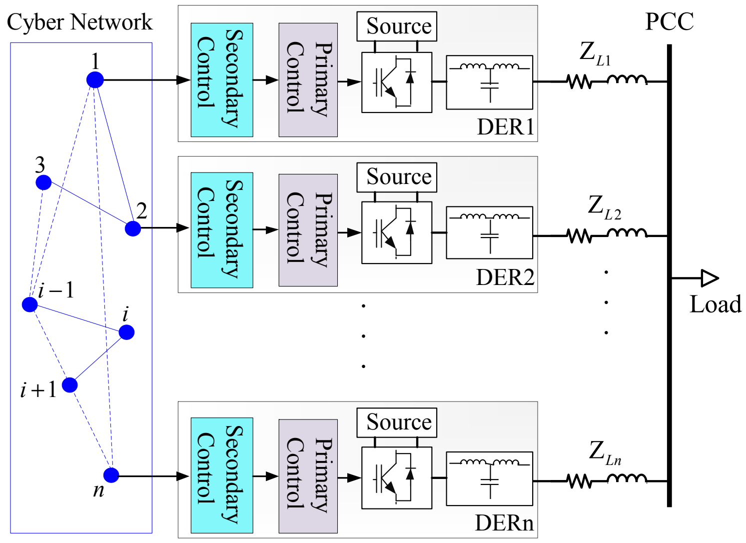

Fig. 4-1 Proposed control structure.

4-2-2 Mechanism of operation

The operation of the proposed control scheme is demonstrated based on Fig. 4-2. For simplicity, the number of DER units is limited to n=2 and the lines are assumed to be purely resistive. Furthermore, the resistance of line 1 is assumed to be larger than line 2. The v_q-i_q droop characteristics for the two DER units are depicted in Fig. 4-2 (a). In this figure, the droop characteristics before and after the activation of the secondary controller are shown by solid and broken lines, respectively. Prior to activating the secondary controller, both units have the same characteristics. However, due to the mismatch between the line impedances, the q-axis component of the local voltage of unit 1 (v_{q1}) is lower than unit 2 (v_{q2}). Therefore, unit 1 supplies a larger q-axis current compared to unit 2. In order to improve the i_q sharing accuracy, the secondary controller of unit 2 increases the secondary voltage, v_{sq2}. Consequently, the v_q-i_q droop characteristic of unit 2 is shifted up and the operating voltages are changed to v'_{q1} and v'_{q2}. As a result, the q-axis load current is equally shared among the units.

The v_d-i_d droop characteristics for the DERs are depicted in Fig. 4-2 (b). Prior to activating the secondary controller, the d-axis components of the local voltages drop to v_{d1} and v_{d2}. In order to improve the voltage regulation, the secondary controllers shift up the d-axis droop characteristics of both units until the d-axis voltages reach v'_{d1} and v'_{d2}. At this stage, the average value of the local voltages is restored to E_0. This way, the MG voltage profile is maintained within the permissible range. Furthermore, by applying a larger secondary voltage to unit 2, the adverse effect of line voltage drop on the sharing accuracy is eliminated. Therefore, i_d is equally shared among the units.

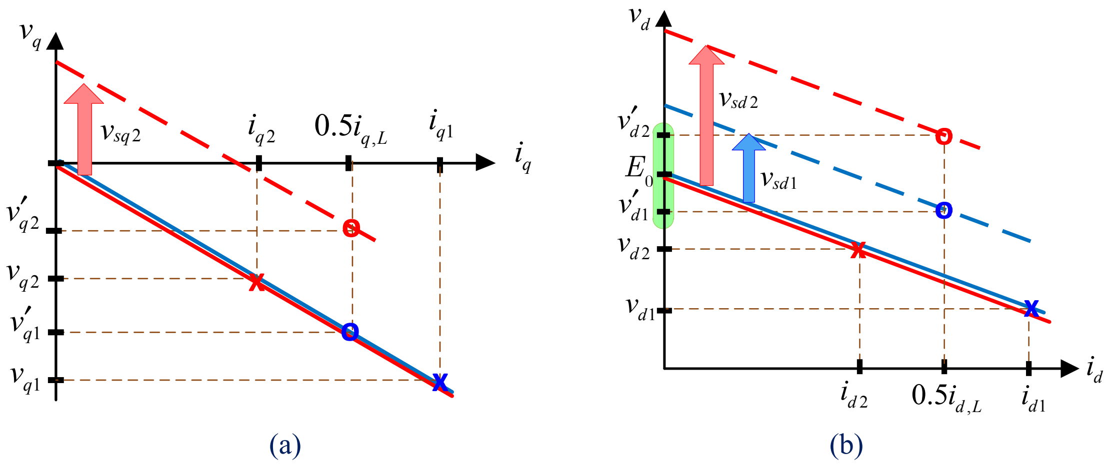

Fig. 4-2 Operation of the proposed controller in a) q-axis and b) d-axis

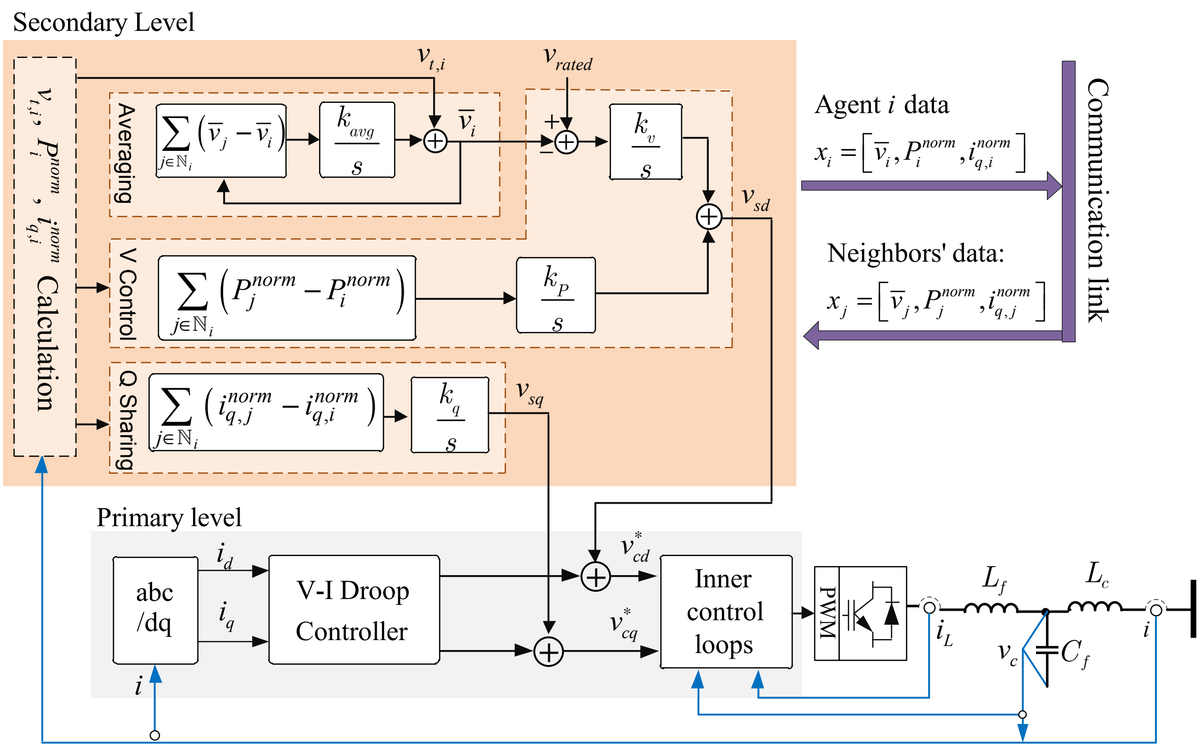

Fig. 4-3 Proposed control method for agent i.

4-2-3 Control scheme

The schematic diagram of the proposed control method for agent i is illustrated in Fig. 4-3. The secondary control level is comprised of four blocks: calculation block, which obtains the terminal voltage, normalized active power and normalized q-axis current; distributed averaging block, which estimates the average value of DER terminal voltages; voltage control block, which improves the voltage regulation and active power sharing accuracy; and Q sharing block, which improves the current sharing accuracy. In the primary level, the inverter reference voltage is obtained by adding the droop and secondary control signals. The inner control loops, which consist of cascaded voltage and current controllers, track the reference voltage with a fast dynamic response. Accordingly, space-vector PWM module assigns appropriate switching signals to drive the inverter.

The secondary control level is designed based on consensus concept. In this framework, an information state x_i is assigned to each control agent. The information states are shared between the agents, i.e., inverters through a sparse communication network. The state of each agent is updated based on the received information form the neighbors. If the distributed communication network contains minimum connectivity, the control agents will reach to consensus, that is, their states will converge to a common value: $x_0 = x_1 = \ldots = x_n$ [69]. Here, the information state is a vector of three variables, including estimated average voltage, $\overline{v}_k$, normalized active power, P_k^{norm} and normalized q-axis current, i_{qk}^{norm}.

The average MG voltage is obtained by using the distributed averaging technique called dynamic consensus [70]. The average voltage estimator of agent i provides the estimation of average voltage magnitude, $\overline{v}_i$, using the information state received from agent j, $\overline{v}_j$, and the local terminal voltage, v_{ti}, as

$$\overline{v}_i(t) = v_{ti}(t) + k_{avg} \int_0^t \sum_{j \in \mathbb{N}_i} \left(\overline{v}_j(\tau) - \overline{v}_i(\tau) \right) d\tau, \tag{4-1}$$

where k_{avg} is the integral gain, and $\mathbb{N}_i$ is the set of neighbors of agent i. Furthermore, the terminal voltage is obtained from capacitor voltage and output current, as following:

$$\begin{bmatrix} v_{td} \\ v_{tq} \end{bmatrix} = \begin{bmatrix} v_{cd} \\ v_{cq} \end{bmatrix} + \begin{bmatrix} R_c & -X_c \\ X_c & R_c \end{bmatrix} \begin{bmatrix} i_d \\ i_q \end{bmatrix} \tag{4-2}$$

$$v_t = \sqrt{v_{td}^2 + v_{tq}^2} \tag{4-3}$$

in which R_c and X_c are the resistance and inductance of the output inductor, respectively.

The normalized active power, P^{norm}, is defined as the ratio of the measured active power on the rated power:

$$P^{norm} = \frac{P}{P^{rated}} \tag{4-4}$$

If the load is shared proportionally among the DER units, the normalized active powers of all units will be equal. With the assumption of resistive network impedance, active power sharing is dependent on the voltage amplitude of individual DERs. In order to properly share the active power and also regulate the voltage within an acceptable range of the nominal value, the d-axis voltage correction term, v_{sd}, is obtained as

$$v_{sd,i} = k_v \int_0^t \left(V^{rated} - \overline{v}_i(\tau) \right) d\tau + k_P \int_0^t \sum_{j \in \mathbb{N}_i} \left(P_j^{norm}(\tau) - P_i^{norm}(\tau) \right) d\tau \tag{4-5}$$

Equation (4-5) implies that the control agents regulate the average voltage at the rated value while attempting to equalize their normalized active powers.

To ensure proper sharing of reactive power, another control module is implemented to provide appropriate q-axis voltage reference for the droop mechanism. Accordingly, the q-axis secondary controller at agent i updates the voltage reference, v_{sq}, by comparing its normalized current, $i_{q,i}^{norm}$, with the normalized current of its neighbors' to find the loading mismatch

$$v_{sq,i} = k_q \int_0^t \sum_{j \in \mathbb{N}_i} \left(i_{q,j}^{norm}(\tau) - i_{q,i}^{norm}(\tau) \right) d\tau \tag{4-6}$$

where k_q is the integral gain. The normalized q axis current, i_q^{norm}, is defined as

$$i_q^{norm} = \frac{i_q}{I_q^{\max}} \tag{4-7}$$

The maximum q-axis current is dynamically updated based on the d-axis current

$$I_q^{\max} = \sqrt{I_{rated}^2 - i_d^2} \tag{4-8}$$

in which I_{rated} refers to the rated DER output current.

Equations (4-6)-(4-8) imply that the control agents attempt to perform reactive power sharing according to the rms current. It should be mentioned that the safe operating region of DERs is limited by their output current rather than a maximum reactive power. Therefore, the proposed approach is more practical compared to the conventional reactive power sharing, which aims at proportional sharing of load reactive power.

4-3 Experimental Results

The proposed method was implemented on a similar test setup as Chapter 2. The control parameters are shown in Table 4-1 and the schematic diagram of the test bed is shown in Fig. 4-4. The links, which are shown as broken lines, connect the neighbor DER units. As seen, the cyber network has a ring-shaped topology. This topology features first order redundancy, i.e., in case that one of the communication links fails, the local controllers remain connected. The proposed control routine is implemented in a dSPACE 1006 digital control system. In order to consider the communication constrains, each of the communication links is emulated in dSPACE as low bandwidth link with data rate of 100 samples per second and delay of 10ms. Two Spectracom ® GPS synchronization systems [71] are used to synchronize the local controllers with the UTC. The DER units are interconnected through a resistive model with R/X ratio of around 7. The MG loads are modelled by a combination of resistive and inductive loads. To consider the worst case scenario, all loads are accumulated at the downstream bus.

Table 4-1 Electrical and control parameters of the test MG

Parameter	Symbol	Value
Inverter nominal power	P^{rated}	1500 W
Line impedance	Z_{L1}	0.66+ j0.07
	Z_{L2}	0.5+ j0.07
	Z_{L3}	0.5+ j0.07
Load impedances (case 1)	Z_{Load1}/ Z_{Load2}	35Ω/ 35+j40 Ω
Load impedances (case 2)	Z_{Load1}/ Z_{Load2}	57Ω/ 34+j47 Ω
Communication Rate	f_{com}	100 samples/s
Communication delay	T_{dcom}	10 ms
DSC Parameters	k_{avg}	1.2 s^{-1}
	k_v	6 s^{-1}
	k_P	0.1 $W.s^{-1}$
	k_q	300 Ω -s^{-1}
Droop coefficients	r_d	5.5 Ω
	r_q	20 Ω

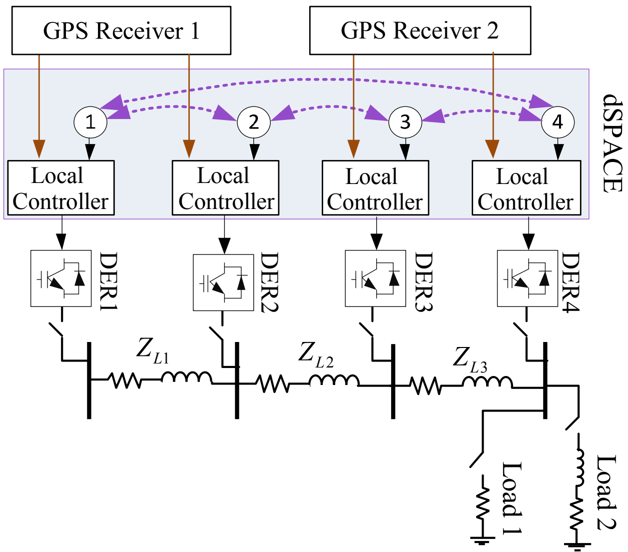

Fig. 4-4 Schematic diagram of the experimental setup

In order to validate the efficacy of the proposed method, two case studies are presented; performance assessment, and plug'n'play capability. The experimental results are captured using dSPACE Control Desk program and plotted in MATLAB. The experimental results for the first study are shown in Fig. 4-5. Initially, load 1 is turned on and the distributed secondary controller (DSC) is disabled. As shown in Fig. 4-5 (a), the sharing of active power between the DERs, provided by the V-I droop mechanism, is affected by the line impedances. Specifically, DER4 provides the largest share (P4) due to its electrical closeness with the load. At t=3s, Load 2 is turned on. It is observed that the load sharing accuracy is improved at higher loading conditions thanks to the adaptive droop function. Nevertheless, a considerable error is observed in both active and reactive power sharing. Additionally, the voltage of DER4 (V4) falls to 207V (see Fig. 4-5(c)), which is out of the permissible range (0.95pu-1.05pu). Subsequent to activation of the DSC at t=6s, the load active power is proportionally shared between the DERs and the voltages are regulated within an acceptable range of the rated voltage. Additionally, the reactive power is properly shared between the DERs according to the available reactive current capacity. Load 2 is turned off and on at t=9 an 12s, respectively. It is observed that the power sharing has an acceptable accuracy and the rms voltages remain within the permissible range during the transients.

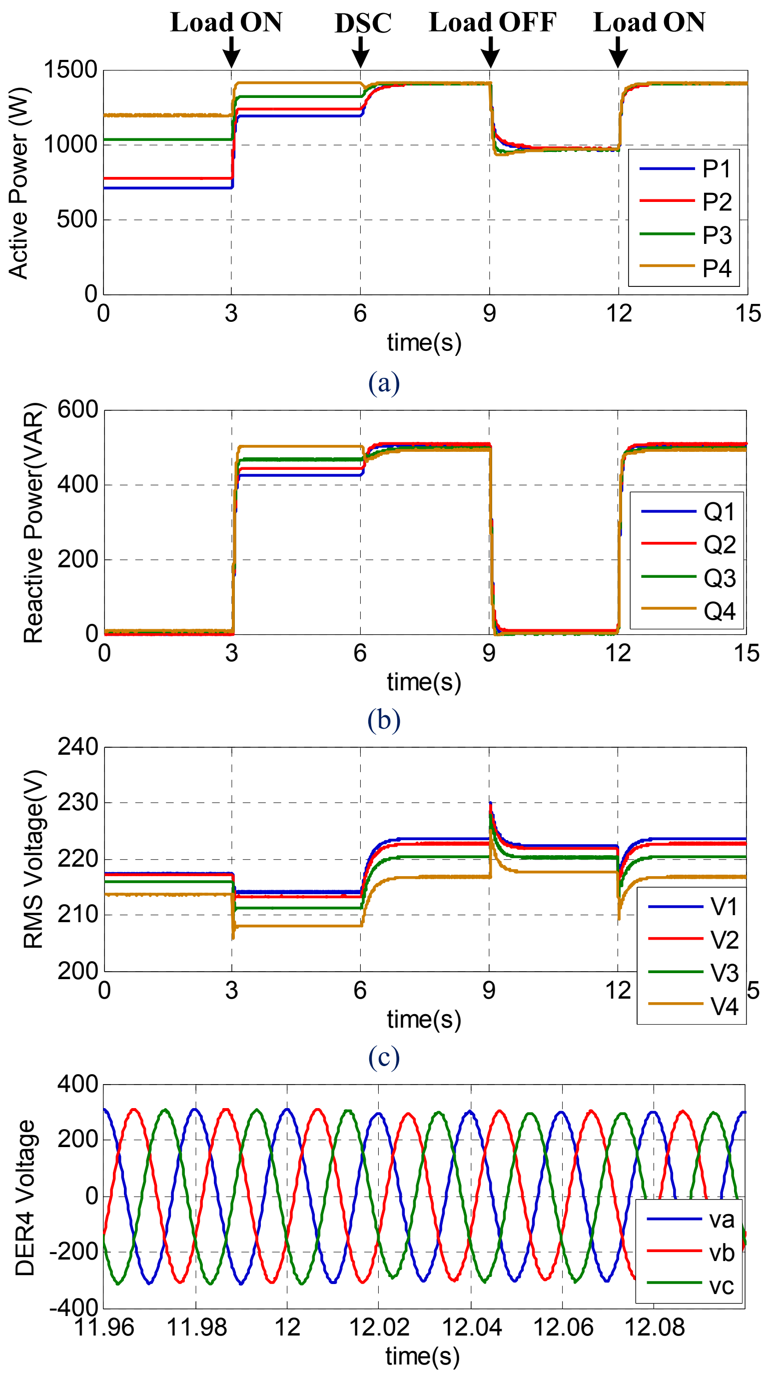

(d)

Fig. 4-5 Performance of the proposed method for the first scenario: a) active powers, b) reactive powers, c) rms voltages and d) DER4 voltage.

In the second case study, plug'n'play capability of the proposed control method is examined. To that end, the electrical connection of DER4 and accordingly all related communication links are disconnected at $t = 2s$. As illustrated in Fig. 4-6, the active and reactive power generations of DERs 1-3 are smoothly increased to compensate for the disconnection of DER4. Moreover, the voltages are maintained within an acceptable range of the rated value. The DER4 is reconnected at $t = 4s$. Following, the powers and voltages are smoothly changed back to their initial value. It should be pointed out that unlike the conventional droop method, the proposed method does not require any additional synchronization mechanisms e.g., PLL prior to reconnection of DER4.

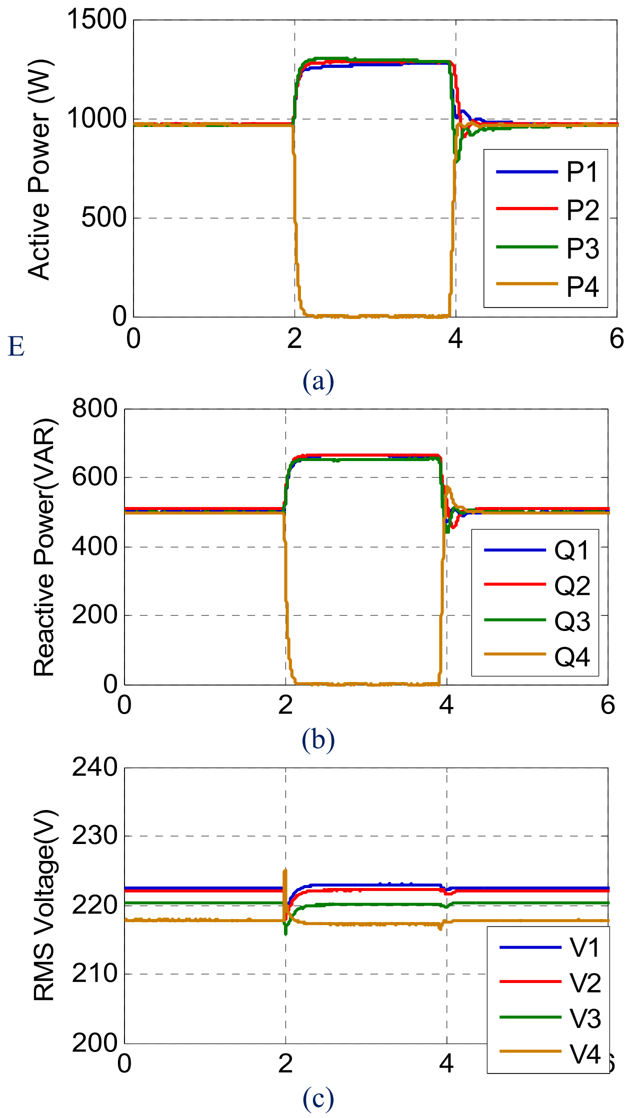

Fig. 4-6 Plug and play capability: a) active powers, b) reactive powers, c) rms voltages.

4-4 Conclusions

In this chapter, a new distributed control framework comprising of primary and secondary control levels is proposed for islanded MGs with resistive line impedances. In the primary level, V-I droop method is adopted as a decentralized control mechanism for fast sharing of load current. For the secondary level, a novel distributed control method is proposed. In this method, each of the control agents alters the d and q axis voltages according to the information received from neighbor agents so as to improve the voltage regulation and ensure proper sharing of active and reactive power. Since the proposed framework uses GPS timing to synchronize the control agents, it has an essential feature that no additional synchronization mechanisms are required while connecting a new DER. Experimental results demonstrate the effectiveness of the proposed method in satisfying the control objectives.

Chapter 5

A distributed control framework for integrated PV-battery based microgrids

5-1 Introduction

The increased penetration of rooftop photovoltaic (PV) panels in low voltage distribution networks might cause several technical problems due to the mismatch between generation and demand throughout the day. Therefore, distribution system operators tend to encourage the installation of energy storage units (ESU) as well as controllable loads, which enable active participation of consumers in load/generation balance [40]. This new infrastructure avails providing the local consumers with a high quality and reliable power source in the context of smart MGs [1].

MGs can operate either in the grid connected or islanded modes. During the grid connected mode, voltage and frequency regulation and load/generation balancing are achieved by the upstream network [72]. Therefore, the control schemes are mainly focused on the economical operation, based on energy prices and electricity markets [73-75]. During the islanded mode, however, a more complex control scheme is necessary to ensure stable and reliable operation. In this mode of operation, specifically, the controller is required to 1) maintain load/generation balance, 2) regulate voltage and frequency, 3) balance the state of charge (SoC) of ESUs, 4) protect the inverters and ESUs from power overload, and 5) protect the ESUs from deep discharging or overcharging.

The most straightforward solution for achieving the aforementioned control objectives is using a central power management system [76-79]. However, the centralized approach exposes a single point of failure, i.e., any failure in the central controller affects the entire system. Moreover, the implementation of centralized controller requires an extensive and costly communication network [4].

An alternative approach is the decentralized scheme, in which each generation and load unit is controlled by a local controller [41, 42, 80-85]. The conventional decentralized control method uses active power-frequency droop to distribute active power between the distributed energy resources (DERs) [41]. However, the conventional droop method ignores the aforementioned objectives 3-5. Adaptive droop schemes, which change the droop coefficient based on the SoC are proposed to balance the SoCs [42, 84, 85]. Furthermore, bus signalling strategies are introduced to trigger different mode changing actions thus protecting the ESUs from deep charging and overcharging [80-83].

The decentralized solutions are mostly limited to ESU and PV units, which are connected to the grid through separate inverters. To reduce the converter losses and the component costs, a hybrid unit can be formed by connecting the PV and ESU in the DC side of an inverter. Although coordination of a single hybrid unit with other DERs in islanded MGs has been recently studied in [82, 83], the proposed methods are not applicable to MGs consisting of multiple hybrid units. In addition, the decentralized methods suffer from frequency and voltage deviations, which degrade the power quality.

Distributed control is a good solution to address the limitation of both centralized and decentralized approaches in implementation of the energy management system. The distributed control frameworks are comprised of local control agents, which are interconnected through a sparse communication network [5]. These control strategies are mostly based on different consensus protocols, which enable regulating some local parameters e.g., voltage, frequency or power generation to a global average value [7]. The distributed control methods favor improved reliability, expandability and lower communication cost compared to the centralized control methods [6].

Distributed control methods have recently gained attraction in various areas of MG control, e.g., for the elimination of voltage and frequency deviations caused by the primary droop controllers [6-10], load power sharing [70], economic profitability [11], voltage control [12], [13], and SoC balancing [14-16] as main ones. However, there is not a single work in the literature, using the potential of distributed control mechanism for coordination of hybrid PV-ESU units in islanded MGs. In this chapter, a novel distributed control framework is proposed to manage the state of each generation/load unit according to the aforementioned control objectives. The main contributions of the presented strategy are as follows:

- In contrast with the existing methods in [41, 42], where coordination of a single hybrid PV-ESU unit with the other DERs is studied, our proposed approach enables coordinated control of MGs consisting of multiple hybrid PV-ESU units.
- A new consensus-based leader-follower strategy is introduced which dynamically changes the communication network topology to ensure SoC balancing despite the power constraints. The leader regulates the voltage in the whole MG, while the followers are responsible to manage the power sharing among the ESUs in the MG. In contrast with

the control method in [8], which incorporates the SoC management objective in active power-frequency droop characteristics and use the distributed controller to mitigate the frequency drifts, we use our current sharing method (proposed in [46]) for power distribution and directly incorporate the SoC management into the distributed control algorithm. The work in [12] and [13] proposes similar leader-follower methodology, but for overvoltage protection during grid-connected mode of operation and are not applicable to the islanded MGs. As opposed to the proposed method, the control schemes in [14-16] do not consider SoC and power constraints.

- A distributed load shedding and PV curtailment strategy is adapted to assure the SoCs are maintained within safe operating region.

The rest of the chapter is organized as follows. The control layout is presented in Section 5-2. The proposed control method is detailed in Sections 5-3 and 5-4. Experimental results are presented in Section 5-5 to verify the efficacy of the method. Section 5-6 concludes the chapter.

5-2 Controller layout

Consider the MG in Fig. 5-1, which is composed of single-phase hybrid DERs and controllable and uncontrollable loads connected to a LV feeder. Each DER is supplied by a rooftop PV panel and an ESU, which are connected to a common DC bus through DC/DC boost converters. The DER is interfaced with the MG through a single phase inverter.

Each of the converters and controllable loads are controlled by a separate module. The ESU control module regulates the DC bus voltage. The PV control module normally adjusts the PV current based on maximum power point tracking method. If the ESUs in the MG are charged to the maximum level, the PV controllers are switched to power curtailment mode to reduce the PV generation. The inverter control module manages the output power based on the total load, total PV generation and SoC of all units. The load control module performs load shedding in case the ESUs are discharged to the minimum level.

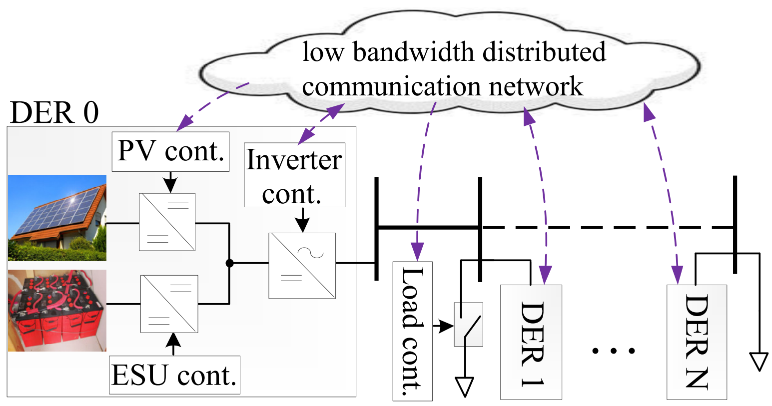

Fig. 5-1 General schematic of the MG control architecture.

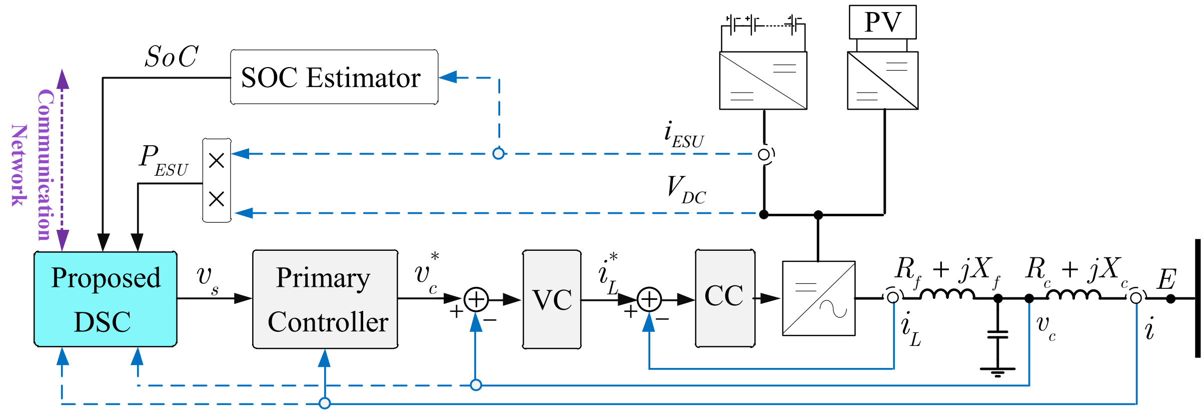

Fig. 5-2 Schematic of the inverter control module

The control modules, which are also referred to as control agents, are interconnected through a low bandwidth distributed communication network. The control framework must ensure load/generation balance, maximize the PV generations, balance the SoCs and regulate the voltage. In addition, the following constraints need to be satisfied:

$$SoC_{\min} < SoC_i < SoC_{\max} \tag{5-1}$$

$$|P_{oi}| < P_i^{rated} \tag{5-2}$$

$$|P_{ESUi}| < P_{ESUi}^{rated} \tag{5-3}$$

in which SoC_i, P_{oi} and P_{ESUi} are the SoC, output active power and ESU active power of inverter i, respectively. The controller should be independent from the network topology and robust with respect to parameter/load variations and communication interrupts. The control structure is detailed in the following sections.

5-3 Inverter control module

As shown in Fig. 5-2, the inverter control module is based on a cascaded structure. The inner loop voltage (VC) and current controllers (CC) use proportional plus resonant method to track the reference voltage with a fast dynamic response. The primary controller adopts V-I droop characteristic to enable decentralized coordination of the DERs. A novel distributed secondary control (DSC) method based on the consensus concept is proposed to achieve the objectives of SoC balancing, restoring the voltage to the nominal value and ensuring safe operation.

5-3-1 Fundamentals of Consensus control strategy

Consensus concept [86] is used to implement the DSC. In this context, each unit is regarded as a control agent which is connected to its direct neighbor through a sparse communication network. The communication network may form a weighted graph, where the agents and communication links are represented by nodes and edges, respectively. The interaction between the agents in this cyber network is quantified in terms of the graph adjacency matrix, $A_G = [a_{ij}] \in R^{N*N}$, in which N is the total number of agents. In case the agent i receives information from agent j, $a_{ij} > 0$ and otherwise, $a_{ij} = 0$. A scalar information state, x_i, is assigned to each agent.

A well-established method for coordination of the agents is to update the information state of agent i according to

$$\dot{x}_i = \sum_{j=0}^{N} a_{ij} \left(x_j - x_i \right) \tag{5-4}$$

Equation (5-4) is commonly referred to as a distributed consensus algorithm in the literature, since it guarantees convergence to a collective decision via local interactions [87]. Defining the convex coefficients $w_{ij} = a_{ij} / \sum_{k=0}^{N} a_{ik}$, one can rearrange (5-4) as

$$\frac{1}{\sum_{k=0}^{N} a_{ik}} \dot{x}_i = -x_i + \sum_{j=0}^{N} w_{ij} x_j \tag{5-5}$$

Therefore, the information state of agent i converges to a weighted average of the information states of its neighbors [67]. If the distributed communication network contains minimum connectivity, each of the information states will converge to a common value: $x_0 = x_1 = \ldots = x_N$ [86].

Although each of the agents can serve as a virtual leader, it is preferable to select the agent which has the least electrical distance from the critical bus of the MG as the leader [34]. Without loss of generality, agent 0 is assigned as the leader and other agents are assigned as followers. The leader does not receive information from the follower agents; thus $a_{0j} = 0$. The follower agent i receives information from its immediate neighbors and the leader (i.e. agent 0).

5-3-2 SoC Balancing

The proposed distributed secondary controller (DSC) realizes the consensus method by introducing a voltage correction term, v_s, into the d-axis droop characteristics. The mechanism of operation of the DSC is explained based on the simplified model of Fig. 5-3. In this model, the dynamics of the VCs, CCs and LCL filters are neglected due to their small time constant compared to the secondary controller. Consequently, the V-I droop controller is simplified to the combination of a voltage source (E^{rated}) and a virtual resistance (r_d). The DSC voltage correction term is represented as a dependent voltage source.

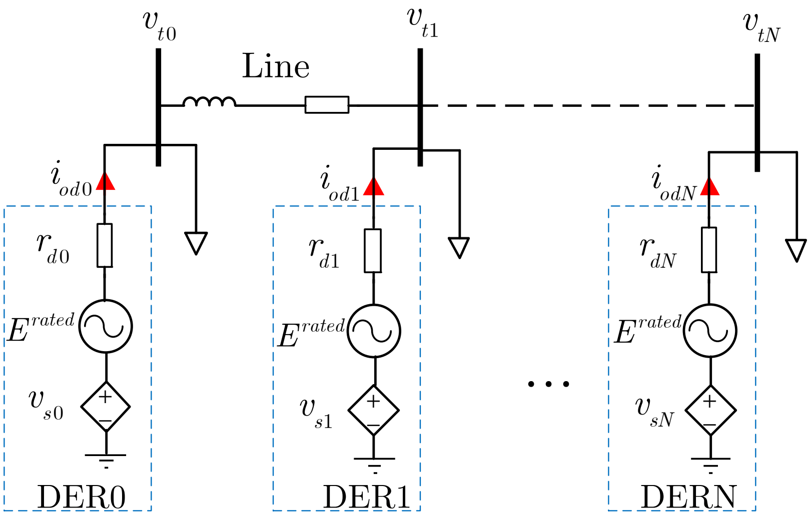

Fig. 5-3 Simplified MG model.

In case the DSC voltage correction terms are zero, the load power is shared between the DERs according to the V-I droop virtual resistances. Additionally, the MG voltage profile deviates from the rated value due to the drop on the virtual resistances as well as the distribution lines. The voltage profile can be improved by setting the DSC offsets of all units to an appropriate common value. However, such a strategy keeps the power sharing between the units unaffected. In order to improve the voltage profile while achieving SoC-dependent power sharing, the DSC voltage correction terms are controlled according to a leader-follower strategy, as explained in the following.

To improve the voltage profile, the leader voltage correction term is calculated as

$$v_{s0} = k_{s0} \int \left(E^{rated} - v_{t0} \right) dt \tag{5-6}$$

in which k_s and v_t are the DSC gain and terminal voltage, respectively.

With the intention of SoC balancing, the information state of unit *i* is defined as

$$x_i = \overbrace{\frac{P_{ESUi}}{C_i}}^{\substack{\text{normalized} \\ \text{ESU power}}} \times \overbrace{\frac{1}{F\left(SoC_i\right)}}^{\substack{\text{SoC-dependent} \\ \text{coefficient}}} \tag{5-7}$$

where P_{ESUi}, C_i and SoC_i are the output power, capacity and state of charge of ESUi, respectively. Moreover, the function $F(\cdot)$ is defined as

$$F\left(SoC_i\right)=\begin{cases} SoC_i - SoC_L \text{ if } P_{ESUi} \geq 0 \\ SoC_H - SoC_i \text{ if } P_{ESUi} < 0 \end{cases} \tag{5-8}$$

in which SoC_L and SoC_H are the lower and higher limits of the SoC, respectively.

For the follower unit *i*, the voltage correction term, v_{si}, is calculated as

$$v_{si} = k_{si}\int\left(P^*_{ESUi} - P_{ESUi}\right)dt \tag{5-9}$$

in which the ESU reference power, P^*_{ESUi}, is calculated according to a weighted average of the neighbors' information states, i.e.,

$$P^*_{ESUi} = C_i F\left(SoC_i\right)\sum_{j=0}^{N} w_{ij}x_j \tag{5-10}$$

in which the coefficients w_{ij} are defined as

$$w_{ij} = \begin{cases} \dfrac{1}{N_i} & \text{if agent } i \text{ receives data from agent } j \\ 0 & \text{otherwise} \end{cases} \tag{5-11}$$

where N_i is the number of the neighbors of agent *i*.

Comparison of equations (5-6) and (5-9) reveals that the leader attempts to restore the voltage to the nominal value while the followers pursue altering the load sharing among the DERs.

Combining (5-7), (5-9) and (5-10), the voltage correction term of the follower agent *i* is expressed as

$$\dot{v}_{si} = k_{si}C_i F\left(SoC_i\right)\left(-x_i + \sum_{j=0}^{N} w_{ij}x_j\right) \tag{5-12}$$

Simplifying (5-12), one can notice that the proposed distributed secondary algorithm is in fact a special form of the well-known consensus protocol in (5-5).

From the model of Fig. 5-3, one can write the DER output current

$$i_{odi} = \frac{E^{rated} + v_{si} - v_{ti,d}}{r_{di}} \tag{5-13}$$

In addition, neglecting the converter losses, the output current is related to the ESU power, i.e.,

$$i_{odi} \cong \frac{P_{ESUi} + P_{PVi}}{v_{ti,d}} \tag{5-14}$$

Combining (5-13) and (5-14), the relation between the voltage correction term and ESU power is obtained

$$v_{si} \cong \frac{r_{di}}{v_{ti,d}} P_{ESUi} + \left(r_{di} \frac{P_{PVi}}{v_{ti,d}} + v_{ti,d} - E^{rated} \right) \tag{5-15}$$

Replacing P_{ESUi} with $x_i C_i F\left(SoC_i\right)$ (as per (5-7)), (5-15) can be expressed as

$$v_{si} \cong \frac{r_{di} C_i F\left(SoC_i\right)}{v_{ti,d}} x_i + \text{constant} \tag{5-16}$$

where the PV power and the grid voltage are assumed constant. Substituting (5-16) in (5-12), the dynamics of the DSC are represented as

$$\frac{r_{di}}{k_{si} v_{ti,d}} \dot{x}_i = -x_i + \sum_{j=0}^{N} w_{ij} x_j \tag{5-17}$$

Equation (5-16) is a special form of (5-5) with coefficients a_{ij} selected as

$$a_{ij} = \begin{cases} \dfrac{1}{N_i} \dfrac{k_{si} v_{ti,d}}{r_{id}} & \text{if agent i receives data from agent j} \\ 0 & \text{otherwise} \end{cases} \tag{5-18}$$

As mentioned in Section 5-3-1, when the consensus strategy converges, all of the information states will reach to a common value. Therefore, (5-7) and (5-8) imply that the surplus power (i.e., total PV generation minus total load) during discharging and charging modes will be dispatched among the DERs according to

$$\frac{P_{ESU0} / C_0}{SoC_0 - SoC_L} = \cdots = \frac{P_{ESUN} / C_N}{SoC_N - SoC_L} \tag{5-19}$$

$$\frac{P_{ESU0} / C_0}{SoC_H - SoC_0} = \cdots = \frac{P_{ESUN} / C_N}{SoC_H - SoC_N} \tag{5-20}$$

Consequently, the ESU with higher SoC is discharged faster (charged slower) than the one with lower SoC [14].

5-3-3 Controller design guidelines

The criteria for the controller design are:

1- The dynamics of the DSC should be much slower compared to the primary control level but much faster compared to the rate of change of SoCs.

2- The proposed consensus algorithm must be stable in spite of the communication constraints.

The first criterion ensures the decoupling of primary and secondary control levels. As detailed in [46], the time constant of the V-I droop controller is around one fundamental cycle, i.e., 20ms. On the other hand, the rate of change of SoC is in the order of minutes-hours. Therefore, the time constant of the DSC should be in the order of seconds.

The effect of communication constraints including the delays and the switching of topology on the consensus algorithm is detailed in [88] and [89]. Defining the Laplacian matrix of the communication network, $L_G = [l_{ij}] \in R^{(N+1)*(N+1)}$, as

$$l_{ij} = \begin{cases} \sum_{k=0,\mathrm{k}\neq i}^{N} a_{ik} & \text{if} \quad i = j \\ -a_{ij} & \text{otherwise} \end{cases} \tag{5-21}$$

the consensus algorithm will converge if the communication delay satisfies the following inequality [88]:

$$T_{dcom} < \frac{\pi}{2\lambda_{\max}(L_G)} \tag{5-22}$$

in which $\lambda_{\max}$ refers to the largest eigenvalue of a matrix and T_{dcom} is the communication delay.

To simplify the design, all nonzero communication coefficients are selected to be identical and equal to a. In other words:

$$\forall i \in \{1,2,...,n\}: \quad \frac{1}{N_i} \frac{k_{si} v_{ti,d}}{r_{id}} = a$$

Using the theorem proposed in [90], an upper bound for the largest eigenvalue of Laplacian matrix is expressed as

$$\lambda_{\max}\left(L_G\right) \le \left(2\max_i\left\{N_i\right\} - 1\right)a \tag{5-23}$$

Substituting (5-23) into (5-22), the upper bound of the communication coefficient is calculated as

$$a < \frac{\pi}{\left(4\max_i\left\{N_i\right\} - 2\right)T_{dcom}} \tag{5-24}$$

Combining (5-24) and (5-18), the upper bound of the DSC gain for agent *i* is obtained as

$$k_{si} < \frac{r_{di}}{v_{ti,d}} \frac{\pi N_i}{\left(4\max_i\left\{N_i\right\} - 2\right)T_{dcom}} \tag{5-25}$$

5-3-4 Power Limiting

Although the proposed distributed method in Section 5-3-2 is effective in terms of SoC balancing, it does not respect the power limits of inverters and ESUs. In order to guarantee safe operation, the proposed consensus algorithm is modified to comprise the power limiting feature.

The minimum and maximum limits of the ESU power are obtained by combining (5-2) and (5-3)

$$P_{\min i} = max\left\{-P_{oi}^{rated} - P_{PVi}, -P_{ESUi}^{rated}\right\} \tag{5-26}$$

$$P_{\max i} = \min\left\{P_{oi}^{rated} - P_{PVi}, P_{ESUi}^{rated}\right\} \tag{5-27}$$

For the follower agents, the ESU reference power, which is calculated from (5-10), is checked versus the maximum and minimum limits, i.e.,

$$P_{\min i} \le P_{ESUi}^{*} \le P_{\max i} \tag{5-28}$$

If the constraint (5-28) is violated, the ESU power is fixed at the corresponding limit. This means that the variable x_i is also fixed. In such a case, the agent *i* is excluded from the algorithm and does not broadcast its state information to the other agents. In order to ensure the integrity of the communication network, the agent is bypassed by sending the information state of agent *i*-1 to the agent *i*+1 and vice-versa.

For the leader agent, ESU power limiting is conducted by amending the state, as follows

$$x_0 = \begin{cases} \frac{P_{ESU0}}{C_0 F\left(SoC_0\right)} + k_{lim}\left(P_{ESU0} - P_L\right) & \text{if} \quad P_{ESU0} < P_L \\ \frac{P_{ESU0}}{C_0 F\left(SoC_0\right)} & \text{if} \quad P_L < P_{ESU0} < P_H \\ \frac{P_{ESU0}}{C_0 F\left(SoC_0\right)} + k_{lim}\left(P_{ESU0} - P_H\right) & \text{if} \quad P_{ESU0} > P_H \end{cases} \tag{5-29}$$

in which $P_L = P_{min0} + P_{marg}$, $P_H = P_{max0} - P_{marg}$, P_{marg} is the power margin and k_{lim} is the limiter coefficient.

If the ESU power is within the defined margins, (5-29) is reduced to (5-7) and the leader power is determined based on its SoC. Otherwise, the magnitude of the leader information state is increased, imposing other agents to increase their share of surplus power. As a result, the leader power is limited.

The power margin, P_{marg}, is a key design parameter; large power margin reduces the functionality of the proposed SoC balancing method, while small values adversely affect the controller dynamics.

The parameter k_{lim} should be selected so that when P_{ESU0} reaches its limit, the absolute value of x_0 is larger than x_{max}. This way, as long as x_0 is below x_{max}, the ESU0 works within its safe operating region. From (5-29), the value of x_0 at the power limits can be expressed as:

$$x_0 = \begin{cases} \frac{P_{ESU0}}{C_0 F\left(SoC_0\right)} + k_{lim}\left(P_{\min 0} - P_L\right) & \text{if} \quad P_{ESU0} = P_{\min 0} \\ \frac{P_{ESU0}}{C_0 F\left(SoC_0\right)} + k_{lim}\left(P_{\max 0} - P_H\right) & \text{if} \quad P_{ESU0} = P_{\max 0} \end{cases} \tag{5-30}$$

However, $C_0 F\left(SoC_0\right)$ is always positive. Therefore,

$$\begin{cases} x_0 < -k_{lim} P_{\text{marg}} & \text{if} \quad P_{ESU0} = P_{\min 0} \\ x_0 > k_{lim} P_{\text{marg}} & \text{if} \quad P_{ESU0} = P_{\max 0} \end{cases} \tag{5-31}$$

So, the absolute value of x_0 is always greater than $k_{lim} P_{\text{marg}}$. Selecting k_{lim} according to:

$$k_{\text{lim}} > \frac{x_{\max}}{P_{marg}} \tag{5-32}$$

it can be ensured that $\left|x_0\right|_{at\,P\text{limit}} > x_{\max}$.

5-3-5 Proposed DSC algorithm

Fig. 5-4 illustrates the cooperative algorithm for the leader agent. As can be seen, the terminal voltage of the inverter is estimated first according to the simplified DER model (see

Fig. 5-3). To restore the voltage drop caused by the primary droop controller, the leader control command is updated based on (5-6). Next, the function $F(SoC_0)$ is calculated according to (5-8) and limited to the range $[F_{\min},\infty)$. This restriction is necessary to prevent the information state from singularity. Following, the information state is obtained according to (5-29) and broadcasted to the follower agents.

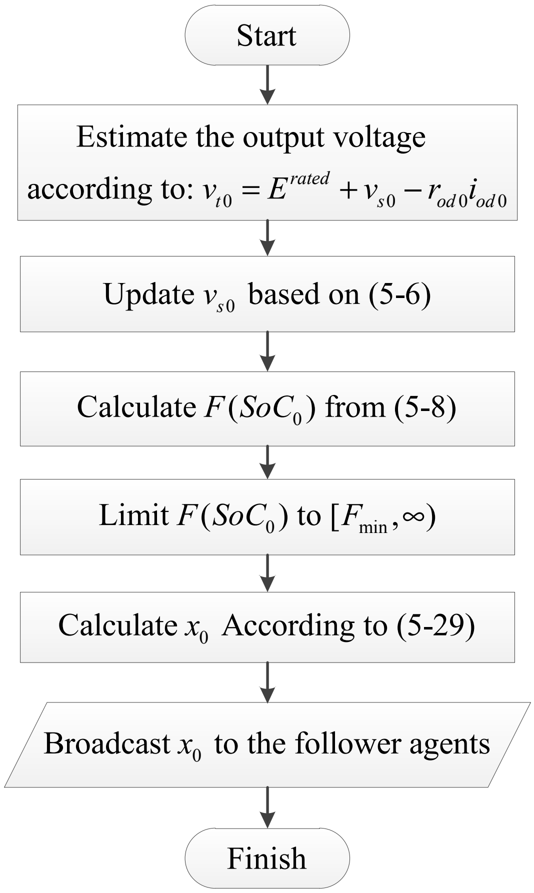

Fig. 5-4 Flowchart of the proposed cooperative algorithm for the leader agent

The consensus algorithm for the follower agent *i* is shown in Fig. 5-5. The agent *i* receives information from its immediate neighbors (agent *i*-1 and agent *i*+1) and the leader. The ESU reference power required for SoC balancing is calculated using (5-10). The algorithm then checks whether the reference power is in the safe operating range. If the reference power is within the safe range, $F(SoC_i)$ is calculated, and limited to $[F_{\min},\infty)$. The information state x_i, is estimated according to (5-7) and broadcasted to the neighbor agents. Once the ESU reference power, P^*_{ESUi}, is out of the safe operating range, the power set point is fixed at the limit and the agent is bypassed by sending the information state of agent *i*-1 to the agent *i*+1 and vice-versa. Finally, the secondary voltage correction term is updated based on (5-9).

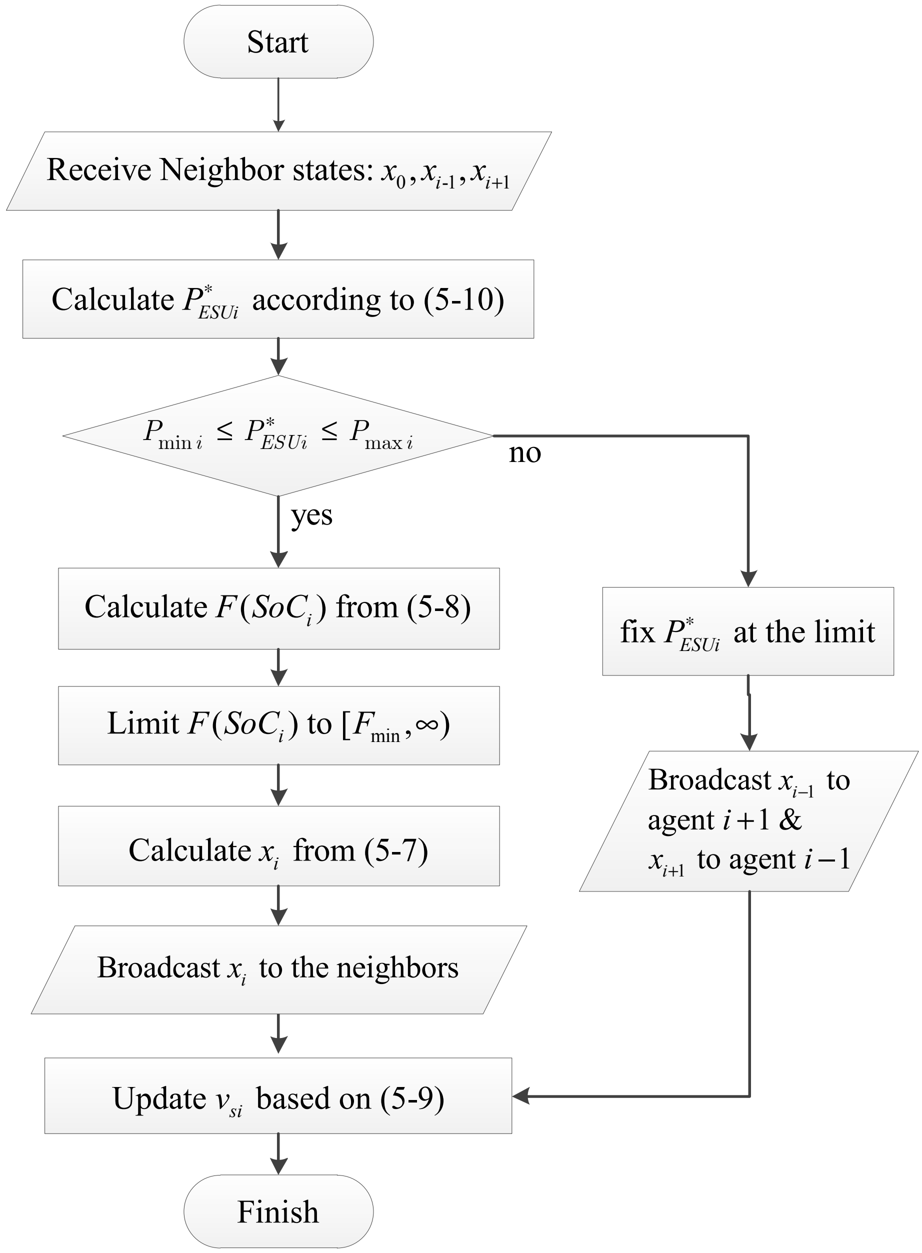

Fig. 5-5 Flowchart of the proposed cooperative algorithm for follower agents.

5-4 Load and PV control modules

The loading and PV generation capacity of the MG is limited not only by the power rating of the DERs but also the SoC constraints. During night time (i.e., no PV generation), the total loading capacity is the summation of the rated power of the ESUs which are charged above the minimum SoC. During day time, the total PV generation capacity is the summation of rated power of ESUs which have not reached the maximum SoC minus the total load. In order to maintain load/generation balance while preventing ESUs from deep discharging and overcharging, a load shedding and PV curtailment method is introduced in this section.

The loads and PVs are controlled based on the average information state of the leader, which is approximately equal to the steady-state information state of all DERs, i.e., x. The operating principle of the load control module is explained based on the diagram shown in Fig. 5-6. The diagram illustrates the variation of ESU current versus SoC for different values of x as a parameter. It is worth mentioning that the margin between SoC_L (SoC_H) and the minimum (maximum) SoC provides a reserve capacity for supplying sensitive loads and managing the transients. For small value of x, the current is shared among the ESUs according to the SoCs, while the ESUs with $SoC < SoC_L$ supply very small currents. However, as x rises, the DERs with higher SoC reach their current limit. As a result, ESUs with lower SoC discharge faster than expected, quickly reaching the minimum charge level. Therefore, it is necessary to shed some part of the MG load in case that x is higher than a positive critical level. Once x is lower than a negative critical level, PV generations must be curtailed.

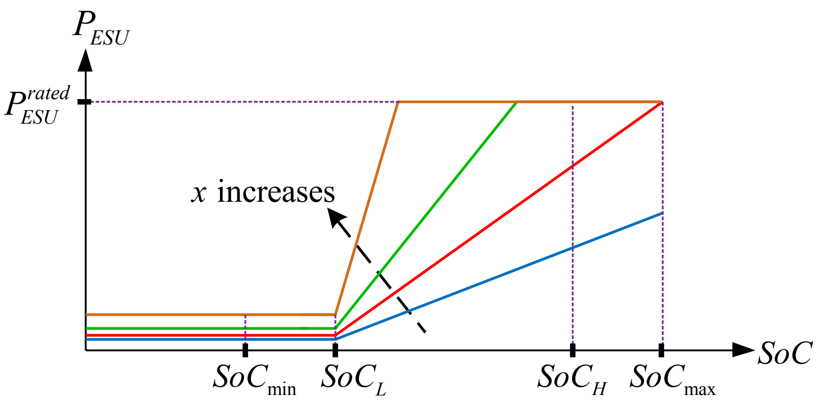

Fig. 5-6 Variations of ESU current versus SoC for different values of x.

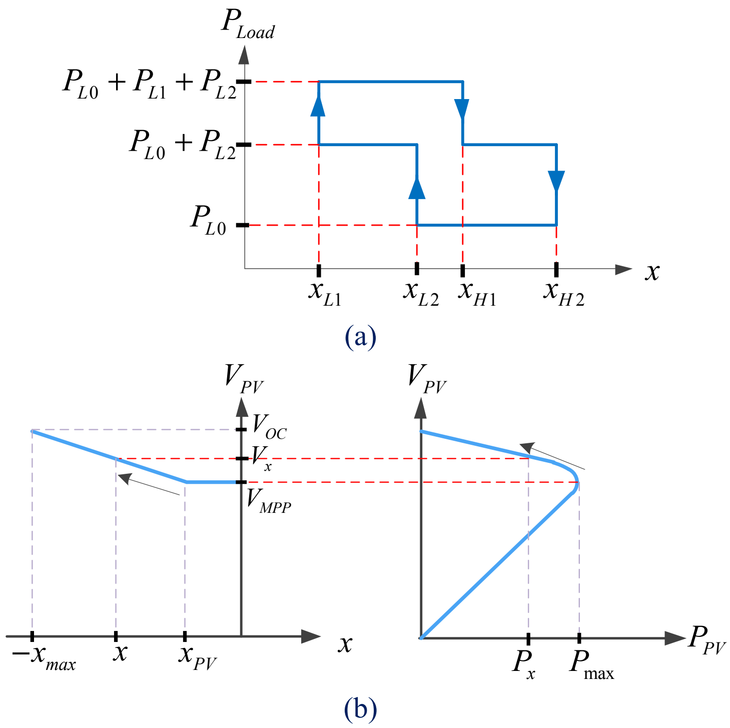

Fig. 5-7 Control characteristics of a) load control and b) PV control modules.

The load shedding is conducted based on a hysteresis characteristic to prevent chattering phenomenon. As an example, the load shedding characteristics for a MG consisting of two controllable loads is shown in Fig. 5-7(a). When x rises above the level x_{H1} or x_{H2}, local loads 1 or 2 are disconnected, respectively. The loads 1 and 2 remain disconnected until x falls below x_{L1} and x_{L2}. Therefore, the chattering phenomenon is prevented.

The PV curtailment characteristic is shown in Fig. 5-7(b). Normally, the PV generations are controlled by maximum power point (MPP) tracking method. As can be observed, once x is decreased below x_{PV}, the PV voltage is increased to reduce the PV generation. Using an identical characteristic for all PV control modules, fair curtailement can be ensured.

5-5 Experimental results

The proposed method has been tested on a laboratory scale MG setup depicted in Fig. 5-8. The experimental setup is similar with the setup used in Chapters 2,3, and 4, except that a single phase MG is implemented by disconnecting the phase “c” of the inverters. Additionally, the LCL filter and line impedances are different. The specifications of the experimental setup are listed in Table 5-1. The underlying MG setup includes four single-phase DER units. Due to the change from three to single phase topology, the capacity of each inverter unit is reduced to 700 W.

The GPS synchronization and communication network are modelled in the dSPACE controller. The communication rate is defined as the number of data samples transmitted through each of the links in 1s. To model a low bandwidth communication network, the communication rate is limited to 50 samples per second in all cases. The communication delay is selected as 20ms for scenarios 1-4 and varied from 20ms to 1s in the fifth scenario. Furthermore, the ESUs, PVs and the corresponding DC/DC converter are modeled in MATLAB and emulated in the dSPACE controller.

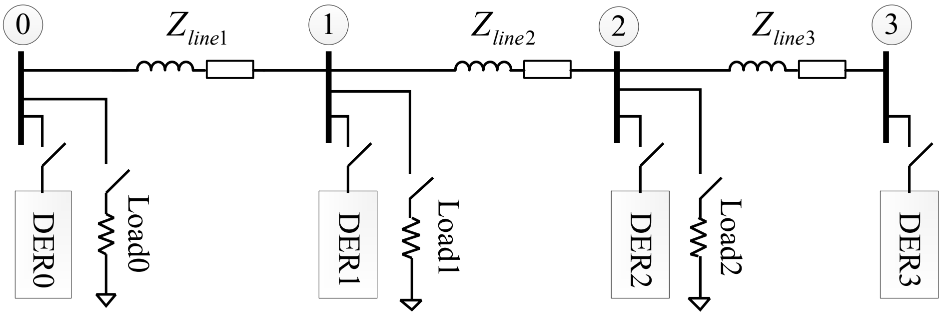

Fig. 5-8 Schematic diagram of the Experimental setup.

Table 5-1 Electrical and control parameters of the test MG

	Parameter	Symbol	Value
	Filter parameters	$L_f/C_f/L_c$	3.6 mH/ 9 µF/3.6 mH
	Line 1 impedance	Z_{line1}	0.18 +j0.07 Ω
	Line 2 impedance	Z_{line2}	0.28+j0.08 Ω
	Line 3 impedance	Z_{line3}	0.38+j0.06 Ω
	Load impedance: Case 1	$R_0/R_1/R_2$	115 /57 /57 Ω
	Load impedance: Case 2	R_0/R_1	230 / 115 Ω
	Load impedance: Case 3	$R_0/R_1/R_2$	115 /115 /57 Ω
	SoC constraints	SoC_{min} - SoC_{max}	50-100 %
	ESU capacities	$C_0/C_1/C_2/C_3$	2.8/4.2/5.6/2.5 kW-min
	Communication Rate	f_{com}	50 samples/s
	Communication delay case 1-4	T_{dcom}	20 ms
Control Parameters	Leader DSC	k_{s0}	1
		k_{lim}	0.1
		P_{marg}	200 W
	Follower DSC	k_{si}	0.014
	Function F	F_{min}	0.01
	SoC limits	SoC_L-SoC_H	55-95%
	PV control thresholds	x_{PV}	-10
		x_{max}	15
	Load 1 control thresholds	x_{L1} - x_{H1}	0.1 -10
	Load 2 control thresholds	x_{L2} - x_{H2}	1 - 15
	Droop coefficients	r_d/r_q	4 / 8.4 Ω

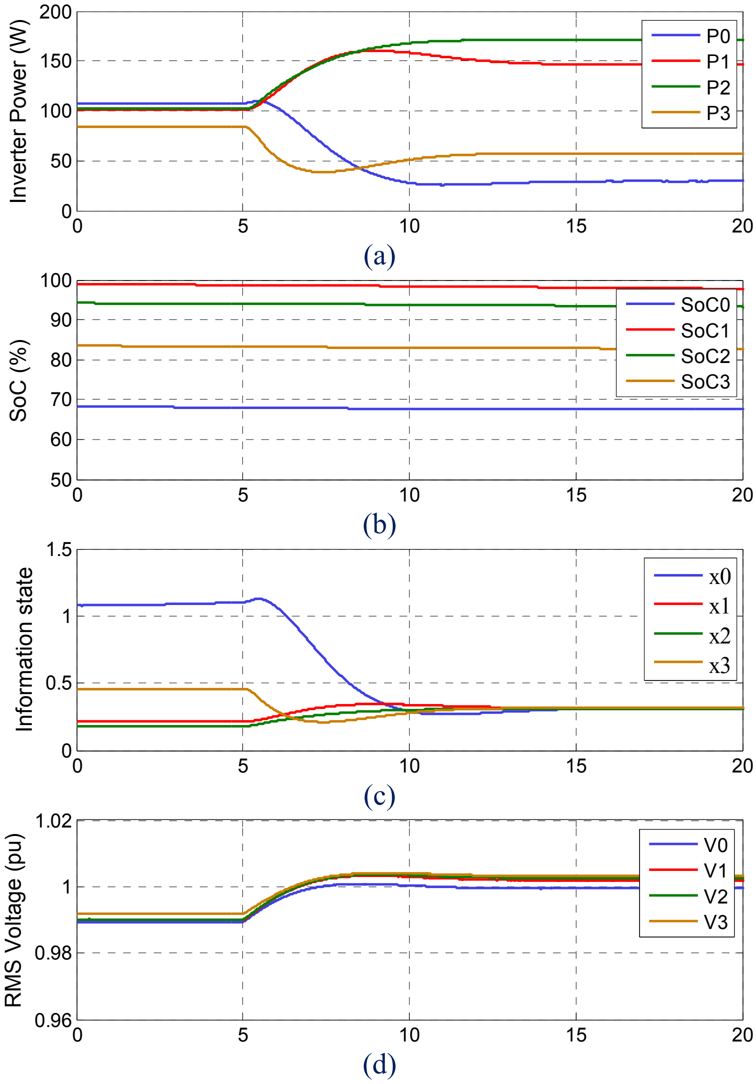

Fig. 5-9 Performance of the proposed method following the DSC activation. (a) inverters' active powers, (b) SoCs, (c) information states, (d) bus voltages.

Efficacy of the proposed control method is verified under the following studies: 1) DSC performance assessment, 2) step load reponse, 3) discharge cycle scenario, 4) day time scenario, and 5) impact of communication delay.

In the first, second and third study, the PV generations are zero and the load is supplied by the ESUs. The experimental results for the first study are provided in Fig. 5-9. Prior to activating the proposed controller, the load active power is shared among the units by means of the V-I droop mechanism. At t=5s, the DSC is activated, where the power set point of each inverter is adjusted so as the information states of the units reach a common value. As shown in Fig. 5-9 (c), the consensus is reached within 10s after activation of the DSC. As a consequence, the set points of inverters' powers are defined according to the SoC and capacity of the ESUs. Particularly, the largest share is dedicated to DER2; the one which has the highest stored energy (SoC=95% and C= 5.6 kW.min), followed by DER1 (SoC=99% and C=4.2 kW.min). Comparison of Fig. 5-9 (b) and (c) reveals that the DSC transient response is much faster compared to the rate of change of SoCs. Therefore, the proposed method is effective in terms of SoC balancing. Additionally, the output voltage of the leader i.e., DER0 is restored to 1pu (See Fig. 5-9 (d)).

In the second test, the response of the system to a step load change is studied by connecting the load 1 to the MG. From Fig. 5-10 (a), it is observed that the active powers of all units rise following the step load change. Since the SoC of DER0 is lower compared to other units, its information state ($x0$) grows rapidly (See Fig. 5-10 (b) and (c)). Consequently, *P1* and *P2* are increased to reduce *P0* and consensus is achieved within 10s. As shown in Fig. 5-10 (d), the DERs output voltage are regulated within a range of the nominal value. The slight voltage deviation of the follower units originates from the voltage drop on the line impedances.

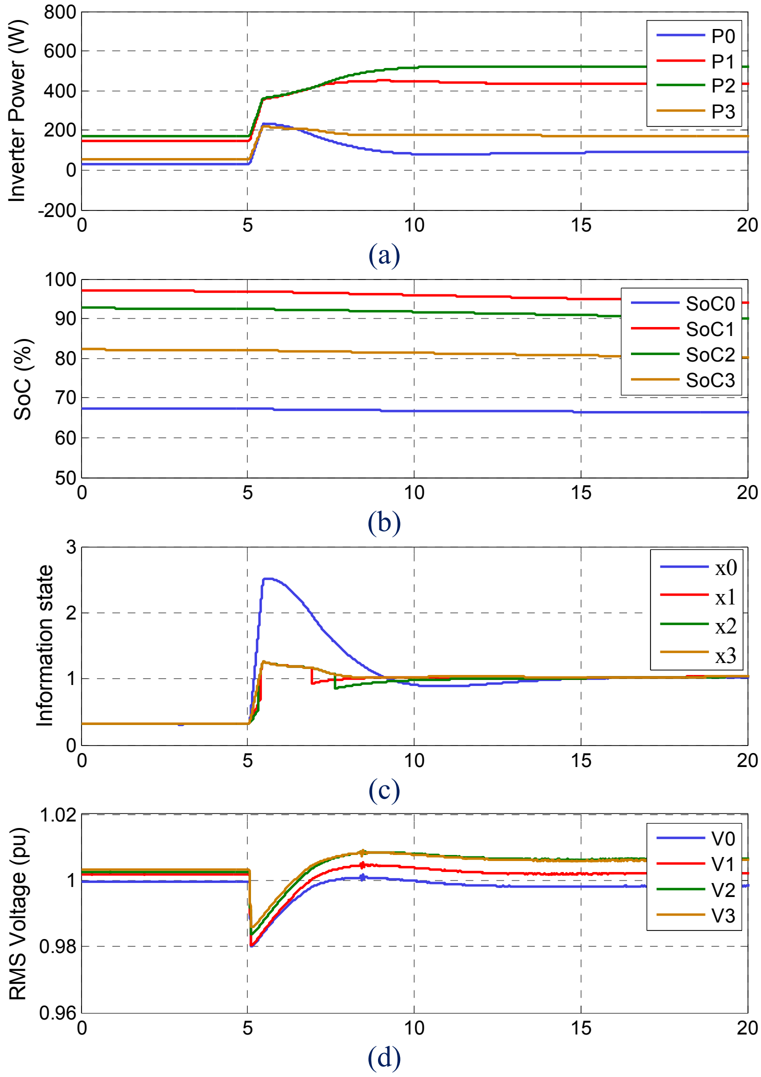

Fig. 5-10 Controller performance in response to a step load change. (a) inverters' active powers, (b) SoCs, (c) information states, (d) bus voltages.

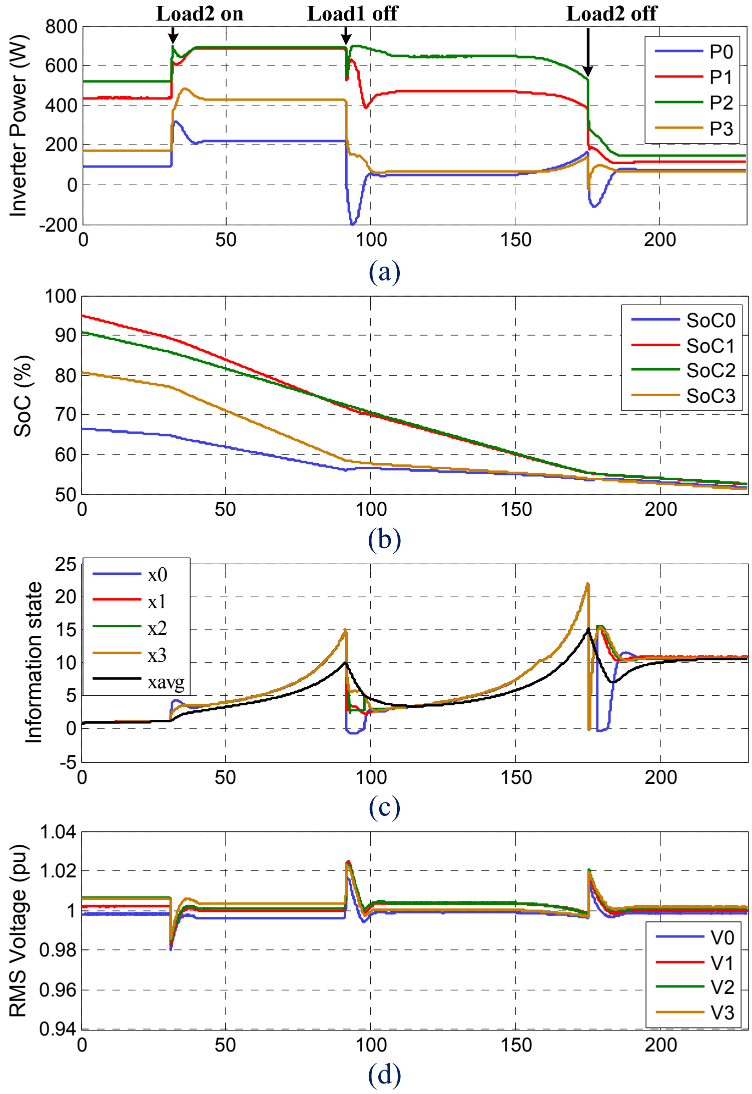

Fig. 5-11 Experimental results for the third scenario. (a) active powers, (b) SoCs, (c) average information state, and d) bus voltages.

The third scenario studies the performance of the proposed control framework over the ESUs discharge cycle. Initially, loads 0 and 1 are connected to the MG. As shown in Fig. 5-11, the information states are at consensus and the load is shared among the DERs according to the corresponding energy capacities. Once load 2 is connected at $t = 20\,\mathrm{s}$, *P1* and *P2* reach their limits, and their powers are fixed at 700 W. This results in an inevitable increase in *P3* and *P0*. Consequently, the SoC3 and SoC0 fall with a relatively fast rate until $t = 80\,\mathrm{s}$, when SoC0 reaches close to the lower SoC limit (i.e., SoC_L=55%). At this point, the average information state, i.e., *xavg*, reaches the trigger point of load 1 (i.e., $x_{H1} = 10$). It is worth mentioning that the delay of *xavg* compared to the agents' states (*x*0-*x*3) is caused by the low-pass filter used for preventing load shedding during transients. The load controller sheds load 1, and subsequently DER 1 and DER 2 exit the power limiting mode, enabling SoC-based load sharing once again. Therefore, the SoCs converge towards SoC_L. At $t = 165\,\mathrm{s}$, all SoCs reach SoC_L and the information state *xavg* reaches the trigger point of load 2 (i.e., $x_{H2} = 15$).

Accordingly, load 2 is also shed from the MG. At this stage, the MG only supplies the sensitive load (i.e., load 0). It should be noted that once all SoCs reach the minimum value (50%) the MG has to be shut down to prevent deep discharging of the ESUs.

In the fourth study, PV generations vary according to a typical profile. Fig. 5-12 illustrates the experimental results for this study. The effect of PV alignment on the received energy is modeled by considering time shifted irradiations, as depicted in Fig. 5-12 (b). Prior to $t = 70\,\mathrm{s}$, the total PV generation is lower than the total load, and the excess demand is shared between the ESUs. For $t > 70\,\mathrm{s}$, the total PV generation goes higher than the total load and the surplus generation is shared among the ESUs according to the available storage capacity. Particularly, the largest share is dedicated to PESU2 (SoC2=55%, C2=5.6 kW.min) followed by PESU1 (SoC1=50%, C1=4.2 kW.min). For $340\,\mathrm{s} < t < 375\,\mathrm{s}$, PESU2 reaches the limit and remains fixed at -700 W. At $t = 380\mathrm{s}$, the SoCs reach close to the higher SoC limit (95%) and the average information state drops below x_{PV} (i.e., -10). At this stage, the PV control modules increase the voltages to reduce the PV generations so as to keep the surplus generation close to zero. As a result, the ESU powers are decreased to around zero and the SoCs are limited below 100%.

At $t = 550\,\mathrm{s}$, the load 1 is switched on. The load change is initially picked up by the ESUs. However, the increase of ESU powers results in a rise of information states. As shown in Fig. 5-12 (f), the information states undergo an oscillation but settle at a common value within 20s. The load change causes the average information state (*xavg*) to change from -14.3 to -13.1. Therefore, the PV control modules increase the PV generations to reduce the ESU power back to around zero. The PV control modules continue increasing the PV powers in order to keep the surplus power generation close to zero. At $t = 670\,\mathrm{s}$, the PV generations are increased to the maximum and hence the PVs are controlled at MPPT. Next, the maximum PV generation drops below the total load due to the low solar irradiance. Therefore, the ESUs powers are increased to maintain load/generation balance. It is worth mentioning that in both case studies (see Fig. 5-11 (d), and Fig. 5-12(g)), the rms voltage is within an acceptable range of the rated value and the frequency is fixed at 50Hz. Therefore, a high power quality is guaranteed.

In the fifth case, effect of communication delay on the performance of the proposed cooperative method is studied. To that end, a step load change is applied to bus 2 and the dynamic response with three different communication delays is recorded. The active power outputs and the information states of the DERs for communication delays of 20 ms, 200 ms and 1 s are depicted in Fig. 5-13. The results show that for delays shorter than 1 s, the proposed controller remains functional. Although large delays may cause low frequency oscillations, the settling time is fast enough for the SoC management application.

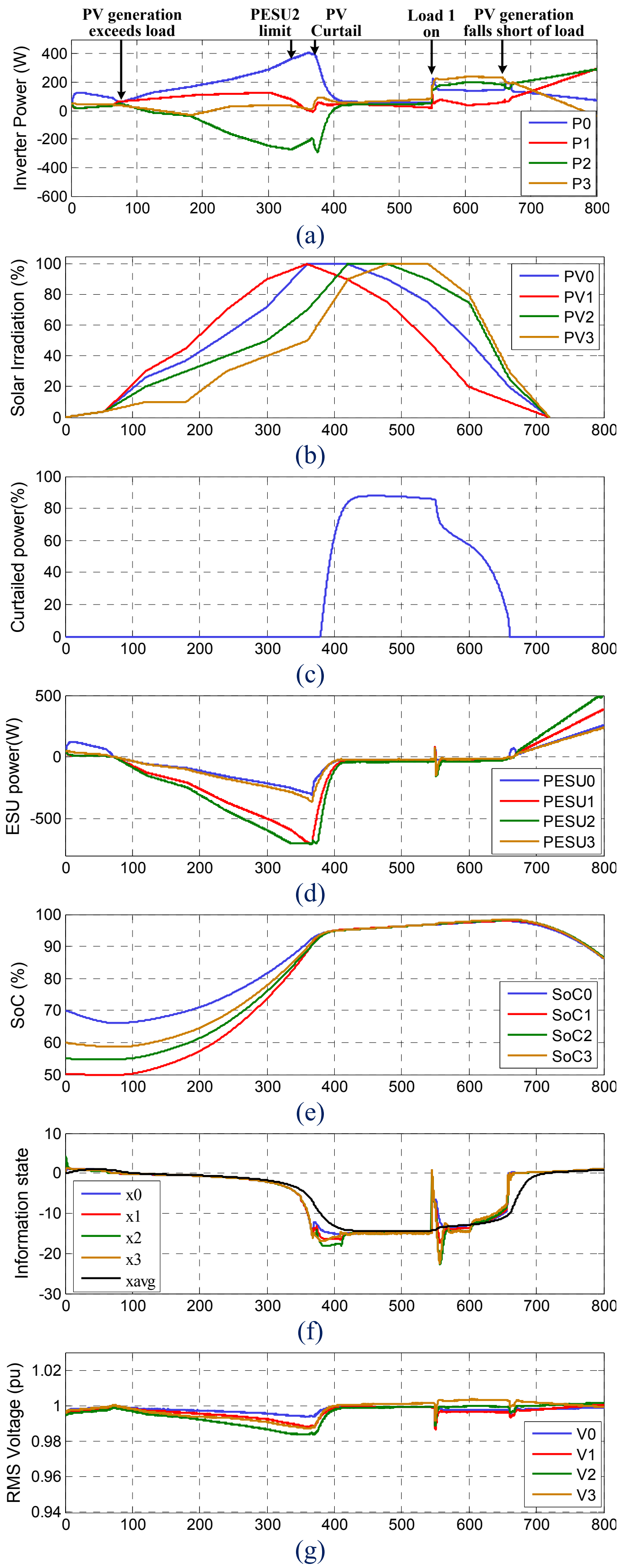

Fig. 5-12 Performance of the proposed control framework for the day scenario. (a) inverters' active powers, (b) solar irradiations, (c) curtailed pv power, (d) ESU powers, (e) SoCs, (f) information state, and (g) bus voltages.

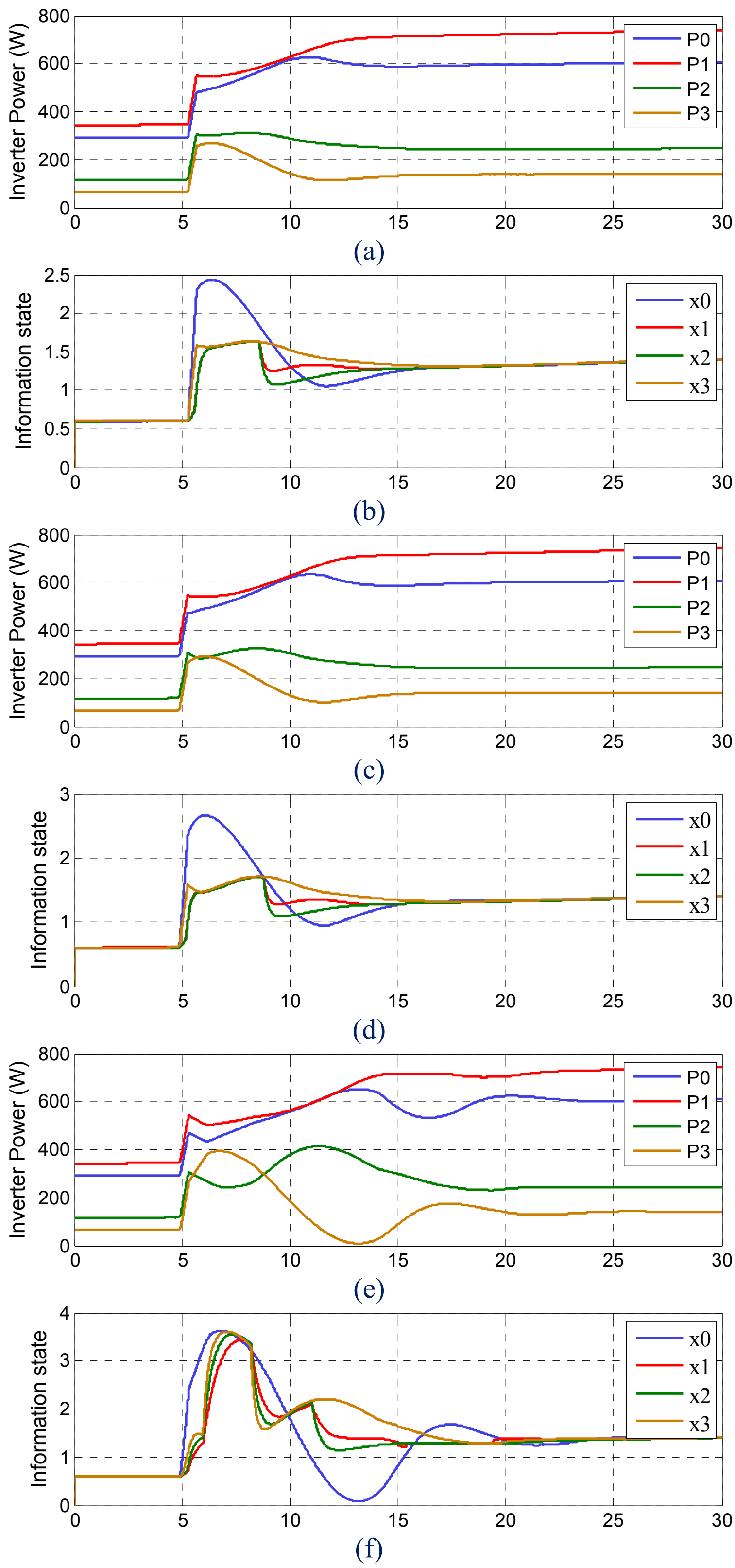

Fig. 5-13 Performance of proposed control method under different communication delays: (a,b) 20 ms, (c,d) 200 ms, and (e,f) 1 s.

5-6 Conclusions

In this chapter, a novel distributed control framework is proposed for MGs comprising of several PV-ESU hybrid units. In the proposed method, the individual units are controlled by decentralized V-I droop mechanism together with dedicated distributed secondary controller, which are interconnected through a low bandwidth communication network. The distributed controllers are coordinated based on a leader-follower framework, where the leader regulates the voltage and the followers manage the sharing of power between the ESUs so as to balance the SoCs. The communication topology is dynamically changed to exempt the units which reach the maximum power from the consensus algorithm. In addition, PV curtailment and load shedding are deployed to protect the ESUs from deep discharging and overcharging. Therefore, safe operation of the ESUs and associated DC/DC and DC/AC converters is guaranteed. The experimental results validate the efficacy of the proposed method in terms of voltage regulation, SoC balancing, and limiting the SoCs/ powers within the safe range. The results also show that the proposed control framework is robust with respect to large communication delays.

Chapter 6

A model predictive supplementary droop controller for unbalanced loading conditions

6-1 Introduction

Unbalanced loading conditions, which are the most common case in low voltage MGs, cause degraded performance of the voltage regulator and droop controller [17]. Moreover, the conventional current limiting mechanisms are not effective under unbalanced conditions. The latter might result in over-currents or circulating current harmonics between DERs.

In contrast to the balanced conditions, the steady-state *d-q* components of the voltage and current are not constant under unbalanced conditions. As a result, PI control method in *d-q* reference frame does not provide zero steady-state error. In order to tackle this issue, deadbeat [23], repetitive [17] and proportional plus resonant (P+R) [64] control methods have been utilized. The aforementioned methods eliminate the steady-state error by incorporating the error frequency components as controller poles.

The application of conventional droop control under unbalanced conditions might produce large negative sequence (NS) voltages. In order to improve the power quality, NS voltage should be reduced. The NS voltage and current can be controlled by adjusting the NS output impedance of DERs [13]-[16], injecting a NS compensating voltage [23] or a combination of both methods [22]. However, an increase of compensation effort or a decrease of NS impedance alters the flow of NS current in MGs, which in turn degrades the NS current sharing accuracy.

In order to improve the reliability, dynamic performance and power quality of islanded MGs, a novel control method is proposed in this chapter. The controller is composed of four control levels, namely, supplementary droop, primary droop, voltage and current controllers. The voltage and current controllers are designed based on P+R method and implemented in the *abc* framework to limit the individual phase currents. The primary droop is based on the recently introduced *V-I* droop control method [91], which ensures significantly faster dynamics and higher damping compared to the conventional droop method. At the highest level of the control hierarchy, a novel supplementary droop controller is introduced to improve the power quality and reliability. The controller prevents active power overload, improves the current limiting mechanism and controls the NS impedance to reduce the voltage unbalance while decreasing NS current sharing error.

The rest of the chapter is organized as follows. The motivation of the study including the overcurrent stress and the voltage unbalance issues in conventional controllers are described in Section 6-2. A mathematical analysis of current sharing among DER units under unbalanced conditions is presented in Section 6-3. The proposed control method is detailed in Sections 6-4 to 6-6. Simulation results are presented in Section 6-7 to verify the efficacy of the proposed method. The practicality of the proposed method is discussed in Section 6-8. Section 6-9 concludes the chapter.

6-2 Motivation of the study

6-2-1 Overcurrent stress

The inverter based low voltage MGs are usually supplied with DERs of small size, which are highly susceptible to over-current. Short circuit faults, machine starting and slow dynamics of droop controllers might result in transient over-currents. On the other hand, unequal sharing of active or reactive power between DERs and voltage variations throughout the MG might result in sustained over-currents during high loading conditions.

In order to prevent the overcurrent stress, the inverter current might be limited by using a saturation block in the current control loop of the inverter. However, the effectiveness of this method is dependent on the reference frame, based on which the current control loop is designed.

As for demonstration, it is assumed that the current tends to have a value of 2pu before being limited. Fig. 6-1 depicts the resulting current waveforms after saturating the αβ0, *dq*0 and *abc* components under balanced and unbalanced (single-phase) conditions. For balanced conditions, while all methods effectively limit the current to 1pu, only *dq*0 case produces a sinusoidal waveform. On the other hand, for unbalanced conditions neither αβ0 nor *dq*0 cases limit the current below 1pu. This necessitates the importance of current limiting in *abc* framework. However, this method deteriorates the current waveform and introduces current harmonics, which circulate between the DERs. A solution for this issue will be addressed in Section 6-6.

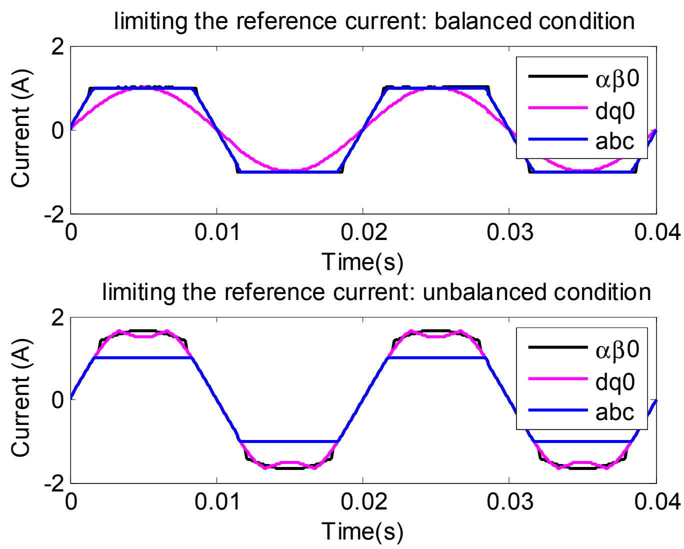

Fig. 6-1 Inverter current after applying saturation in different reference frames under balanced and unbalanced conditions

6-2-2 Voltage unbalance

Voltage unbalance is quite a common issue in low voltage MGs, where the majority of loads are single-phase. On the other hand, the International Electro-technical Commission (IEC) recommends limiting of voltage unbalance below 2% [92]. The voltage unbalance can be reduced by injecting a NS compensating signal to the inverter reference voltage. However, the compensation deteriorates the current sharing between DERs. A method for reducing the circulating currents while limiting the voltage unbalance below the acceptable limit is introduced in Section 6-5.

6-3 Mathematical analysis of unbalanced conditions

6-3-1 Symmetrical components

The symmetrical components of three-phase voltages can be extracted from the three-phase phasors, as follows:

$$\begin{bmatrix} V^0 \\ V^+ \\ V^- \end{bmatrix} = A^{-1} \begin{bmatrix} V_a \\ V_b \\ V_c \end{bmatrix} \tag{6-1}$$

where V_a, V_b and V_c are the voltage phasors, V^0, V^+ and V^- refer to zero, positive and NS components and the inverse transformation matrix A^{-1} is defined as [48]:

$$A^{-1} = \frac{1}{3}\begin{bmatrix} 1 & 1 & 1 \\ 1 & a & a^2 \\ 1 & a^2 & a \end{bmatrix} \tag{6-2}$$

with a=1∠120°. The voltage unbalance is defined as the ratio of the NS voltage over the positive sequence voltage:

$$V_{UN}\left(\%\right) = \frac{V^-}{V^+} \tag{6-3}$$

One way to extract the phasors from instantaneous voltages is using single-phase Park transformation. In this method, the *d* and *q* components of the voltage v_x (x=*a, b* or *c*) are calculated by introducing a virtual two phase system, as follows [93]:

$$\begin{bmatrix} v_{xd} \\ v_{xq} \end{bmatrix} = \begin{bmatrix} \cos\theta_x & \sin\theta_x \\ -\sin\theta_x & \cos\theta_x \end{bmatrix}\begin{bmatrix} v_{x\alpha} \\ v_{x\beta} \end{bmatrix} \tag{6-4}$$

in which the virtual α and β components are defined as

$$v_{x\alpha} = v_x \tag{6-5}$$

$$v_{x\beta} = v_x\left(t - \frac{\pi/2}{\omega_0}\right). \tag{6-6}$$

The parameter θ_x is the angle of the synchronous rotating reference frame of phase *x*,

$$\theta_a = \omega t \tag{6-7}$$

$$\theta_b = \omega_0 t - \frac{2\pi}{3} \tag{6-8}$$

$$\theta_c = \omega_0 t - \frac{4\pi}{3} \tag{6-9}$$

with ω_0 being the fundamental frequency. The phase difference between the reference frames is selected so that the *dq* components of the three phases are identical under balanced conditions.

The voltage phasors can be expressed in terms of single-phase *dq* components, as follows:

$$\begin{bmatrix} V_a \\ V_b \\ V_c \end{bmatrix} = \begin{bmatrix} v_{ad} + jv_{aq} \\ a^2\left(v_{bd} + jv_{bq}\right) \\ a\ \left(v_{cd} + jv_{cq}\right) \end{bmatrix} \tag{6-10}$$

in which coefficients a and a^2 are introduced to compensate the phase difference between the single phase reference frames. Substituting (6-10) in (6-1), the NS voltage can be expressed

$$V^- = \frac{1}{3}\left\{ v_{ad} + jv_{aq} + a\left(v_{bd} + jv_{bq}\right) + a^2\left(v_{cd} + jv_{cq}\right)\right\} \tag{6-11}$$

Rearranging the real and imaginary parts of the right hand side (RHS) of (6-11), the NS voltage can be expressed, as follows:

$$\begin{bmatrix} v_d^- \\ v_q^- \end{bmatrix} = \frac{1}{3}\begin{bmatrix} 1 & 0 & \cos\frac{2\pi}{3} & \cos\frac{7\pi}{6} & \cos\frac{4\pi}{3} & \cos\frac{11\pi}{6} \\ 0 & 1 & \sin\frac{2\pi}{3} & \sin\frac{7\pi}{6} & \sin\frac{4\pi}{3} & \sin\frac{11\pi}{6} \end{bmatrix}\begin{bmatrix} v_{ad} \\ v_{aq} \\ v_{bd} \\ v_{bq} \\ v_{cd} \\ v_{cq} \end{bmatrix} \tag{6-12}$$

in which v_d^- and v_q^- are the real and imaginary parts of the voltage, respectively. Defining

$$v^- = \begin{bmatrix} v_d^- & v_q^- \end{bmatrix}^T, \tag{6-13}$$

$$v_{dq} = \begin{bmatrix} v_{ad} & v_{aq} & v_{bd} & v_{bq} & v_{cd} & v_{cq} \end{bmatrix}^T, \tag{6-14}$$

$$C_{neg} = \frac{1}{3}\begin{bmatrix} 1 & 0 & \cos\frac{2\pi}{3} & \cos\frac{7\pi}{6} & \cos\frac{4\pi}{3} & \cos\frac{11\pi}{6} \\ 0 & 1 & \sin\frac{2\pi}{3} & \sin\frac{7\pi}{6} & \sin\frac{4\pi}{3} & \sin\frac{11\pi}{6} \end{bmatrix}, \tag{6-15}$$

(6-12) can be expressed in the closed form:

$$v^- = C_{neg} v_{dq} \tag{6-16}$$

Similar analysis can be applied for the current.

6-3-2 Sharing of negative sequence current in islanded MGs

Consider the MG in Fig. 6-2, which is composed of two dispatchable DERs and an unbalanced load. The NS voltages at buses 1 and 2 can be expressed in terms of the NS output impedances of DER1 (Z_1^-) and DER2 (Z_2^-), as follows:

$$V_{t1}^- = -Z_1^- I_1^- \tag{6-17}$$

$$V_{t2}^- = -Z_2^- I_2^- \tag{6-18}$$

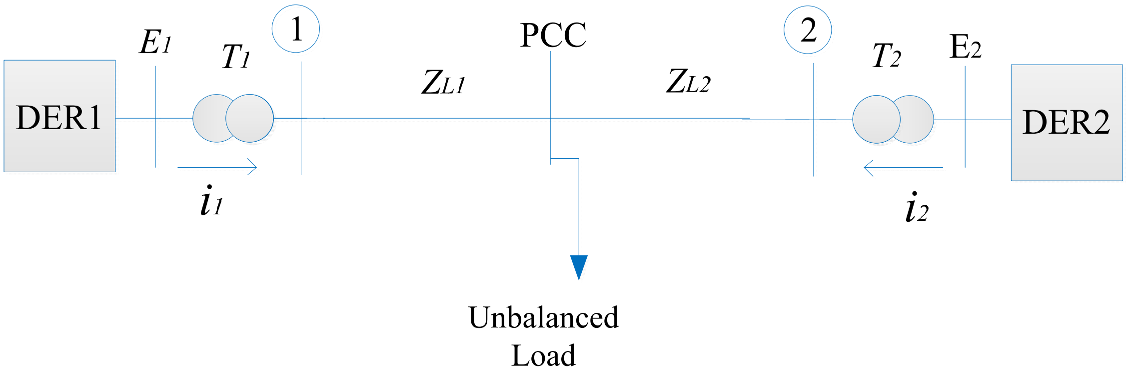

Fig. 6-2 Sample MG

Therefore, the load NS current is shared between the DERs according to:

$$\frac{I_1^-}{I_{Load}^-} = \frac{Z_{L2} + Z_2^-}{Z_{L1} + Z_{L2} + Z_1^- + Z_2^-} \tag{6-19}$$

$$\frac{I_2^-}{I_{Load}^-} = \frac{Z_{L1} + Z_1^-}{Z_{L1} + Z_{L2} + Z_1^- + Z_2^-} \tag{6-20}$$

in which Z_{L1} and Z_{L2} are the impedances of line 1 and 2, respectively.

From (6-19) and (6-20), it is observed that the sharing of NS current is dependent on the DER NS impedances as well as the line NS impedances. In addition, (6-17) and (6-18) show that full compensation of the NS voltage at the DER terminals is equivalent to selecting $Z_1^- = Z_2^- = 0$, which implies sharing of NS current is according to the line impedances only. In practice, however, it is desirable to share the NS current between the DERs according to the current ratings of the DERs. This can be achieved by introducing virtual NS impedances in DER outputs. The NS impedances can be selected as inversely proportional to the DER rating to provide even NS current sharing between the DERs.

The NS current sharing error is maximum when either of the lines has zero impedance. Assuming $Z_{L2} = 0$ and using (6-19) and (6-20), the NS current sharing is obtained as:

$$\frac{I_2^-}{I_1^-} = \frac{Z_1^-}{Z_2^-} + \frac{Z_{L1}}{Z_2^-} \tag{6-21}$$

Therefore, the sharing error is dependent on the ratio of the line impedance on NS impedance of the DER2. The virtual NS impedances are limited by the permissible voltage unbalance and are typically in the same order as the line impedances. Consequently, the NS current sharing is poor. Poor sharing of the NS current adversely effects the current sharing of individual phases. The problem gets worse as the load becomes more unbalanced. In order to investigate the problem under worst case conditions, a single phase load with a current of $i_{Load,a} = I\angle\theta$ is assumed. So:

$$I_{load}^{0} = I_{load}^{+} = I_{load}^{-} = \frac{I\angle\theta}{3}$$

Assuming that the positive and zero sequence currents are shared accurately, we have:

$$I_2^0 = I_2^+ = \frac{I\angle\theta}{3} * \frac{I_{2,rated}}{I_{1,rated} + I_{2,rated}}$$

On the other hand,

$$I_2^- = \frac{I\angle\theta}{3} * \frac{Z_L + Z_1^-}{Z_L^- + Z_1^- + Z_2^-}$$

Therefore, the phase currents of DER2 can be expressed as:

$$I_{a2} = \left(\frac{I_{2,rated}}{I_{1,rated} + I_{2,rated}}\right) I\angle\theta + k_z I\angle\theta \tag{6-22}$$

$$I_{b2} = k_z I\angle\left(120° + \theta\right) \tag{6-23}$$

$$I_{c2} = k_z I\angle\left(-120° + \theta\right) \tag{6-24}$$

in which k_z is a non-dimensional positive factor, defined as:

$$k_z = \frac{\left(Z_1^- + Z_L^-\right) I_{1,rated} - Z_2^- I_{2,rated}}{3\left(I_{1,rated} + I_{2,rated}\right)\left(Z_1^- + Z_2^- + Z_L^-\right)} \tag{6-25}$$

If k_z is zero, the load current will be proportionally shared between the DERs and phase b and *c* currents will be zero. However, in the practical case of $k_z > 0$, the phase *a* current of DER2 will be increased as shown in (6-22). This increase might result in over-current stresses during high loading conditions. In addition, while no load is connected to phases *b* and *c*, the DER currents are nonzero according to (6-23) and (6-24). In other words, the phase *b* and *c* currents will circulate between DER 1 and DER2, hence giving rise to additional power losses in the lines as well as DERs.

The aforementioned issues originate from the fact that the DER2 experiences larger NS voltage and tends to apply larger NS compensation. Such compensation is equivalent to reduction of the voltage of the lightly loaded phase, which in turn results in a negative d-axis current in the lightly loaded phase. On the other hand, the active power of the DERs which contribute to power sharing is positive. So, the *d*-axis component of the *abc* currents is also expected to be positive. Therefore, a negative *d-axis* current is associated with the flow of circulating currents into the DER. In the proposed method, this characteristic is used to detect and identify the direction of the circulating currents. The circulating currents are then reduced by adjusting the NS impedance, as explained in Section 6-5.

6-4 Controller layout

In order to tackle the aforementioned issues, a novel control method is proposed. The controller is composed of four levels, including the supplementary droop, primary droop, voltage and current controllers, as shown in Fig. 6-3. The inverter reference voltage is obtained as a combination of the no load voltage (E_0), primary and supplementary droop signals. For phase a, the reference voltage is defined as:

$$\begin{bmatrix} v_{cd}^{a*} \\ v_{cq}^{a*} \end{bmatrix} = \begin{bmatrix} E_0 \\ 0 \end{bmatrix} + \begin{bmatrix} R_T & -X_T \\ X_T & R_T \end{bmatrix} \begin{bmatrix} i_{od}^{a} \\ i_{oq}^{a} \end{bmatrix} - R_0 \begin{bmatrix} i_{od}^{a} \\ i_{oq}^{a} \end{bmatrix} + \begin{bmatrix} u_{a,d} \\ u_{a,q} \end{bmatrix} \tag{6-26}$$

in which v_c^{a*}, i_o^a, u_a are the reference voltage, output current, and the supplementary control action of phase a, respectively. Moreover, R_T, X_T and R_0 are the resistance and reactance of the output inductor (or transformer), and the droop coefficient, respectively. The reference voltage for other phases is obtained similarly.

The second term on the RHS of (6-26) compensates the voltage drop on the isolation transformer, the third term droops the voltage according to a resistive characteristic to ensure an overdamped response [91], and the fourth terms is the supplementary controller signal.

The primary droop ensures coordinated operation of DERs and stability of the MGs. On the other hand, the supplementary controller is responsible for minimizing the voltage unbalance, limiting the DER active power generation, limiting the inverter current to eliminate the circulating current harmonics and reducing the circulating currents. In order to satisfy the first three objectives, the Model Predictive Control (MPC) technique, which is a powerful tool for solving control problems with constraints, is adopted. The NS reference voltage is adjusted by the gain scheduled NS droop so as to reduce the circulating currents.

Both MPC and primary droop controller are designed in synchronous rotating reference frame. In order to obtain dc d and q components under unbalanced conditions, single-phase Park transformation (block T) is utilized to refer the parameters of each phase to the corresponding reference frame. Phase b and c reference frames lag the phase a reference frame by 120° and 240°, respectively. So, the *d-q* parameters of all phases will be equal under balanced condition.

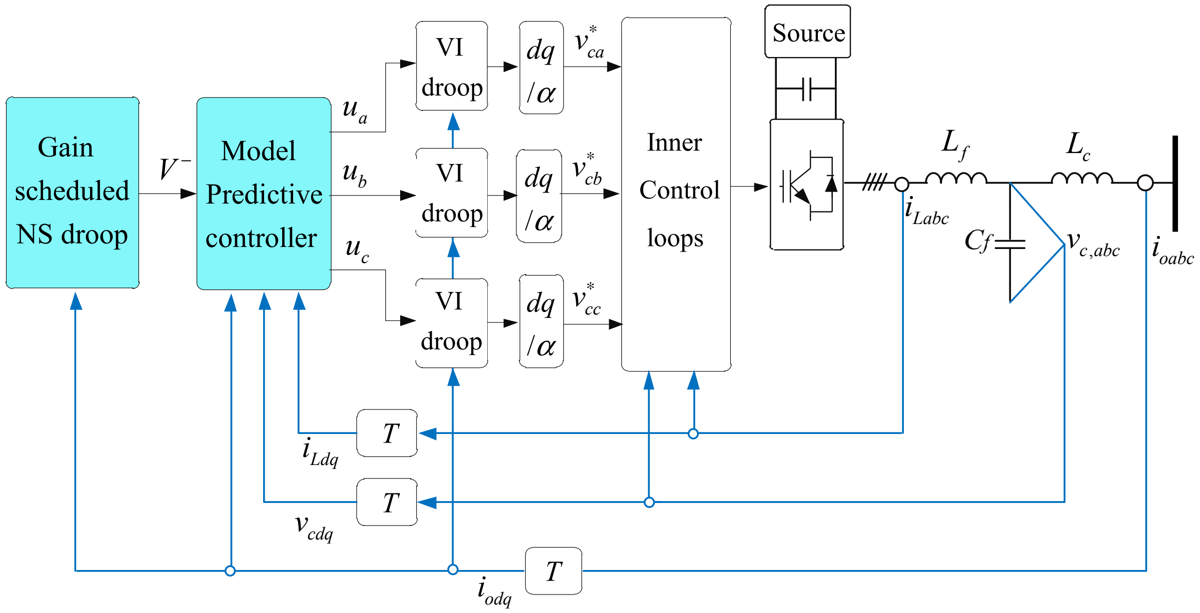

Fig. 6-3 Proposed controller

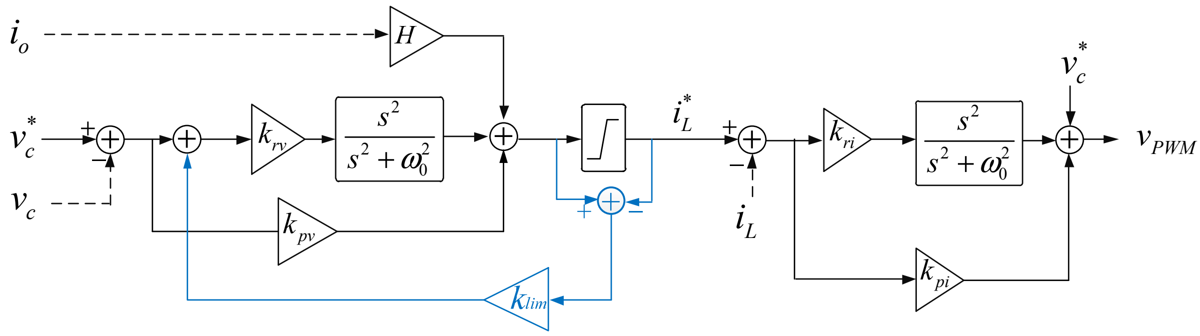

Fig. 6-4 Block diagram of the phase a cascaded controller

The voltage and current controllers are designed based on the *abc* reference frame to regulate the inverter voltage while limiting the maximum inductor current. The phase *a* voltage and current controllers are detailed in Fig. 6-4. The voltage controller utilizes P+R filters along with feed-forward signal from the output current to produce the inductor current reference. In order to protect the inverter from overcurrent stresses, the reference current is limited by using an anti-windup saturation scheme. The current control loop, which has the highest bandwidth in the control hierarchy, tracks the reference current with minimum transient error. This ensures that the inverter current is effectively limited upon the occurrence of disturbances. The current controller output is then added to the voltage feed-forward signal to obtain the reference voltage for the PWM block.

The PWM switching signals from the PWM block are fed to a four-leg inverter. The inverter is followed by an LC filter and a transformer, which eliminate high frequency harmonics and provide isolation, respectively. The DER is connected to the PCC by means of a four-wire line.

6-5 Gain-scheduled negative sequence droop

As detailed in Section 6-3-2, a mismatch of the NS impedance between the unbalanced load and individual DERs causes circulating currents in the lightly loaded phases. The DERs which are closer to the load experience larger NS voltage and tend to apply larger NS compensation. Such compensation is equivalent to reduction of the voltage of the lightly loaded phase, which in turn results in a negative d-axis current in the lightly loaded phase. On the other hand, the active power of the DERs which contribute to power sharing is always positive. As a result, the *d*-axis component of the *abc* currents are also expected to be positive. Therefore, negative sign of the *d-axis* current implies flow of circulating currents. More importantly, they imply that the DER is closer to the unbalanced load compared to the other DERs in the MG. In the proposed scheme, this characteristic is utilized to reduce the circulating currents.

The gain scheduled NS droop is illustrated in Fig. 6-5. In the first step, the *d-axis* current of the lightly loaded phase is selected. The current transients are eliminated through a low pass filter and then inverted to obtain the signal *w*. For the DER unit which is electrically closer to the load, the *d* axis current of the lightly loaded phase becomes negative and *w* will become positive. To reduce current sharing error, the resistance of the DER is increased for positive values of *w*. The value of resistance is calculated by means of two hysteresis blocks. The hysteresis loops are activated when *w* goes above a higher threshold and remain active until it is drops below a lower threshold. The output of the hysteresis blocks is 1 when activated and 0 otherwise. The hysteresis signal is then multiplied by a gain (k_{H1} and k_{H2}) and added to an offset (k_0) to obtain the NS impedance factor. The NS impedance factor is in turn multiplied by the maximum NS impedance ($R^-_{\max}$) to obtain the negative sequence impedance. The NS reference voltage is then obtained from the NS current and the NS impedance.

The circulating currents activate one or both of the hysteresis blocks of the DERs which is closer to the load. This increases the NS impedance of the DERs and reduces the mismatch of the total NS impedance between the DERs and the load. Therefore the circulating currents drop. Such drop, however, does not change the NS impedance so long as the d-axis currents are below the threshold.

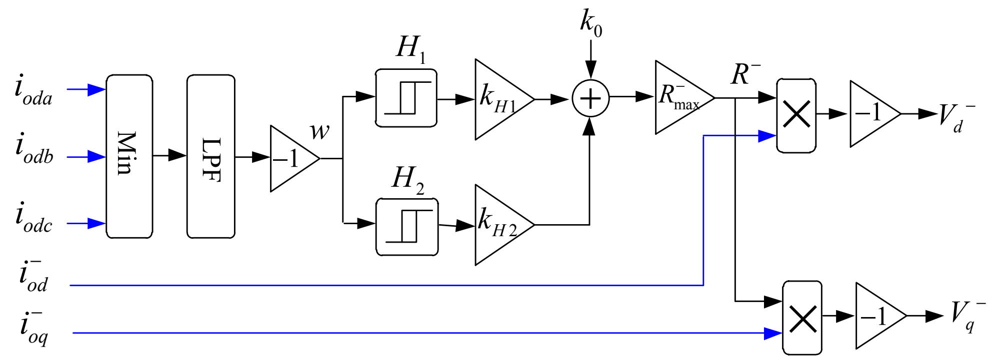

Fig. 6-5 NS gain scheduled droop

6-6 Model predictive control strategy

6-6-1 Control structure

The block diagram of the proposed MPC is depicted in Fig. 6-6. An unknown control action $u(k)$ is applied to the plant. The plant response to the control action is predicted and compared with the desirable response to obtain the error. The optimum control action is calculated by solving the optimization problem of minimizing the error while satisfying the constraints.

Here, the plant includes the power circuit, the cascaded controllers and the primary droop controller. The control action is the vector of supplementary droop signals, i.e,

$$u = \begin{bmatrix} u_d^a & u_q^a & u_d^b & u_q^b & u_d^c & u_q^c \end{bmatrix}^T \tag{6-27}$$

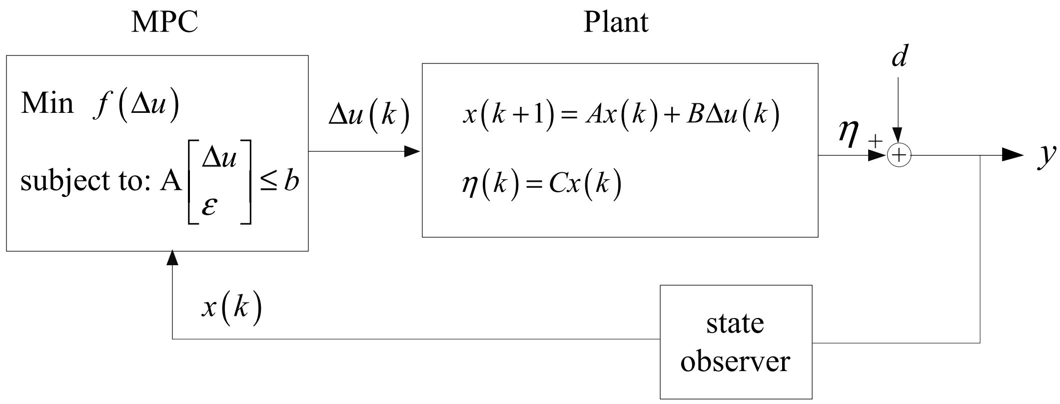

Fig. 6-6 MPC structure

The desirable response is defined as regulating the NS voltage to its reference value, which is determined by the gain-scheduled negative sequence droop block. So, the objective function is defined as:

$$\min \left\| v^-(k+1) - V^- \right\|^2 \tag{6-28}$$

in which $v^- = \begin{bmatrix} v_d^- & v_q^- \end{bmatrix}$ and V^- are the NS voltage at the DER terminal and the NS voltage reference, respectively. The output constraints are defined as limiting the active power and peak current within the safe operating range, i.e,

$$p(k+1) \le P_{\max} \tag{6-29}$$

$$\hat{i}_{abc}(k+1) \le \mathrm{I}_{max} \tag{6-30}$$

in which, the predicted active power and the vector of peak inductor currents are expressed as $p(k+1)$ and $\hat{i}_{abc}(k+1)$, respectively. The maximum permissible value of the active power and current are denoted by P_{max} and I_{max}, respectively. To ensure smooth transient response, the control move, $\Delta u(k)$, is limited to b:

$$\left|\Delta u(k)\right| \le b \tag{6-31}$$

Furthermore, in order to prevent overvoltage, the supplementary droop signal (i.e., u) must remain negative:

$$u(k) \le 0 \tag{6-32}$$

6-6-2 Derivation of the Plant model

The prerequisite for realizing the MPC is to derive the plant model. For each phase, a single-phase model is derived based on the synchronous rotating reference frame of the phase. To that end, each of the P+R controllers is approximated as two PI controllers in d and q axis [64].

The dynamic equations of the LC filter, output transformer, line and the cascaded PI controllers are detailed in Chapter 3 (Section 3-3) and repeated here for convenience:

$$s\begin{bmatrix} i_{Ld} \\ i_{Lq} \end{bmatrix} = \begin{bmatrix} -\frac{R_f}{L_f} & \omega_0 \\ -\omega_0 & -\frac{R_f}{L_f} \end{bmatrix}\begin{bmatrix} i_{Ld} \\ i_{Lq} \end{bmatrix} + \frac{1}{L_f}\begin{bmatrix} v_{dd} \\ v_{dq} \end{bmatrix} - \frac{1}{L_f}\begin{bmatrix} v_{cd} \\ v_{cq} \end{bmatrix} \tag{6-33}$$

$$s\begin{bmatrix} v_{cd} \\ v_{cq} \end{bmatrix} = \begin{bmatrix} 0 & \omega_0 \\ -\omega_0 & 0 \end{bmatrix}\begin{bmatrix} v_{cd} \\ v_{cq} \end{bmatrix} + \frac{1}{C_f}\begin{bmatrix} i_{Ld} \\ i_{Lq} \end{bmatrix} - \frac{1}{C_f}\begin{bmatrix} i_{od} \\ i_{oq} \end{bmatrix} \tag{6-34}$$

$$s\begin{bmatrix} i_{od} \\ i_{oq} \end{bmatrix} = \begin{bmatrix} -\dfrac{R_T + R_l}{L_T + L_l} & \omega_0 \\ -\omega_0 & -\dfrac{R_T + R_l}{L_T + L_l} \end{bmatrix} \begin{bmatrix} i_{od} \\ i_{oq} \end{bmatrix} + \frac{1}{L_T + L_l} \begin{bmatrix} v_{cd} \\ v_{cq} \end{bmatrix} - \frac{1}{L_T + L_l} \begin{bmatrix} v_{pccd} \\ v_{pccq} \end{bmatrix} \tag{6-35}$$

where v_d is the PWM voltage.

The P+R controller is equivalent to the combination of two PI controllers in positive and negative rotating reference frame [64]. So, the P+R controller can be approximated by PI controllers in the positive rotating reference frame:

$$\begin{bmatrix} v_{dd} \\ v_{dq} \end{bmatrix} = \begin{bmatrix} k_{pi} + \dfrac{k_{ri}}{s} \end{bmatrix} \left(\begin{bmatrix} i^*_{Ld} \\ i^*_{Lq} \end{bmatrix} - \begin{bmatrix} i_{Ld} \\ i_{Lq} \end{bmatrix} \right) + \begin{bmatrix} v^*_{cd} \\ v^*_{cq} \end{bmatrix} \tag{6-36}$$

$$\begin{bmatrix} i^*_{Ld} \\ i^*_{Lq} \end{bmatrix} = \begin{bmatrix} k_{pv} + \dfrac{k_{rv}}{s} \end{bmatrix} \left(\begin{bmatrix} v^*_{cd} \\ v^*_{cq} \end{bmatrix} - \begin{bmatrix} v_{cd} \\ v_{cq} \end{bmatrix} \right) + H \begin{bmatrix} i_{od} \\ i_{oq} \end{bmatrix} \tag{6-37}$$

The last terms on the RHS of (6-36) and (6-37) are the feedforward signals. In order to express the controllers' dynamics in state-space form, the integrals of the voltage and current errors are defined as state-variables:

$$e_{vd} = 1/s\left(v^*_{cd} - v_{cd}\right) \tag{6-38}$$

$$e_{vq} = 1/s\left(v^*_{cq} - v_{cq}\right) \tag{6-39}$$

$$e_{id} = 1/s\left(i^*_{Ld} - i_{Ld}\right) \tag{6-40}$$

$$e_{iq} = 1/s\left(i^*_{Lq} - i_{Lq}\right) \tag{6-41}$$

Using (6-33)-(6-41), the combination of cascaded controller, LC filter, isolation transformer and line is described in the state-space form, as follows:

$$\dot{x}_a = A_0 x_a + B_1 v^*_{ca} + \Gamma_1 w_a \tag{6-42}$$

in which "a" refers to phase a. Also, x_a, v^*_{ca} and w_a are the state vector, inverter reference voltage and disturbance vector, which are defined as

$$x_a = \begin{bmatrix} i^a_{Ld} & i^a_{Lq} & v^a_{cd} & v^a_{cq} & e^a_{vd} & e^a_{vq} & e^a_{id} & e^a_{iq} & i^a_{od} & i^a_{oq} \end{bmatrix}^T, \tag{6-43}$$

$$v^*_{ca} = \begin{bmatrix} v^{a*}_{cd} & v^{a*}_{cq} \end{bmatrix}^T, \tag{6-44}$$

$$w_a = \left[v_{PCCd}^a \quad v_{PCCq}^a \right]^T, \tag{6-45}$$

respectively. Moreover, the matrices A_0, B_1 and Γ_1 are obtained as

$$A_0 = \begin{bmatrix} \frac{-R_f - k_{pi}}{L_f} & \omega_0 & \frac{-k_{pv}k_{pi} - 1}{L_f} & 0 & \frac{k_{pi}k_{rv}}{L_f} & 0 & \frac{k_{ri}}{L_f} & 0 & 0 & 0 \\ -\omega_0 & \frac{-R_f - k_{pi}}{L_f} & 0 & \frac{-k_{pv}k_{pi} - 1}{L_f} & 0 & \frac{k_{pi}k_{rv}}{L_f} & 0 & \frac{k_{ri}}{L_f} & 0 & 0 \\ \frac{1}{C_f} & 0 & 0 & \omega_0 & 0 & 0 & 0 & 0 & -\frac{1}{C_f} & 0 \\ 0 & \frac{1}{C_f} & -\omega_0 & 0 & 0 & 0 & 0 & 0 & 0 & -\frac{1}{C_f} \\ 0 & 0 & -1 & 0 & 0 & 0 & 0 & 0 & 0 & 0 \\ 0 & 0 & 0 & -1 & 0 & 0 & 0 & 0 & 0 & 0 \\ -1 & 0 & -k_{pv} & 0 & k_{rv} & 0 & 0 & 0 & H & 0 \\ 0 & -1 & 0 & -k_{pv} & 0 & k_{rv} & 0 & 0 & 0 & H \\ \frac{k_{pi}H}{L_f} & 0 & \frac{1}{L_T + L_l} & 0 & 0 & 0 & 0 & 0 & -\frac{R_l + R_T}{L_T + L_l} & \omega_0 \\ 0 & \frac{k_{pi}H}{L_f} & 0 & \frac{1}{L_T + L_l} & 0 & 0 & 0 & 0 & -\omega_0 & -\frac{R_l + R_T}{L_T + L_l} \end{bmatrix} \tag{6-46}$$

$$B_1 = \begin{bmatrix} \frac{k_{pi}k_{pv} + 1}{L_f} & 0 & 0 & 0 & 1 & 0 & k_{pv} & 0 & 0 & 0 \\ 0 & \frac{k_{pv}k_{pi} + 1}{L_f} & 0 & 0 & 0 & 1 & 0 & k_{pv} & 0 & 0 \end{bmatrix}^T \tag{6-47}$$

$$\Gamma_1 = \begin{bmatrix} 0 & 0 & 0 & 0 & 0 & 0 & 0 & 0 & \frac{-1}{L_T + L_l} & 0 \\ 0 & 0 & 0 & 0 & 0 & 0 & 0 & 0 & 0 & \frac{-1}{L_T + L_l} \end{bmatrix}^T \tag{6-48}$$

Substituting (6-26) in (6-42), the plant dynamics are expressed in the following form:

$$\dot{x}_a = A_1 x_a + B_1 u_a + B_1 \begin{bmatrix} E_0 \\ 0 \end{bmatrix} + \Gamma_1 w_a \tag{6-49}$$

$$y_a = C_1 x_a \tag{6-50}$$

where y_a is the vector of phase a measured signals,

$$y_a = \left[i_{Ld}^a \quad i_{Lq}^a \quad v_{cd}^a \quad v_{cq}^a \quad i_{od}^a \quad i_{oq}^a \right] \tag{6-51}$$

and A_1 and C_1 are obtained as follows:

$$A_1 = A_0 + B_1 \begin{bmatrix} 0_{2*8} & \begin{matrix} R_T - R_0 & -\omega_0 L_T \\ \omega_0 L_T & R_T - R_0 \end{matrix} \end{bmatrix} \tag{6-52}$$

$$C_1 = \begin{bmatrix} I_4 & & 0 \\ & 0_{4*4} & \\ 0 & & I_2 \end{bmatrix} \tag{6-53}$$

The continuous time plant model is then discretized by using zero order hold method. The per-phase discrete time model is described as:

$$x_a(k+1) = A_2 x_a(k) + B_2 u_a(k) + B_2 \begin{bmatrix} E_0 \\ 0 \end{bmatrix} + \Gamma_2 w_a(k) \tag{6-54}$$

in which subscript “2” is used for discretized model.

The predictive control algorithm produces the control moves Δu_a rather than u_a. Therefore, it is convenient to regard the system input as Δu_a and the plant as having this signal as its input. To that end, an alternative state-space representation can be utilized with the following features:

1- The plant input is $\Delta u_a(k)$ and the output which will be produced without a disturbance is represented as $\eta(k)$.

2- The disturbance is modelled in the plant output. So, the measured output ($y_a(k)$) is the summation of $\eta(k)$ and the disturbance, $d(k)$

3- The augmented state is defined as

$$\xi(k) = \begin{bmatrix} \Delta x_a(k) \\ \eta(k) \end{bmatrix} \tag{6-55}$$

Using (6-54), the future state change can be predicted from the current state change, as follows:

$$\Delta x_a(k+1) = A_2 \Delta x_a(k) + B_2 \Delta u_a(k)$$

Furthermore, the future change in the plant output is expressed as

$$\begin{aligned} \eta(k+1) &= C_1 \Delta x(k+1) + \eta(k) \\ &= C_1\left(A_2 \Delta x_a(k) + B_2 \Delta u_a(k)\right) + \eta(k) \\ &= C_1 A_2 \Delta x_a(k) + \eta(k) + C_1 B_2 \Delta u_a(k) \end{aligned}$$

Therefore, the future augmented state can be expressed as [94]

$$\xi(k+1) = A_{\xi}\xi(k) + B_{\xi}\Delta u_a\left(k\right) \tag{6-56}$$

where, $A_{\xi} = \begin{bmatrix} A_2 & 0 \\ C_1 A_2 & I \end{bmatrix}$, $B_{\xi} = \begin{bmatrix} B_2 \\ C_1 B_2 \end{bmatrix}$. Furthermore, the system output is expressed as

$$y_a\left(k\right) = C_{\xi}\xi(k) + d_{\xi}\left(k\right) \tag{6-57}$$

where, $C_{\xi} = \begin{bmatrix} 0 & I \end{bmatrix}$.

The above representation has some advantages from the realization point of view. Recall that in (6-54) the state prediction ($x(k+1)$) is dependent on the w_a (PCC voltage), which is unknown to the local controller. This dependency is removed in (6-56) by replacing x_a with Δx_a. Moreover, the effect of variations of PCC voltage (Δw_a), the errors due to measurement, PWM switching and the inherent delay of single-phase Park transformation are included in the model as output disturbance (d).

Expanding (6-55) and (6-56), the three-phase plant is model is described, as follows:

$$x(k+1) = Ax(k) + B\Delta u\left(k\right) \tag{6-58}$$

$$y = Cx(k) + d\left(k\right) \tag{6-59}$$

6-6-3 Prediction of negative sequence voltage

Since the voltage drop on the transformer is compensated by the primary droop controller, only the MPC and primary droop actions contribute to the NS terminal voltage. Therefore, the NS voltage at the next time step can be estimated as:

$$v^{-}\left(k+1\right) = C_{neg}v_{dq} = C_{neg}\left(-R_0 i_{odq}\left(k+1\right) + u\left(k\right)\right) \tag{6-60}$$

in which $i_{odq}\left(k+1\right)$ is the predicted output current. The phase a output current prediction is related to the predicted state, as follows:

$$\begin{bmatrix} i_{oq}^{a}\left(k+1\right) \\ i_{od}^{a}\left(k+1\right) \end{bmatrix} = \begin{bmatrix} 0_{2*14} & I_2 \end{bmatrix}\xi\left(k+1\right) \tag{6-61}$$

in which I_k refers to identity matrix of order k. Expanding (6-61) to three phases, we have:

$$i_{odq}\left(k+1\right) = C_{io}x\left(k+1\right) \tag{6-62}$$

where

$$C_{io}=\begin{bmatrix}0_{2*14} & I_{2*2} & 0_{2*14} & 0_{2*2} & 0_{2*14} & 0_{2*2}\\ 0_{2*14} & 0_{2*2} & 0_{2*14} & I_{2*2} & 0_{2*14} & 0_{2*2}\\ 0_{2*14} & 0_{2*2} & 0_{2*14} & 0_{2*2} & 0_{2*14} & I_{2*2}\end{bmatrix} \tag{6-63}$$

Substituting (6-62) in (6-60), we have:

$$v^{-}(k+1)=-R_d C_{neg} C_{io} x(k+1)+C_{neg} u(k) \tag{6-64}$$

The future state, $x(k+1)$, is predicted from the plant model, as per (6-58). Substituting (6-58) into (6-64), the negative sequence voltage at the next time step is obtained according to

$$v^{-}(k+1)=\overbrace{\left[-R_d C_{neg} C_{io} A x(k)+C_{neg} u(k)\right]}^{\Psi(k)}+\overbrace{\left[-R_d C_{neg} C_{io} B\right]}^{\Theta(k)}\Delta u(k) \tag{6-65}$$

6-6-4 Active power prediction

The active power at the next time step is expressed as follows:

$$p(k+1)=\sum_{x=a,b,c} i_{Ldq}^{x}(k+1)\cdot v_{cdq}^{x}(k+1) \tag{6-66}$$

where, '$\cdot$' denotes dot product. Equation (6-66) is linearized by using Taylor expansion, as follows:

$$p(k+1)=p(k)+\sum_{x=a,b,c} i_{Ldq}^{x}(k)\Delta v_{cdq}^{x}(k+1)+v_{cdq}^{x}(k)\Delta i_{Ldq}^{x}(k+1) \tag{6-67}$$

The change in the active power of phase x ($x=a,b,c$) can be expressed as:

$$\Delta p_x(k+1)=\begin{bmatrix}v_{cd}^{x}(k) & v_{cq}^{x}(k) & i_{Ld}^{x}(k) & i_{Lq}^{x}(k)\end{bmatrix}\begin{bmatrix}\Delta i_{Ld}^{x}(k+1)\\ \Delta i_{Lq}^{x}(k+1)\\ \Delta v_{cd}^{x}(k+1)\\ \Delta v_{cq}^{x}(k+1)\end{bmatrix} \tag{6-68}$$

Equation (6-68) can be written in terms of the current measurement, $y_a(k)$ and future state variables, $\xi(k+1)$, as follows:

$$\Delta p_x(k+1)=\left\{\begin{bmatrix}1&0&0&0&0&0\\0&1&0&0&0&0\\0&0&1&0&0&0\\0&0&0&1&0&0\end{bmatrix} y_a(k)\right\}^{T}\times\left[I_4 \;\; 0_{4*12}\right]_{4*16}\xi(k+1) \tag{6-69}$$

Therefore, the change in total active power is predicted as follows:

$$p(k+1) = p(k) + \{C_{py}y(k)\}^T \{C_{px}x(k+1)\} \tag{6-70}$$

in which C_{py} and C_{px} are appropriate matrices with 0 and 1 elements. Substituting (6-58) into (6-70), the active power at the next time step is expressed as

$$p(k+1) = \overbrace{p(k) + (C_{py}y(k))^T C_{px}Ax(k)}^{\omega_p(k)} + \overbrace{(C_{py}y(k))^T C_{px}B}^{\Omega_p(k)}\Delta u(k) \tag{6-71}$$

6-6-5 Peak current prediction

The phase a inductor peak current at the next time step can be expressed in terms of the d-q current components:

$$\hat{i}_a(k+1) = \sqrt{\hat{i}_{Lda}^2(k+1) + \hat{i}_{Lqa}^2(k+1)} \tag{6-72}$$

Equation (6-72) can be linearized using Taylor expansion, as follows:

$$\hat{i}_a(k+1) = \hat{i}_a(k) + \frac{i_{Lda}(k)}{\hat{i}_a(k)}\Delta i_{Lda}(k+1) + \frac{i_{Lqa}(k)}{\hat{i}_a(k)}\Delta i_{Lqa}(k+1) \tag{6-73}$$

Rearranging the terms, (6-73) is rewritten in the matrix form, as following:

$$\hat{i}_a(k+1|k) = \hat{i}_a(k) + \begin{bmatrix} \frac{i_{Lda}(k)}{\hat{i}_a(k)} & \frac{i_{Lqa}(k)}{\hat{i}_a(k)} \end{bmatrix} [I_2 \quad 0_{2*14}]\xi_a(k+1) \tag{6-74}$$

Expanding (6-74) to three phases, the peak inductor currents can be predicted as:

$$\begin{bmatrix} \hat{i}_a(k+1) \\ \hat{i}_b(k+1) \\ \hat{i}_c(k+1) \end{bmatrix} = \begin{bmatrix} \hat{i}_a(k) \\ \hat{i}_b(k) \\ \hat{i}_c(k) \end{bmatrix} +$$

$$\overbrace{\begin{bmatrix} \frac{i_{Ld}^a(k)}{\hat{i}_a(k)} & \frac{i_{Lq}^a(k)}{\hat{i}_a(k)} & 0 & 0 & 0 & 0 \\ 0 & 0 & \frac{i_{Ld}^b(k)}{\hat{i}_b(k)} & \frac{i_{Lq}^b(k)}{\hat{i}_b(k)} & 0 & 0 \\ 0 & 0 & 0 & 0 & \frac{i_{Ld}^c(k)}{\hat{i}_c(k)} & \frac{i_{Lq}^c(k)}{\hat{i}_c(k)} \end{bmatrix}}^{C_{peak1}(k)} \overbrace{\begin{bmatrix} I_2 & 0_{2*14} & & & & 0 \\ & & I_2 & 0_{2*14} & & \\ 0 & & & & I_2 & 0_{2*14} \end{bmatrix}}^{C_{peak2}(k)} x(k+1) \tag{6-75}$$

Substituting (6-58) into (6-75), we have:

$$\hat{i}_{abc}(k+1) = \overbrace{\hat{i}_{abc}(k) + C_{peak1}(k)C_{peak2}Ax(k)}^{\omega_i(k)} + \overbrace{C_{peak1}(k)C_{peak2}B}^{\Omega_i(k)}\Delta u(k) \tag{6-76}$$

6-6-6 MPC formulation

At this stage, the optimization problem can be represented in terms of the unknown control move, $\Delta u(k)$, and the current state. Replacing (6-65) into (6-28) and introducing the weighting matrix Q_1, the objective function is expressed as

$$f = \left\| \Theta(k)\Delta u(k) + \Psi(k) - V^{-}(k) \right\|_{Q1}^{2} \tag{6-77}$$

Furthermore, combining (6-29), (6-30), (6-71) and (6-76), the power and current constraints are expressed as:

$$\Omega \Delta u(k) \leq \omega \tag{6-78}$$

in which $\Omega = \begin{bmatrix} \Omega_p & 0 \\ 0 & \Omega_i \end{bmatrix}$ and $\omega = \begin{bmatrix} P_{\max} - \omega_p \\ \mathrm{I}_{\max} - \omega_i \end{bmatrix}$. In order to prevent large oscillations and ensure convergence of the optimization problem, the power and current constraints are softened by introducing a slack variable ε, as follows:

$$\Omega \Delta u(k) \leq \omega + \varepsilon \tag{6-79}$$

$$\varepsilon \geq 0 \tag{6-80}$$

Adding penalties for the control action, control moves and slack variable, the objective function is expressed, as follows:

$$f = \left\| \Theta(k)\Delta u(k) + \Psi(k) - V^{-}(k) \right\|_{Q1}^{2} + \left\| \Delta u(k) \right\|_{R}^{2} + \left\| \Delta u(k) + u(\mathrm{k}-1) \right\|_{S}^{2} + \left\| \varepsilon(k) \right\|_{Q2}^{2} \tag{6-81}$$

in which R, S and Q2 are penalty matrices. Finally, the optimization problem can be expressed in the standard form, as follows:

$$\min f = \begin{bmatrix} \Delta u \\ \varepsilon \end{bmatrix}^{T} \begin{bmatrix} H_{\Delta u} & 0 \\ 0 & Q_2 \end{bmatrix} \begin{bmatrix} \Delta u \\ \varepsilon \end{bmatrix} + 2 \begin{bmatrix} \Delta u \\ \varepsilon \end{bmatrix}^{T} \begin{bmatrix} G_{\Delta u} \\ 0 \end{bmatrix} \tag{6-82}$$

subject to:

$$A_{const}\begin{bmatrix}\Delta u\\ \varepsilon\end{bmatrix}\le b_{const} \tag{6-83}$$

in which

$$H_{\Delta u}=\Theta(k)^T Q_1\Theta(k)+R+S \tag{6-84}$$

$$G_{\Delta u}=\Theta(k)^T Q_1\left[\Psi(k)-V^-(k)\right]+Su(\mathrm{k}-1) \tag{6-85}$$

$$A_{const}=\begin{bmatrix} I_{6*6} & -I_{6*6} & 0_{4*6} & \Omega_{4*6} & I_{6*6}\\ 0_{6*4} & 0_{6*4} & -I_{4*4} & -I_{4*4} & 0_{6*4}\end{bmatrix}^T \tag{6-86}$$

$$b_{const}=[b \quad b \quad 0 \quad \omega \quad -u(k-1)]^T \tag{6-87}$$

At each time step, the optimization is solved by using online active set strategy [95], which is recently introduced as a computationally efficient optimization algorithm for MPC application. The optimization algorithm computes the optimum control move (Δu). The control action is then obtained as the cumulative sum of the control move.

6-6-7 MPC tuning

In order to facilitate tuning of the MPC penalty factors, each factor is normalized, as

$$\bar{F}=F\times P^2 \tag{6-88}$$

where F is the penalty factor, $\bar{F}$ is the normalized penalty factor, and P is the permissible range of variations of the corresponding parameter. The permissible range of the control action is selected as 0.1*nominal voltage to prevent excessive voltage drops. Moreover, the permissible range of the voltage unbalance error, active power and peak current slack variable are selected as 0.001*nominal voltage, 0.01*nominal current and 0.01*nominal power, respectively.

The normalized penalty factors $\bar{Q}_1$ and $\bar{Q}_2$ are selected as unity to ensure the voltage unbalance error and current and power overload are prioritized according to the corresponding range of variations. The dynamics of the MPC is dependent on the control move penalty factor $\bar{R}$. As $\bar{R}$ is increased, the control action becomes slower but with less oscillations. Since the purpose of the MPC is improvement of power quality, $\bar{R}$ is selected large enough to ensure a stable, smooth dynamic response, with low sensitivity to parameter variations. The control action penalty factor $\bar{S}$ pushes the control action towards smaller values. This parameter is selected heuristically so that the control action falls with an acceptable rate after the disturbance is removed.

6-7 Simulation Results

In order to verify the effectiveness of the proposed method, it is applied to the CIGRE benchmark MG [96] which has been illustrated in Fig. 2-14 and detailed in Chapter 2, Section 2-5. The MG is composed of 5 DERs interconnected through a four-wire network. DERs 1-4 are dispatchable, that is, they can provide desirable active power according to droop characteristics. The dispatchable DERs might be supplied from intermittent energy sources such as PVs and wind turbines coupled with energy storage. Alternatively, controllable energy resources such as microturbines might be used to provide active power response. DER 5 is supplied with a PV energy source and controlled in constant current mode at unity power factor (PF=1). A detailed model of the system including inverter switches is built in MATLAB/Simulink and time-domain simulations are conducted with the conventional and the proposed method. The MPC is implemented in Simulink by using the open-source solver qpOASES. The PF of loads 1, 3, 4 and 5 is selected as 0.8 to represent common situation in LV networks. Other simulation parameters are shown in tables 5-1 and 5-2. To investigate the dynamic and steady-state response, three scenarios are devised.

Table 6-1 Benchmark parameters

Parameter \ DER unit	DER1	DER2	DER3	DER4	DER5
Rated power (kW)	30	15	23	3	10
Rated current (A)	90	45	70	9	30
Filter inductance (L_f, mH)	1.8	4	2.4	20	5.5
Filter equivalent resistance (R_f, Ω)	0.184	0.3	0.24	2	0.5
Transformer equivalent inductance (L_T, mH)	1.2	1.4	1.1	8.2	3.1
Transformer equivalent resistance	0.09	0.14	0.1	0.8	0.3

Table 6-2 Control parameters

Description	Parameter	Value	Unit
Inverter switching frequency	f_{sPWM}	20	kHz
MPC sample time	T_{sMPC}	2	ms
MPC Penalty Factors	R	1	pu
	S	0.09	pu
Gain-Scheduled Negative Sequence Droop Parameters	$Th1/Th2$	$\pm 0.05/\pm 0.10$	pu
	k_0	0.3	pu
	k_{H1}	0.3	pu
	k_{H2}	0.4	pu
	R^-	0.041	pu
Primary droop coefficient	R_0	0.1	pu

In the first scenario, all of the loads are single-phase loads, connected to phase *a*. Solar irradiance is constant at 200W/m^2. At t=0.2s, a step load increase of P=19kW/PF=0.7 is applied to bus 2. The load increase is picked up by all of the DERs. Nevertheless, the current rise is larger in case of DER2, which is closest to the disturbance. Simulation results for the proposed method are shown in Fig. 6-7. The inverter current of DER2 is shown in Fig. 6-7(a). Subsequent to the load rise, the current controller limits the instantaneous inverter current, clipping the current waveform. The distortion, however, is removed after a few cycles through the action of MPC. The compensation of NS voltage causes circulating currents in the phase b and c. The circulating currents, however, are reduced to less than 0.1pu thanks to the gain scheduled NS droop. At t=0.4s, the load is disconnected from bus 2. Subsequently, the currents drop to their initial value.

The active power generations of the DERs are depicted in Fig. 6-7(b). It is observed that the load increase is shared between the dispatchable DERs. During t=0.2s to t=0.35s the active power of DER2 gradually drops as a result of the MPC action. Subsequent to the load disconnection, the active powers of the DERs drop. The transient change of active power is larger for DER2, which is closer to the load. As a consequence, the active power of DER2 goes negative for less than 1 cycle. Nevertheless, the average power of DER2 is positive.

As shown in Fig. 6-7(c), v_a drops to 0.95 following the load increase. The decrease in v_a gives rise to NS and zero sequence voltages. The LCs compensate the NS voltage according to the gain scheduled NS droop. Since the zero sequence voltage remains unchanged, the magnitude of the phase voltages differ. The steady-state voltage imbalances at buses 1-5 settle at 0.55%, 1.76%, 0.45%, 0.6%, 0.68%, respectively.

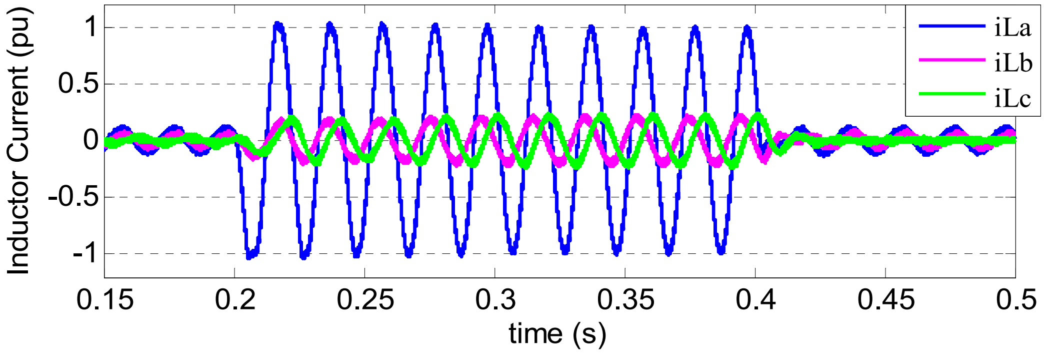

(a)

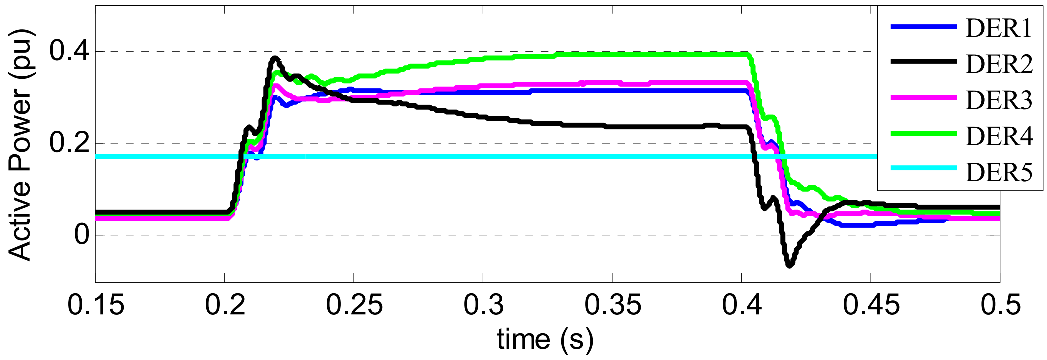

(b)

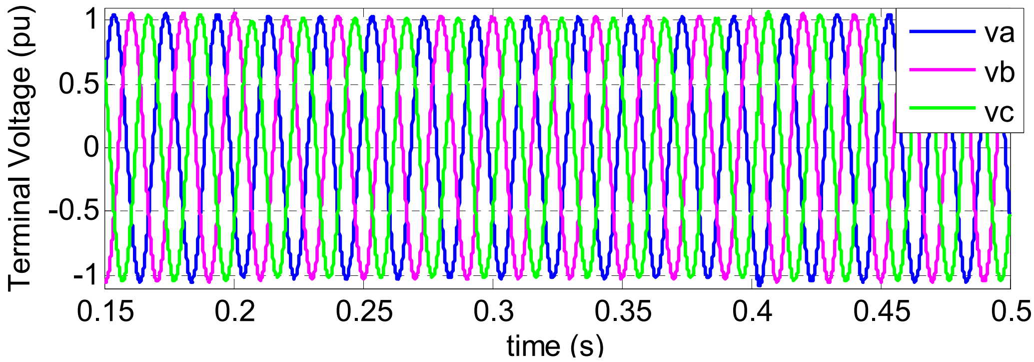

(c)

Fig. 6-7 Performance of the proposed method-case 1. (a) DER2 current, (b) DER powers (c) DER2 voltage

Simulations are repeated for the conventional *P-f/ Q-E* droop method [1] with P+R cascaded controllers implemented in the αβ0 framework. The parameters of the *P-f* and *Q-E* droop controllers are listed in table 6-3. The parameters of the cascaded controllers are selected the same as the proposed controller.

Table 6-3 Conventional droop controller parameters

Description	Parameter	Value	Unit
P-f droop coefficient	k_P	2	rad/s
Active power reference	P_0	0	W
No-load frequency	f_0	50	Hz
Q-E droop coefficient	k_Q	0.06	pu
Reactive power reference	Q_0	0	VAR
No-load Voltage	E_0	1	pu
Low-pass filter cut-off frequency	ω_{cLPF}	30	rad/s

The conventional method provides equal sharing of the steady-state active power, as shown in Fig. 6-8(b). However, the poor sharing of Q results in a sustained overcurrent with a magnitude of 1.5pu in the DER2, as shown in Fig. 6-8(a). The overcurrent can be prevented by implementing the cascaded controller in *abc* framework. However, as mentioned in Section 6-2-1, that method causes circulating current harmonics. As shown in Fig. 6-8(c) the v_a drops to less than 0.9pu. The poor voltage regulation is caused by two factors: Firstly, the Q-E droop characteristic varies the reference voltage of the inverter between 0.96 to 1.04. Secondly, in contrast to the proposed method, the voltage drop across the DER transformer is not compensated in this case. The voltage imbalance at bus 1-5 is 2.6%, 3.1%, 2.6%, 2.6% and 2.7%, respectively.

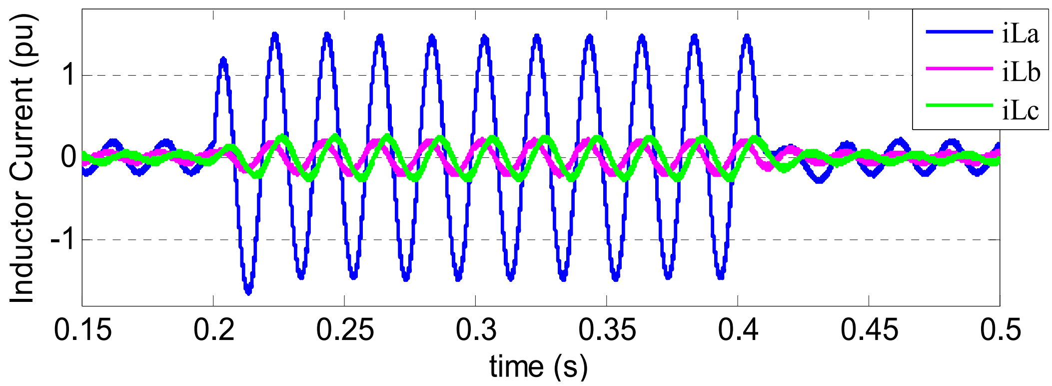

(a)

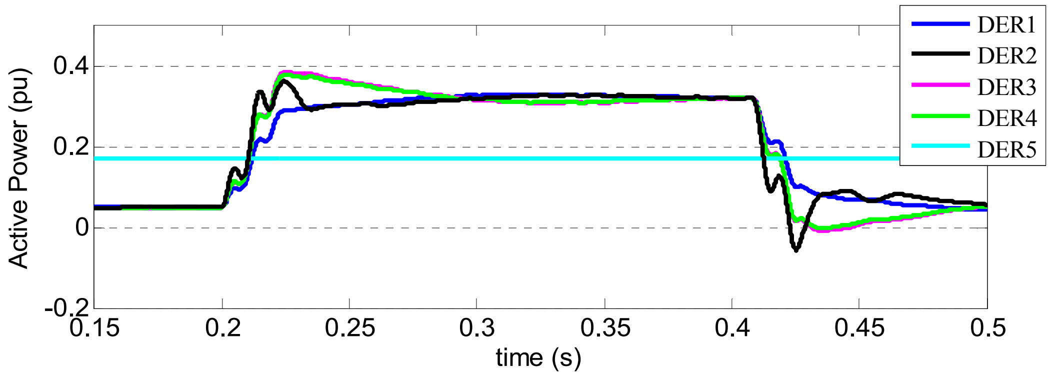

(b)

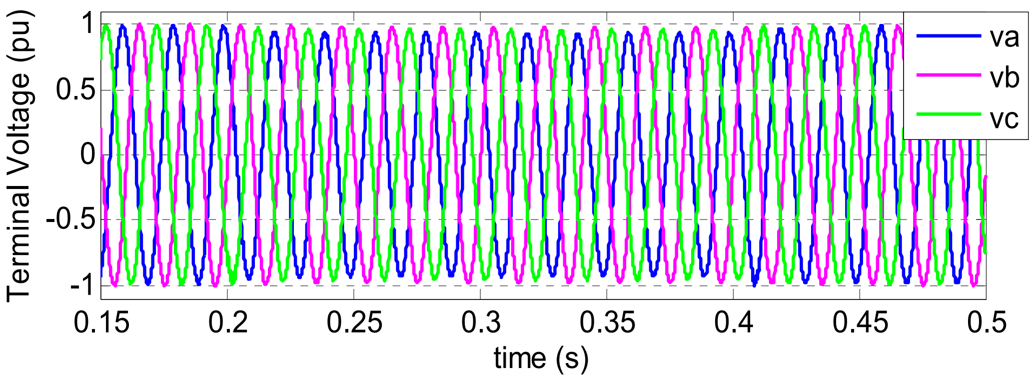

(c)

Fig. 6-8 Performance of the conventional method-case 1. (a) DER2 current, (b) DER powers (c) DER2 voltage

In the second scenario, loads 1, 3, 4 and 5 are three-phase loads. Solar irradiance is constant at 200W/m^2. At t=0.2s an unbalanced load composing of a three-phase load with P=45.6 kW/PF=0.8 and a single-phase load with P=3.8kW/Pf=0.8 is connected to bus 2. Simulation results for the proposed method are illustrated in Fig. 6-9. Subsequent to load rise, the i_{La} of DER2 increases but is effectively limited by the MPC. Also, the active power of DER2 reaches is limited to the rated value. The voltage imbalance is around 0.1-0.2%.

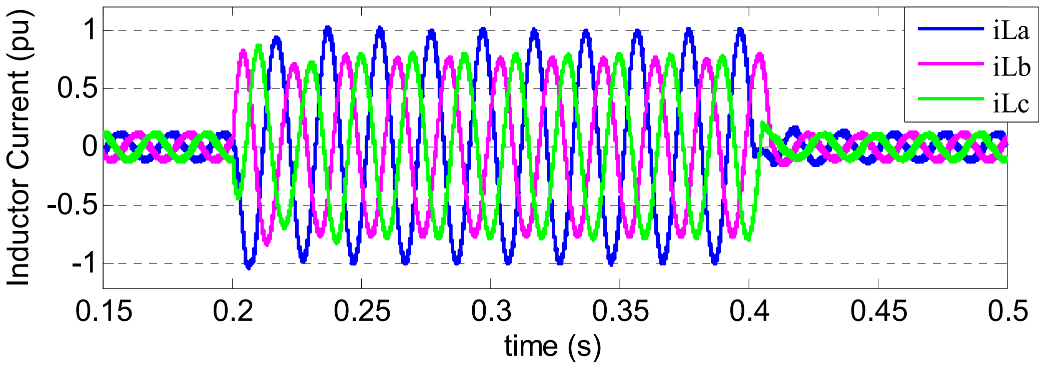

(a)

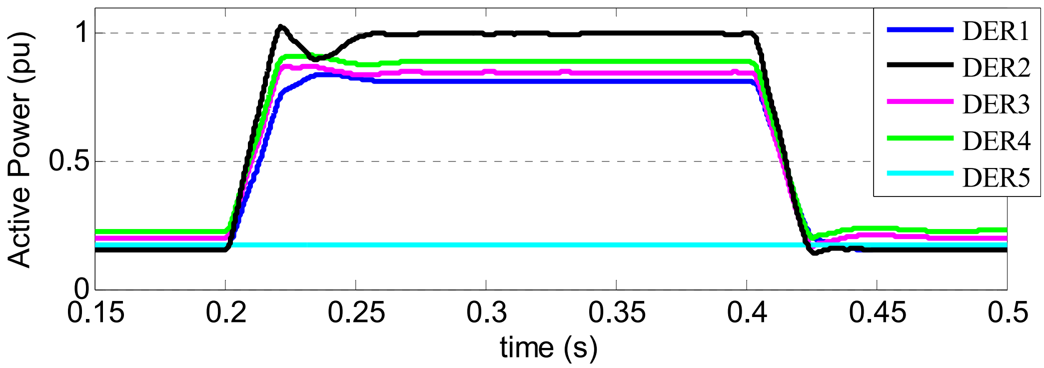

(b)

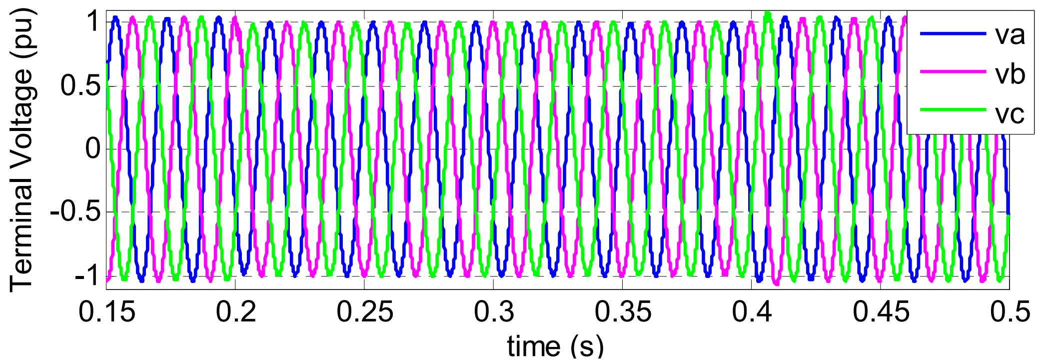

(c)

Fig. 6-9 Simulation results of the proposed method-case 2: a) DER2 current, b) DER powers c) DER2 voltage

Simulation results for the second scenario with the conventional method are illustrated in Fig. 6-10. Since the load is less unbalanced in this case, the current limiting mechanism of the conventional controller is more effective. However, the DER2 still experiences a peak inverter current of 1.19pu. The voltage v_a at bus 2 falls to around 0.87pu. The voltage imbalance is around 0.6%.

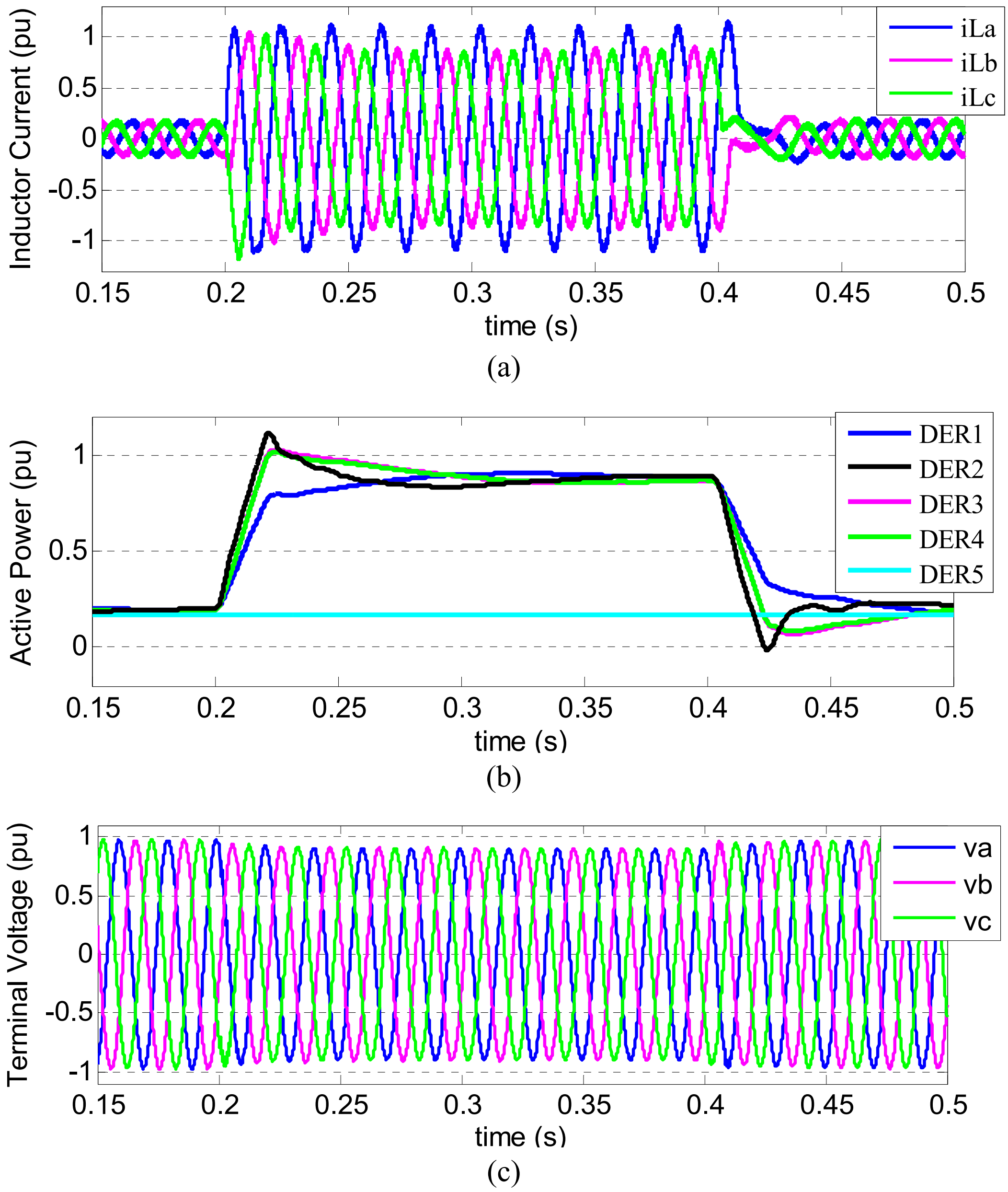

Fig. 6-10 Simulation results of the conventional method-case 2: a) DER2 current, b) DER powers c) DER2 voltage

In the third scenario, load 2 is composed of a three-phase load with P=45.6 kW/PF=0.9 and a single-phase load with P=1.9kW/PF=0.9. Other loads are three-phase loads. The solar irradiance is initially 1000 W/m^2 but drop to 200W/m^2 at t=0.2s. As a result, the generation of DER5 drops from 1pu to 0.2pu. Simulation results for this proposed method are illustrated in Fig. 6-11. In order to maintain the load/generation balance the active powers of the dispatchable DERs are increased, as shown in Fig. 6-11(b). It is observed that the active power of DER2 is effectively limited to 1pu and the excess load is shared between DERs 1, 3 and 4. The instantaneous current and voltage of DER2 are only slightly affected by the disturbance. The voltage imbalance is around 0.1-0.2%.

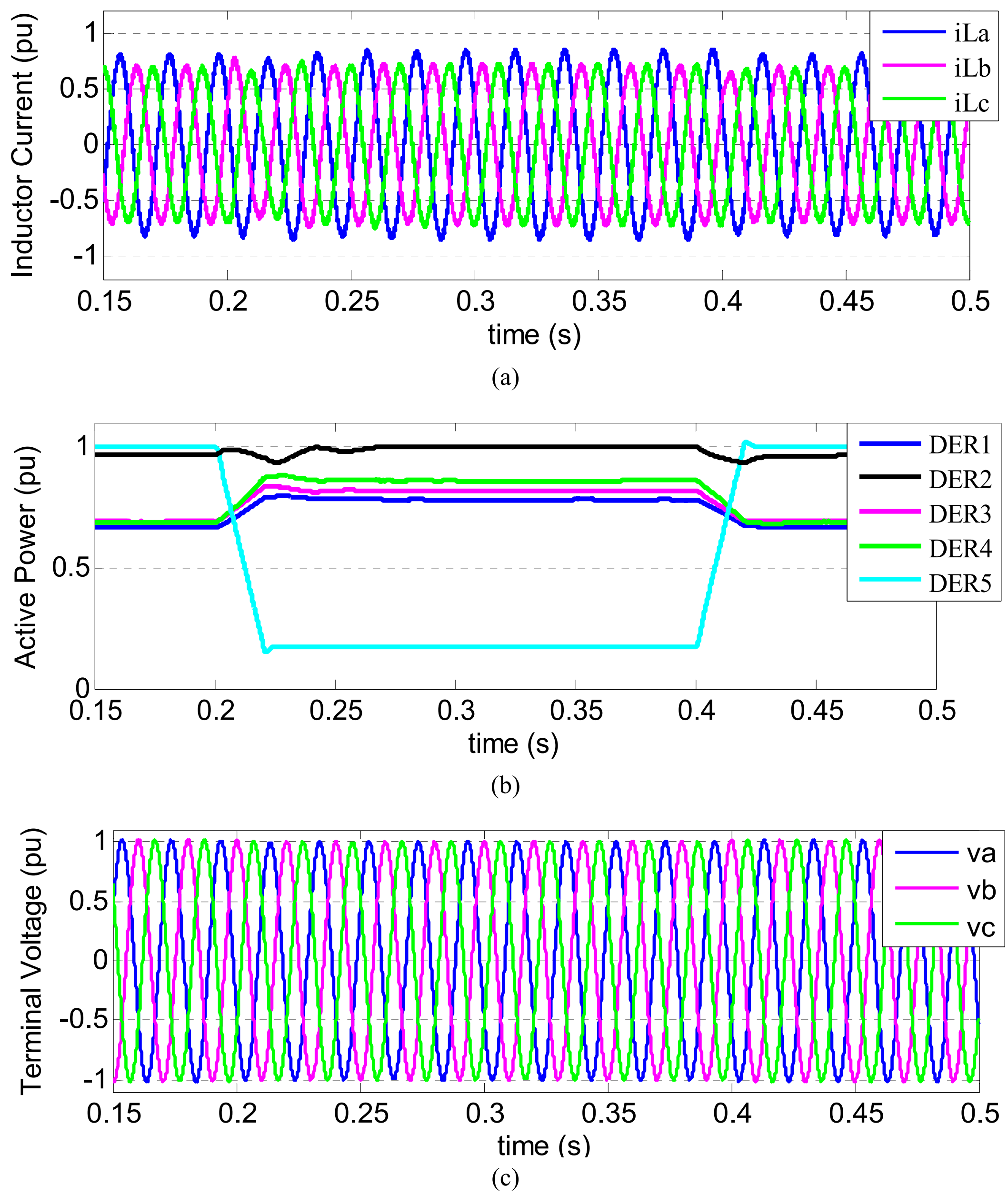

Fig. 6-11 Performance of the proposed method-case 3: a) DER2 current, b) DER powers c) DER2 voltage

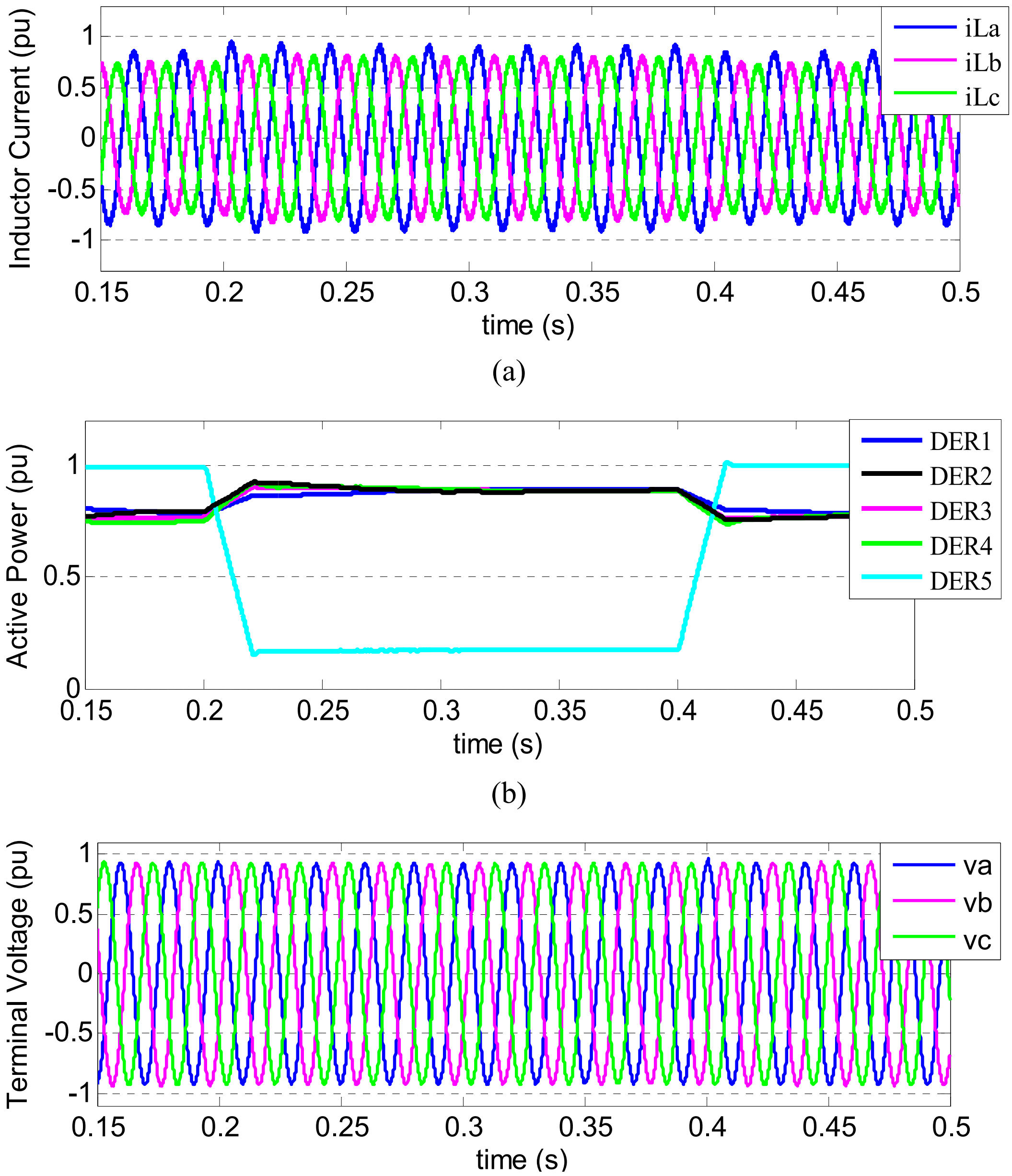

(c)

Fig. 6-12 Performance of the conventional method-case 3: a) DER2 current, b) DER powers c) DER2 voltage

Simulation results for the third scenario with the conventional method are illustrated in Fig. 6-12. It is observed that the current of DER2 is within the limits in this case. This is a result of improved current sharing of the conventional droop method at higher PFs, where Q is small. Nevertheless, voltage regulation is poor compared to the proposed method.

Comparison of the simulation results reveals important improvements in terms of power quality and overcurrent stresses. Specifically, the proposed method effectively limits the inverter currents without introducing current harmonics. The voltage profile is within the permissible range of 1.05pu to 0.95pu. The maximum voltage imbalance is 1.7%, which is lower than the 2% standard limit. Although the active power sharing is not ideal but the active power of each DER is limited to its rated value.

The proposed method is designed independent from the network topology and loading conditions. In order to verify the design, 13 additional scenarios, including single-phase, three-phase unbalanced step load changes at bus 1,3,4 and 5 and also two phase step load changes at each of the buses are simulated. In each scenario, the step load power is selected as the maximum permissible demand of the corresponding bus and other loads are weighted in accordance with the total generation capacity.

A summary of simulation results are listed in Table 6-4. The maximum voltage is equal to the no-load voltage in all cases. In cases 1 and 4 the minimum voltage is 0.98 and the voltage imbalances are 1.4% and 1.5%, respectively. For case 2 the accumulation of a large load at bus 2 causes the minimum voltage to drop to 0.95pu and the imbalance to increase to 1.7%. In case 3, despite the large magnitude of the disturbance, the voltage regulation is better thanks to the larger size of DER3 compared to DER2. Since DER5 does not contribute to voltage regulation, the voltage imbalance is the largest in case 5. Nevertheless, both voltage deviation and voltage imbalance are within the permissible range in all cases. Moreover, the THDI is less than 0.5%.

In order to investigate the robustness of the MPC, the impedances of the transformer and the LC filter of DER2 have been altered by a factor of ±30% and simulations have been repeated for each case. The results showed no considerable difference with the original simulation.

Table 6-4 Simulation results for the proposed method

Disturbance location / Description	bus1	bus2	bus3	bus4	bus5
Step load power/phase (kW)	4	19.2	13.3	4	12.5
Max Voltage (pu)	1.05	1.05	1.05	1.05	1.05
Min Voltage (pu)	0.98	0.95	0.98	0.97	0.95
Max voltage imbalance (%)	1.4	1.7	1.2	1.5	1.9
Max THDI (%)	0.4	0.5	0.4	0.5	0.5

6-8 Discussion

From the implementation viewpoint, the primary droop and cascaded controllers are similar to the conventional droop control method. The execution time of the MPC is measured in MATLAB by running the MPC code on a 2.6 GHz Intel core i5 PC (without using parallel processing). The time required for 10^6 executions is measured manually as around 200s. So, the MPC execution time is calculated as 200μs. Therefore, the implementation of MPC with a sample time of 2ms is feasible with the DSPs available in the market. A GPS receiver is required to synchronize the time zero of the LCs. Although GPS synchronization adds to the complexity of the controller, it brings the advantage of fixed frequency operation.

Simulation results show that the active powers of the DERs are not equal. The sharing error originates from line voltage drops [91] and the MPC control action. As a result, the sharing is not ideal. Ideal sharing is neither an economical nor a technical requirement for low voltage MGs. In other words, optimal sharing, which is achieved through the action of secondary controllers, is different from ideal sharing. However, ideal sharing might be desirable to prevent DERs from active power and current overload during high loading conditions. In the proposed method, this problem is circumvented through the action of MPC.

6-9 Conclusions

Unbalanced load currents might adversely affect the performance of decentralized controllers. Moreover, they cause the conventional current limiting mechanisms to malfunction. While the former results in voltage unbalance and circulating currents between DERs, the latter might result in over-current stress or circulating harmonic currents.

In this chapter, a novel control method is introduced to tackle the aforementioned issues while providing high power quality. The controller utilizes V-I droop control method to provide fixed frequency operation with a fast dynamic response. Moreover, a supplementary droop controller is introduced as a mechanism for limiting the current and active power to the rated value and reducing the voltage unbalance. The method is tested on CIGRE benchmark MG. Simulation results demonstrate that the proposed controller improves the power quality by limiting the voltage unbalance below 2% and eliminating the circulating current harmonics. Moreover, the active power generation is limited to the rated value.

Chapter 7

Accurate current sharing and power quality improvement under nonlinear loading conditions

7-1 Introduction

Unbalanced and nonlinear loads, which are quite common in MGs, not only degrade the power quality but also adversely affect the performance of droop control schemes in terms of sharing accuracy. In particular, the conventional droop scheme, which is focused on fundamental active and reactive power sharing, cannot ensure equal sharing of harmonic currents, which are produced by nonlinear loads. To alleviate those shortcomings, several modified droop control methods have been developed [24-27], among which virtual impedance-based schemes are the most widely accepted [25].

The virtual impedance schemes achieve a fast dynamic response by modifying the DG voltage according to the DG output current. Furthermore, proper sharing of negative sequence and harmonic currents is achieved by selecting the virtual impedance of each unit inversely proportional with its power rating. However, in weak islanded MG, where the line impedance is considerable, accurate load current sharing requires large virtual impedances which may produce a large voltage distortion [28]. Therefore, there is a trade-off between current sharing accuracy and power quality.

To compensate for the voltage drop on the lines, a virtual capacitance [29] or an adaptive negative virtual resistance [30] can be employed. However, those schemes require the knowledge of line impedances and network topology. An alternative approach is using a hierarchical control structure, composed of primary and secondary levels [31]. The primary controller comprises local DG controllers, which use a combination of droop control method and virtual impedance to coordinate the power generation of DGs and share the harmonic loads between them. The secondary controller produces compensating signals so as to improve the voltage quality in a so-called Sensitive Load Bus (SLB). The compensation signals are broadcasted to the local controllers to adjust the DG reference voltage accordingly. The hierarchical control scheme has been further elaborated in [97] to enhance the frequency regulation. However, the methods of [31] and [97] have some important limitations:

1) In order to minimize the communication bandwidth and reduce the adverse effects of communication delays, the voltage of the sensitive load bus is transformed to synchronous rotating frame (dq-frame) and then transformed back to stationary frame (αβ-frame) in local controllers. On the other hand, each controller uses the phase angle of its local voltage for Park transformations. Since the voltage angle varies throughout the MG, this process results in transformation errors, which may degrade the performance when the DGs are electrically far. Consequently, current sharing and also voltage quality might deteriorate.

2) The selective virtual impedance scheme is not only complex to implement but also suffers from slow dynamic response.

3) The voltage drop across the lines degrades the performance of virtual impedance scheme in terms of current sharing accuracy. The effect of line impedances can be compensated by means of distributed control techniques as discussed in [98] and [99-101]. However, since the secondary controller is characterized by slow dynamic response, it does not prevent transient overcurrent stresses.

4) The control methods proposed in [31] and [97] are based on the assumption of inductive network impedances. However, the low voltage MGs are mainly resistive in practice.

In this chapter, a novel hierarchical control framework, comprised of primary and secondary control levels is proposed to alleviate the aforementioned problems. The main contributions of the presented method are as follows:

- While the basic V-I droop method proposed in Chapter 2 is implemented in the dq reference frame, the proposed scheme is implemented in abc reference frame to enable fast sharing of harmonic components. Moreover, the droop coefficient is adaptively updated according to the peak current to ensure improved accuracy at high loading conditions. This approach highlights the significance of limiting the peak output current of each DG unit within its current ratings.
- In contrast with [25, 31, 97-101] , which add a virtual impedance to the conventional droop scheme to enable sharing of the harmonic currents, the proposed primary controller integrates the fundamental and harmonic current sharing into a single V-I droop controller. Therefore, the structure of the proposed primary controller is significantly simpler compared to [25, 31, 97-101].
- In order to improve the power quality and alleviate the effect of line impedances on the active power sharing, a novel secondary control scheme is proposed. The secondary controller includes a distributed power sharing controller and a

centralized voltage conditioning scheme. The distributed power sharing controller acts upon an agent-based structure, in which each agent modifies the d-axis fundamental voltage of the corresponding DG unit according to the difference between the normalized power of the unit and the neighbor units. The voltage conditioning scheme uses a simple integral controller to compensate the voltage deviations and distortions at the SLB.

The majority of the content of this chapter has been published in [102]. The rest of the chapter is organized as follows. The problem of proportional current sharing in islanded MGs and the conventional solutions are addressed in Section 7-2. The proposed method is introduced in Section 7-3. Experimental results are presented in Section 7-4 to demonstrate the efficacy of the proposed method. The chapter is concluded in Section 7-5.

7-2 Proportional current sharing in islanded MGs

In this section, the conventional current sharing strategies and their shortcomings are discussed.

7-2-1 Virtual resistance scheme

The conventional droop method suffers from several issues including slow dynamics, frequency and voltage fluctuations and degraded sharing accuracy under nonlinear and/or unbalanced loading conditions [103]. One solution for improving the dynamic performance and sharing accuracy is to introduce a virtual resistance in the DG output [25]:

$$v_c^* = E^{1+} - R_v i_o \tag{7-1}$$

in which v_c^*, R_v and i_o are the reference voltage, virtual resistance and output current, respectively. Furthermore, E^{1+} is the fundamental reference voltage obtained from P-V/Q-f droop control method [25]. In order to perform proper current sharing, the virtual impedance of each unit is selected inversely proportional to its power rating:

$$R_{v1}.S_{rated1} = R_{v2}.S_{rated2} = \cdots = R_{vN}.S_{ratedN} \tag{7-2}$$

in which S_{ratedk} is the rated apparent power of unit k. This scheme is used along with the P-V/Q-f droop method to allow equal sharing of negative sequence and harmonic components.

The effect of virtual resistance on the sharing of harmonic currents can be analyzed based on the equivalent model of Fig. 7-1. The dynamics of the inner voltage control loop is neglected in this equivalent circuit as its time constant is much smaller compared with the droop controller. Using KVL and KCL, the output current of unit k is obtained as

$$i_{ok}^h = \frac{\left(R_{vk} + z_{ck}^h\right)^{-1}}{\sum_{i=1}^{N}\left(R_{vi} + z_{ci}^h\right)^{-1}} i_{Load}^h \tag{7-3}$$

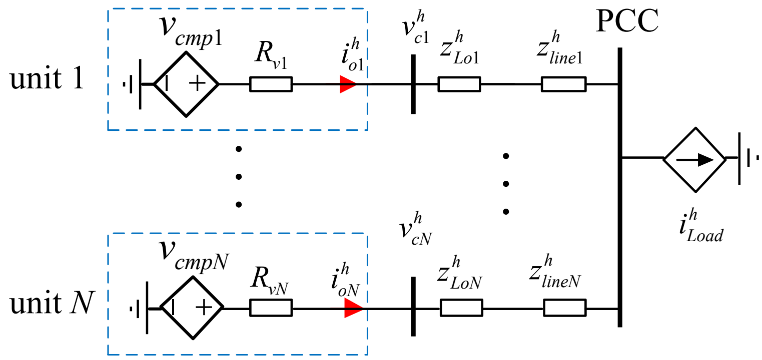

Fig. 7-1 Equivalent model of the MG for negative sequence and harmonics

where $z_{ck}^h = z_{Lok}^h + z_{linek}^h$ and z_{Lok}^h and z_{linek}^h are the impedance of output inductor and line of unit k, respectively. Moreover, the effect of compensation voltage, v_{cmp}, is neglected.

Comparing (7-2) and (7-3), it is observed that the accuracy of current sharing is adversely affected by the output inductor and line impedances. Accurate current sharing necessitates selecting a virtual resistance much larger than $\left(z_{ck}^h + z_{linek}^h\right)$. On the other hand, the value of virtual resistance is limited by the permissible voltage deviations. Therefore, the sharing accuracy of the virtual resistance method might be poor in practice.

7-2-2 Selective virtual impedance scheme

Since the fundamental power factor is higher than 0.7 in practice, the fundamental voltage deviations caused by a virtual resistance is higher compared with a virtual inductance with the same impedance. In order to attain a desirable voltage regulation while taking advantage of the improved damping of the virtual resistance, the virtual impedance scheme is adopted. In this method, the reference voltage corresponding to harmonic order h (h=1+,1-,2+,2-,…) is defined as

$$v_c^{h*} = E^h - Z_v^h i_o^h \tag{7-4}$$

in which E_k^h is equal to E_k^{1+} for the fundamental positive sequence component and zero, otherwise. Moreover, Z_v^h is the virtual impedance matrix, which is defined as

$$Z_v^h = \begin{bmatrix} R_v^h & -X_v^h \\ X_v^h & R_v^h \end{bmatrix} \tag{7-5}$$

This virtual impedance method is commonly implemented in $\alpha\beta$ reference frame. The main challenge for implementation of the virtual impedance scheme is extraction of the αβ components corresponding to each of the dominant harmonics. An straightforward solution for extraction of a harmonic components h is transforming the signal to the synchronous rotating reference frame (SRRF) rotating with angular speed of $h\omega_0$, averaging the d and q components of the signal to remove the other components and transforming the averaged components back to the αβ frame [97]. However, the averaging filters incur a delay, which slows down the current sharing dynamics. In order to improve the current sharing dynamics, a multi-resonant frequency-locked loop harmonic extraction method is proposed in [104]. Nonetheless, this method is complex and computationally expensive.

7-2-3 Effect of secondary harmonic compensation on current sharing

The voltage drops across the virtual impedance, DGs output inductors and the lines give rise to voltage distortions at the PCC. In order to improve the quality of voltage, secondary harmonic compensation schemes are adopted [31, 97, 98, 101]. In these methods, a secondary controller calculates a compensation command for each of the dominant harmonics. The compensation commands are broadcasted to the local controllers via a communication network. Based on the received commands, each local controller adds a compensation voltage to its output voltage.

With the intention of reducing the communication bandwidth, the compensation commands are broadcasted in the form of d and q components. This necessitates the utilization of Park and inverse Park Transformations at the secondary and local controllers, respectively. Such transformations cause an error in the received compensation command due to the mismatch between the reference angles of the secondary and local controllers.

The effect of transformation error on the current sharing among the DERs can be analyzed based on the MG model in Fig. 7-1. In order to simplify the analysis, it is assumed that the compensation command is directly injected into the reference voltage of the inverter and N=2. The compensation signal computed at local controller *i*, v_{cmpi}^{h} is related to the secondary controller command, v_{cmp}^{h}, as follows:

$$\begin{bmatrix} v_{cmpi,d}^{h} \\ v_{cmpi,q}^{h} \end{bmatrix} = \begin{bmatrix} \cos(h\delta_i) & \sin(h\delta_i) \\ -\sin(h\delta_i) & \cos(h\delta_i) \end{bmatrix} \begin{bmatrix} v_{cmpd}^{h} \\ v_{cmpq}^{h} \end{bmatrix} \tag{7-6}$$

in which δ_i is the difference between the reference angle of the local controller i (θ_{refi}) and the secondary controller (θ_{refs}):

$$\delta_i = \theta_{refi} - \theta_{refs}, \tag{7-7}$$

It should be pointed out the angles θ_{refi} and θ_{refs} are conventionally extracted from the local voltages by means of a PLL [31, 97, 98, 101]. Therefore, an unintentional mismatch exists between θ_{refi} and θ_{refs} due to the line impedances. As a result, the compensation voltages of each local controller varies depending on the corresponding voltage angle and the harmonic order. From Fig. 7-1, the current of unit 1 is calculated using superposition theorem as

$$i_{o1}^{h}=\frac{R_{v2}+z_{c2}^{h}}{\sum_{i=1}^{2}\left(R_{vi}+z_{ci}^{h}\right)}i_{Load}^{h}+\begin{bmatrix}\cos\left(h\delta_{1}\right)-\cos\left(h\delta_{2}\right) & \sin\left(h\delta_{1}\right)-\sin\left(h\delta_{2}\right)\\-\sin\left(h\delta_{1}\right)+\sin\left(h\delta_{2}\right) & \cos\left(h\delta_{1}\right)-\cos\left(h\delta_{2}\right)\end{bmatrix}\frac{v_{cmp}^{h}}{\sum_{i=1}^{2}\left(R_{vi}+z_{ci}^{h}\right)} \tag{7-8}$$

Equation (7-8) implies that the transformation error alters the current sharing between the units. Moreover, the effect of transformation error is escalated at higher order harmonics. This unintentional and uncontrolled issue might cause circulating harmonic currents among the units and expose some units to overcurrent stresses under high loading conditions. In Section 7-3, a solution is proposed to tackle this problem.

7-3 Proposed Control Method

In order to improve the current sharing accuracy in islanded MGs while ensuring high power quality, a novel control strategy is proposed in this chapter. The proposed control method for a general MG consisting of N DGs and several loads, which can be balanced, unbalanced, linear or nonlinear is depicted in Fig. 7-2. The control framework is comprised of primary and secondary control levels. At the primary level, a new droop controller is proposed to enable sharing of load current among the DG unit with a fast dynamic response. The secondary control level includes a voltage conditioning module and distributed power sharing control agents. The individual control agents and the voltage conditioning module are interconnected through a low bandwidth communication (LBC) network. Additionally, the DG units are synchronized by means of GPS timing technology.

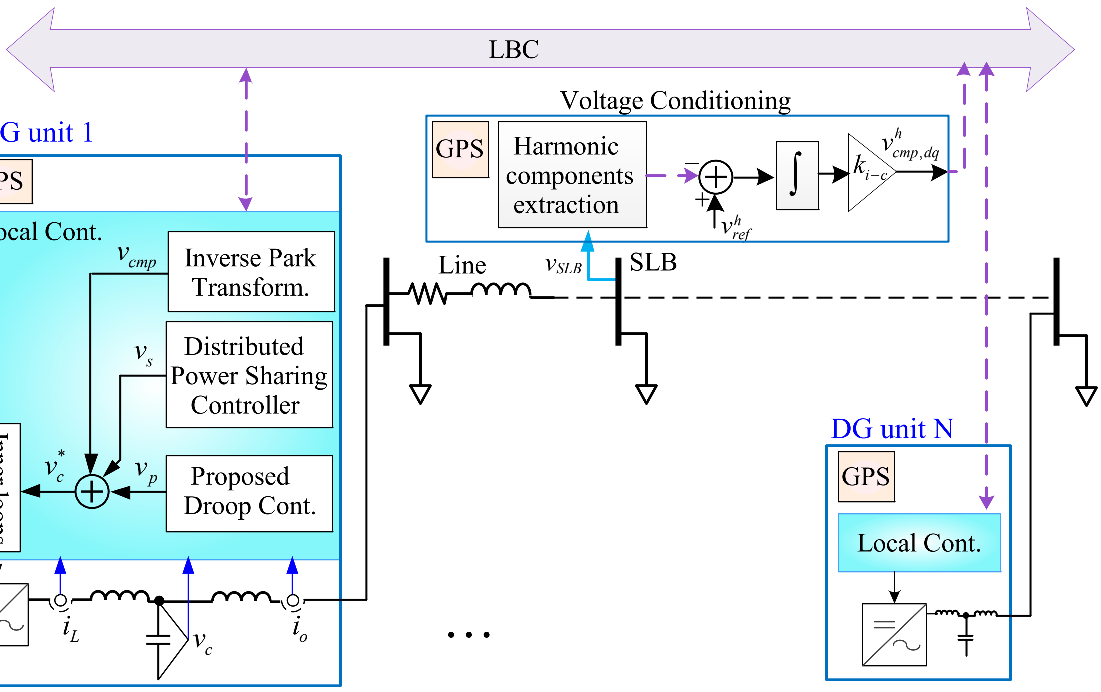

Fig. 7-2 Proposed control framework

7-3-2 Droop control strategy

In this section, a new decentralized control method as an extension for V-I droop concept [46] is proposed to enable fast and accurate current sharing. In this method, the primary control action of unit *k* is defined according to the following adaptive voltage-current droop law:

$$v_{pk,abc} = E_{0abc} - r_{vk}\left(\hat{i}_{ok}\right)i_{ok} \tag{7-9}$$

in which r_{vk} is the adaptive virtual resistance, which is adjusted according to the largest peak of the *abc* output currents, $\hat{i}_{ok}$. Furthermore, the no-load reference voltage, E_{0abc}, is a balanced sinusoidal voltage with rated amplitude and frequency:

$$E_{0abc} = \left[E_0 \sin\theta_s \quad E_0 \sin\left(\theta_s - \frac{2\pi}{3}\right) \quad E_0 \sin\left(\theta_s - \frac{4\pi}{3}\right) \right]^T \tag{7-10}$$

Equation (7-10) implies that the phase *a* no-load reference voltage of each DG unit is aligned with the *d* axis of the global SRRF.

The proposed droop controller provides a simple and unified droop scheme for sharing of fundamental active and reactive power as well as harmonic components. The salient feature of the proposed droop method is the emphasis on the accurate sharing of instantaneous current instead of power (conventional droop [105]) or d and q components of current (basic V-I droop [46]).

The adaptive virtual resistance is defined as

$$r_{vk}\left(\hat{i}_{ok}\right) = R_{vk}\, g\left(\hat{i}_{ok}\right) \tag{7-11}$$

in which R_{vk} is the maximum virtual resistance, which is selected based on the maximum permissible voltage deviations. Moreover, *g*(.) is a monotonic piecewise linear function with a maximum value of 1.

The mechanism of operation of the proposed droop method is explained based on the model in Fig. 7-1. Consider a MG composed of two DG units with equal power ratings. Using current division rule, the output current of unit 1 is expressed as

$$i_{o1}^h = \frac{\left(r_{v2} + z_{c2}^h\right)}{\left(r_{v2} + z_{c2}^h\right) + \left(r_{v1} + z_{c1}^h\right)} i_{Load}^h , \tag{7-12}$$

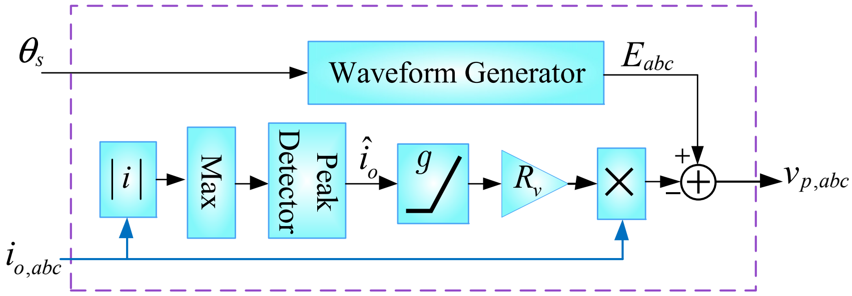

Fig. 7-3 Proposed droop control method

Substituting (7-11) into (7-12) and rearranging the terms, the following expression is obtained:

$$i_{o1}^h = \frac{1}{2} i_{Load}^h + \frac{1}{2} * \frac{g\left(\hat{i}_{o2}\right) - g\left(\hat{i}_{o1}\right) + \dfrac{z_{c2}^h - z_{c1}^h}{R_v}}{g\left(\hat{i}_{o1}\right) + g\left(\hat{i}_{o2}\right) + \dfrac{z_{c1}^h + z_{c2}^h}{R_v}} i_{Load}^h , \tag{7-13}$$

Ideally, the load current is shared equally between the units and the second term on the Right Hand Side (RHS) of (7-13) is zero. In practice, however, the mismatch between the line impedances gives rise to the sharing error. By using the presented adaptive virtual resistance, if the peak current of unit 1 is larger than unit 2, the term $g\left(\hat{i}_{o2}\right) - g\left(\hat{i}_{o1}\right)$ goes negative, hence reducing the current of unit 1. Otherwise, $g\left(\hat{i}_{o2}\right) - g\left(\hat{i}_{o1}\right)$ goes positive, thus increasing the current of unit 1. Therefore, the proposed scheme improves the current sharing accuracy compared to the conventional virtual resistance method. Additionally, the sharing accuracy is improved at higher loading conditions due to the higher slope of the function $g(.)$. This way, the DGs are protected from overcurrent stresses without imposing additional voltage distortion. It is worth mentioning that although the increase of r_{vk} causes higher voltage distortion at high loading conditions, since g_{max}=1, the maximum distortion is the same as the fixed resistance case.

The block diagram of the proposed droop scheme is depicted in Fig. 7-3. An absolute value block followed by a max block detects the phase with the largest instantaneous magnitude of current. A classic peak detector [106] then extracts the largest peak of the output currents. The adaptive virtual impedance is calculated according to (7-11) and multiplied by the instantaneous currents to obtain the virtual resistance voltage drop. Finally, the primary control action is achieved by subtracting the virtual resistance drop from the no-load voltage.

7-3-3 Distributed power sharing controller

The adaptive droop method proposed in Section 7-3-2, resolves the challenge of accurate load sharing at high loading conditions to prevent overloading. However, it might be technically or economically desirable to accurately share the active power at low/medium loading conditions as well. To achieve this objective, a novel distributed power sharing control method is proposed in this section.

Assuming the output voltage is aligned with the d-axis, the active power is proportional to the d-axis current. Therefore, it is possible to modify the active power by adjusting the fundamental d-axis current i_{od}^{1+}. On the other hand, due to the resistive nature of the network impedance, i_{od}^{1+} is dependent on the v_{cd}^{1+}. Therefore, it is possible to alter the sharing of active power among the DG units by modifying the v_{cd}^{1+} of the individual units.

The operation of the power sharing controller for a MG comprising of two DG units is illustrated in Fig. 7-4. For simplicity, the DGs are assumed identical and the impedance of line 2 is assumed zero. In case of Fig. 7-4 (a), the voltage correction terms are zero. So, both DG1 (solid line) and DG2 (broken line) droop characteristics start from E_0 and drop with a rate of r_v. However, due to the voltage drop on line 1, the voltage of DG1 is higher. As a result, DG1 supplies a smaller current compared to DG2. In case of Fig. 7-4 (b), a negative voltage correction term is applied to DG2. As a result, the droop characteristic of DG2 is shifted down and even current sharing is achieved.

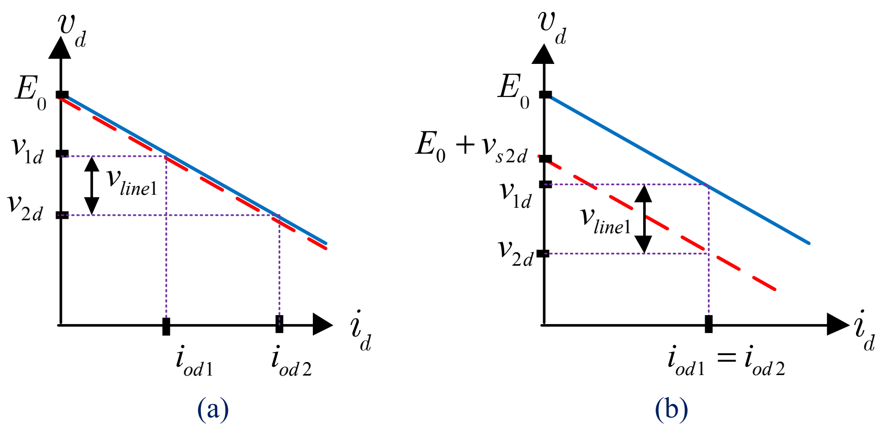

Fig. 7-4 Sharing of d-axis current among two DGs. (a) Before and (b) after adding the voltage correction.

The schematic diagram of the power sharing controller is illustrated in Fig. 7-5. In order to achieve proportional power sharing among the units, the voltage correction term for DG unit i is updated based on the consensus protocol [69]. In this method, each local controller is regarded as a control agent. The information state of agent i, x_i is defined as the normalized active power of the unit:

$$x_i = P_i^{norm} = \frac{P_i}{P_i^{rated}} \tag{7-14}$$

in which P_i and P_i^{rated} refer to the total (fundamental plus harmonic) active power and rated power of unit *i*, respectively. The information states are shared between the agents, through a sparse communication network. The state of each agent is updated based on the received information form the neighbors, as following:

$$v_{si,d} = \int_0^t \sum_{j=1}^{n} a_{ij} \left(x_j(\tau) - x_i(\tau) \right) d\tau \tag{7-15}$$

in which the communication weight, a_{ij} , is a constant positive number if agent *i* receives information from agent *j* and zero, otherwise. If the distributed communication network contains minimum connectivity, all of the states will converge to a common value: $x_0 = x_1 = \ldots = x_n$ [67]. In other words, the load active power will be proportionally shared among the DGs.

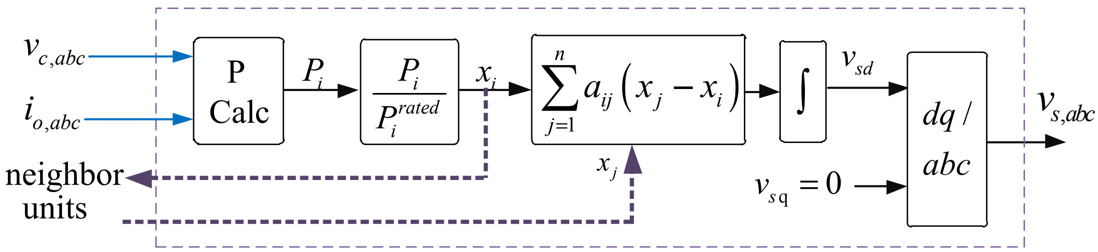

Fig. 7-5 Distributed power sharing controller.

7-3-4 Voltage conditioning module

As shown in Fig. 7-2, the voltage conditioning module is composed of a harmonic extraction block and an integral controller. The harmonic components of the SLB voltage are extracted according to the method proposed in [107]. The compensation signal corresponding to harmonic order *h*, v_{cmp}^h , is then computed by means of an integral controller, as follows:

$$v_{cmp,d}^h = k_c \int \left(v_{refd}^h - v_{SLBd}^h \right) dt \tag{7-16}$$

$$v_{cmp,q}^h = k_c \int \left(v_{refq}^h - v_{SLBq}^h \right) dt \tag{7-17}$$

in which k_c and v_{SLB}^h are the integral controller gain and h^{th} harmonic component of the SLB voltage, respectively. In order to regulate the fundamental voltage at the rated value and eliminate the harmonic distortions, the reference voltage, v_{ref}^h is set as $v_{refd}^{1+} = E_0$, $v_{refq}^{1+} = 0$ for fundamental component and zero for other components. The compensation signals are broadcasted to the DGs. At the DG level, the compensation voltage is transformed back to the *abc* frame and injected to the DG reference voltage.

Since all of the local controllers are synchronized by means of GPS technology, the Park / inverse Park transformation errors, which are addressed in Section 7-2-3 are eliminated. Therefore, all DG units exert an identical compensation voltage, and the current sharing remains unchanged.

7-4 Controller design

The design of the proposed droop controller comprises the selection of the maximum virtual resistance R_v , the droop function $g(.)$, and the time constant of the peak detector. The maximum instantaneous voltage deviation, $\Delta\hat{v}_{\max}$, following a step load change is related to R_v as:

$$\Delta\hat{v}_{\max} = R_v\hat{i}_{o\max} \tag{7-18}$$

Assuming a maximum step load change of 1pu and a maximum voltage deviation of 10%, the maximum virtual resistance is selected as 0.1pu. It is worth mentioning that according to the small signal analysis presented in [46] and [63], a virtual resistance of 0.1pu also satisfies the stability criterion.

The design of the piecewise linear function $g(.)$ involves the selection of a set of breaking points. With the intention of simplifying the implementation while ensuring accurate current sharing at high loading condition, three breaking points are used (points B, C, D), as depicted in Fig. 7-6. For a loading of less than 60% ($\hat{i}_o / I_{\max} < 0.6$), $g(.)$ is fixed at g_B. For higher output currents, the function $g(.)$ is increased until it reaches 1 at 100% loading.

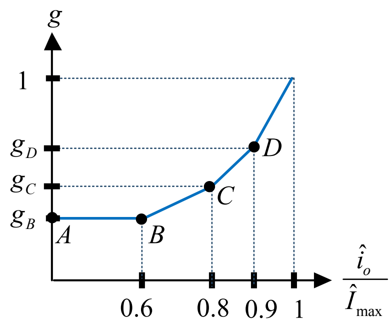

Fig. 7-6 Adaptive virtual resistance function

The values g_B , g_C and g_D are calculated by solving the following optimization problem:

$$\min \quad Cf = \sum_{x\in\{A,B,C,D\}} C_x e_x \tag{7-19}$$

$$st.\ g(0) = g_B, \tag{7-20}$$

$$g(1) = 1, \tag{7-21}$$

where *Cf* is the cost function, C_x and e_x are the penalty factor and current sharing error corresponding with the point *x* (*x*=A,B,C,D), respectively. To emphasize the importance of accurate current sharing at high loading conditions, the penalty factors are selected as $C_A = 1$, $C_B = 2$, $C_C = 4$, $C_D = 16$. Furthermore, the current sharing error is calculated according to (7-13). Solving (7-19) –(7-21) numerically, the values g_A, g_B and g_C are obtained as 0.33, 0.46 and 0.62, respectively.

The peak detector instantaneously increases the adaptive virtual resistance during step load rises. When the load drops, however, the virtual resistance drops with a time constant τ. The parameter τ must be much larger than the time constant of the droop controller as well as the period of the peak current signal to decouple the dynamics of the droop controller from the peak detector and ensure smooth variations of the virtual resistance. On the other hand, the peak detector must be fast enough to allow the virtual resistance settle at steady-state before the next load rise.

The designing of inner control loops and the secondary controller has been addressed in detail in [6, 31, 108].

7-5 Experimental results

The proposed method has been prototyped in the MG laboratory of Aalborg University with a similar setup used in Chapter 3. The schematic diagram and photo of the test bed are shown in Fig. 7-7. The MG supplies a linear balanced load as well as a nonlinear unbalanced load, which is comprised of a single phase rectifier connected between phase *a* and *b*. This MG was assembled based on two experimental setups. Each of the setups is equipped with a GPS receiver and a dSPACE 1006 digital control platform. An Ethernet communication link is used for broadcasting the secondary controller signal to the local controllers.

The specifications of the test bed as well as the control parameters are listed in Table 7-1. The load impedances are selected so that the full load current is close to the inverters rated power. The R/X ratio of lines is selected around 7 to mimic typical low voltage feeders [51]. To model a low bandwidth communication link, the data rate is limited to 100 sample/s and an intentional delay of 10 ms is introduced for each of the links.

The performance of the proposed method is verified under seven different scenarios.

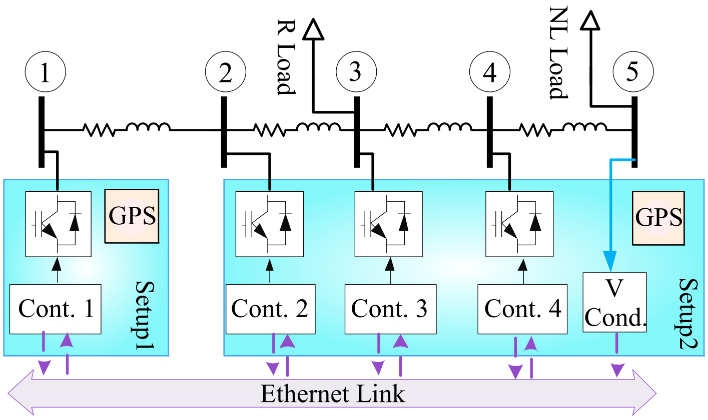

(a)

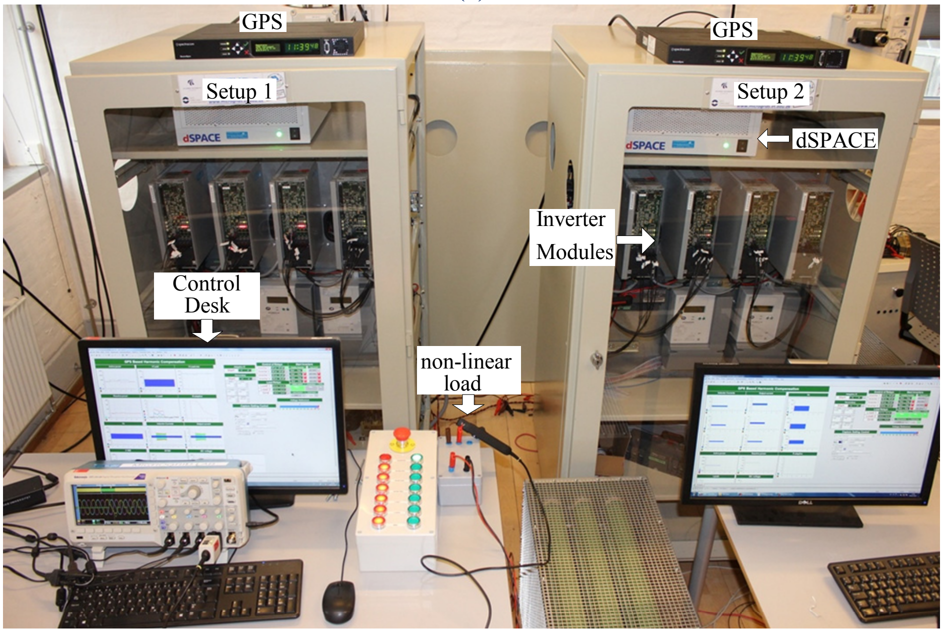

(b)

Fig. 7-7 Laboratory-scale test microgrid: a) schematic diagram, and b) Photo of the setup

Table 7-1 Parameters of the test MG

Description	Parameter	Value	Unit
Resistive Load	R_l	57	Ω
Nonlinear Load (DC side)	R_{NL}	130	Ω
	C_{NL}	115	µF
Line Impedances	$Z_{line1\text{-}2}$	0.22+j0.03	Ω
	$Z_{line2\text{-}3}$	0.22+j0.03	Ω
	$Z_{line3\text{-}4}$	0.5+ j0.06	Ω
	$Z_{line4\text{-}5}$	0.5+j0.06	Ω
Communication rate	f_{com}	100	Sample/s
Communication delay	T_{dcom}	10	ms
V-I droop	R_v	6	Ω
	τ	1	s
Distributed secondary controller gain	a_{ij}	50	V/s
Voltage conditioning gain	k_c	5	1/s

7-5-1 Effect of adaptive virtual resistance and secondary control

In the first study, the effect of the proposed adaptive droop function and secondary controller on the current sharing accuracy and power quality is studied. The experimental results for this case are shown in Fig. 7-8. Prior to t=3s, a fixed virtual resistance is adopted by setting the droop function in equation (11), equal to 1. From Fig. 7-8(a), it is observed that P1, P2, P3, and P4 are 910 W, 960 W, 1020W, 1050W, respectively. Therefore, the DGs which are electrically closer to the load pick up a larger share from the load. The sharing error is also reflected in peak current, as shown in Fig. 7-8(b). The rms voltages at the SLB are within the standard range of 0.95pu to 1.05pu thanks to the smart selection of the virtual resistance. However, as shown in Fig. 7-8(e), the SLB voltage quality is degraded. Particularly, the unbalance factor (UF) is at 2.7%, and the positive and negative sequence components of the third harmonic (H3+ , H3-) are at around 1.7%. Furthermore, the positive and negative components of the fifth harmonic (H5+,H5-) are at around 0.6%, respectively. It is worth mentioning that the higher order harmonics are negligible, hence are not shown for brevity.

Around t=3s, the adaptive virtual resistance is activated. As shown in Fig. 7-8 (c), the DGs which are electrically closer to the load adopt a larger virtual resistance. This way, the adverse effect of line impedances on current sharing accuracy is reduced. As a result, the load sharing accuracy is improved, as depicted in Fig 7-8 (b).

Around t=6s, the secondary controller is activated. Consequently, the SLB voltage is regulated at 1pu and the voltage distortions are eliminated. The harmonic compensation results in an increase of the load current, which in turn causes the DG currents to increase. Consequently, the adaptive virtual resistances are increased to improve the sharing accuracy (See Fig. 7-8 (b)).

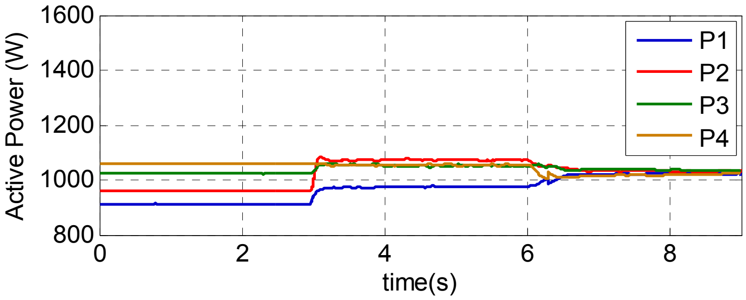

(a)

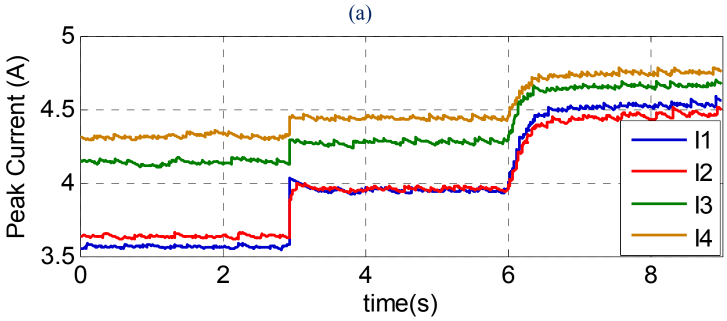

(b)

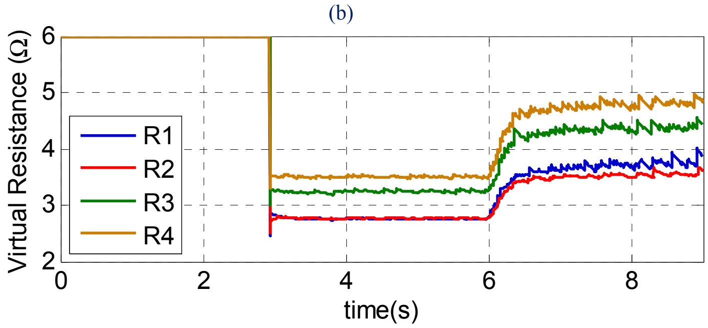

(c)

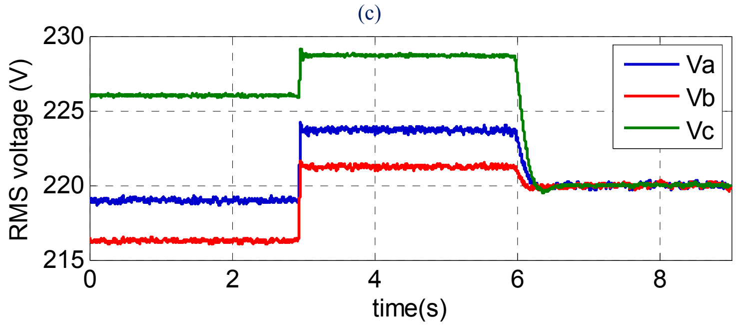

(d)

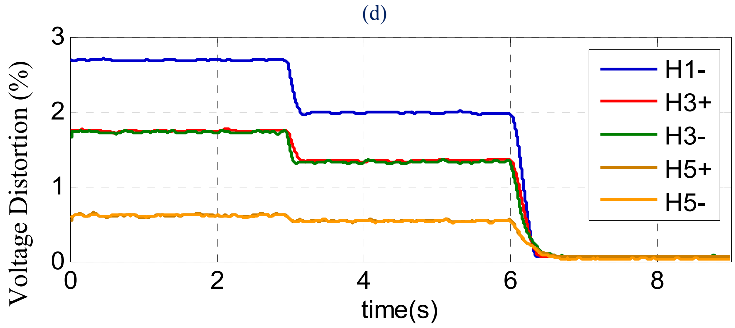

(e)

Fig. 7-8 Experimental results for the first study: a) active power, b) peak current, c) virtual resistance, d) SLB RMS voltage, and e) SLB harmonic distortion

7-5-2 Step load response

In the cases 2,3,4,6 and 7 the nonlinear load is switched on and off to study the step load response. The second case study examines the performance of conventional method based on power droops, which is discussed in Section 7-2-1. The parameters of the conventional method are listed in Table 7-2. The droop coefficients are designed based on the eigenvalue analysis [46] and the virtual resistance is selected so as to limit the voltage deviations within permissible range (0.95-1.05pu). The experimental results for the second study are illustrated in Fig. 7-9. As shown in Figs. 7-9 (a) and (c), DG unit 4, which is electrically closer to the nonlinear load, supplies the largest share of active power (P4) and current (I4) followed by units 3, 2, and 1. In other words, the load sharing is dependent on the electrical distance of the DG units from the load. As a consequence, I4 exceeds the rated value (5A). On the other hand, because reactive power coordination is conducted based on frequency, which is a global parameter as opposed to voltage, reactive power sharing is accurate (see Fig. 7-9 (b)). As shown in Fig. 7-9 (d), the SLB voltage is distorted following the connection of the nonlinear load. As a consequence, the third and fifth harmonic of line *ab* are increased to 2.8% and 1.2%, respectively (See Fig. 7-9 (e)). Furthermore, the THD is around 3.2%, 1.5% and 1.8% for lines *ab*, *bc* and *ca*, respectively.

Table 7-2 Control parameters of the virtual resistance method

Description	**Value**	**Unit**
P-V droop coefficient	0.0075	V/W
Q-f droop coefficient	0.00001	Hz/W
Virtual resistance	3	Ω

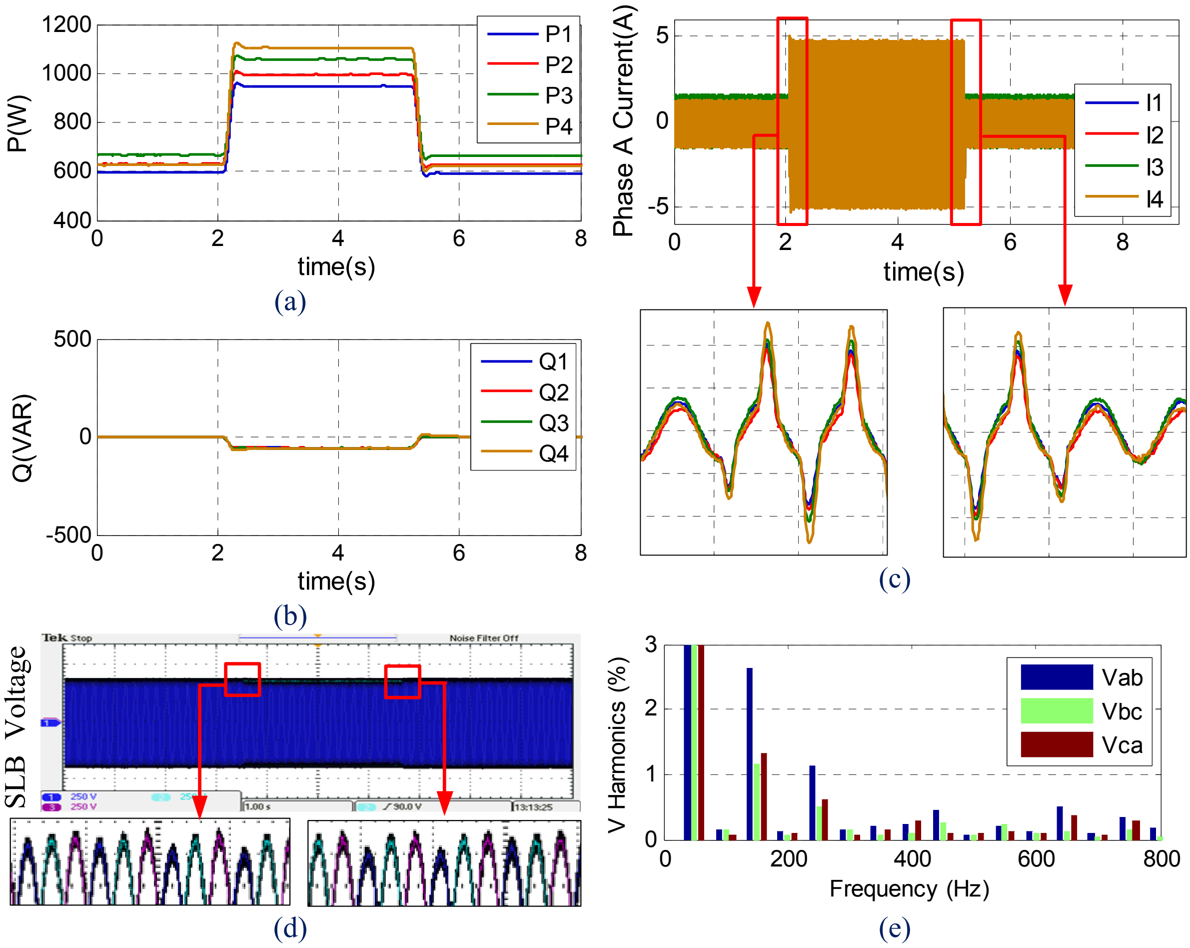

Fig. 7-9 Step load response of the conventional method: a) Active power, b) Reactive power, c) DG currents, d) SLB voltage, and e) Voltage harmonics

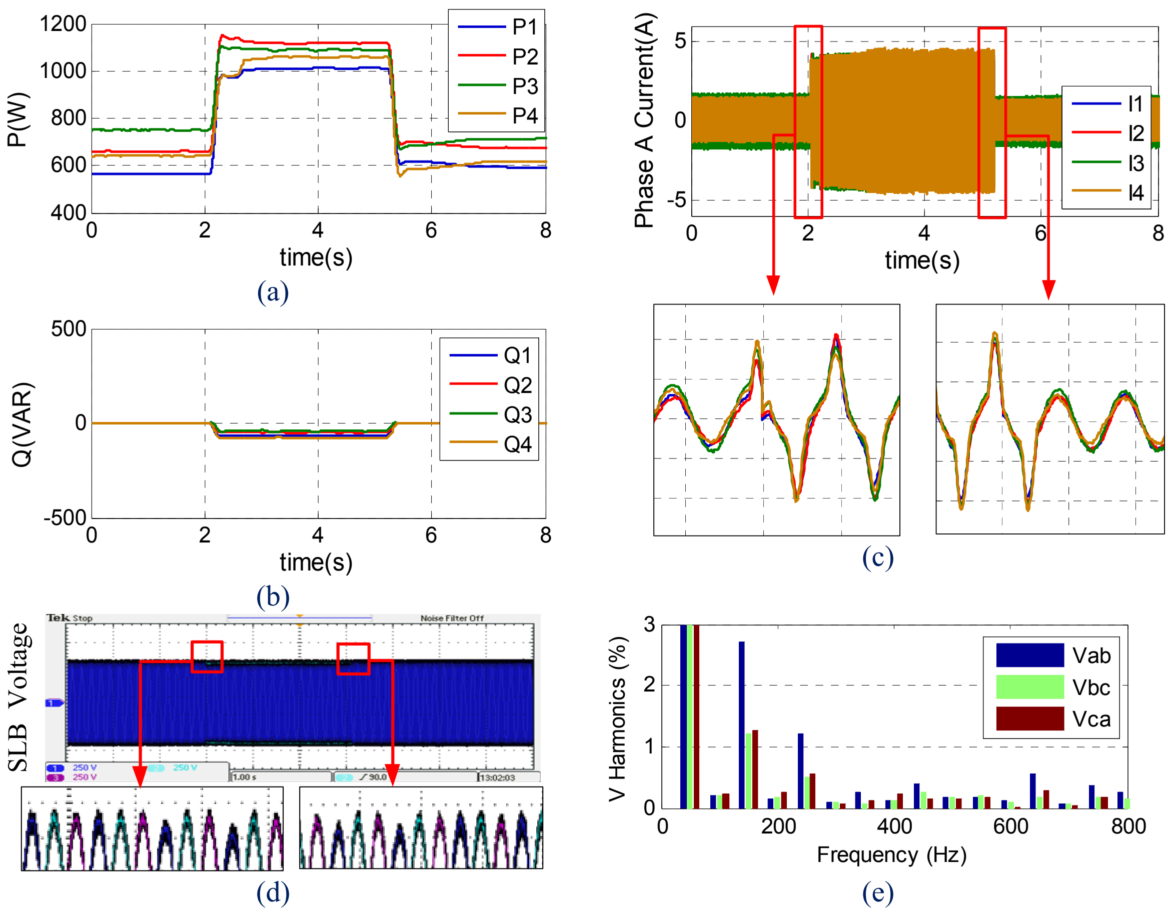

Fig. 7-10 Step load response of the proposed droop method without secondary control: a) Active powers, b) Reactive powers, c) Phase *a* currents, d) SLB voltage, and e) Voltage harmonics

In the third case, the step load change response of the proposed droop method without secondary control layer is investigated. The experimental results for the third case are illustrated in Fig. 7-10. Comparing Fig. 7-9 (c) and 7-10(c) reveals the improved current sharing accuracy of the proposed droop method. The enhanced current sharing is achieved by adaptive adjustment of virtual resistances according to the output current. Specifically, the virtual resistance of unit 4 is increased above other units, which results in the decrease of P4 below P3 and P2 (see Fig. 7-10 (a)). As shown in Fig. 7-10 (b), although reactive power sharing is not ideal, the sharing error is less than 0.01pu. Moreover, the voltage harmonics are almost the same as the conventional method, as shown in Figs. 9 (d) and (e).

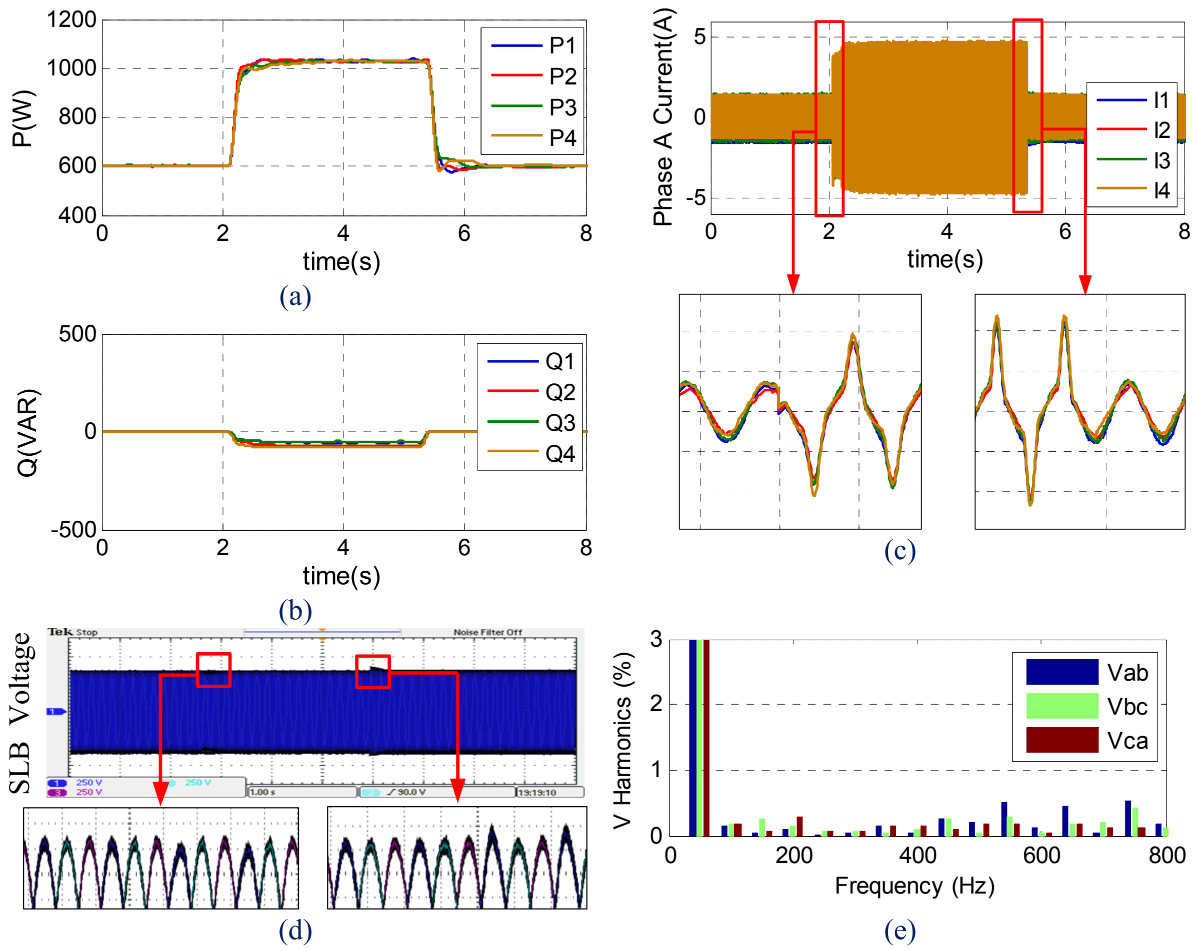

Fig. 7-11 Step load response of the proposed method: a) Active powers, b) Reactive powers, c) Phase *a* currents, d) SLB voltage, and e) Voltage harmonics

In the fourth case, the proposed method with secondary control layer is tested. The experimental results for this case are shown in Fig. 7-11. Comparison of Fig. 7-10 (a) and 7-11 (a) reveals that the secondary control scheme improves the accuracy of active power sharing. Since the dynamics of the secondary control layer are relatively slow, the SLB voltage experiences transient distortions following the load changes (see Fig. 7-11(d)). However, the instantaneous voltages are within the permissible range of 0.95pu to 1.05pu.

Furthermore, as shown in Fig. 7-11 (e), the third and fifth harmonics of the SLB voltage are eliminated in the steady-state. As a result, the voltage THD corresponding to lines *ab*, *bc* and *ca* is reduced from 3.3%, 1.5% and 1.8% in the third case to 1 %, 0.8% and 0.85%, respectively.

7-5-3 Plug and play operation

The fifth study demonstrates the Plug and Play (P'n'P) feature of the proposed strategy. In this scenario, the DG unit 4 is disconnected from and reconnected to the MG at t=1s and t=6.5s, respectively. As shown in Fig. 7-12 (a) and (b), following the outage of unit 4, the power and current of units 1-3 are increased to maintain the load/generation balance. It is worth mentioning that although unit 4 is electrically disconnected from the MG but its voltage remains synchronized with the grid thanks to the GPS synchronization technology. This facilitates the reconnection of unit 4 and ensures a smooth reconnection. From Fig. 7-12 (c) and (d) it is observed that the voltage deviation and harmonic distortion exhibit a small increase during the transients but are changed back to zero within less than a second.

7-5-4 Effect of network impedance

Although the proposed droop control method is developed for MGs with low X/R ratio, it is also applicable to the MGs with inductive network impedance. In the sixth case, the effect of network X/R ratio on the current sharing accuracy is investigated by performing the step load change test under the following conditions: 1) lines are modeled by 0.22Ω resistors, 2) lines are modeled by 0.5mH inductors. The experimental results for the resistive and inductive line cases are shown in Fig. 7-13 (a) and (b), respectively. It is observed that in case of inductive network, I4 contains more distortion compared to other units. The reason is the degraded current sharing accuracy at high order harmonics due to the larger line impedance at higher frequencies. Nevertheless, the peak current of all units are almost the same in both resistive and inductive cases. Therefore, overcurrent stresses are prevented regardless of the network X/R ratio.

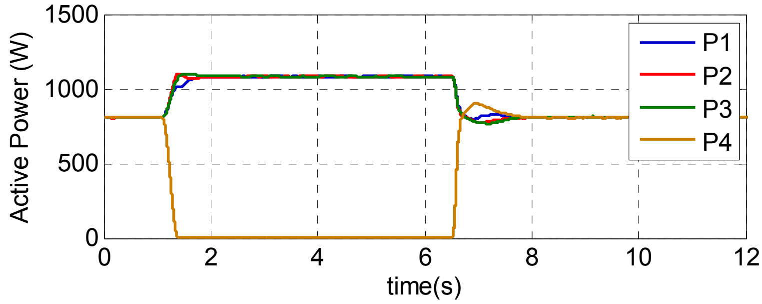

(a)

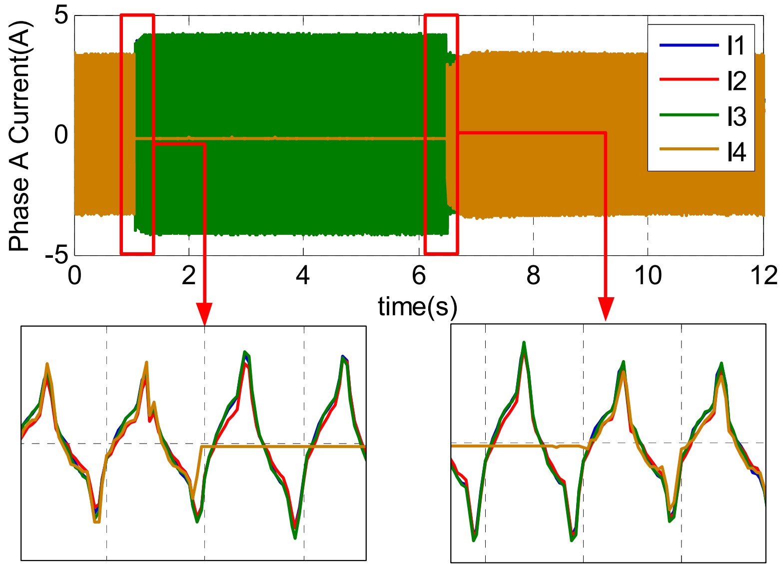

(b)

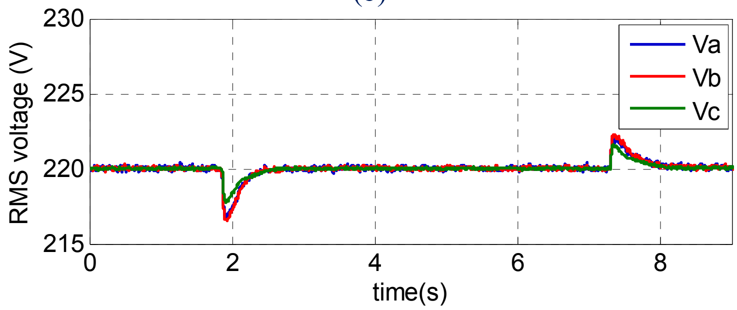

(c)

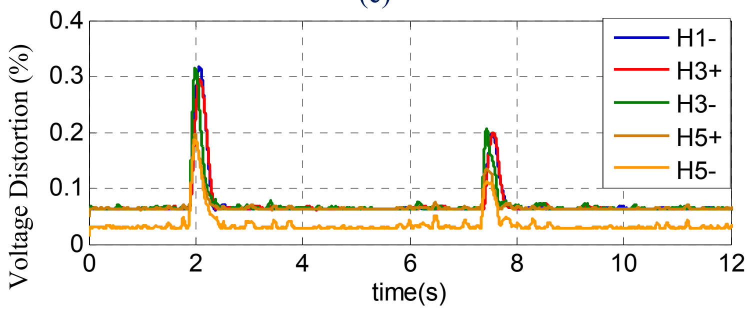

(d)

Fig. 7-12 Response of the proposed method to outage and reconnection of unit 4: a) active powers, b) current waveforms, and c) RMS voltage and d) harmonic distortion

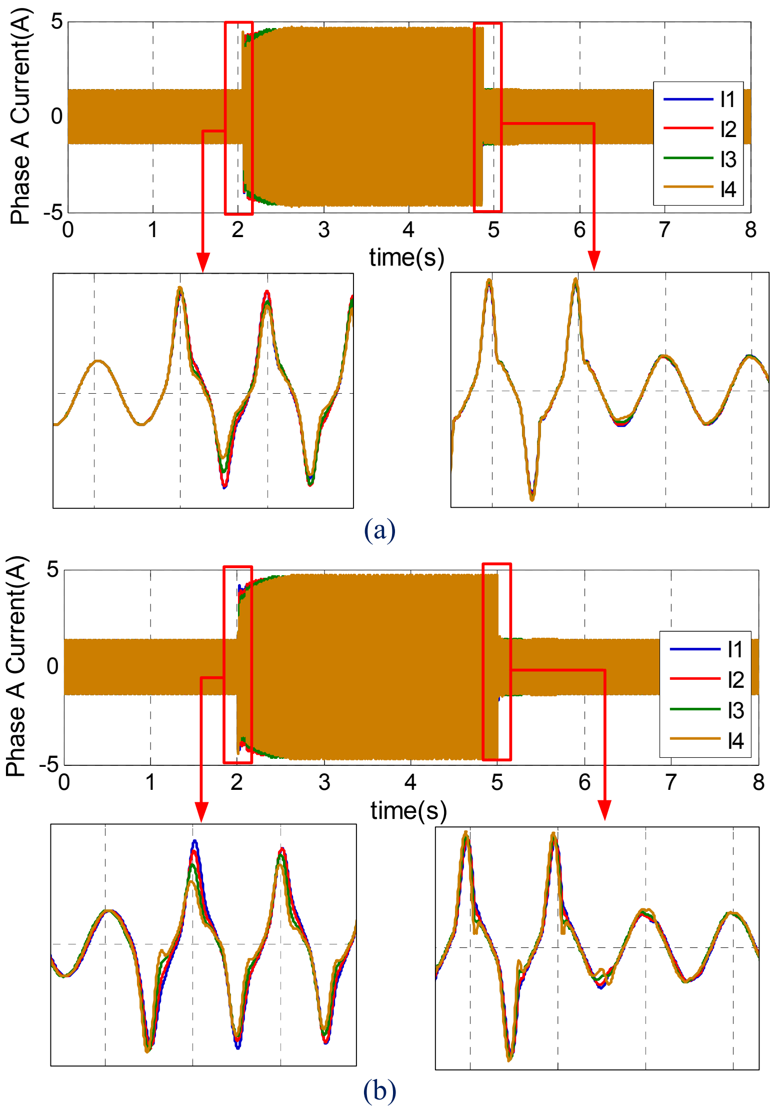

Fig. 7-13 Effect of network impedance on the performance of the proposed method: a) resistive network and b) inductive network.

7-5-5 Effect of communication delays

In the last case, the effect of communication delays on the step load response is studied. To that end, the communication delay is increased from 10ms to 100ms and 200ms and the step load change test is repeated. As illustrated in Fig. 7-14, although the increase of communication delay slows down the distributed secondary controller, but the proposed method exhibits an acceptable performance for delays of up to 200ms. It should be pointed out that modern communication technologies exhibit a much smaller delay (around 10-40ms) [109].

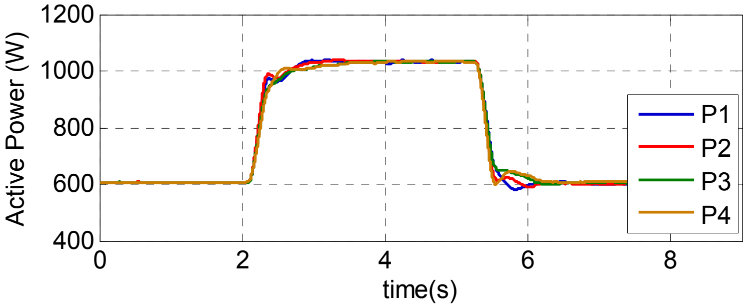

(a)

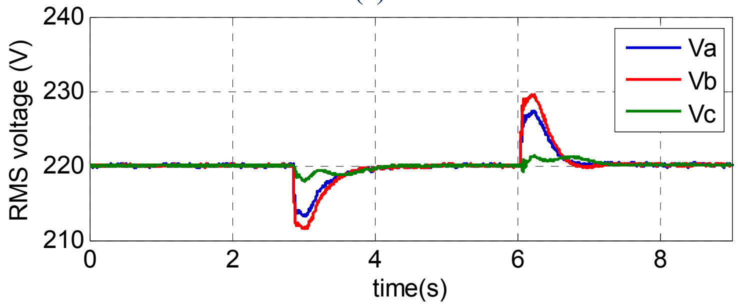

(b)

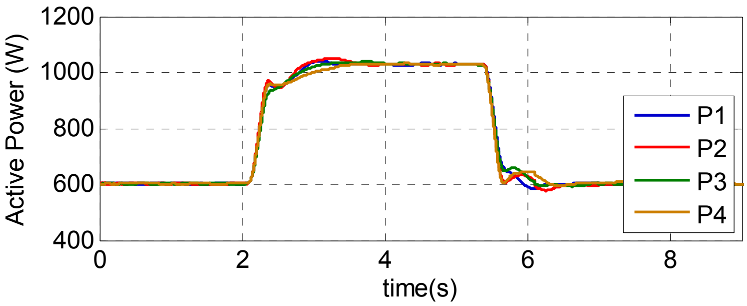

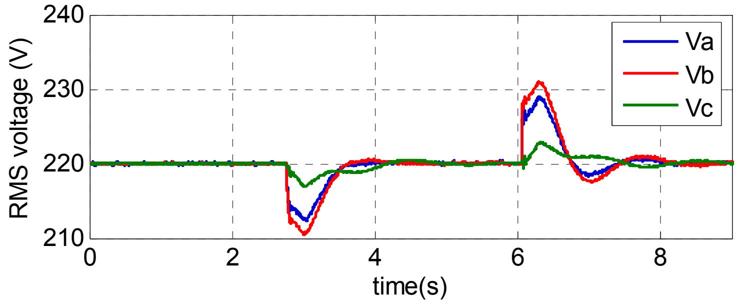

(b)

Fig. 7-14 Performance of proposed control method under different communication delays. (a) and (b) 100 ms (c) and (d) 200 ms

7-6 Summary and conclusions

The islanded MGs solely rely on the local DG units for voltage support and load/generation balance. On the other hand, the individual power electronic interfaced DG units have a relatively small capacity and are susceptible to overcurrent stresses. Therefore, an accurate load sharing strategy is crucial to prevent activating the overcurrent protection systems and possible damages.

In this chapter, a new hierarchical control structure is proposed for improving power quality and current sharing accuracy of MGs. The control framework is comprised of primary level, which is responsible for fast and accurate sharing of instantaneous load current among the DG units and the secondary control, which facilitates accurate sharing of active power as well as compensating voltage distortions caused by nonlinear and unbalanced load currents. The proposed control framework takes advantage of GPS timing technology as a means for achieving fixed frequency operation and eliminating the transformation errors resulting from Park / inverse Park Transformations.

The proposed control architecture is independent of the system topology and does not require knowledge of line impedances. Since the current sharing is managed by the primary control level, which has a fast dynamic response, transient currents are also properly shared among the units. On the other hand, the large time constant of the secondary level enables implementation of the method with a low bandwidth communication network. Experimental results demonstrate the efficacy of the presented approach in terms of current sharing accuracy and power quality.

Chapter 8

Conclusions and Future Work

8-1 Conclusions

In this thesis, a new droop control technique based on voltage-current characteristics was proposed to enhance the dynamic response of low voltage MGs. Furthermore, the proposed droop method is used as the basis for the development of more advanced decentralized and distributed control schemes, which pursue improvement of robustness, flexibility and power quality. The summarized conclusions of the thesis are listed in the following.

The conventional droop method is based on governor systems used for frequency control in power systems. Because of the substantial differences between low voltage MGs and power systems (R/X ratio, inertia of the generations, load characteristics), the conventional method does not exhibit a satisfactory dynamic response in low-voltage MGs.

In Chapter 2, a new droop control scheme is proposed to enhance the dynamic response of load sharing in MGs. In this method, GPS timing technology is used to synchronize the time reference of each DER unit with the universal coordinated time. This way, the frequency can be fixed at the rated value. Furthermore, the reference voltage of each DER is drooped versus its current. This strategy eliminates the delay associated with measurement of power in conventional droop method and hence results in a significant improvement in the dynamic response.

The integration of GPS technology in the proposed control method as well as other recent work [33, 38, 39, 110] boosts the power quality and simplifies plug and play operation. However, the GPS-based control schemes are vulnerable to GPS signal failure. In Chapter 3 of the thesis, a new synchronization strategy is proposed to enhance the robustness of the V-I droop method with respect to GPS signal failure. By using an adaptive Q-f droop controller as a backup, each DER is able to remain synchronized with the rest of the MG during GPS signal interruptions.

Generally, the accuracy of active and/or reactive power sharing of droop schemes is dependent on the line impedances. Furthermore, the droop characteristics change the voltage magnitude with the load, which degrades the power quality. In Chapter 4 of the thesis, a distributed secondary control method is presented to enhance voltage regulation and improve the sharing accuracy. Unlike the existing secondary control methods, the proposed scheme takes into account the high R/X ratio of line impedances in low voltage MGs.

The operation of MGs is affected by the limitations of energy resources. Specifically, if the DER is supplied by a combination of PV and battery storage, SoC of batteries and the intermittency of the PV should be considered in the power sharing policy. In Chapter 5, a distributed control framework is proposed to manage the sharing of power among the ESUs so as to balance the SoCs. In addition, PV curtailment and load shedding are deployed to protect the ESUs from deep discharging and overcharging. Therefore, safe operation of the ESUs and associated DC/DC and DC/AC converters is guaranteed.

Unbalanced and nonlinear loads, which are common in low voltage MGs degrade the power quality. In addition, sharing of negative sequence and harmonic components of the load current is a challenging task. In Chapter 6, a model predictive supplementary droop controller is introduced as a mechanism for limiting the current and active power to the rated value and reducing the voltage unbalance.

In Chapter 7, a hierarchical control framework comprising of primary and secondary control levels is proposed for accurate load sharing and power quality improvement in MGs. At the primary level, modified V-I droop characteristics is introduced to enable accurate sharing of instantaneous current among the DER units. The secondary level facilitates accurate sharing of active power as well as compensating voltage distortions. The distinctive feature of this control strategy compared to the existing hierarchical schemes is simple structure, emphasis on the instantaneous current sharing and elimination of the transformation errors resulting from Park / inverse Park Transformations.

It is worth mentioning the challenges faced during this PhD project. The first challenge was the development of a decentralized control method, which is in accordance with the fast dynamics of the inverter-based DERs and has a simple structure. The solution was V-I droop scheme, which addresses the aforementioned objectives by employing current sharing instead of power sharing. Another problem was definition of a suitable plant model for the MPC controller. From practical point of view, experimental implementation of GPS synchronization was an important issue. While the GPS receivers and dSPACE controllers were available on the market, there was neither any standard hardware nor software available for interconnecting dSPACE with the GPS receiver. To solve this issue, an interface board was designed and implemented to enable connection of the 1-pps signal of the GPS to one of the digital inputs of the dSPACE controller. Furthermore, an S-function was developed in MATLAB and included in the Simulink model to enable time synchronization.

8-2 Scope of the future work

This research work opens up a new approach for load sharing and voltage control in low voltage islanded MGs. There is more to explore in this line of research. Suggested research work is listed below.

8-2-1 Network-based time synchronization

The proposed approach makes use of GPS technology for time synchronization. Another approach is to use communication networks to synchronize the inverter units. In this method, a control unit broadcasts a time stamp signal to another unit. The received signal is then used to align the local time of the second unit with the first one. To improve the synchronization accuracy, the time delay corresponding with transmitter, receiver and also time of arrival of the signal can be estimated and compensated by the receiver.

The network-based synchronization method has been widely utilized in wireless sensor networks [111]. Nevertheless, the applicability of this method to MG control applications is yet to be investigated. The main issues in this line of work are the accuracy of timing, cost of implementation, reliability and expandability.

8-2-2 V-I droop method for active distribution networks

The thesis is mainly focused on the islanded MGs, which are limited in size and power capacity. However, the V-I droop concept can also be applied to active distribution networks, which include several MG clusters. In that sense, the DERs can be coordinated by some form of modified V-I droop function. Furthermore, by using GPS technology, the MG clusters remain synchronized with the rest of the network. This way, each of the clusters can be connected/disconnected from the system without incurring transient current overshoot and/or oscillations.

8-2-3 GPS synchronization for both control and protection

GPS technology is well-known in power industry for its application in protection systems. In this context, GPS receivers are used as the core of phase measurement units (PMUs), which are interconnected together through communication links. A supervisor receives the measured phase angles and calculates the state of the system.

On the other hand, the V-I droop method suggests the integration of GPS timing technology into each of the DER units. In addition to advantages provided in terms of control, GPS technology provides the backbone for the realization of sophisticated and advanced protection schemes in which each DER serves as a PMU.

References

[1] A. Purvins, H. Wilkening, G. Fulli, E. Tzimas, G. Celli, S. Mocci*, et al.*, "A European supergrid for renewable energy: local impacts and far-reaching challenges," *Journal of Cleaner Production,* vol. 19, pp. 1909-1916, 11 2011.

[2] P. Basak, S. Chowdhury, S. Halder nee Dey, and S. P. Chowdhury, "A literature review on integration of distributed energy resources in the perspective of control, protection and stability of microgrid," *Renewable and Sustainable Energy Reviews,* vol. 16, pp. 5545-5556, 10// 2012.

[3] C. Ahumada, R. Cardenas, D. Saez, and J. M. Guerrero, "Secondary Control Strategies for Frequency Restoration in Islanded Microgrids With Consideration of Communication Delays," *Smart Grid, IEEE Transactions on,* vol. PP, pp. 1-1, 2015.

[4] A. Bidram and A. Davoudi, "Hierarchical Structure of Microgrids Control System," *IEEE Trans. Smart Grid,* vol. 3, pp. 1963-1976, May 2012.

[5] A. Bidram, A. Davoudi, and F. L. Lewis, "A Multiobjective Distributed Control Framework for Islanded AC Microgrids," *Industrial Informatics, IEEE Transactions on,* vol. 10, pp. 1785-1798, Aug. 2014.

[6] Q. Shafiee, J. M. Guerrero, and J. C. Vasquez, "Distributed Secondary Control for Islanded Microgrids-A Novel Approach," *Power Electronics, IEEE Transactions on,* vol. 29, pp. 1018-1031, Feb. 2014.

[7] A. Bidram, F. L. Lewis, and A. Davoudi, "Distributed Control Systems for Small-Scale Power Networks: Using Multiagent Cooperative Control Theory," *Control Systems, IEEE,* vol. 34, pp. 56-77, Dec. 2014.

[8] W. Dan, T. Dragicevic, J. C. Vasquez, J. M. Guerrero, and G. Yajuan, "Secondary coordinated control of islanded microgrids based on consensus algorithms," in *Proc. Energy Conv. Cong. Expo. (ECCE)*, 2014, pp. 4290-4297.

[9] C. Ahumada, R. Cardenas, D. Saez, and J. M. Guerrero, "Secondary Control Strategies for Frequency Restoration in Islanded Microgrids With Consideration of Communication Delays," *Smart Grid, IEEE Transactions on,* 2015.

[10] J. Schiffer, T. Seel, J. Raisch, and T. Sezi, "Voltage Stability and Reactive Power Sharing in Inverter-Based Microgrids With Consensus-Based Distributed Voltage Control," *Control Systems Technology, IEEE Transactions on,* vol. PP, pp. 1-1, Apr. 2015.

[11] X. Yinliang, Z. Wei, G. Hug, S. Kar, and L. Zhicheng, "Cooperative Control of Distributed Energy Storage Systems in a Microgrid," *Smart Grid, IEEE Transactions on,* vol. 6, pp. 238-248, Jan. 2015.

[12] Y. Wang, K. T. Tan, X. Y. Peng, and P. L. So, "Coordinated Control of Distributed Energy Storage Systems for Voltage Regulation in Distribution Networks," *Power Delivery, IEEE Transactions on,* vol. PP, pp. 1-1, 2015.

[13] G. Mokhtari, G. Nourbakhsh, and A. Ghosh, "Smart Coordination of Energy Storage Units (ESUs) for Voltage and Loading Management in Distribution Networks," *IEEE Trans. Power Syst.,* vol. 28, pp. 4812-4820, Nov. 2013.

[14] Q. Shafiee, T. Dragicevic, F. Andrade, J. C. Vasquez, and J. M. Guerrero, "Distributed consensus-based control of multiple DC-microgrids clusters," in *Proc. 40th Annu. Conf. IEEE Ind. Electron. Soc. (IECON)*, 2014, pp. 2056-2062.

[15] L. Chendan, T. Dragicevic, J. C. Vasquez, J. M. Guerrero, and E. A. A. Coelho, "Multi-agent-based distributed state of charge balancing control for distributed energy storage units in AC microgrids," in *Proc. 30th IEEE Appl. Power Electron. Conf. Expo. (APEC)*, 2015, pp. 2967-2973.

[16] Q. Shafiee, T. Dragicevic, J. C. Vasquez, and J. M. Guerrero, "Hierarchical Control for Multiple DC-Microgrids Clusters," *Energy Conversion, IEEE Transactions on,* vol. 29, pp. 922-933, Dec. 2014.

[17] M. B. Delghavi and A. Yazdani, "Islanded-Mode Control of Electronically Coupled Distributed-Resource Units Under Unbalanced and Nonlinear Load Conditions," *IEEE Trans. Power Del.,* vol. 26, pp. 661-673, Apr. 2011.

[18] D. De and V. Ramanarayanan, "Decentralized Parallel Operation of Inverters Sharing Unbalanced and Nonlinear Loads," *IEEE Trans. Power Electron.,* vol. 25, pp. 3015-3025, Dec. 2010.

[19] M. Hamzeh, H. Karimi, and H. Mokhtari, "Harmonic and Negative-Sequence Current Control in an Islanded Multi-Bus MV Microgrid," *IEEE Trans. Smart Grid,* vol. 5, pp. 167-176, Jan. 2014.

[20] M. Hamzeh, H. Karimi, and H. Mokhtari, "A New Control Strategy for a Multi-Bus MV Microgrid Under Unbalanced Conditions," *IEEE Trans. Power Syst.,* vol. 27, pp. 2225-2232, Nov. 2012.

[21] L. Quanwei, T. Yong, L. Xunhao, D. Yan, and H. Xiangning, "Voltage unbalance and harmonics compensation for islanded microgrid inverters," *Power Electronics, IET,* vol. 7, pp. 1055-1063, May 2014.

[22] M. Savaghebi, A. Jalilian, J. C. Vasquez, and J. M. Guerrero, "Autonomous Voltage Unbalance Compensation in an Islanded Droop-Controlled Microgrid," *IEEE Trans. Ind. Electron.,* vol. 60, pp. 1390-1402, Nov. 2013.

[23] R. Majumder, A. Ghosh, G. Ledwich, and F. Zare, "Load sharing and power quality enhanced operation of a distributed microgrid," *Renewable Power Generation, IET,* vol. 3, pp. 109-119, Jun. 2009.

[24] Y. A. R. I. Mohamed and E. F. El-Saadany, "Adaptive Decentralized Droop Controller to Preserve Power Sharing Stability of Paralleled Inverters in Distributed Generation Microgrids," *IEEE Trans. Power Electron.,* vol. 23, pp. 2806-2816, Nov. 2008.

[25] J. M. Guerrero, J. Matas, V. Luis Garcia de, M. Castilla, and J. Miret, "Decentralized Control for Parallel Operation of Distributed Generation Inverters Using Resistive Output Impedance," *IEEE Trans. Ind. Electron.,* vol. 54, pp. 994-1004, Apr. 2007.

[26] L. Yun Wei and K. Ching-Nan, "An Accurate Power Control Strategy for Power-Electronics-Interfaced Distributed Generation Units Operating in a Low-Voltage Multibus Microgrid," *IEEE Trans. Power Electron.,* vol. 24, pp. 2977-2988, Dec. 2009.

[27] J. M. Guerrero, V. Luis Garcia de, J. Matas, M. Castilla, and J. Miret, "Output Impedance Design of Parallel-Connected UPS Inverters With Wireless Load-Sharing Control," *IEEE Transactions on Industrial Electronics,* vol. 52, pp. 1126-1135, Aug. 2005.

[28] M. Savaghebi, J. C. Vasquez, A. Jalilian, J. M. Guerrero, and T. L. Lee, "Selective harmonic virtual impedance for voltage source inverters with LCL filter in microgrids," in *Energy Conversion Congress and Exposition (ECCE), 2012 IEEE*, 2012, pp. 1960-1965.

[29] A. Micallef, M. Apap, C. Spiteri-Staines, and J. M. Guerrero, "Mitigation of Harmonics in Grid-Connected and Islanded Microgrids Via Virtual Admittances and Impedances," *IEEE Transactions on Smart Grid,* p. Early access, 2015.

[30] P. Sreekumar and V. Khadkikar, "A New Virtual Harmonic Impedance Scheme for Harmonic Power Sharing in an Islanded Microgrid," *IEEE Transactions on Power Delivery,* vol. Early access, 2015.

[31] M. Savaghebi, A. Jalilian, J. C. Vasquez, and J. M. Guerrero, "Secondary Control for Voltage Quality Enhancement in Microgrids," *IEEE Trans. Smart Grid,* vol. 3, pp. 1893-1902, Jul. 2012.

[32] K. De Brabandere, B. Bolsens, J. Van den Keybus, A. Woyte, J. Driesen, and R. Belmans, "A Voltage and Frequency Droop Control Method for Parallel Inverters," *Power Electronics, IEEE Transactions on,* vol. 22, pp. 1107-1115, 2007.

[33] R. Majumder, A. Ghosh, G. Ledwich, and F. Zare, "Angle droop versus frequency droop in a voltage source converter based autonomous microgrid," in *Proc. Power & Energy Society General Meeting*, 2009, pp. 1-8.

[34] E. Rokrok and M. E. H. Golshan, "Adaptive voltage droop scheme for voltage source converters in an islanded multibus microgrid," *Generation, Transmission & Distribution, IET,* vol. 4, pp. 562-578, 2010.

[35] R. Majumder, B. Chaudhuri, A. Ghosh, R. Majumder, G. Ledwich, and F. Zare, "Improvement of Stability and Load Sharing in an Autonomous Microgrid Using Supplementary Droop Control Loop," *IEEE Trans. Power Syst.,* vol. 25, pp. 796-808, May 2010.

[36] M. B. Delghavi and A. Yazdani, "An Adaptive Feedforward Compensation for Stability Enhancement in Droop-Controlled Inverter-Based Microgrids," *Power Delivery, IEEE Transactions on,* vol. 26, pp. 1764-1773, 2011.

[37] R. Majumder, A. Ghosh, G. Ledwich, and F. Zare, "Enhancing stability of an autonomous microgrid using a gain scheduled angle droop controller with derivative feedback," *International Journal of Emerging Electric Power Systems,* vol. 10, pp. 1-30, Jan. 2010.

[38] A. H. Etemadi, E. J. Davison, and R. Iravani, "A Decentralized Robust Control Strategy for Multi-DER Microgrids - Part I: Fundamental Concepts," *Power Delivery, IEEE Transactions on,* vol. 27, pp. 1843-1853, Sept. 2012.

[39] S. Riverso, F. Sarzo, and G. Ferrari-Trecate, "Plug-and-Play Voltage and Frequency Control of Islanded Microgrids With Meshed Topology," *Smart Grid, IEEE Transactions on,* vol. 6, pp. 1176-1184, May 2015.

[40] A. Ipakchi and F. Albuyeh, "Grid of the future," *Power and Energy Magazine, IEEE,* vol. 7, pp. 52-62, 2009.

[41] F. Katiraei, M. R. Iravani, and P. W. Lehn, "Small-signal dynamic model of a micro-grid including conventional and electronically interfaced distributed resources," *Generation, Transmission Distribution, IET,* vol. 1, pp. 369-378, May 2007.

[42] T. Dragicevic, J. M. Guerrero, J. C. Vasquez, and D. Skrlec, "Supervisory Control of an Adaptive-Droop Regulated DC Microgrid With Battery Management Capability," *Power Electronics, IEEE Transactions on,* vol. 29, pp. 695-706, 2014.

[43] A. Bidram and A. Davoudi, "Hierarchical Structure of Microgrids Control System," *Smart Grid, IEEE Transactions on,* vol. 3, pp. 1963-1976, 2012.

[44] S. M. Ashabani and Y. A. R. I. Mohamed, "General Interface for Power Management of Micro-Grids Using Nonlinear Cooperative Droop Control," *Power Systems, IEEE Transactions on,* vol. 28, pp. 2929-2941, 2013.

[45] A. Haddadi, A. Yazdani, G. Joos, and B. Boulet, "A Gain-Scheduled Decoupling Control Strategy for Enhanced Transient Performance and Stability of an Islanded Active Distribution Network," *Power Delivery, IEEE Transactions on,* vol. 29, pp. 560-569, 2014.

[46] M. S. Golsorkhi and D. D. C. Lu, "A Control Method for Inverter-Based Islanded Microgrids Based on V-I Droop Characteristics," *Power Delivery, IEEE Transactions on,* vol. 30, pp. 1196-1204, Jun. 2015.

[47] M. S. Golsorkhi and D. D. C. Lu, "A decentralized power flow control method for islanded microgrids using V-I droop," in *Proc. Iranian Conference on Electrical Engineering (ICEE)*, 2014, pp. 604-609.

[48] J. J. Grainger, *Power System Analysis*: McGraw-Hill Education 2003.

[49] P. Kundur, *Power System Stability And Control*: McGraw-Hill Education 1994.

[50] J. Rocabert, A. Luna, F. Blaabjerg, Rodri, x, and P. guez, "Control of Power Converters in AC Microgrids," *Power Electronics, IEEE Transactions on,* vol. 27, pp. 4734-4749, 2012.

[51] A. Engler and N. Soultanis, "Droop control in LV-grids," in *Future Power Systems, 2005 International Conference on*, 2005, pp. 6 pp.-6.

[52] R. Majumder, "Some Aspects of Stability in Microgrids," *Power Systems, IEEE Transactions on,* vol. 28, pp. 3243-3252, 2013.

[53] P. H. Divshali, A. Alimardani, S. H. Hosseinian, and M. Abedi, "Decentralized Cooperative Control Strategy of Microsources for Stabilizing Autonomous VSC-Based Microgrids," *Power Systems, IEEE Transactions on,* vol. 27, pp. 1949-1959, 2012.

[54] H. Jinwei, L. Yun Wei, J. M. Guerrero, F. Blaabjerg, and J. C. Vasquez, "An Islanding Microgrid Power Sharing Approach Using Enhanced Virtual Impedance Control Scheme," *Power Electronics, IEEE Transactions on,* vol. 28, pp. 5272-5282, Nov. 2013.

[55] W. Lewandowski, J. Azoubib, and W. J. Klepczynski, "GPS: primary tool for time transfer," *Proceedings of the IEEE,* vol. 87, pp. 163-172, 1999.

[56] S. M. Lasassmeh and J. M. Conrad, "Time synchronization in wireless sensor networks: A survey," in *IEEE SoutheastCon 2010 (SoutheastCon), Proceedings of the*, 2010, pp. 242-245.

[57] M. Jaya Bharata Reddy, D. V. Rajesh, P. Gopakumar, and D. K. Mohanta, "Smart Fault Location for Smart Grid Operation Using RTUs and Computational Intelligence Techniques," *Systems Journal, IEEE,* vol. 8, pp. 1260-1271, 2014.

[58] P. Moore and P. Crossley, "GPS applications in power systems. I. Introduction to GPS," *Power Engineering Journal,* vol. 13, pp. 33-39, 1999.

[59] Y. Quan and G. Liu, "Compensation Local Clock_s Drift by Timestamp Stream," in *Proc. Innovative Computing, Information and Control*, 2007, pp. 524-524.

[60] M. Bollen, Z. Jin, O. Samuelsson, and J. Bjornstedt, "Performance indicators for microgrids during grid-connected and island operation," in *PowerTech, 2009 IEEE Bucharest*, 2009, pp. 1-6.

[61] H. N. Papathanassiou S, Strunz K., "A benchmark low voltage microgrid network", CIGRE symposium on power systems with dispersed generation, 2005, p. 1–8.

[62] P. Karlsson and J. Svensson, "DC bus voltage control for a distributed power system," *Power Electronics, IEEE Transactions on,* vol. 18, pp. 1405-1412, 2003.

[63] M. Golsorkhi, D. Lu, and J. Guerrero, "A GPS-Based Decentralized Control Method for Islanded Microgrids," *IEEE Transactions on Power Electronics,* Apr. 2016.

[64] R. Teodorescu, F. Blaabjerg, M. Liserre, and P. C. Loh, "Proportional-resonant controllers and filters for grid-connected voltage-source converters," *Electric Power Applications, IEE Proceedings,* vol. 153, pp. 750-762, 2006.

[65] J. M. Guerrero, M. Chandorkar, T. Lee, and P. C. Loh, "Advanced Control Architectures for Intelligent Microgrids ; Part I: Decentralized and Hierarchical Control," *IEEE Trans. Ind. Electron.,* vol. 60, pp. 1254-1262, April 2013.

[66] C. W. F. Guo, J. Mao and Y.-D. Song, "Distributed Secondary Voltage and Frequency Restoration Control of Droop-Controlled Inverter-Based Microgrids," *IEEE Trans. Ind. Electron.,* vol. vol. 62, no. 7, pp. 4355–4364, July 2015.

[67] J. W. Simpson-Porco, Q. Shafiee, F. Dorfler, J. C. Vasquez, J. M. Guerrero, and F. Bullo, "Secondary Frequency and Voltage Control of Islanded Microgrids via Distributed Averaging," *Industrial Electronics, IEEE Transactions on,* vol. 62, pp. 7025-7038, Nov. 2015.

[68] L. Lin-Yu and C. Chia-Chi, "Consensus-Based Droop Control Synthesis for Multiple DICs in Isolated Micro-Grids," *Power Systems, IEEE Transactions on,* vol. 30, pp. 2243-2256, 2015.

[69] R. Olfati-Saber, J. A. Fax, and R. M. Murray, "Consensus and Cooperation in Networked Multi-Agent Systems," *Proceedings of the IEEE,* vol. 95, pp. 215-233, Jan. 2007.

[70] J. Schiffer, T. Seel, J. Raisch, and T. Sezi, "Voltage Stability and Reactive Power Sharing in Inverter-Based Microgrids With Consensus-Based Distributed Voltage Control," *Control Systems Technology, IEEE Transactions on,* vol. 24, pp. 96-109, Jan. 2016.

[71] http://spectracom.com. *SecureSync Time & Frequency Reference System*. Available: http://spectracom.com/products-services/precision-timing/securesync-time-and-frequency-reference-system

[72] M. Zhixin, X. Ling, V. R. Disfani, and F. Lingling, "An SOC-Based Battery Management System for Microgrids," *Smart Grid, IEEE Transactions on,* vol. 5, pp. 966-973, Mar. 2014.

[73] A. Hooshmand, B. Asghari, and R. K. Sharma, "Experimental Demonstration of a Tiered Power Management System for Economic Operation of Grid-Tied Microgrids," *Sustainable Energy, IEEE Transactions on,* vol. 5, pp. 1319-1327, Oct. 2014.

[74] T. Wang, D. O'Neill, and H. Kamath, "Dynamic Control and Optimization of Distributed Energy Resources in a Microgrid," *Smart Grid, IEEE Transactions on,* vol. 6, pp. 2884-2894, Nov. 2015.

[75] H. Kanchev, L. Di, F. Colas, V. Lazarov, and B. Francois, "Energy Management and Operational Planning of a Microgrid With a PV-Based Active Generator for Smart Grid Applications," *Industrial Electronics, IEEE Transactions on,* vol. 58, pp. 4583-4592, Oct. 2011.

[76] M. J. Hossain, H. R. Pota, M. A. Mahmud, and M. Aldeen, "Robust Control for Power Sharing in Microgrids With Low-Inertia Wind and PV Generators," *Sustainable Energy, IEEE Transactions on,* vol. 6, pp. 1067-1077, Jul. 2015.

[77] L. Nian, C. Qifang, L. Jie, L. Xinyi, L. Peng, L. Jinyong*, et al.*, "A Heuristic Operation Strategy for Commercial Building Microgrids Containing EVs and PV System," *Industrial Electronics, IEEE Transactions on,* vol. 62, pp. 2560-2570, Apr. 2015.

[78] K. T. Tan, X. Y. Peng, P. L. So, Y. C. Chu, and M. Z. Q. Chen, "Centralized Control for Parallel Operation of Distributed Generation Inverters in Microgrids," *Smart Grid, IEEE Transactions on,* vol. 3, pp. 1977-1987, Dec. 2012.

[79] W. Caisheng and H. Nehrir, "Power management of a stand-alone wind/photovoltaic/fuel-cell energy system," in *Proc. IEEE Power and Energy Society General Meeting*, 2008, pp. 1-1.

[80] W. Dan, T. Fen, T. Dragicevic, J. C. Vasquez, and J. M. Guerrero, "Autonomous Active Power Control for Islanded AC Microgrids With Photovoltaic Generation and Energy Storage System," *Energy Conversion, IEEE Transactions on,* vol. 29, pp. 882-892, Dec. 2014.

[81] A. Urtasun, E. L. Sanchis, P. Sanchis, and L. Marroyo, "Frequency-Based Energy-Management Strategy for Stand-Alone Systems With Distributed Battery Storage," *Power Electronics, IEEE Transactions on,* vol. 30, pp. 4794-4808, Sept. 2015.

[82] H. Mahmood, D. Michaelson, and J. Jin, "Decentralized Power Management of a PV/Battery Hybrid Unit in a Droop-Controlled Islanded Microgrid," *Power Electronics, IEEE Transactions on,* vol. 30, pp. 7215-7229, Dec. 2015.

[83] H. Mahmood, D. Michaelson, and J. Jin, "A Power Management Strategy for PV/Battery Hybrid Systems in Islanded Microgrids," *Emerging and Selected Topics in Power Electronics, IEEE Journal of,* vol. 2, pp. 870-882, Dec. 2014.

[84] L. Xiaonan, S. Kai, J. Guerrero, and H. Lipei, "SoC-based dynamic power sharing method with AC-bus voltage restoration for microgrid applications," in *Proc. 38th Annu. Conf. IEEE Ind. Electron. Soc. (IECON)*, 2012, pp. 5677-5682.

[85] L. Xiaonan, S. Kai, J. M. Guerrero, J. C. Vasquez, and H. Lipei, "Double-Quadrant State-of-Charge-Based Droop Control Method for Distributed Energy Storage Systems in Autonomous DC Microgrids," *Smart Grid, IEEE Transactions on,* vol. 6, pp. 147-157, 2015.

[86] R. Olfati-Saber, J. A. Fax, and R. M. Murray, "Consensus and Cooperation in Networked Multi-Agent Systems," *in Proceedings of the IEEE,* vol. 95, pp. 215-233, Jan. 2007.

[87] D. P. Spanos, R. Olfati-Saber, and R. M. Murray, "Dynamic consensus on mobile networks," in *IFAC world congress*, 2005, pp. 1-6.

[88] R. Wei and R. Beard, "Distributed Consensus in Multi-vehicle Cooperative Control Theory and Applications," ed: London: Springer-Verlag, 2008.

[89] F. Xiao and L. Wang, "Asynchronous Consensus in Continuous-Time Multi-Agent Systems With Switching Topology and Time-Varying Delays," *IEEE Transactions on Automatic Control,* vol. 53, pp. 1804-1816, Sept. 2008.

[90] O. Rojo, R. Soto, and H. Rojo, "An always nontrivial upper bound for Laplacian graph eigenvalues," *Linear Algebra and its Applications,* vol. 312, pp. 155-159, Jun. 2000.

[91] M. Golsorkhi and D. Lu, "A Control Method for Inverter-Based Islanded Microgrids Based on V-I Droop Characteristics," *IEEE Trans. Power Del.,* vol. PP, pp. 1-1, 2014.

[92] A. von Jouanne and B. Banerjee, "Assessment of voltage unbalance," *IEEE Trans. Power Del.,* vol. 16, pp. 782-790, Oct. 2001.

[93] P. C. Krause, O. Wasynczuk, and S. D. Sudhoff, *Analysis of electric machinery*: IEEE Press, 1995.

[94] J. M. Maciejowski, *Predictive control: with constraints*. New York: Prentice Hall, 2002.

[95] H. J. Ferreau, H. G. Bock, and M. Diehl, "An online active set strategy to overcome the limitations of explicit MPC," *International Journal of Robust and Nonlinear Control,* vol. 18, pp. 816-830, Jul. 2008.

[96] S. Papathanassiou, N. Hatziargyriou, and K. Strunz, "A benchmark low voltage microgrid network," in *Proceedings of the CIGRE Symposium: Power Systems with Dispersed Generation*, 2005, pp. 1-8.

[97] Y. Han, P. Shen, X. Zhao, and J. M. Guerrero, "Control Strategies for Islanded Microgrid Using Enhanced Hierarchical Control Structure With Multiple Current-Loop Damping Schemes," *IEEE Transactions on Smart Grid,* Sept. 2015.

[98] M. Lexuan, M. Savaghebi, T. Fen, T. Dragicevic, J. C. Vasquez, and J. M. Guerrero, "Dynamic consensus algorithm based distributed voltage harmonic compensation in islanded microgrids," in *Power Electronics and Applications (EPE'15 ECCE-Europe), 2015 17th European Conference on*, 2015, pp. 1-9.

[99] J. He, Y. W. Li, and F. Blaabjerg, "An Enhanced Islanding Microgrid Reactive Power, Imbalance Power, and Harmonic Power Sharing Scheme," *IEEE Transactions on Power Electronics,* vol. 30, pp. 3389-3401, June 2015.

[100] H. Mahmood, D. Michaelson, and J. Jin, "Accurate Reactive Power Sharing in an Islanded Microgrid Using Adaptive Virtual Impedances," *Power Electronics, IEEE Transactions on,* vol. 30, pp. 1605-1617, March 2015.

[101] M. Savaghebi, Q. Shafiee, J. C. Vasquez, and J. M. Guerrero, "Adaptive virtual impedance scheme for selective compensation of voltage unbalance and harmonics in microgrids," in *Proc. IEEE Power & Energy Society General Meeting*, 2015, pp. 1-5.

[102] M. S. Golsorkhi, D. Lu, M. Savaghebi, J. C. Vasquez, and J. M. Guerrero, "A GPS-Based Control Method for Load Sharing and Power Quality Improvement in Microgrids," in *Proc. International Power Electronics and Motion Control Conference (IPEMC-ECCE Asia)*, 2016.

[103] J. M. Guerrero, P. C. Loh, M. Chandorkar, and T.-L. Lee, "Advanced control architectures for intelligent MicroGrids – Part I: decentralized and hierarchical control," IEEE Trans. Ind. Electron., vol. 60, no. 4, pp. 1254-1262, Apr. 2013.

[104] P. Rodriguez, A. Luna, I. Candela, R. Mujal, R. Teodorescu, and F. Blaabjerg, "Multiresonant Frequency-Locked Loop for Grid Synchronization of Power Converters Under Distorted Grid Conditions," *IEEE Transactions on Industrial Electronics,* vol. 58, pp. 127-138, Jan. 2011.

[105] J. M. Guerrero, J. C. Vasquez, J. Matas, V. de, L. G. a, and M. Castilla, "Hierarchical Control of Droop-Controlled AC and DC Microgrids, A General Approach Toward Standardization," *Industrial Electronics, IEEE Transactions on,* vol. 58, pp. 158-172, Jan. 2011.

[106] C. D. Presti, F. Carrara, A. Scuderi, and G. Palmisano, "Fast Peak Detector with Improved Accuracy and Linearity for High-Frequency Waveform Processing," in *Proc. IEEE International Symposium on Circuits and Systems (ISCAS)*, 2007, pp. 3884-3887.

[107] M. Savaghebi, A. Jalilian, J. C. Vasquez, and J. M. Guerrero, "Secondary control for voltage quality enhancement in microgrids," IEEE Trans. Smart Grid, vol. 3, no. 4, pp. 1893-1902, Dec 2012.

[108] L. Yunwei, D. M. Vilathgamuwa, and L. Poh Chiang, "Microgrid power quality enhancement using a three-phase four-wire grid-interfacing compensator," *IEEE Trans. Ind. Appl.,* vol. 41, pp. 1707-1719, Nov. 2005.

[109] M. A. G. Sayani, B. K. Singh, J. Coulter, and K. E. Tepe, "Segment wise communication delay measurement for Smart Grid applications," in *Communications (QBSC), 2014 27th Biennial Symposium on*, 2014, pp. 139-143.

[110] A. H. Etemadi, E. J. Davison, and R. Iravani, "A Generalized Decentralized Robust Control of Islanded Microgrids," *Power Systems, IEEE Transactions on,* vol. 29, pp. 3102-3113, Nov. 2014.

[111] M. L. Sichitiu and C. Veerarittiphan, "Simple, accurate time synchronization for wireless sensor networks," in *Wireless Communications and Networking, 2003. WCNC 2003. 2003 IEEE*, 2003, pp. 1266-1273 vol.2.